

Adsorbate-adsorbate interactions on metal and metal oxide surfaces: critical role in surface structures and reactions

vorgelegt von
Master of science
Xunhua Zhao
aus Hubei, China

von der Fakultät II – Mathematik und Naturwissenschaften
der Technischen Universität Berlin
zur Erlangung des akademischen Grades
Doktor der Naturwissenschaften
Dr. rer. nat.

genehmigte Dissertation

Promotionsausschuss:

Vorsitzender: Prof. Dr. rer. nat. Martin Kaupp, TU Berlin
1. Gutachter: Prof. Dr. rer. nat. Reinhard Schomäcker, TU Berlin
2. Gutachter: Prof. Dr. rer. nat. Matthias Scheffler, FHI Berlin

Tag der wissenschaftlichen Aussprache: 10. 12. 2015

Berlin 2015
D 83

Abstract

Surface science/engineering of metals and metal oxides is crucial for a broad range of technologies. In surface science, there are two fundamental and technologically important questions: what are the surface composition and structure at realistic temperature and pressure conditions, and how are the surface properties affected by dynamics and chemical kinetics. Answering these questions is needed for the rational design of improved or new functional materials.

In this thesis, we focus on one particular aspect of the above problems: the adsorbate-adsorbate interactions on solid surfaces. Even though adsorbate-surface interactions have been well studied theoretically for many systems including the systems we are interested in, adsorbate-adsorbate interactions are much less understood. Nevertheless, there are hints in previous experimental reports that adsorbate-adsorbate interactions play a big role in many technologically important systems. The difficulties in studying such interactions computationally are several-fold. In particular, the extended nature of the surface, and at the same time the translational symmetry breaking due to the interactions between adsorbates, require large models and advanced techniques to resolve the atomic structure of the surface.

Two different systems are studied in this work: (i) water on alkaline-earth metal-oxide surfaces, and (ii) hydrocarbon species on the Ru(0001) surface. In the former case, our interest was triggered by a puzzling formation of one-dimensional (1D) features observed on CaO(001) terraces with scanning tunneling microscopy [1]. In the case of hydrocarbons on Ru(0001), recent experiments [2] indicated the presence of CH₂ on the surface at realistic temperatures after exposure to methane, which is in contradiction with previous theoretical predictions. In this case, our goal is to understand the stability of the CH₂ intermediate in particular, and to analyze the effects of coadsorption on the surface chemistry of hydrocarbons in general.

To resolve the atomic structure of the 1D features on CaO(001), we developed a genetic algorithm (GA) approach for interfaces. Using the GA, we found stable 1D structures on MgO(001) and CaO(001) but not on SrO(001). Our analysis showed that the stability of the 1D structures is determined by the interplay between adsorbed water-water and water-surface interactions. A balance between these interactions results in the thermodynamic stability of the 1D structures on CaO(001) at the experimental conditions, confirmed by the *ab initio* atomistic thermodynamics analysis. We also found that the most stable tetramer breaks the 4-fold symmetry of the surface, which paves the way for the 1D structure growth.

In the second part of our work, we found that coadsorbed hydrogen qualitatively changes the preferred site and the stability of CH₂ species, which is crucial for understanding the mechanism of Fischer-Tropsch synthesis. In addition to explaining the experimental results [2], hydrogen coadsorption is found to strongly influence the C-C bond-formation reactions: while it generally reduces all the coupling reaction barriers, some reaction paths become more favoured in the presence of the coadsorbed hydrogen. Our study resolves some of the controversies between existing theoretical and experimental studies.

For both systems studied in this thesis, we demonstrate the key role of adsorbate-adsorbate interactions, and the necessity for further studies of these complex phenomena. The methodology that we have developed, in particular the genetic algorithm approach, can be used for other surface systems, as well as for other surface properties, such as reconstruction or optimization of a property other than energy.

Zusammenfassung

Oberflächenwissenschaft und -technik von Metallen und Metalloxiden ist sehr bedeutend in vielen Technologiebereichen. In der Oberflächenwissenschaft gibt es zwei fundamentale und technologisch wichtige Fragestellungen: Welche Oberflächenstrukturen liegen bei realistischen Temperaturen und Drücken vor, und wie werden diese Oberflächeneigenschaften durch Dynamik und Kinetik beeinflusst. Die Beantwortung dieser beiden Fragen wird für die Entwicklung von verbesserten und neuen funktionellen Materialien benötigt.

In dieser Doktorarbeit fokussieren wir uns auf einen bestimmten Aspekt der oben genannten Probleme: Die Adsorbat-Adsorbat-Wechselwirkungen auf Festkörperoberflächen. Obwohl Adsorbat-Oberflächen-Wechselwirkungen schon eingehend theoretisch für etliche Systeme untersucht wurden — unter anderem auch für jene Systeme unserer Studie — sind die Adsorbat-Adsorbat-Wechselwirkungen nur wenig verstanden. Dennoch geben Experimente Hinweis darauf, dass eben diese Wechselwirkungen zwischen den Adsorbaten eine große Rolle in vielen technologisch wichtigen Systemen spielen. Die Schwierigkeiten in der theoretisch-numerischen Behandlung dieser Wechselwirkungen sind vielfältig. Insbesondere werden für die Beschreibung der Oberflächen in Verbindung mit Wechselwirkungen, die deren Translationssymmetrie aufheben, große Modelle und fortgeschrittenere Techniken benötigt, um die atomare Struktur der Oberfläche aufzulösen.

Zwei unterschiedliche Systeme werden wir in dieser Arbeit studieren: (i) Wasser auf Erdalkalimetalloxid Oberflächen und (ii) Kohlenwasserstoffverbindungen auf der Ru(0001)-Oberfläche. Im erstgenannten Beispiel haben wir unseren Fokus auf die Bildung von eindimensionalen (1D) Strukturen gelegt, welche mit Hilfe von Rastertunnelmikroskopie auf CaO(001)-Terrassen beobachtet wurden [1]. Im Falle der Kohlenwasserstoffe auf Ru(0001) zeigen kürzlich durchgeführte Experimente [2] bei realistischen Temperaturen die Anwesenheit von CH₂ an dieser Oberfläche nach einer Exponierung mit Methan. Dies steht jedoch im Widerspruch zu bisherigen theoretischen Vorhersagen. Darum ist es unser Ziel, im Einzelnen die Stabilität des CH₂-Zwischenproduktes zu analysieren und im Allgemeinen die Bedeutung der Koadsorption für die Oberflächenchemie zu verstehen.

Um die atomare Struktur des 1D Adsorbates auf CaO(001) zu verstehen, haben wir einen Generischen Algorithmus (GA) für Grenzflächen entwickelt. Mit Hilfe dieses GAs lassen sich auf MgO(001) und CaO(001) stabile 1D Strukturen vorhersagen, jedoch nicht auf SrO(001). Unsere Analyse zeigt, dass die Stabilität der 1D Strukturen durch das Zusammenspiel der Wasser-Wasser- und Wasser-Oberfläche-Wechselwirkungen zustande kommt. Die Balance zwischen diesen Wechselwirkungen bei den entsprechenden experimentellen Bedingungen führt zur thermodynamischen Stabilität der 1D Strukturen auf CaO(001), welche durch atomistische ab initio Thermodynamik bestätigt wird. Ebenso werden wir zeigen, dass das stabilste Tetramer die Vierfachsymmetrie der Oberfläche zerstört, welche den Weg zum Wachsen von 1D Strukturen bereitet.

Im zweiten Teil dieser Arbeit demonstrieren wir, wie koadsorbiertes Wasserstoff qualitativ die bevorzugte Adsorptionsposition und die Stabilität der CH₂-Spezies beeinflusst. Dieses Verständnis ist von enormer Bedeutung für den Mechanismus der Fischer-Tropsch-Synthese. Neben der Erklärung von experimentellen Ergebnissen, finden wir, dass die Wasserstoff-Koadsorption die Bildung von C-C-Bindungsreaktionen stark beeinflusst: Während generell alle Kopplungsreaktionsbarrieren herabgesetzt werden, werden einige Reaktionspfade durch die Anwesenheit des koadsorbierten Wasserstoffs besonders bevorzugt.

Für beide hier analysierten Systeme möchten wir die Schlüsselrolle der Adsorbat-Adsorbat-Wechselwirkung und die Notwendigkeit von weiterführenden Untersuchungen dieser komplexen Phänomene hervorheben. Die von uns entwickelte Methodik, im Besonderen der Ansatz des Generischen Algorithmus, kann sowohl für andere Oberflächensysteme, als auch für andere Oberflächeneigenschaften wie Rekonstruktion oder zur Optimierung anderer Eigenschaften als Energie verwendet werden.

Contents

1. Introduction	1
I. Describing and exploring potential-energy surfaces	5
2. Characterizing potential-energy surfaces	6
2.1. The Born-Oppenheimer potential-energy surface	6
2.2. Local optimization	8
2.3. Finding transition states and minimum energy paths	8
2.3.1. Nudged elastic band method	9
2.3.2. String method	9
2.4. Simulations of vibrational spectra	10
2.4.1. The harmonic approximation	11
2.4.2. Infrared (IR) spectra from molecular dynamics	13
2.5. Free-energy surface – <i>ab initio</i> atomistic thermodynamics	16
3. Exploring PES – implementation of genetic algorithm for surfaces	20
3.1. Introduction of global optimization	20
3.2. Our genetic algorithm implementation	22
4. <i>Ab initio</i> methods for electronic-structure calculations	26
4.1. Many-electron problem	26
4.2. Hartree-Fock theory	27
4.3. Density-functional theory	29
4.3.1. Hohenberg-Kohn theorems	29
4.3.2. The Kohn-Sham equations	30
4.3.3. Exchange-correlation approximations and hybrid functionals	32
4.4. Beyond Hartree-Fock, local, semilocal, and hybrid DFT: MP2, RPA, rPT2	35
4.5. Dispersion correction to the approximate DFT functionals	37
4.5.1. Tkatchenko-Scheffler (TS) scheme	38
4.5.2. Many-body effects of van der Waals interactions	39
4.5.3. The vdW ^{surf} method	40
4.6. Electronic-structure code of choice: FHI-aims	42
II. Water on alkline-earth metal-oxide surfaces	44
5. Interaction of water with alkaline-earth metal-oxide surfaces	45

6. Formation of water chains on CaO(001) surface	48
6.1. Computational Details	48
6.2. Validation of DFT functionals and the atomic models	50
6.3. Structures of water adsorbed on CaO(001)	52
6.4. Temperature-pressure phase diagram	57
6.5. Vibrational spectra of water on CaO(001)	57
7. Interaction of water with MgO(001) and SrO(001) surfaces	64
7.1. Structures of water adsorbed on MgO(001)	64
7.2. Temperature-pressure phase diagram	70
7.3. Structures of water adsorbed on SrO(001)	71
7.4. Discussion: What distinguishes CaO(001) from MgO(001) and SrO(001)? . . .	73
III. Hydrocarbon species on Ru(0001) surface	77
8. CH_x chemistry at the Ru(0001) surface: An introduction	78
9. CH_x+H_y adsorption on Ru(0001)	81
9.1. Surface model and computational settings	81
9.2. Convergence tests	82
9.3. Adsorption geometries and energies	85
9.3.1. Adsorption at the top and bridge sites	85
9.3.2. Adsorption at the hollow sites	86
9.4. Thermodynamic stability analysis	92
10. CH₂ dissociation: The effects of coadsorbed hydrogen	94
10.1. Reaction paths	94
10.2. Discussion	97
11. C-C coupling and C-chain propagation at high (T, p_{H_2})	99
11.1. Formation of C2 under UHV conditions	101
11.1.1. Adsorption and thermodynamics	101
11.1.2. Formation paths	105
11.1.3. Discussions	105
11.2. C-C coupling at high (T, p_{H_2}) and new insights into chain propagation mechanism of Fischer-Tropsch synthesis	106
11.2.1. C1 species under at high (T, p_{H_2})	107
11.2.2. C2 formation from C1-C1 coupling precursors	108
11.2.3. Carbon chain growth mechanisms on Ru(0001) at high (T, p_{H_2})	112
IV. Concluding remarks	116
12. Conclusions and outlook	117

12.1. Concluding remarks	117
12.2. Outlook	118
Appendices	120
A. Convergence tests for basis sets and thickness of the oxide slab model	121
B. FHI-aims standard NAO basis sets for H, C, O, Mg, Ca, Sr, and Ru.	123
C. vdW parameters	126
Bibliography	127

1. Introduction

Metals and metal oxides are key components for a wide range of applications due to their tailorable physical and chemical properties. As an example, catalysts containing precious metals such as platinum and palladium convert NO_x and CO in exhaust gas into non-toxic N_2 and CO_2 [3, 4]. Gas sensors [5, 6, 7], which typically detect oxygen depletion, as well as flammable and toxic gases, is another prominent example where metals and metal oxides play a key role. Furthermore, these materials are used at a large scale in chemical industry as catalysts to accelerate reactions and decrease reaction temperature and/or pressure. Chemical commodities produced by the catalytic processes [8, 9, 10, 11, 12, 13] include fertilizers, liquid fuels, and chemical precursors such as ethylene, which is the most produced among all organic products. In this thesis, focus is put on surface properties of one type of metal oxides (alkaline metal oxide (001) surface) and one metal system (Ru(0001) surface). Nevertheless, the phenomena investigated and the methods developed/illustrated in this thesis are relevant for other systems as well.

Alkaline-earth metal oxides have been found to have catalytic activity for variety of reactions [14, 15, 16, 17], including oxidative coupling of methane (OCM) [18, 19, 14]. Traditional ways to convert methane, the main component of the natural gas, involve dry or steam reforming to a mixture of mainly hydrogen and CO (syngas), which can then be converted to liquid fuels and chemical precursors via additional processes [20]. The disadvantages of this scheme are the high temperatures and pressures required for the generation of syngas, as well as low energy efficiency due to the two-stage approach. Therefore, direct conversion of methane into chemicals, starting with ethylene, is highly desirable. The oxidative coupling of methane is such a direct way to convert methane.

Activating hydrocarbons, especially methane, while avoiding its full oxidation, proved to be extremely challenging. Alkaline earth metal oxides, doped or pure, were found to be promising catalysts to convert methane into ethylene in an oxidative atmosphere. For interested reader, recent advances about catalytic OCM chemistry and engineering can be found in a critical review [14]. Here, we mainly focus on one aspect of this intricate chemistry: the interaction of water with the alkaline-earth metal-oxide surfaces. In addition, we investigate the interaction between methane and MgO surface containing structural defects such as steps and corners.

From a broader perspective, interaction of water with oxide surfaces is of general interest in a wide range of disciplines due to the abundance of water and its often strong effects on the surface, e.g. corrosion. A specific motivation for this project is the formation of one-dimensional structures on CaO(001) thick (>20 layers) Mo-supported films exposed to water vapor, observed by scanning tunnelling microscopy (STM) at ultra-high vacuum conditions [1]. The formation of such stable adsorbate super-structures from small molecules highlights the importance of adsorbate-adsorbate interaction, which has been much less studied compared to adsorbate-substrate interactions. While the adsorbate-substrate interaction typically dominates the main features of the adsorbate, i.e., adsorption/desorption, reaction/stabilization, the

adsorbate-adsorbate interaction have also been found to have a profound influence on the surface species. In particular, water forms diverse types of structures on metal surfaces [21, 22, 23]. Modelling the adsorbate-adsorbate interactions presents several challenges. First, the adsorbate super-structures formed on the surface may require large super-cell sizes in periodic models to represent the adsorbate-substrate system. Second, weak but long-range interactions such as van der Waals forces can have a significant contribution to the superstructure stability. Since conventional DFT functionals do not describe accurately such weak interactions, more advanced methods need to be used. Furthermore, the experiments are done at finite temperature and pressure, while the results obtained directly from DFT calculations of surfaces correspond to zero temperature and pressure.

The above challenges are related to the accuracy of the potential-energy surface (PES) or the free-energy surface. Exploring the potential-energy surface at a high level of theory is another major challenge. One problem is to exhaustively search for low-energy structures. Since the number of possible configurations increases exponentially with the number of adsorbed atoms and/or molecules, finding the low-energy structures becomes extremely challenging. Due to the fact that adsorbed water molecules can be partially dissociated [24, 25], and hydrogen bonding networks [26] can form, the adsorbate-adsorbate interactions and superstructure formation problem require a global optimization algorithm.

The second project presented in this thesis addresses another case of adsorbate-adsorbate interaction and its influence on reaction paths and energetics at realistic temperature and pressure conditions [2]. CH_x ($x = 0-3$) are important intermediates in hydrocarbon chemistry where two prominent examples are the steam reforming of methane [27, 28, 29] and the Fischer-Tropsch synthesis (FTS) of long-chain hydrocarbons from the syngas [30, 31, 32, 33, 34, 35]. Knowing the relative stability of the CH_x intermediates is of great importance for understanding the methane conversion mechanisms [36, 37, 38]. For instance, CH_2 has been proposed to be the building block in FTS from 1920s [30] by the inventors of the process and got strong support in 1980s from isotope experiments [39, 40]. However, the mechanism of carbon chain growth by adding CH_2 units has been challenged during last 15 years mainly due to the obvious instability of CH_2 compared to other CH_x species, according to previous theoretical [41, 37, 35] and experimental [32] studies. Despite a very low calculated dissociation barrier for $\text{CH}_2 \rightarrow \text{CH} + \text{H}$ on the Ru(0001) surface, CH_2 has been recently observed by vibrational sum-frequency generation spectroscopy on Ru dosed with methane, and has been found to persist on the surface up to relatively high annealing temperatures [2]. By correlating the signal intensity with the annealing temperature, we derived the apparent activation energy for CH_2 dissociation, and found that it is more than four times larger than previous reported theoretical results. Our analysis revealed that two additional factors had to be included into theoretical modelling in order to reconcile theory and experiment: finite temperature and pressure, as well as the large configurational space for adsorbed species. In particular, we found that hydrogen atoms coadsorbed with CH_x species have a dramatic influence on the dissociation barrier of CH_2 .

Conventional generalized gradient approximations (GGA) to the DFT functional (e.g. PBE [42]) in many cases provide a good trade-off between accuracy and computational cost. However, they suffer from the self-interaction error, which leads to an artificial electron delocalization. Thus, GGAs fail to describe properties of materials that are affected by the self-interaction error, in particular in oxides, where the localized 2p orbitals of O play an important role in bond

formation/breaking. In hybrid functionals (such as HSE06 [43, 44]), a fraction of the local or semilocal exchange is replaced with the exact exchange, which reduces the self-interaction error. However, the fraction of the exact exchange is a parameter which needs to be validated. Also, neither PBE nor HSE06 describe the long-range dispersion (van der Waals, vdW) interaction correctly. To address these issues, we use an *ab initio* many-body vdW correction [45], and benchmark the corrected functionals against a state-of-the-art method in the framework of DFT, namely, renormalized second-order perturbation theory (rPT2) [46]. First-principles genetic algorithm (GA) [47, 48, 49] for surface structures is implemented to explore the potential energy surface and search for low-energy structures. Transition states are searched using the string method [50]. To take into account effects of finite temperature and pressure, *ab initio* atomistic thermodynamics [51, 52, 53] is employed. Finite-temperature vibrational spectra are derived from the time-autocorrelation function obtained with *ab initio* molecular dynamics (MD).

For water interacting with alkaline-earth metal-oxide surfaces, we calculate relative stability of adsorbed water structures on MgO(001), CaO(001) and SrO(001) using density-functional theory with the hybrid functional HSE06 and many-body dispersion interaction correction, combined with the *ab initio* atomistic thermodynamics. Low-energy structures at coverages up to 1.25 monolayer (ML) are obtained with a first-principles genetic algorithm. Finite-temperature anharmonic vibrational spectra are calculated using *ab initio* molecular dynamics. We find a range of $(T, p_{\text{H}_2\text{O}})$ conditions where 1D structures are thermodynamically stable on CaO(001) [1] while 1D structures are found to be thermodynamically stable on a stretched MgO(001) surface. The orientation and vibrational spectra of the 1D structures on CaO(001) are in agreement with experiments. Through detailed analysis, the formation of the 1D structures on CaO(001) is found to be initiated by a symmetry breaking in the adsorbed water tetramer, as well as by a balance between water-water and water-substrate interactions, determined by the lattice constant of the substrate.

For the CH_x species on Ru(0001) surface, we show the important role of coadsorbed hydrogen through density-functional theory calculations. All possible CH_x+yH configurations with adsorbates at hollow sites are calculated for a (2×2) slab model. CH_x dissociation barriers are obtained using the string method. We further demonstrate, by calculating the surface phase diagram for one-carbon species on Ru(0001) as a function of H_2 chemical potential, that the stabilization of CH_2 by coadsorbed hydrogen requires non-equilibrium conditions. The calculated barrier for the CH_2 dissociation in the presence of hydrogen is significantly increased, and is close to the one recently measured by vibrational sum-frequency generation spectroscopy [2]. Our results also explain why CH_2 was not observed when C or CH are hydrogenated on Ru(0001) [54], although it is observed after methane or methyl iodide (CH_3I) decomposition [55]. Furthermore, the role of CH_2 in the chain growth mechanism under FT conditions is investigated.

The thesis is organized in three main parts. It starts with a discussion of the first-principles methodology for exploring the PES, followed by the study of water structures on alkaline-earth metal-oxide surfaces, and the analysis of the effects of coadsorbed hydrogen on CH_x stability and C-C coupling reactions. In the first part, the concept of the PES is introduced, followed by three aspects of characterizing the PES (Chp. 2): transition-state searching, and the calculation of vibrational spectra and free-energy surface. A method to explore the global minimum on the PES (Chp. 3)-genetic algorithm-is described with our detailed implementations. The *ab initio* electron structure calculations (Chp. 4) behind every point of PES is described thereafter.

Density-functional theory (DFT) is introduced with conventional functionals, as well as more advanced hybrid functionals, random-phase approximation (RPA) methods and many-body dispersion correction in the framework of DFT. The results and discussion of the interaction of water with oxide surfaces are split into two parts: (i) the identification of 1D structure form on CaO(001) (Chp. 6), and (ii) water structures form on MgO(001) and SrO(001), as well as the general trends in the interaction of water with alkaline-earth metal oxides (Chp. 7). The results and discussion of the hydrogen coadsorption effects on CH_x are presented in three parts: (i) the surface phase diagrams for $\text{CH}_x + y\text{H}@\text{Ru}(0001)$ (Chp. 9); (ii) the pathways for CH_2 dissociation on both the bare Ru(0001) surface and the surface with the coadsorbed hydrogen (Chp. 10); (iii) and finally we present results on the carbon chain growth (Chp. 11) at typical high-pressure and high-temperature conditions where coadsorption of hydrogen plays a critical role in the C-C bond-formation mechanism.

Part I.

Describing and exploring potential-energy surfaces

2. Characterizing potential-energy surfaces

In principle, a complete information about the atomic system of interest can be obtained by solving the Schrödinger equation. In practice, the exact solution of this equation for polyatomic systems is not feasible and approximations are necessary. Separating the dynamics of nuclei and electrons is usually the first step, which is discussed in the following section. As a result of this separation, it becomes possible to treat the electrons as quantum particles in the static field created by nuclei at each point in time, while the nuclei are treated quasiclassically. Thus, for a given chemical composition, the total energy of the system is a function of nuclear positions. Such a dependency can be understood by using the analogy of landscape in two dimensions, so it is called potential-energy surface (PES). This framework enables to understand and also simulate a large amount of physical and chemical phenomena, including polyatomic structures and chemical reactions. The corresponding approximations are described in Chp. 4. Like in the case of an actual landscape, there are special points on PES, namely local minima and transition states, which determine molecular structures and reaction rates. The local minima are also characterized by the curvature of PES around the minimum, which is reflected in vibrational frequencies. Details on the concept of PES (Sec. 2.1), methods for finding transition states (Sec. 2.3), and approaches to calculating vibrational spectra (Sec. 2.4) are described in this chapter.

2.1. The Born-Oppenheimer potential-energy surface

The key to accessing the ground-state energy and related properties of an atomic system with many electrons at \mathbf{r}_i with spin σ_i ($i = 1, \dots, N_{\text{el}}$) and nuclei at \mathbf{R}_I ($I = 1, \dots, N_{\text{nuc}}$) is solving the time-independent Schrödinger equation:

$$\hat{\mathcal{H}}|\Phi(\mathbf{R}_1, \dots, \mathbf{R}_{N_{\text{nuc}}}, \mathbf{x}_1, \dots, \mathbf{x}_{N_{\text{el}}})\rangle = \mathcal{E}|\Phi(\mathbf{R}_1, \dots, \mathbf{R}_{N_{\text{nuc}}}, \mathbf{x}_1, \dots, \mathbf{x}_{N_{\text{el}}})\rangle, \quad (2.1)$$

where $\hat{\mathcal{H}}$ is the Hamilton operator and $\Phi(\mathbf{R}_1, \dots, \mathbf{R}_{N_{\text{nuc}}}, \mathbf{x}_1, \dots, \mathbf{x}_{N_{\text{el}}})$ is the many-particle wave function which is defined in the Hilbert space, \mathbf{x}_i denotes the combination of spatial orbital and spin orbital: $\mathbf{x}_i = \{\mathbf{r}_i, \sigma_i\}$ ($i = 1, \dots, N_{\text{el}}$). In general, the variational principle can be applied to obtain the the ground-state eigenvalue \mathcal{E}_0 and eigenvector Φ_0 :

$$\mathcal{E}_0 = \langle \Phi_0 | \hat{\mathcal{H}} | \Phi_0 \rangle \leq \langle \Phi | \hat{\mathcal{H}} | \Phi \rangle, \quad (2.2)$$

where Φ is an arbitrary but normalized element of the same Hilbert space.

The many-particle Hamiltonian without relativistic effects for an atomic system contains the kinetic energy of both electrons and nuclei and potential energy which arises from the Coulomb interaction between each pair of charged particles:

$$\hat{\mathcal{H}} = \hat{T}_{\text{n}} + \hat{T}_{\text{e}} + V_{\text{n-n}} + V_{\text{e-e}} + V_{\text{e-n}}. \quad (2.3)$$

The different contributions (atomic units are used) are the kinetic energy of the nuclei

$$\hat{T}_n = - \sum_{k=1}^{N_{\text{nuc}}} \frac{1}{2M_k} \Delta_{\mathbf{R}_k}, \quad (2.4)$$

where M_k is the ratio of the mass of nucleus k and the mass of an electron, the kinetic energy of the electrons

$$\hat{T}_e = - \sum_{i=1}^{N_{\text{el}}} \frac{\Delta_{\mathbf{r}_i}}{2} = \sum_{i=1}^{N_{\text{el}}} \hat{t}_i^e, \quad (2.5)$$

the nuclear-nuclear interaction

$$V_{n-n} = \sum_{\substack{k,k'=1 \\ k \neq k'}}^{N_{\text{nuc}}} \frac{Z_k Z_{k'}}{2|\mathbf{R}_k - \mathbf{R}_{k'}|}, \quad (2.6)$$

the electron-electron interaction

$$V_{e-e} = \sum_{\substack{i,i'=1 \\ i \neq i'}}^{N_{\text{el}}} \frac{1}{2|\mathbf{r}_i - \mathbf{r}_{i'}|}, \quad (2.7)$$

and the electron-nuclear interaction

$$V_{e-n} = - \sum_{i=1}^{N_{\text{el}}} \sum_{k=1}^{N_{\text{nuc}}} \frac{Z_k}{|\mathbf{r}_i - \mathbf{R}_k|} = \sum_{i=1}^{N_{\text{el}}} v_i^{\text{ext}}. \quad (2.8)$$

For all elements, the nuclei are 10^3 - 10^5 times heavier than an electron, so that their motions are typically assumed to take place on much larger time scales, compared to which the time needed for electrons to adjust to the nuclear positions is negligibly small. This implies that the nuclei can be considered as moving on the potential energy surface for a particular electronic state, unless the electronic states are (near-)degenerate, in which case the potential energy surfaces for the electronic states are non-adiabatically coupled. Neglecting the non-adiabatic coupling is known as the Born-Oppenheimer approximation. Based on this approximation, the atomic system's wave function can be written as a product of the electronic and the nuclear wave functions $|\Phi\rangle = |\Psi\rangle|\chi\rangle$. For a system consisting of nuclei at $\mathbf{R} = [\mathbf{R}_1, \dots, \mathbf{R}_{N_{\text{nuc}}}]$, the electronic structure is described by the electronic Schrödinger equation

$$\hat{H}|\Psi(\mathbf{R}, \mathbf{x})\rangle = E(\mathbf{R})|\Psi(\mathbf{R}, \mathbf{x})\rangle, \quad (2.9)$$

where where $\hat{H} = \hat{T}_e + V_{e-e} + V_{e-n}$ is the many-electron Hamiltonian. Eq. 2.9 can then be solved, though numerically, by applying the variational principle for given nuclei positions. Due to its importance and richness of methods, a separated chapter (Chp. 4) is devoted to the many-electron problem. The nuclear motion is described by the nuclear Schrödinger equation

$$\hat{H}_{\text{nuc}}|\chi(\mathbf{R})\rangle = [\hat{T}_n + V_{n-n} + E(\mathbf{R})]|\chi(\mathbf{R})\rangle = \mathcal{E}_{\text{BO}}|\chi(\mathbf{R})\rangle, \quad (2.10)$$

\mathcal{E}_{BO} is the Born-Oppenheimer approximation to the energy \mathcal{E} of the full coupled system in Eq. 2.1, including electronic, vibrational, and translational contributions. The effective potential in which nuclei move, as a function of nuclei positions, forms the Born-Oppenheimer potential energy surface: $V_{\text{BO}}(\mathbf{R}) = V_{n-n}(\mathbf{R}) + E(\mathbf{R})$

2.2. Local optimization

Local minima of the potential-energy surface represent stable or metastable atomic structures. They can be found using local optimization methods starting from a given geometry. This is also a necessary step in global optimization methods, such as basin hopping and genetic algorithm. The local optimization scheme used in this thesis is the Broyden-Fletcher-Goldfarb-Shanno (BFGS) method. A brief sketch of the method is as follows. The Taylor series of a function $f(\mathbf{R})$ is:

$$f(\mathbf{R}) = f(\mathbf{R}_n + \Delta\mathbf{R}) \simeq f(\mathbf{R}_n) + \nabla f(\mathbf{R}_n)^T \Delta\mathbf{R} + \frac{1}{2} \Delta\mathbf{R}^T H(\mathbf{R}_n) \Delta\mathbf{R}, \quad (2.11)$$

where $\nabla f(\mathbf{R})$ is the gradient and H is the Hessian matrix and "T" denotes transpose of the matrix. A stationary point can be found by taking derivative of the above expression with respect to $\Delta\mathbf{R}$ and setting it to zero:

$$\nabla f(\mathbf{R}_n + \Delta\mathbf{R}) \simeq \nabla f(\mathbf{R}_n)^T + H(\mathbf{R}_n) \Delta\mathbf{R} = 0 \quad (2.12)$$

Then $\Delta\mathbf{R} = -\nabla f(\mathbf{R}_n) H^{-1}(\mathbf{R}_n)$. In Newton's method, each iteration includes calculating the gradient and Hessian matrix for the current position, and then evaluating $\Delta\mathbf{R}$. Since the Hessian matrix $H(\mathbf{R}_n)$ is computationally expensive to obtain, it is approximated in different ways in quasi-Newton methods. The BFGS method adopts a way to calculate the current Hessian by adding approximated updates to the (inverse) Hessian based on the previous iteration. The detailed update scheme can be found in textbooks (e.g. [56]). It is not surprising that BFGS in general converges faster than algorithms that do not involve Hessian, such as the gradient descent method and the conjugated gradient method.

2.3. Finding transition states and minimum energy paths

Besides local minimization, finding minimum-energy path (MEP) connecting neighbouring local minima of interest is also an important part of exploring a potential-energy surface. According to the transition-state theory [57], the rate of a reaction can be estimated from the initial local minimum and the saddle point on the potential energy surface. Mathematically, the saddle points are critical points satisfying:

$$\nabla(V(\mathbf{R})) = 0, \quad (2.13)$$

where $V(\mathbf{R})$ is the potential energy of the polyatomic system, as a function of the nuclei positions \mathbf{R} and ∇ denotes the gradient.

Several methods were developed to find saddle points. The Dimer method [58] is a general and effective approach to find saddle points. However, since the information about the final state is not used in this method, there is no guarantee that the saddle point found by the method is the target one. Nudged elastic band (NEB) methods [59, 60], especially the climbing-image variant (CI-NEB) [61] are very popular methods to find saddle points. They use an evolving nudged elastic chain of structure images to connect the initial state and the final state, and yield not only

the saddle point, but also the minimum-energy path. In the string method [50, 62], the initial and final states are connected by an intrinsically parametrized string instead of a chain of images. In this section, the CI-NEB method and the string method are briefly reviewed. A more detailed derivation and benchmarks can be found in the original publications.

2.3.1. Nudged elastic band method

The basic idea of the NEB method is to connect two adjacent local minima with an elastic chain of states, then evolve the chain of states until some criteria are satisfied. Let $(\mathbf{x}_0, \mathbf{x}_1, \dots, \mathbf{x}_N)$ be initial positions of the image structures in the configurational space, with \mathbf{x}_0 and \mathbf{x}_N being the positions of the initial and final states, respectively. The energy for the chain is defined as:

$$E = E(\mathbf{x}_1, \mathbf{x}_2, \dots, \mathbf{x}_N) = \sum_i V(\mathbf{x}_i) + \frac{k\Delta s}{2} \sum_{j=1}^N \left| \frac{\mathbf{x}_j - \mathbf{x}_{j-1}}{\Delta s} \right|^2, \quad (2.14)$$

where $V(\mathbf{x}_i)$ is the potential energy of the configuration \mathbf{x}_i , Δs is a numerical parameter whose value is typically comparable to the distance between adjacent images, and k is another parameter, proportional to the spring constant. The chain is moved according to the normal component of the potential force and tangential component of the spring force:

$$\dot{\mathbf{x}}_i \propto -\nabla V(\mathbf{x}_i)^\perp + (\mathbf{F}_i^s \cdot \hat{\tau}_i) \hat{\tau}_i, \quad i = 1, 2, \dots, N-1, \quad (2.15)$$

where $\dot{\mathbf{x}}_i$ represents the displacement of the image i in one move and \perp denotes the normal component of a vector, $\mathbf{F}_i^s = k(\mathbf{x}_{i+1} + \mathbf{x}_{i-1} - 2\mathbf{x}_i)/\Delta s$, $\hat{\tau}_i$ denotes the tangential vector along the elastic band at \mathbf{x}_i . Since the two terms in the right-hand side of Eq. 2.15 are perpendicular to each other, as $\dot{\mathbf{x}}_i$ vanishes, both of them should approach zero for $\dot{\mathbf{x}}_i$ to vanish. In particular, in equilibrium

$$-\nabla V(\mathbf{x}_i)^\perp = 0, \quad i = 1, 2, \dots, N, \quad (2.16)$$

i.e., each image is on the minimum-energy path. The potential problem for NEB method is that the true saddle point lies between two images and its energy is generally underestimated. The climbing-image nudged elastic band (CI-NEB) method cures this problem by introducing a climbing image after the convergence of NEB. The climbing image, unlike other images in the chain, moves towards the saddle point following the potential with the component along the elastic band inverted:

$$\dot{\mathbf{x}}_{\max}^{\text{climb}} \approx -\nabla V(\mathbf{x}_{\max})^\perp + 2\nabla V(\mathbf{x}_{\max}) \cdot \hat{\tau}_{\max} \hat{\tau}_{\max}, \quad (2.17)$$

where "max" denotes the image with highest energy along the path.

2.3.2. String method

As indicated by its name, the string method uses a string to connect the initial and final states. The string is parametrized dynamically according to known points along the string. Suppose γ is a string that connects initial and final states. Then finding the MEP is equivalent to finding a solution to the equation:

$$-(\nabla V)^\perp(\gamma) = 0, \quad (2.18)$$

where $(\nabla V)^\perp$ is the component of ∇V normal to γ :

$$(\nabla V)^\perp(\gamma) = (\nabla V) - (\nabla V \cdot \hat{\tau})\hat{\tau}, \quad (2.19)$$

with $\hat{\tau}$ being the unit tangential vector along the string γ . The numerical steps begin with parametrization of the string γ :

$$\gamma = \{\varphi(\alpha) : \alpha \in [0,1]\} \quad (2.20)$$

The MEP satisfies $(\nabla V)^\perp(\gamma_{\text{MEP}}) = 0$, so it is a global minimum of the functional:

$$F[\gamma] = \int_0^1 |(\nabla V)^\perp(\varphi(\alpha))|^2 d\alpha \quad (2.21)$$

over all possible paths between $\alpha = 0$ and $\alpha = 1$. In practice, the string is parametrized using a discrete number of points (images) $\{\varphi_i(t), i = 1, 2, \dots, N\}$. The parametrization is done by interpolating the string between the images. The path tangential can then be calculated directly from the interpolation.

The problem of minimizing $F[\varphi]$ can be cast into a dynamic form [50]). The images are evolved via the evolution step and reparametrization step:

1. *Evolution* The discrete points along the string are evolved over time interval Δt according to the potential force:

$$\dot{\varphi}_i = -(\nabla V)^\perp(\varphi_i) \quad (2.22)$$

2. *Reparametrization* The points are redistributed along the string. This redistribution plays a role similar to that of the springs in NEB, but is more flexible due to the freedom to choose the image density based on the intrinsic properties of the string.

2.4. Simulations of vibrational spectra

A vibrational spectrum can serve as a signature of chemical bonds and how they are affected by nearby species. In particular, vibrational spectroscopy (often referred to as infrared (IR) spectroscopy due to the typical range of photon energies for transitions between vibrational states) can be used to identify surface intermediates and peptide structures, with the help of theory [21, 63]. As described in the following, vibrations of an atomic system characterize important features of the potential-energy surface (PES) for that system. Calculating vibrational frequencies allows to calculate not only vibrational spectra, but also the vibrational free energy. Thus, simulation of molecular vibrations plays an important role in exploring both the PES and the free-energy surface (FES) at a finite temperature. In this thesis, we use first-principles modelling to simulate IR spectra, either at $T = 0$ K or at finite temperatures. At $T = 0$ K, the IR spectra are calculated within the harmonic approximation, while the IR spectra at finite temperatures are derived from auto-correlation of dipole moments obtained from *ab initio* molecular-dynamics simulations.

2.4.1. The harmonic approximation

Under the Born-Oppenheimer (BO) approximation, the dynamics of nuclei and electrons is decoupled, with the nuclei moving on the Born-Oppenheimer PES $V_{\text{BO}}(\{\mathbf{R}_I\})$. If the nuclear quantum effects can be neglected, the nuclear motion is described by Newton's second law:

$$M_I \ddot{\mathbf{R}}_I = \mathbf{F}_I = -\frac{\partial V_{\text{BO}}(\{\mathbf{R}_I\})}{\partial \mathbf{R}_I}, \quad (2.23)$$

where $V_{\text{BO}}(\{\mathbf{R}_I\})$ is defined as:

$$V_{\text{BO}}(\{\mathbf{R}_I\}) = V_{\text{nn}}(\{\mathbf{R}_I\}) + E(\{\mathbf{R}_I\}) = \frac{1}{2} \sum_I^N \sum_{J \neq I}^N \frac{Z_I Z_J}{|\mathbf{R}_I - \mathbf{R}_J|} + E^e(\{\mathbf{R}_I\}). \quad (2.24)$$

The first term is the nuclear-nuclear Coulomb interaction energy, and the second term is the total energy for a given nuclear configuration $\{\mathbf{R}_I\}$. In this thesis, $V_{\text{BO}}(\{\mathbf{R}_I\})$ is always obtained by *ab initio* calculations.

Let us define a set of atomic coordinates \hat{q}_I referenced to a local minimum on the PES: $\hat{q}_I = (\mathbf{R}_I - \mathbf{R}_{I,0})$. We can expand the PES around this local minimum for a small $|\hat{q}_I|$:

$$V_{\text{BO}}(\{\hat{q}_I\}) = V_{\text{BO}}(0) + \sum_I^{3N} \left(\frac{\partial V_{\text{BO}}}{\partial \hat{q}_I} \right)_0 \cdot \hat{q}_I + \frac{1}{2} \sum_I^{3N} \sum_J^{3N} \left(\frac{\partial^2 V_{\text{BO}}}{\partial \hat{q}_I \partial \hat{q}_J} \right)_0 \cdot \hat{q}_I \hat{q}_J + \dots, \quad (2.25)$$

where the first term is a constant offset and the second term is zero for a local minimum configuration. The third term plays a major role in molecular vibrations. If higher-order terms are neglected, the equation of motion (Eq. 2.23) can be rewritten as:

$$m_I \ddot{\hat{q}}_I = -\frac{\partial V_{\text{BO}}}{\partial \hat{q}_I} = -\sum_J^{3N} \left(\frac{\partial^2 V_{\text{BO}}}{\partial \hat{q}_I \partial \hat{q}_J} \right)_0 \cdot \hat{q}_J. \quad (2.26)$$

It is convenient to further rewrite the equation by defining mass-weighted coordinates $q_I = \sqrt{m_I} \hat{q}_I$:

$$\ddot{q}_I = -\sum_J^{3N} \left(\frac{\partial^2 V_{\text{BO}}}{\partial q_I \partial q_J} \right)_0 \cdot q_J. \quad (2.27)$$

Eq. 2.27 can be recast into an eigenvalue problem by substituting $q = \mathbf{A} \cos(\omega t + \phi)$. This form implies that all atoms oscillate at the same frequency ω with different amplitudes which are defined in \mathbf{A} . The result is:

$$\omega^2 \mathbf{A} = \mathbf{H} \mathbf{A}, \quad (2.28)$$

where $\mathbf{H} = \left(\frac{\partial^2 V_{\text{BO}}}{\partial q_I \partial q_J} \right)_0$ is the Hessian matrix in mass-weighted coordinates. Since the matrix \mathbf{H} is symmetric, the matrix $\mathcal{A} = (\mathbf{A}_1 \mathbf{A}_2 \dots \mathbf{A}_{3N})$ can be chosen to be unitary: $\mathcal{A}^T \mathcal{A} = \mathcal{A} \mathcal{A}^T = 1$. Solving Eq. 2.28 gives a series of vibrational modes, known as *normal modes*:

$$\mathbf{q}(t) = \mathbf{A}_n \cos(\omega_n t + \phi_n), \quad n = 1, 2, \dots, 3N. \quad (2.29)$$

In general, a system with N atoms has $3N$ spatial degrees of freedom, three of which correspond to the translations, and another three (or two for a linear molecule) describe the rigid rotations. The remaining $3N - 6$ (or $3N - 5$) degrees of freedom correspond to the inter-molecular vibrations. Thus, Eq. 2.28 should have six/five zero eigenvalues and $(3N - 6)/(3N - 5)$ positive eigenvalues for a molecule at its local energy minimum. A negative eigenvalue indicates that the molecule is at a saddle point rather than a local minimum. In this thesis, the Hessian matrix entering Eq. 2.26 is calculated by finite differences of analytic gradients: a small displacement (0.0025 \AA , carefully tested for the numerical stability) of atoms along the Cartesian coordinates is performed, and the numerical derivatives of the gradients are then calculated.

The amplitude matrix \mathcal{A} generates the transformation to the so-called normal coordinates:

$$\mathbf{Q} = \mathcal{A}^T \mathbf{q}. \quad (2.30)$$

The normal coordinates are extremely useful because the potential energy decouples in these coordinates:

$$V_{\text{BO}} = \frac{1}{2} \mathbf{q}^T \mathbf{H} \mathbf{q} = \frac{1}{2} \mathbf{q}^T (\mathcal{A} \mathcal{A}^T) \mathbf{H} (\mathcal{A} \mathcal{A}^T) \mathbf{q} = \frac{1}{2} (\mathbf{q}^T \mathcal{A}) (\mathcal{A}^T \mathbf{H} \mathcal{A}) (\mathcal{A}^T \mathbf{q}) = \frac{1}{2} \sum_{I=1}^{3N} \omega_I^2 Q_I^2. \quad (2.31)$$

Since in all cases interesting for us the vibrational degrees of freedom can be decoupled from rotations and translations without sacrificing the accuracy [64], the Schrödinger equation for the nuclei in normal coordinates is:

$$-\frac{\hbar^2}{2} \sum_I^{N_{\text{vib}}} \frac{\partial^2 \Phi_V}{\partial Q_I^2} + \frac{1}{2} \sum_I^{N_{\text{vib}}} \omega_I^2 Q_I^2 \Phi_V = E_V \Phi_V, \quad (2.32)$$

where $N_{\text{vib}} = 3N - 6$ for a non-linear molecule, $N_{\text{vib}} = 3N - 5$ for a linear molecule, and Φ_V is the vibrational wave function. Since in the harmonic approximation the motion of nuclei along each normal coordinate is decoupled from the rest, Φ_V has the following form:

$$\Phi_V = \Phi_1(Q_1) \Phi_2(Q_2) \dots \Phi_{N_{\text{vib}}}(Q_{N_{\text{vib}}}), \quad (2.33)$$

where each Φ_I is a solution of the single-mode Schrödinger equation:

$$-\frac{\hbar^2}{2} \frac{\partial^2 \Phi_I}{\partial Q^2} + \frac{1}{2} \omega_I^2 Q^2 \Phi_I = E_{I,V} \Phi_I. \quad (2.34)$$

The total vibrational energy is then the sum of energies in each vibrational mode:

$$E = \sum_I^{N_{\text{vib}}} \hbar \omega_I (n_I + \frac{1}{2}), \quad (2.35)$$

where n_I is the vibrational quantum number defining a state of a harmonic oscillator.

In the following, methods for the calculation of vibrational spectra are discussed. According to Fermi's golden rule [65], transition dipole moment representing transition from state n to state n' is:

$$(\boldsymbol{\mu})_{n,n'} = \int \Phi_n^* \boldsymbol{\mu} \Phi_{n'} dQ, \quad (2.36)$$

where the integration is performed over all normal coordinates Q , Φ_n and $\Phi_{n'}$ are the vibrational wave functions for the initial and final states, respectively, and $\boldsymbol{\mu}$ is the dipole moment operator. The latter can be expanded in terms of normal coordinates around the energy minimum:

$$\boldsymbol{\mu} = \boldsymbol{\mu}(0) + \sum_I^{N_{\text{vib}}} \left(\frac{\partial \boldsymbol{\mu}}{\partial Q_I} \right)_0 \cdot Q_I + \dots \quad (2.37)$$

Typically, contributions of terms of higher order in Q_I than linear to the transition dipole moment are much smaller than the linear term, and can therefore be neglected. This is the so-called electrical harmonic approximation. Since the harmonic approximation has been already introduced in the description of the potential, the calculated harmonic IR spectra are in fact doubly approximated. Keeping only the linear terms in Eq. 2.37, we obtain the approximation for the transition dipole moment:

$$(\boldsymbol{\mu})_{n,n'} \approx \boldsymbol{\mu}(0) \int \Phi_n^* \Phi_{n'} dQ + \sum_I^{N_{\text{vib}}} \left(\frac{\partial \boldsymbol{\mu}}{\partial Q_I} \right)_0 \cdot \int \Phi_n^* Q_I \Phi_{n'} dQ. \quad (2.38)$$

Since the harmonic-oscillator wave functions are orthonormal, the first term in Eq. 2.37 vanishes except the case of $n = n'$, which indicates no vibrational transition and contributes nothing to IR spectra. From the second term it is clear that the transition between the vibrational states actually only takes place for $n = n' \pm 1$ since for the harmonic oscillator wave functions the integral is zero otherwise. The intensity of an IR transition is expressed through the transition dipole moment as follows:

$$I_I = \frac{N_A \pi}{3c} \left| \left(\frac{\partial \boldsymbol{\mu}}{\partial Q_I} \right)_0 \right|^2, \quad (2.39)$$

where N_A is Avogadro's constant, and c is the light velocity. Detailed derivation of this expression can be found in [64].

Unlike the case of a finite atomic cluster, where all components of the dipole moment are in general non-zero, it has been found that for metal surface [66] or thin oxide films on metal surface [67, 68], the components parallel to the surface usually do not contribute to the IR intensity. This is known as the surface selection rule [69]. It originates from the fact that the in-plane component of the adsorbate dipole moment induces an opposite dipole moment in the substrate, so that these dipole moments cancel each other. In contrast, the adsorbate-induced normal component of dipole moment in the substrate enhances the overall dipole moment. Thus, our calculations of the IR intensity count only the surface-normal component of the dipole moment.

2.4.2. Infrared (IR) spectra from molecular dynamics

Due to the double-harmonic approximation employed in the method introduced in the last section, its reliability is limited to systems at low enough temperatures, at which the system explores the neighbourhood of the local minimum on the PES during thermal motion. Experiments, however, are usually done at finite temperature, where the harmonic-oscillator approach is questionable in several aspects [1, 70]. IR spectra at finite temperatures without the harmonic approximation can be derived from molecular dynamics (MD) simulations via dipole-dipole time autocorrelation [71].

Molecular dynamics

MD simulates the motion of a collection of atoms at finite temperature. All the MD simulations in this thesis are performed on the Born-Oppenheimer ground-state PES ($V_{\text{BO}}(\{\mathbf{R}_I\})$) which is calculated from first principles. The nuclei are treated as classic particles which obey Newton's equations of motion:

$$M_I \ddot{\mathbf{R}}_I = \mathbf{F}_I = -\nabla_I V_{\text{BO}}(\{\mathbf{R}_I\}). \quad (2.40)$$

Given the position \mathbf{R}_I and the velocity $\dot{\mathbf{R}}_I$ of a particle I at starting time t , the position of the particle after a short time Δt can be written as a Taylor series:

$$\mathbf{R}_I(t + \Delta t) = \mathbf{R}_I(t) + \dot{\mathbf{R}}_I(t)\Delta t + \frac{1}{2}\ddot{\mathbf{R}}_I(t)\Delta t^2 + \frac{1}{6}\ddot{\mathbf{R}}_I(t)\Delta t^3 + O(\Delta t^4) + \dots \quad (2.41)$$

Using Eq. 2.40, it can be rewritten as:

$$\mathbf{R}_I(t + \Delta t) = \mathbf{R}_I(t) + \mathbf{v}_I(t)\Delta t + \frac{\mathbf{F}_I(t)}{2M_I}\Delta t^2 + \frac{1}{6}\ddot{\mathbf{R}}_I(t)\Delta t^3 + O(\Delta t^4) + \dots \quad (2.42)$$

Analogously, for a time difference $-\Delta t$, $\mathbf{R}_I(t - \Delta t)$ is:

$$\mathbf{R}_I(t - \Delta t) = \mathbf{R}_I(t) - \mathbf{v}_I(t)\Delta t + \frac{\mathbf{F}_I(t)}{2M_I}\Delta t^2 - \frac{1}{6}\ddot{\mathbf{R}}_I(t)\Delta t^3 + O(\Delta t^4) + \dots \quad (2.43)$$

Adding Eq. 2.42 to Eq. 2.43 yields:

$$\mathbf{R}_I(t + \Delta t) + \mathbf{R}_I(t - \Delta t) = 2\mathbf{R}_I(t) + \frac{\mathbf{F}_I(t)}{2M_I}\Delta t^2 + O(\Delta t^4) + \dots, \quad (2.44)$$

and

$$\mathbf{R}_I(t + \Delta t) = 2\mathbf{R}_I(t) - \mathbf{R}_I(t - \Delta t) + \frac{\mathbf{F}_I(t)}{2M_I}\Delta t^2 + O(\Delta t^4) + \dots, \quad (2.45)$$

i.e., up to the third order in Δt :

$$\mathbf{R}_I(t + \Delta t) \approx 2\mathbf{R}_I(t) - \mathbf{R}_I(t - \Delta t) + \frac{\mathbf{F}_I(t)}{2M_I}\Delta t^2. \quad (2.46)$$

This is the essence of the Verlet algorithm used for the numerical simulations of a particle's trajectory. At each time step, there is an error of $O(\Delta t^4)$ in the particle's position.

An ensemble of particles evolving according to the above equations of motion is called micro-canonical ensemble, where energy is strictly a constant. To simulate a system at constant temperature, one can include a heat bath in the simulation, known as the thermostat. The thermostat used in this thesis is the one proposed by Bussi, Donadio, and Parrinello (BDP) [72] which does not suffer from the ergodicity problem[cite], and correctly predicts the time-correlation properties [73]. A detailed account of different thermostats, their numerical advantages and disadvantages, is given in [74]. Here we focus on the approach used in our work.

According to the equipartition theorem, the kinetic energy is equally distributed in each degree of freedom of the system, and each degree takes $k_B T/2$. The instantaneous temperature is given as:

$$T_k = \frac{E_k}{3Nk_B}, \quad (2.47)$$

where E_k is instantaneous kinetic energy of the system:

$$E_k = \frac{1}{3Nk_B} \sum_I^N M_I \mathbf{v}_I^2, \quad (2.48)$$

\mathbf{v}_I is the velocity which follows Boltzmann-Maxwell distribution:

$$p(\mathbf{v}_I) = \left(\frac{M_I}{2\pi k_B T} \right)^{3/2} \exp \left(\frac{-M_I \mathbf{v}_I^2}{2k_B T} \right), \quad (2.49)$$

where T is an ensemble average of T_k defined by:

$$T = \frac{2}{3Nk_B} \left\langle \sum_I^N \frac{M_I \mathbf{v}_I^2}{2} \right\rangle \quad (2.50)$$

The instantaneous temperature fluctuates during the simulation and the thermostat is used to keep the average temperature constant. The steps of the BDP thermostat are the following:

1. The trajectory is updated according to Newton's equations of motion.
2. The instantaneous kinetic energy is calculated.
3. The instantaneous kinetic energy is updated for one time step by a stochastic scheme which contains both a velocity rescaling term and a white noise term.
4. Finally, the velocity is updated via rescaling by a factor α (see Ref. [72] for the definition) to satisfy the updated instantaneous kinetic energy in step 3.

Time autocorrelation

MD simulations provide directly the trajectory of the atoms as well as the properties of the system at each time step in the MD process. The vibrational spectra can be derived from the trajectory through the time-autocorrelation function:

$$C(t) = \langle A(0) \cdot A(t) \rangle, \quad (2.51)$$

where A is the property of interest. In case of vibrational spectra, the time-autocorrelation of the dipole moment has to be evaluated. It is generally assumed in this thesis that nuclei behave as classical particles. A brief description of how an IR spectrum can be derived from MD simulations is given in the following paragraphs. A more detailed derivation and explanations can be found in a textbook, e.g. by McQuirrie [75].

Let us consider a small external electric field $\mathbf{E}(t) = \epsilon E_0 \cos(\omega t)$ which perturbs the system Hamiltonian \hat{H}^0 by:

$$\lambda \hat{V}(t) = -\mathbf{E}(t) \cdot \hat{\boldsymbol{\mu}} = E_0 (\epsilon \cdot \hat{\boldsymbol{\mu}}) \cos(\omega t), \quad (2.52)$$

where $\hat{\boldsymbol{\mu}}$ is the dipole moment operator. According to the Fermi's golden rule, the transition probability from the initial state i to a final state j is:

$$P_{i \rightarrow f}(\omega) = \frac{\pi E_0^2}{2\hbar^2} |\langle f | (\epsilon \cdot \hat{\boldsymbol{\mu}}) | i \rangle|^2 [\delta(\omega_{fi} - \omega) + \delta(\omega_{fi} + \omega)], \quad (2.53)$$

where $\omega_{fi} = (E_f - E_i)/\hbar$, E_f and E_i are the energies of the final and initial states, respectively. The energy loss from radiation to the system is calculated as follows:

$$-\frac{d}{dt}E_{\text{rad}} = \sum_i \sum_f \rho_i \hbar \omega_{fi} P_{i \rightarrow f}, \quad (2.54)$$

where ρ_i are the Boltzmann statistic weights denoting the probability of the system to be at the initial state i before the perturbation is switched on. Using the Fourier transform representation of the delta-function, manipulation of Eq. 2.54 (detailed derivation can be found in [75]) yields the absorption coefficient:

$$I(\omega) \propto \sum_i \rho_i \omega (1 - e^{-\frac{\hbar\omega}{k_B T}}) \int_{-\infty}^{\infty} \langle i | \hat{\mu}(0) \cdot \hat{\mu}(t) | i \rangle e^{-i\omega t} dt. \quad (2.55)$$

Since the system should be ergodic, the ensemble average can be written as a time average:

$$I(\omega) \propto \omega (1 - e^{-\frac{\hbar\omega}{k_B T}}) \int_0^{\infty} \langle \hat{\mu}(0) \cdot \hat{\mu}(t) \rangle e^{-i\omega t} dt \quad (2.56)$$

Eq. 2.56 can be used to calculate vibrational spectra from MD trajectories at the given temperature, including effects of anharmonicity. However, there is a desymmetrization of the peaks caused by the fact that the requirement of detailed balance is not included in classical dynamics [76]. This effect has been extensively studied, and several corrections to the line-shape were suggested and tested by comparing to the centroid molecular dynamics [76]. The one that we use, known as "quantum harmonic correction", has been shown to give the best agreement with experimental data [70, 77], and can be accounted for by simply multiplying Eq. 2.56 by $(-\frac{\omega\hbar}{k_B T})/(1 - \exp(-\frac{\omega\hbar}{k_B T}))$. This yields:

$$I(\omega) \propto \omega^2 \int_0^{\tilde{t}} \langle \mu(0) \cdot \mu(t) \rangle e^{-i\omega t} dt \quad (2.57)$$

2.5. Free-energy surface – *ab initio* atomistic thermodynamics

DFT calculations typically directly provide a system's electronic structure and total energy which reflect properties of the system at zero temperature. However, the properties of interest are often influenced and sometimes even completely determined by finite temperature and pressure. This "temperature and pressure" gap can be bridged by *ab initio* atomistic thermodynamics (aiAT) [78, 79, 51, 52, 53].

The idea of aiAT was first developed to study defects [78, 79, 51] in semiconductors, and then adopted for surfaces [52, 53]. A surface in contact with a gaseous atmosphere at certain temperature and pressure tends to minimize its Gibbs free energy to reach the thermodynamic equilibrium. The change of the surface Gibbs free energy upon adsorption/desorption of species onto/from the surface is characterized by the chemical potential of that species. By definition, in thermodynamic equilibrium the chemical potential of an atomic species is independent on its location: at the surface, in the subsurface, in the bulk, or in the gas phase.

As an example, let us consider an atmosphere of hydrogen gas. Using the ideal-gas approximation, the chemical potential of H can be written as a function of temperature and H_2 pressure:

$$\mu_H(T, p) = \frac{1}{2}\mu_{H_2}(T, p) = \frac{1}{2}(-k_B T \ln Z_{H_2}^{\text{tot}} + pV)/N \quad (2.58)$$

where Z_{H_2} is the partition function of the ideal hydrogen gas. As stated previously, the Born-Oppenheimer approximation is adopted in this thesis. Under this approximation, the electronic degrees of freedom are decoupled from the H_2 vibrational and rotational degrees of freedom. The vibrational and rotational degrees of freedom are also decoupled due to their different time scales. Then $Z_{H_2}^{\text{tot}}$ can be written in the form:

$$Z_{H_2}^{\text{tot}} = \frac{1}{N!}(q_{H_2})^N = \frac{1}{N!}(q^{\text{trans}} q^{\text{rot}} q^{\text{vib}} q^{\text{electr}} q^{\text{nucl}})^N, \quad (2.59)$$

where q^{nucl} is the contribution due to nuclear degrees of freedom (in particular, nuclear spin). Substituting Eq. 2.59 into Eq. 2.58 yields:

$$\mu_H(T, p) = -\frac{1}{2N} \left[k_B T \ln \left(\frac{1}{N!} (q^{\text{trans}})^N \right) - pV \right] + \frac{\mu^{\text{rot}}}{2} + \frac{\mu^{\text{vib}}}{2} + \frac{\mu^{\text{electr}}}{2} + \frac{\mu^{\text{nucl}}}{2} \quad (2.60)$$

Using the translational partition function

$$q^{\text{trans}} = V \left(\frac{2\pi m k_B T}{h^2} \right)^{\frac{3}{2}}, \quad (2.61)$$

together with the ideal gas assumption $pV = Nk_B T$ and the Sterling approximation $\ln N! = N \ln N - N$, yields:

$$-\frac{1}{2N} \left[k_B T \ln \left(\frac{1}{N!} (q^{\text{trans}})^N \right) - pV \right] = -\frac{k_B T}{2} \ln \left[\left(\frac{2\pi m}{h^2} \right)^{\frac{3}{2}} \frac{(k_B)^{\frac{5}{2}}}{p} \right] \quad (2.62)$$

For a rigid-body rotor which represents a heteronuclear diatomic molecule, the rotational partition function:

$$q^{\text{rot}} = \sum_{J=0}^{\infty} (2J+1) e^{-\frac{h^2 J(J+1)}{2Ik_B T}} = \sum_{J=0}^{\infty} (2J+1) e^{-\frac{\Theta}{T} J(J+1)}, \quad (2.63)$$

where $\Theta = \frac{h^2}{2Ik_B}$ and I is the moment of inertia. At temperatures that are of interests to us, $\frac{\Theta}{T} \ll 1$, and the above expression can be approximated by:

$$q^{\text{rot}}(T) \approx \int_0^{\infty} (2J+1) e^{-\frac{\Theta}{T} J(J+1)} dJ = \int_0^{\infty} e^{-\frac{\Theta}{T} J(J+1)} d[J(J+1)] = \frac{T}{\Theta}, \quad (2.64)$$

so that

$$\mu^{\text{rot}}(T) \approx -k_B T \ln \left(\frac{T}{\Theta} \right). \quad (2.65)$$

In general, the rotational contribution to the chemical potential of a non-linear polyatomic molecule can be written as:

$$\mu^{\text{rot}}(T) \approx -k_B T \ln \left[\frac{\pi^{1/2}}{\sigma^{\text{sym}}} \left(\frac{T^3}{\Theta_A \Theta_B \Theta_C} \right)^{1/2} \right], \quad (2.66)$$

where Θ_A , Θ_B , and Θ_C are calculated using the principal moments of inertia, and σ^{sym} is a symmetry number indicating the number of indistinguishable orientations that the molecule can have. In particular, $\sigma^{\text{sym}} = 1$ for heteronuclear diatomic molecules and $\sigma^{\text{sym}} = 2$ for homonuclear diatomic molecules, such as H_2 .

The vibrational partition function is:

$$q^{\text{vib}} = \prod_{i=1}^{N_{\text{vib}}} \sum_{n_i=0}^{\infty} \exp \left[-\frac{\hbar \omega_i}{k_B T} \left(n_i + \frac{1}{2} \right) \right] = \sum_{n_i=0}^{N_{\text{vib}}} \frac{\exp(-\frac{\hbar \omega_i}{2k_B T})}{1 - \frac{\hbar \omega_i}{k_B T}}, \quad (2.67)$$

where $N_{\text{vib}} = 3N - 6$ for an N -atomic non-linear molecule, and $N_{\text{vib}} = 3N - 5$ for a linear molecule. The vibrational contribution to the chemical potential is:

$$\mu^{\text{vib}}(T) = \sum_{n_i=0}^{N_{\text{vib}}} \left[\frac{\hbar \omega_i}{2} + k_B T \ln \left(1 - \exp(-\frac{\hbar \omega_i}{k_B T}) \right) \right] \quad (2.68)$$

At $T = 0$ K, Eq. 2.68 gives vibrational free energy at zero Kelvin, known as the zero-point energy:

$$E^{\text{ZPE}} = \sum_{n_i=0}^{N_{\text{vib}}} \frac{\hbar \omega_i}{2} \quad (2.69)$$

Since for most molecules (including the ones of interests to us) the electronic excitation energies are large compared to $k_B T$, only the ground electronic state contributes to q^{electr} :

$$\mu^{\text{electr}} \approx E^{\text{total}} - k_B T \ln(n^{\text{spin}}), \quad (2.70)$$

where E^{total} is the ground state total energy, and n^{spin} is the electronic spin degeneracy at the ground state.

The nuclear state is rarely changed during a chemical process, so μ^{nucl} is considered to be zero.

To sum up, the chemical potential of a non-linear polyatomic molecule can be written as:

$$\mu(T, p) = E^{\text{total}} - k_B T \left\{ \ln \left[\left(\frac{2\pi m}{h^2} \right)^{\frac{3}{2}} \frac{(k_B)^{\frac{5}{2}}}{p} \right] + \ln \left[\frac{\pi^{1/2}}{\sigma^{\text{sym}}} \left(\frac{T^3}{\Theta_A \Theta_B \Theta_C} \right)^{1/2} \right] - \sum_{n_i=0}^{3N-6} \left[\frac{\hbar \omega_i}{2} + k_B T \ln(1 - e^{-\frac{\hbar \omega_i}{k_B T}}) \right] + \ln(n^{\text{spin}}) \right\} \quad (2.71)$$

Eq. 2.71 can be further rewritten in the following form:

$$\mu(T, p) = E^{\text{total}} + E^{\text{ZPE}} + \Delta\mu(T, p^0) + k_B T \ln \left(\frac{p}{p^0} \right), \quad (2.72)$$

where all the temperature dependence at the reference pressure is contained in $\Delta\mu(T, p^0)$. The significance of Eq. 2.72 is that it allows to calculate the chemical potential by using tabulated experimental data at standard pressure $p^0 = 1$ atm, instead of using Eq. 2.71. However, this should be done with care, since calculating chemical potential from first principles may (or may not) result in an additional cancellation of errors.

The surface Gibbs free energy is calculated according to:

$$\Delta G = E(\Delta x_1, \dots, \Delta x_N) - E_{\text{ref}} + \Delta F_{\text{vib}}(T) - \sum_{i=1}^N \Delta x_i \mu_i(T, p_i), \quad (2.73)$$

where E_{ref} is the total energy of a reference system (e.g., bare surface), $E(\Delta x_1, \dots, \Delta x_N)$ is the total energy of the system where the number of atoms of species i differs by Δx_i from the reference system, μ_i is the chemical potential of species i with the partial pressure p_i , and ΔF_{vib} is the change in the vibrational free energy with respect to the reference system.

3. Exploring PES – implementation of genetic algorithm for surfaces

3.1. Introduction of global optimization

Finding the low-energy minima (including the global minimum) on a potential-energy surface is tremendously important for simulating complex systems, with a very large number of possible configurations. Examples of such complex systems include metal [80] or oxide [81, 82] clusters, semiconductor surfaces [48], crystals [83], and proteins [84]. The importance of finding the global minimum (GM) stems from the fact that typically structures observed at realistic conditions are close to GM. Since the number of possible configurations grows exponentially with the number of degrees of freedom (i.e., with the number of different species and the number of atoms), it becomes impossible to identify by intuition low-energy structural motifs. This is the global optimization problem, which can be addressed in several different ways. Deterministic methods [85] were developed for global optimization, however, they are only applicable for very small systems. Stochastic-heuristic methods are the only option for systems larger than a few atoms, although there is no guarantee of finding the GM by such methods. In general, there are two groups of stochastic methods enabling the search for GM in atomic systems. The first group includes simulated annealing, basin hopping, metadynamics and minima-hopping methods, with the efficiency of all of them depending strongly on the starting point (the initial guess). The second group includes particle-swarm optimization and evolutionary algorithms, whose most popular implementation form is known as genetic algorithm (GA). Both the particle-swarm optimization and evolutionary methods use random (with certain constraints) structures as the initial guess. These stochastic methods will be briefly reviewed in this chapter, and the details of our genetic algorithm implementation will be introduced.

GA was first proposed by Holland in 1970s [47] in the context of artificial intelligence. It mimics the process of natural evolution where a population of species adapt themselves to the perpetually novel and evolving environment by selection, inter-mating, mutation, etc.. An agent is defined to be adaptive if the action of the agent can be assigned a value (e.g. performance, fitness, payoff) and the agent behaves so as to increase this value over time. It is speculated that the high fitness value reflects good genes, which are hard to identify and characterize directly. Based on this speculation, offspring of agents with higher fitness are more likely to also have high fitness, possibly higher than any one in the population.

In the context of global optimization for atomic structures, the typical value to optimize is the total energy at 0 K. With respect to this value, a list of fitness values can be calculated. Two *parents* are chosen with a bias to structures with high fitness. The mating operation (crossover) is done in two steps: cutting the two selected structures and then combining two parts originating from different *parents* to form new structures. Although not guaranteed, the hope is that the cutting-recombination process passes winning geometry motifs to the new structure. In contrast

to bio-systems, where it is found that genes show in general high independence and are not likely to be damaged during the mating process [86, 87], in the atomic systems structural motifs could be damaged by cutting, especially in systems not larger than a few hundred atoms. This is a drawback of GA, in particular when it is compared to molecular-dynamics-based methods. The advantages of GA are the memory of the stable structural motifs found during the evolutionary process (i.e., coarse-graining of the potential-energy surface exploration), and the absence of the problem with overcoming high energy barriers between basins of the potential-energy surface.

The GA optimization of structures with two-dimensional translational symmetry was first performed by Chuang *et al.* [48]. They implemented a force-field based GA to study the high-index surfaces of silicon, and indeed found a number of novel atomic configurations. The GA was implemented as follows. Fitness was calculated for a list of initial randomly generated structures, then two structures were selected with a bias to high fitness values. The crossover operation was done in two steps: first, separate each parent structure into the set of relaxed layers and the remaining unrelaxed part, and then cut the relaxed parts of the two *parents* with a random plane and recombine two relaxed parts from the *parents*. This basic scheme is followed by Sierka *et al.* [49], who implemented a DFT-based GA and introduced a mutation operation in their implementation.

Different from the case of GA for cluster structure optimization, GA for periodic systems is always limited by periodic boundary conditions, so that superstructures with larger-scale periodicity or non-periodic cannot be found by GA. To go beyond the short-range periodicity, the cluster-expansion (CE) method [88] can be used together with periodic GA. In the CE method, the Hamiltonian of the system is expressed in terms of occupations of lattice sites, and is parameterized in terms of one-body, two-body, etc., terms, based on accurate energies calculated for a set of configurations. In conjunction with GA, CE is used to predict the energy for a given configuration, while GA is used to find the structures appropriate for an accurate parameterization of the CE in the relevant part of the configurational space. Such a CE+GA scheme has been demonstrated to be successful in modelling alloy systems [88, 89] and atom adsorption on well-defined crystal surfaces [90].

However, our water/oxide systems are beyond what the current state of CE can handle, for two major reasons. First, water is partially dissociated, so that there are three different species (H, OH, and H₂O). Moreover, OH and H₂O can have significantly different (in terms of energy) orientations depending on the coordination with surrounding adsorbates, which increases the number of different “species” in the context of CE dramatically. Second, it is difficult to define a discrete lattice of adsorption sites needed for the parameterization of the CE Hamiltonian, since the position of adsorbates with respect to surface atoms is strongly affected by bonding with neighboring species. In order to check the sensitivity of the predicted relative stability of the adsorbed structures to the size of the unit cell, we performed a GA search for one particular water coverage within a larger surface unit cell ((4×5) versus (3×4)) of CaO(001), and found a stable 1D structure (containing 6 water molecules per unit cell) identical to the most stable 1D structure for 6H₂O@(3×4) unit cell (see the text below for details).

3.2. Our genetic algorithm implementation

Our GA implementation follows Chuang and Sierka, and is outlined in Fig. 3.1. On top of this general scheme, we have made improvements in specific blocks to enhance the computational efficiency. Below, details of our implementation are described block-by-block in the following order: random-structure generation, selection of *parents*, crossover, structure similarity checking, and mutations. The implementation details are illustrated using the example of a global energy minimization for superstructures formed by water molecules adsorbed on CaO(001) [1]. Note that the implementation is quite general, and can be directly used for other surface systems, e.g. for surfaces of a solid from a different crystal family.

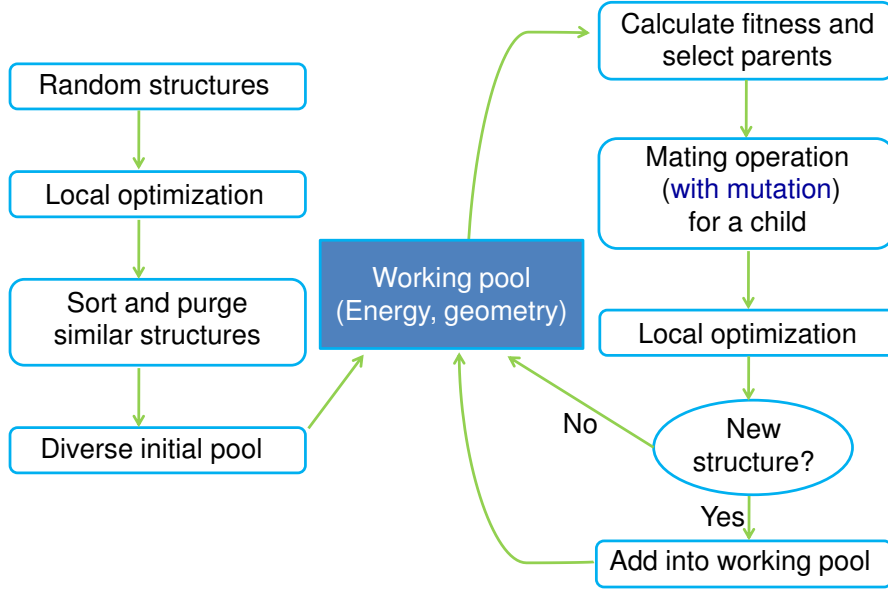


Figure 3.1.: Overview of the GA implementation for surface structures.

The initial pool of structures The initial pool of structures is filled with about 50 structures which represent randomly distributed sampling points in the configurational space. As a first step, the models of the clean surface and the free adsorbates are prepared, then the adsorbate molecules are rotated randomly, and afterwards placed randomly at some distances (within a certain range) above the surface. The minimum distance between any two atoms is forced to be above a threshold. These atomic structures are then relaxed to the nearest local minimum. The relaxed structures are then sorted according to their total energy, and two lists are created: the ordered list of the total energies, and the list of corresponding structures. If there are structures that are similar according to the criteria described in detail below, only one of them is kept in the pool to insure the population diversity.

Selection The selection of parent structures from the pool is done based on the fitness value of each structure, calculated based on its total energy:

$$f_i = \sum_{k=1}^i \frac{\exp(-\eta_k/a)}{\sum_{j=1}^N \exp(-\eta_j/a)}, \quad (3.1)$$

where

$$\eta_i = (E_i - E_N)/(E_0 - E_N), \quad (3.2)$$

E_i is the total energy of the structure i , E_0 is the lowest energy among E_i 's, E_N is the highest energy, a is a constant that defines the decay speed of the preference according to the energy. N is not necessarily the total number of structures in the pool, only a subset of structures can be used to generate new ones. Next, a random number $R \in (0, 1]$ is generated, and the i th structure in the list is selected as a *parent* if

$$f_i \geq R > f_{i-1} \quad (3.3)$$

It is worth noting that the total energies in Eq. 3.2 can be substituted by any property that the user intends to optimize. In our case, a minimum of total energy indicates the most stable structure at 0 K, neglecting the temperature and pressure effects. In principle, free energy can be also minimized directly in a similar way.

Crossover operation

The crossover operation (see Fig. 3.2) that we use is similar the the one employed by Chuang [48], except that the cutting plane is not enforced to be perpendicular to the surface. There is an option to specify a number of layers in the slab that are not involved in crossover. The rest of the surface layers and adsorbates are sectioned by a randomly orientated plane. Two compensating parts from the two different *parents* are recombined to form a *child*. The *child* is kept only if all the following conditions are satisfied: (i) the resulting structure has a desired atomic composition, (ii) there are no interatomic distances that are shorter than a certain threshold, and (iii) there are no single atom or a group of atoms that are separated from the rest of the system by a distance larger than a threshold. The accepted *child* structure undergoes further local minimization at the *ab initio* level.

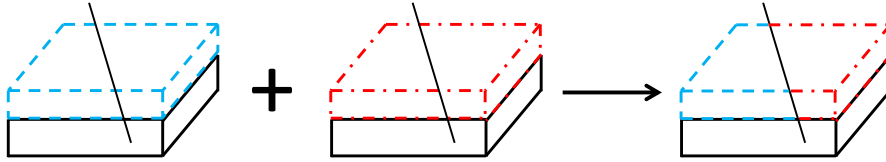


Figure 3.2.: Illustration of the crossover operation for a surface structure in our GA implementation. The black line crossing the surface model represents a random plane that separates the surface layers into two parts.

Similarity check In order to avoid redundant calculations and maintain the diversity of the structure population, it is important to ensure that only structures that are *essentially different* from all other structures in the pool after local energy minimization are added to the pool. According to Chuang *et al.*, two structures are different only if their total energies are close in some range defined by a user input parameter. This scheme is problematic when there are degenerate configurations (isomers), because it would keep only one isomer in this case. As is illustrated by Fig. 3.3, the task of identifying similar surface structures is very different from the case of clusters due to the translational and other symmetries of the substrate. In our implementation, we employ both the energy and a geometric criterion to distinguish the structures. Two structures are considered *essentially different* if their total energies are different by more than a

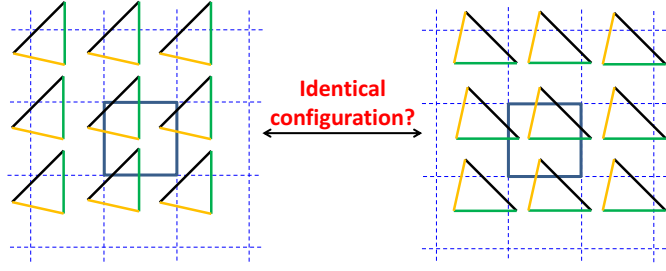


Figure 3.3.: Illustration of checking for similarity for adsorbate structures with periodic boundary conditions. The triangle formed by the thick yellow, black, and green lines represents the adsorbate structure whose coordinates are within the reference unit cell (square shape in this example) outlined by the thick blue lines. The dashed lines outline periodic images of the reference unit cell. Each cell formed by the dashed lines is a surface supercell having the same size as in Fig. 3.2.

threshold (typically 0.05 eV). If the structures are not different according to the energy criterion, their geometries are compared by checking interatomic distances in the following way. First, all distances between atoms of the adsorbed species within the supercell and its nearest periodic images are calculated. The periodic images are involved to account for a possible translation or another symmetry operation that converts one structure into the other. Two sets of N interatomic distances, d_1^i and d_2^i , $i = 1, \dots, N$, are obtained. Second, the distances in each set are sorted from smallest to largest, and then compared one by one between the two sets (due to the periodic boundary conditions, only the distances that are smaller than the largest distance within the supercell need to be compared). The two structures are considered to be *essentially different*, if there exists i such that

$$(d_1^i - d_2^i) > \delta(d_1^i + d_2^i)/2 \quad (3.4)$$

The value of δ should be chosen so that, on one hand, different structures are not erroneously identified as similar, and, on the other hand, essentially similar structures are not missed by the similarity-checking procedure. Based on GA test runs, it is found that $\delta=0.05$ works well for our systems of interest.

Mutation Like in natural evolution, mutation plays an important role in adding diversity to a population. In our structure optimization method, mutations are implemented as part of the crossover operation, and include adding or removing one atom or group of atoms (e.g. an H or OH group), or rotating one group of atoms around the surface normal passing through the position of a randomly chosen multi-coordinated atom (e.g. O in a surface OH group) within the group. Typically, the probability of mutation in crossover operations is less than 5%.

Parallelization One of the merits of GA is the high parallel efficiency (scalability). A linear scaling is achieved in our implementation by running DFT structure relaxations on different CPUs and merging the results to a common energy file and the corresponding structure file. An illustration of the parallelization scheme is shown in Fig. 3.4. The routine job the GA code does during the evolution process is the following: it generates a child, checks everything required, then distributes it to an available set of processors for the local optimization; once the local opti-

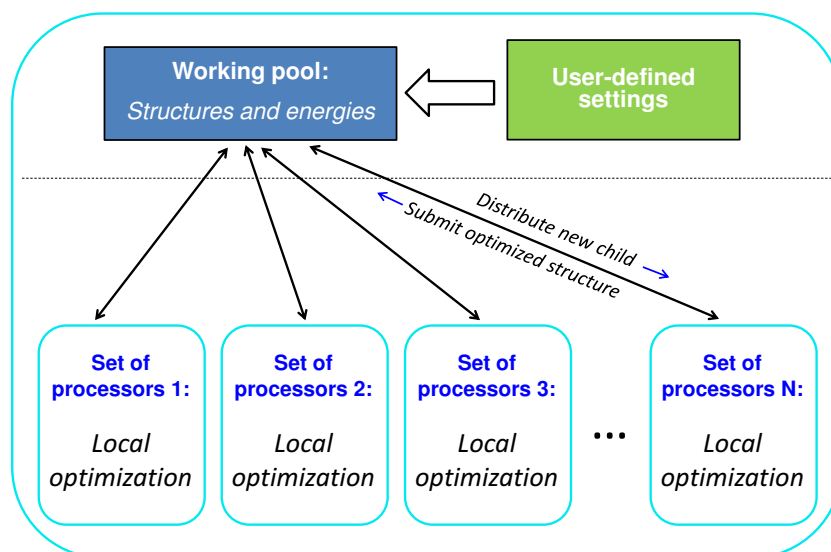


Figure 3.4.: Illustration of the parallelization of our genetic algorithm implementation (see text for details).

mization is finished, the optimized structure and energy are communicated to a master processor which merges the results into the working pool. Since the bookkeeping operations take a few seconds or less and the time for a typical DFT local optimization is of the order of 10^3 seconds or longer, the genetic algorithm scales linearly with the number of processors.

4. *Ab initio* methods for electronic-structure calculations

The many-body problem of electrons in external potential is exactly described by the Schrödinger equation, but the exact solution of this equation is not feasible for more than 2 electrons. Therefore, numerical solutions have to be adopted. Robust approximate methods do exist that allow for calculating electronic structure and in particular ground-state properties for systems with thousands of electrons. One of the main classes of approximated methods are based on assumptions on the many-electron wave function, namely the Hartree-Fock (HF) method and methods based on it, including configuration interaction (CI), Møller-Plesset perturbation theory, and the coupled-cluster approximation (CCA). The other main class of *ab initio* methods is derived from the density-functional theory (DFT), which is based on the exact correspondence between the electron density distribution and the wave function for a given many-electron system, so that all properties of the system are fully defined by the electron density. In DFT, all many-body complexity is packed in the exchange-correlation energy functional, which is subsequently approximated based on electron local density (local density approximation, LDA) or also density gradients (generalized gradient approximation, GGA), or a mixture of LDA or GGA with the non-local HF exchange (hybrid functionals). The random-phase approximation (RPA) has been relatively recently introduced in the DFT context to treat the exchange-correlation energy by calculating the response functions of a series of fictitious systems along an adiabatic connection (AC) path. The *ab initio* methods used in this work are described in more detail in the following paragraphs.

4.1. Many-electron problem

Within the Born-Oppenheimer approximation, the nuclei move on the potential-energy surface, which is given by the ground-state electronic energy (2.10). What remains to be solved is the many-electron problem Eq. 2.9. This can be done by transforming the problem into a set of single-electron equations. A mean-field theory is an approximation that allows to do this, and is adopted by many methods as a first step to solve the many-electron problem. The mean-field Halmiltonian is a sum of effective single-electron Hamiltonians

$$\hat{H}^{\text{MF}} = \sum_{i=1}^{N_{\text{el}}} \hat{h}_i^{\text{MF}} = \sum_{i=1}^{N_{\text{el}}} \left(\hat{t}_i^{\text{e}} + v_i^{\text{ext}} + v_i^{\text{MF}} \right), \quad (4.1)$$

where v_i^{MF} is the average potential experienced by i th electron due to the presence of the other electrons. The resulting effective single-electron Schrödinger equations

$$\hat{h}_i^{\text{MF}} |\varphi_i\rangle = \epsilon_i |\varphi_i\rangle, \quad (4.2)$$

can be solved iteratively. The mean-field ground state energy E_0^{MF} is

$$E_0^{\text{MF}} = \langle \Psi_0^{\text{MF}} | \hat{H}^{\text{MF}} | \Psi_0^{\text{MF}} \rangle, \quad (4.3)$$

where Ψ_0^{MF} is the mean-field many-electron ground-state wave function. In Hartree theory, Ψ_0^{MF} is a product of single-particle wave functions, and in Hartree-Fock theory Ψ_0^{MF} is a single Slater determinant constructed of the single-particle wave functions. The latter is discussed in more detail below. In different mean-field approaches, E_0^{MF} and Ψ_0^{MF} are either directly used to approximate the energy of the full electronic Hamiltonian or they are chosen as a reference for a further perturbative treatment.

4.2. Hartree-Fock theory

The Hartree-Fock theory, also known as molecular-orbital theory, is one of the mean-field approximations developed to reduce the complexity of the $3N_{\text{el}}$ -dimensional electronic problem (in general, also the spin of each electron is an additional degree of freedom). Using the Rayleigh-Ritz variational principle [91], Hartree [92] derived the mean-field approximation corresponding to the motion of each electron in an average potential of all the other electrons. The many-electron wave function was approximated as a product of single-electron wave functions. Since the mean-field potential depends on solutions of the Hartree equations, a self-consistent approach is required to solve the problem, and such an approach was also developed by Hartree. An effective potential is initially guessed to solve the Hartree equations, whose solutions are used to build a new effective potential, and the procedure is repeated until self-consistency is reached.

The Hartree-Fock approximation additionally takes into account the fermionic nature of electrons. Within the Hartree-Fock approximation, the many-electron ground-state wave function is approximated by a single Slater determinant Ψ^{HF} of N_{el} spin-orbitals φ_i :

$$\Psi^{\text{HF}} = \frac{1}{\sqrt{N_{\text{el}}!}} \begin{vmatrix} \varphi_1(\mathbf{x}_1) & \varphi_2(\mathbf{x}_1) & \cdots & \varphi_{N_{\text{el}}}(\mathbf{x}_1) \\ \varphi_1(\mathbf{x}_2) & \varphi_2(\mathbf{x}_2) & \cdots & \varphi_{N_{\text{el}}}(\mathbf{x}_2) \\ \vdots & \vdots & \ddots & \vdots \\ \varphi_1(\mathbf{x}_{N_{\text{el}}}) & \varphi_2(\mathbf{x}_{N_{\text{el}}}) & \cdots & \varphi_{N_{\text{el}}}(\mathbf{x}_{N_{\text{el}}}) \end{vmatrix} \quad (4.4)$$

$\varphi_i(\mathbf{x}_j) = \varphi_i(\mathbf{r}_j, \sigma_j)$ denotes the single-particle wave function of the j th electron, located at \mathbf{r}_j and with spin σ_j (spin up or spin down) in state i (comprising both orbital and spin quantum numbers). A determinant is by definition antisymmetric upon interchanging columns or rows of the matrix, and becomes zero if any two columns or rows are identical. Thus, the Slater determinant is antisymmetric upon swapping the coordinates of any two electrons, and fulfills the Pauli exclusion principle.

According to the variational principle, the expectation value of the electronic Hamiltonian \hat{H} evaluated at any state is always larger or equal to the exact ground-state energy E_0 . For a single Slater determinant Eq. 4.4, E_0^{HF} can be minimized with respect to the choice of spin-orbitals under the constraint of normalization introduced with Lagrange multipliers ϵ_i (the more general orthonormality condition would require introducing a matrix of Lagrange multipliers, which however can be always diagonalized without changing any observable). This yields the Hartree-Fock equations:

$$\left\{-\frac{1}{2}\nabla_i^2 + v_{\text{ext}}(\mathbf{x}) + \sum_{j \neq i} \left[\int d\mathbf{x}' \frac{|\varphi_j(\mathbf{x}')|^2}{|\mathbf{r} - \mathbf{r}'|} \right] \right\} \varphi_i(\mathbf{x}) - \sum_{j \neq i} \left[\int d\mathbf{x}' \frac{\varphi_j^*(\mathbf{x}') \varphi_i(\mathbf{x}')}{|\mathbf{r} - \mathbf{r}'|} \right] \varphi_j(\mathbf{x}) = \epsilon_i \varphi_i(\mathbf{x}) \quad (4.5)$$

The kinetic-energy operator $-\frac{1}{2}\nabla_i^2$ and the external potential $v_{\text{ext}}(\mathbf{x})$ (including the Coulomb attraction to nuclei and possibly the interaction with external electric fields) are one-electron operators while in the third and fourth term two-center integrals are involved. It is convenient to define a coulomb operator

$$\hat{J}_j(\mathbf{r}) = \int d\mathbf{x}' \frac{|\varphi_j(\mathbf{x}')|^2}{|\mathbf{r} - \mathbf{r}'|} \quad (4.6)$$

which accounts the average local potential (also known as Hartree potential) at \mathbf{r} , created by electron at orbital φ_j . Likewise, a exchange operator $\hat{K}_j(\mathbf{x})$ can also be defined:

$$\hat{K}_j(\mathbf{x}) \varphi_i(\mathbf{x}) = \left[\int d\mathbf{r}' \frac{\varphi_j^*(\mathbf{x}') \varphi_i(\mathbf{x}')}{|\mathbf{r} - \mathbf{r}'|} \right] \varphi_j(\mathbf{x}) \quad (4.7)$$

which arises from the antisymmetry requirement of the wave function.

With definitions of the coulomb operator and the exchange operator, the Hartree-Fock equations can be rewritten as:

$$\left\{-\frac{1}{2}\nabla_i^2 + v_{\text{ext}}(\mathbf{x}) + \sum_{j \neq i} [\hat{J}_j(\mathbf{r}) - \hat{K}_j(\mathbf{x})] \right\} \varphi_i(\mathbf{x}) = \epsilon_i \varphi_i(\mathbf{x}), \quad (4.8)$$

and the part within parenthesis is called Fock operator $\hat{F}(\mathbf{x})$.

Comparing the Hartree-Fock equations with Eq. 4.1 indicates that the Hartree potential plus the exchange potential is the effective mean field v_i^{MF} exerted by the other electrons in the Hartree-Fock approximation.

In general, the Hartree-Fock equations need to be solved numerically. Since the solutions $\varphi_i(\mathbf{x})$ have to be known to construct the Fock operator, a self-consistent scheme is required: the effective single-particle Hamiltonian is first obtained from an initial guess of the set of $\varphi_i(\mathbf{x})$, then the Hartree-Fock equations are solved to renew all $\varphi_i(\mathbf{x})$. These steps are repeated until self-consistency is reached. The Hartree-Fock ground-state wave function Ψ_0^{HF} is then the Slater determinant of N_{el} single-particle orbitals with energies ϵ_i . The Hartree-Fock total energy E_0^{HF} is

$$\begin{aligned} E_0^{\text{HF}} = \langle \Psi_0^{\text{HF}} | \hat{H} | \Psi_0^{\text{HF}} \rangle &= \sum_{i=1}^{N_{\text{el}}} \int d\mathbf{x} \varphi_i^*(\mathbf{x}) \left(-\frac{1}{2}\nabla_i^2 + v_{\text{ext}}(\mathbf{x}) \right) \varphi_i(\mathbf{x}) \\ &+ \frac{1}{2} \sum_{i,j=1}^{N_{\text{el}}} \int d\mathbf{x} d\mathbf{x}' \frac{|\varphi_i(\mathbf{x})|^2 |\varphi_j(\mathbf{x}')|^2}{|\mathbf{r} - \mathbf{r}'|} \\ &- \frac{1}{2} \sum_{i,j=1}^{N_{\text{el}}} \int d\mathbf{x} d\mathbf{x}' \frac{\varphi_i^*(\mathbf{x}) \varphi_i(\mathbf{x}') \varphi_j^*(\mathbf{x}') \varphi_j(\mathbf{x})}{|\mathbf{r} - \mathbf{r}'|}. \end{aligned} \quad (4.9)$$

The second term in Eq. 4.9 is the Hartree energy E^H , and the last term is the Hartree-Fock exchange energy E_{xx} . The Coulomb interaction of an electron with itself ($i = j$ in the Hartree term) cancels exactly with the corresponding Hartree-Fock exchange term, so that the Hartree-Fock theory is free of the self-interaction. For this reason, the Hartree-Fock exchange is often called “exact exchange”.

The energy contributions that are not included in the Hartree-Fock theory are known as correlation energy. The correlation energy accounts for the mean-field (dynamic correlation) and the single-determinantal (non-dynamic, or static, correlation) approximations. The correlation energy can in principle be determined very accurately by quantum chemistry methods based on Hartree-Fock orbitals, in particular by the configuration interaction (CI) and coupled-cluster (CC) approaches. However, such approaches suffer from a prohibitive scaling of computation effort with system size. Density-functional theory, on the other hand, takes a different approach from the the above methods, reformulating the many-electron problem such that the explicit functional form of exchange and correlation energy with respect to electron density remains to be determined.

4.3. Density-functional theory

In contrast to the wave-function based approaches, density-functional theory (DFT) focuses on the electron density. The idea that all properties of a many-electron system can be calculated solely from the information on the electron density was proposed at the same time when Hartree developed his theory (1927-1928). Using the homogeneous electron gas (HEG) model, Thomas (1927) and Fermi (1928) independently described how the energy of an electronic system can be calculated exclusively from the electron density. Although too crude, the original idea of the Thomas-Fermi approximation paved a way to the later development of the density-functional theory (DFT). Hohenberg and Kohn proved the one-to-one correspondence between a ground-state electron density and an external potential, which implied that all physical properties of a many-electron system including the many-body wave-function can be determined solely from the density [93]. Later, in 1964, Kohn and Sham proposed a practical way of calculating the total electronic energy of a system based on single-particle Schrödinger equations with an effective mean field [94]. Although the Kohn-Sham method is in principle exact, in practice the exact expression for the exchange-correlation energy as a functional of the density is not known. The search for an accurate approximation to the exchange-correlation (XC) functional became the focus in further development of DFT. The local-density approximation (LDA), the generalized gradient approximation (GGA), hybrid approaches combining the Hartree-Fock and the GGA exchange, and the random-phase approximation for the correlation are prominent examples of XC functional approximations that are described in following subsections.

4.3.1. Hohenberg-Kohn theorems

Theorem 1 The external potential for a system of electrons is uniquely determined by the electron density $n(\mathbf{r})$ which has the normalization relation:

$$N_{\text{el}} = \int d^3r \, n(\mathbf{r}). \quad (4.10)$$

This theorem can be proven by contradiction followed from the assumption that there exist two different external potentials for any given electron density. Since $n(\mathbf{r})$ determines the external potential $v_{\text{ext}}(\mathbf{r})$, it also determines the ground-state wave function, which in principle can be obtained by solving the full many-body Schrödinger equation. Consequently, ground-state physical properties are fully determined by the electron density.

Theorem 2 For any external potential $v_{\text{ext}}(\mathbf{r})$, the density that minimize the total energy is the exact ground-state density. This theorem suggests a practical way to calculate the ground state energy. Any trial density for which $\int n^{\text{trial}}(\mathbf{r}) d^3r = N_{\text{el}}$ yields an energy greater or equal to the ground-state energy of the system $E[n_0^{\text{trial}}(\mathbf{r})] \geq E_0$, so that E_0 can be approached by applying a variational principle. In orbital-free DFT, one calculates the energy for a certain trial density and improves it iteratively in analogy with the self-consistent field method known from the Hartree-Fock theory. But a successful approximation to Eq. 4.5, especially for the kinetic-energy functional, is rather difficult to obtain. Therefore, the approach using single-electron orbitals invented by Kohn and Sham in 1965 received a great approval [94].

4.3.2. The Kohn-Sham equations

The problem with the kinetic energy $T = \langle \Phi | E_{\text{kin}} | \Phi \rangle$ is that its explicit expression in terms of electron density is unknown. Kohn and Sham introduced the concept of a non-interacting reference system which has the same electron density as the interacting system [94]. Contrary to the many-body problem, the Schrödinger equation for the non-interacting system can be relatively easily solved. The respective normalized single-particle states $|\varphi_i\rangle$ are often referred to as Kohn-Sham orbitals or states. These single-particle orbitals are used to construct a Slater determinant Ψ^{KS} , which corresponds to the many-electron wave function of the fermionic system, in analogy with the Hartree-Fock theory (Eq. 4.4), but with a different mean-field potential.

The electron density of the true system $n(\mathbf{r})$ can then be expressed as that of the fictitious reference system $n^{\text{KS}}(\mathbf{r})$ according to

$$n(\mathbf{r}) = n^{\text{KS}}(\mathbf{r}) = \sum_{i=1}^{N_{\text{el}}} |\varphi_i(\mathbf{r})|^2. \quad (4.11)$$

In contrast with the interacting system, the kinetic-energy functional of the non-interacting reference system can be written explicitly as

$$E_{\text{kin}}^{\text{KS}}[n(\mathbf{r})] = -\frac{1}{2} \sum_{i=1}^{N_{\text{el}}} \int d^3r \varphi_i^*(\mathbf{r}) \nabla^2 \varphi_i(\mathbf{r}). \quad (4.12)$$

Of course, this is not the exact kinetic energy of the interacting system due to the fact that the true many-body wave function is not a Slater determinant.

The full electron-electron interaction energy can be split into the classical electrostatic energy as a functional of density $n(\mathbf{r})$, which is the Hartree energy E_{H} (compare Eq. 4.9),

$$E_{\text{H}}[n(\mathbf{r})] = \frac{1}{2} \int d^3r d^3r' \frac{n(\mathbf{r})n(\mathbf{r}')}{|\mathbf{r} - \mathbf{r}'|}, \quad (4.13)$$

and an unknown remaining term $E_{e-e}[n(\mathbf{r})] - E_H[n(\mathbf{r})]$. The Hohenberg-Kohn functional may then be written in terms of the energy quantities for the non-interacting reference system as

$$F[n(\mathbf{r})] = E_{\text{kin}}^{\text{KS}} + E_H[n(\mathbf{r})] + \underbrace{E_{\text{kin}} - E_{\text{kin}}^{\text{KS}} + E_{e-e}[n(\mathbf{r})] - E_H[n(\mathbf{r})]}_{E_{\text{xc}}[n(\mathbf{r})]}, \quad (4.14)$$

where the kinetic energy correction as well as the deviation of the real electron-electron interaction energy from the Hartree energy are summarized as the exchange-correlation energy functional $E_{\text{xc}}[n(\mathbf{r})]$.

Solving the variational problem under the constraint Eq. 4.10, where ϵ_j enter as Lagrange parameters,

$$\partial_{\varphi_i^*} \left(F[n(\mathbf{r})] + \int n(\mathbf{r}) v_{\text{ext}} d\mathbf{r} - \sum_{j=1}^{N_{\text{el}}} \epsilon_j \left(\int d^3r |\varphi_j(\mathbf{r})|^2 - 1 \right) \right) = 0, \quad (4.15)$$

leads to a set of effective single-particle Schrödinger equations, the Kohn-Sham (KS) equations

$$\left\{ -\frac{1}{2} \nabla_{\mathbf{r}}^2 + v_H(\mathbf{r}) + v_{\text{xc}}(\mathbf{r}) + v_{\text{ext}}(\mathbf{r}) \right\} \varphi_i(\mathbf{r}) = \epsilon_i \varphi_i(\mathbf{r}). \quad (4.16)$$

These equations exactly describe non-interacting quasi-electrons moving in an effective, local, potential

$$v_{\text{eff}}(\mathbf{r}) = v_H(\mathbf{r}) + v_{\text{xc}}(\mathbf{r}) + v_{\text{ext}}(\mathbf{r}), \quad v_{\text{xc}}(\mathbf{r}) = \frac{\partial E_{\text{xc}}[n(\mathbf{r})]}{\partial n(\mathbf{r})}, \quad (4.17)$$

where the mean-field potential defined in Eq. 4.1 is the sum of the Hartree potential and the exchange-correlation potential. The Kohn-Sham equations must be solved self-consistently, since the effective potential (Eq. 4.17) depends on $n(\mathbf{r})$, which is calculated from the solutions $\varphi_i(\mathbf{r})$ via Eq. 4.11.

After solving the Kohn-Sham equations, DFT total energy of the interacting system can be calculated using the sum over the KS eigen-energies of the non-interacting system

$$E_0^{\text{DFT}}[n] = \sum_{i=1}^{N_{\text{el}}} \epsilon_i - E_H[n] + E_{\text{xc}}[n] - \int d^3r v_{\text{xc}}([n(\mathbf{r})]) n(\mathbf{r}). \quad (4.18)$$

Eq. 4.18 in principle gives the exact value of ground state energy of the interacting system, if all the terms in the equation can be obtained exactly. However, the exact form of the exchange-correlation term is unknown and some approximation for it is necessary.

Reformulating the variational problem in terms of wave functions instead of densities partly spoils the beauty of the Hohenberg-Kohn theorem, but it is necessary, since it gives explicit description of the kinetic energy of the non-interacting reference system. Strictly speaking, single-particle eigenstates $\varphi_i(\mathbf{r})$ of the KS reference system do not have a physical meaning. Nevertheless, the corresponding eigen energies ϵ_i are often good approximations to the electronic single-particle ionization energies of the true interacting system ([95]). Since the exchange-correlation functional is not generally known, the next step must be to find an approximate expression for $v_{\text{xc}}([n(\mathbf{r})])$. Contrary to the wave-function methods, which allow for successive improvement of accuracy, there is no obvious systematic way to do so for the exchange-correlation functional. Still, already rather crude approximations have proven to lead to a good agreement with experimental observations and valuable physical insight.

4.3.3. Exchange-correlation approximations and hybrid functionals

The exchange and correlation were studied before the birth of Kohn-Sham DFT in the background of the Thomas-Fermi theory. For the HEG system, the exchange can be written as an analytic expression [96], while the correlation energy density can be determined numerically with extremely high precision for intermediate densities [97]. For low and high density limit, the solution is known exactly.[cite] Assuming that the exchange and correlation can be locally described by the HEG model, the exchange-correlation energy can be expressed as a function of the electron density only. This became known as the local-density approximation (LDA) [94, 97, 98]:

$$E_{xc}[n] \approx E_{xc}^{LDA}[n] = \int d^3r n(\mathbf{r}) \epsilon_{xc}^{HEG}[n]. \quad (4.19)$$

Despite neglecting the true non-locality of $E_{xc}[n]$, the Kohn-Sham method with LDA works well for systems with slowly varying electron density, as for example for metallic solids and *sp*-bonded semiconductors [99], largely due to an error cancellation when appropriate energy differences are computed. Still, there are many cases when the error cancellation is far from complete. For example, LDA generally predicts over-binding, which leads for example to over-estimated cohesive or binding energies, especially for atoms and small molecules with a strong variation of electron density in space. Moreover, LDA introduces an electron self-interaction error, which means that Kohn-Sham orbitals that are highly localized may be destabilized.

To cure some of the deficiencies in LDA, the dependence of the exchange-correlation energy on the gradient of the electron density was introduced in the generalized gradient approximation (GGA), which is usually termed “semi-local” since it includes information on the density in an infinitesimal neighbourhood of \mathbf{r} :

$$E_{xc}[n] \approx E_{xc}^{GGA}[n, |\nabla n|] = \int d^3r n(\mathbf{r}) \epsilon_{xc}^{GGA}[n, |\nabla n|]. \quad (4.20)$$

The exchange-correlation energy density $\epsilon_{xc}^{GGA}[n, |\nabla n|]$ can be separated into exchange and correlation contributions. The exchange energy density is expressed as that of the homogeneous electron gas multiplied with an enhancement factor $F_x[n, |\nabla n|]$,

$$\epsilon_x^{GGA}[n, |\nabla n|] = \epsilon_x^{HEG}[n] F_x[n, |\nabla n|]. \quad (4.21)$$

In the proximity of an electron the probability of finding another electron is reduced. The density gradient provides additional possibilities for the depletion of electrons (also called exchange-correlation hole), effectively increasing the exchange-energy density compared to that of HEG. The enhancement factor $F_x[n, |\nabla n|] \geq 0$ accounts for this effect. In the HEG limit, where $|\nabla n| \rightarrow 0$, the local density approximation is recovered. However, it is not obvious how the exact functional form of $F_x[n, |\nabla n|]$ should be chosen to take into account the full exchange effect. Different GGA flavors have been suggested, determining the enhancement factor in accordance with certain physical constraints or using parameters obtained by fitting certain properties of a class of systems to experimental results. One of the very successful GGA functionals, the Perdew-Burke-Ernzerhof (PBE) functional [42], takes the following form for the exchange enhancement factor: $F_x[n(\mathbf{r})]$

$$F_x(s) = 1 + k_F - \frac{k_F}{1 + \frac{\mu s^2}{k_F}}, \quad (4.22)$$

where the reduced density gradient s is defined as

$$s = \frac{|\nabla n(\mathbf{r})|}{2k_F(\mathbf{r})n(\mathbf{r})}. \quad (4.23)$$

The constants μ and k_F are determined by making the PBE exchange-correlation energy E_{xc}^{PBE} reproduce the limit of known linear-response for the uniform electron gas, and by making E_{xc}^{PBE} obey the Lieb-Oxford criterium, which provides an upper bound for $F_x(s)$ [100]. In most cases, GGA functionals improve on bulk properties of solids such as cohesive energies and lattice constants, as compared to LDA [101, 102, 103]. Considering molecules, atomization energies can be calculated more accurately using GGA than using LDA, while only a small improvement is achieved for ionization energies and electron affinities (for details see Ref. [104] and references therein).

A major drawback of the local and semi-local exchange-correlation functionals is the incomplete correction for self-interaction. This deficiency can lead to systematic errors for systems where localization plays an important role, e. g. surfaces or defects. On the contrary, Hartree-Fock theory does not suffer from the self-interaction error, but its lacking of correlation energy leads to large errors in the description of chemical bonding. Combining local or semi-local functionals with Hartree-Fock exchange seems therefore a plausible approach. Even though, the attempts [105] to combine Hartree-Fock method with density functional theory were unsuccessful before Becke's paper in 1993 [106]. Becke analysed the correlation-exchange energy from the perspective of the adiabatic connection relation [107, 106] which formally accounts the exchange-correlation energy in an exact way:

$$E_{xc} = \int_0^1 d\lambda U_{xc}^\lambda \quad (4.24)$$

where U_{xc}^λ is the exchange-correlation potential energy at the intermediate coupling strength λ ($1 \geq \lambda \geq 0$). In Eq. 4.24, the fully interacting system ($\lambda=1$) and the noninteracting Kohn-Sham reference system ($\lambda=0$) are connected through a continuum of partially interacting systems, all sharing a common electron density. As a linear interpolation, a half-half scheme [106] was proposed:

$$E_{xc}^{\text{hyb}}[n] \simeq \frac{1}{2}U_{xc}^{\lambda=0} + \frac{1}{2}U_{xc}^{\lambda=1} \quad (4.25)$$

where the first term is exchange-potential energy of non-interacting system, thus actually correlation energy free and can be calculated in an exact manner (like in HF method) based on Kohn-Sham orbitals while the second term is for the fully interacting system which can be approximately calculated from density functional approach. As a consequence, the exchange-correlation approximation is no longer local.

Following the interpolation logic, a general one-parameter scheme [108] was proposed later:

$$E_{xc}^{\text{hyb}}[n] = \alpha(E_x^{\text{HF}}[\varphi_i[n]] - E_x^{\text{DFT}}[n]) + E_{xc}^{\text{DFT}}[n], \quad (4.26)$$

where $E_x^{\text{HF}}[\varphi_i[n]]$ is the exact exchange calculated as in Hartree-Fock method (see Eq. 4.7) based on, however, Kohn-Sham orbitals.

The optimum value of α was argued by Perdew and Ernzerhof [109] to be around 0.25, based on Göling-Levy perturbation theory [110], although it was also recognized that α is a parameter that may depend on both the system and the particular property to be evaluated [109]. These arguments leads to a successful parameter-free hybrid functional PBE0 [111], corresponding to the choice $E_{xc}^{DFT} = E_{xc}^{PBE}$ in Eq. 4.26 and $\alpha=0.25$.

While the hybrid exchange-correlation energy expressed in Eq. 4.26 meets the expectations on reducing the self-interaction error and works well for molecules [112], calculating the exact exchange in periodic boundary conditions is computationally expensive, especially for systems with metallic character, due to a slow decay of the exchange energy [43] with distance. Moreover, the long-range part of the exchange should mostly cancel with the exact correlation [113, 114, 115]. Since only approximate correlation is used in the Eq. 4.26, remaining terms from the long-range part of the Hartree-Fock exchange introduce some error. Thus, it is desirable to include only a short-range part of Hartree-Fock exchange, and partition the Coulomb operator $\frac{1}{r} = \frac{1}{|r-r'|}$ in E_{xx} (Eq. 4.7) accordingly. The Heyd-Scuseria-Ernzerhof functional (HSE [43, 116]) partitions the Coulomb potential for exchange into a long-range (LR) and a short-range (SR) part by using the computationally convenient error function

$$\frac{1}{r} = \underbrace{\frac{\text{erfc}(\omega r)}{r}}_{\text{SR}} + \underbrace{\frac{\text{erf}(\omega r)}{r}}_{\text{LR}}, \quad (4.27)$$

where ω is an adjustable parameter which defines separation range.

The exchange-correlation approximation then reads:

$$E_{xc}^{\text{HSE}}(\alpha, \omega) = \alpha E_{xx}^{\text{SR}}(\omega) + (1 - \alpha) E_x^{\text{PBE,SR}}(\omega) + E_x^{\text{PBE,LR}}(\omega) + E_c^{\text{PBE}}. \quad (4.28)$$

There are two prominent limiting cases for E_{xc}^{HSE} . If ω is zero, a fraction α of the full exchange energy is replaced by the exact exchange, and the original hybridization scheme is recovered. As ω approaches infinity or for $\alpha = 0$, E_{xc}^{HSE} reduces to the pure GGA functional E_{xc}^{PBE} . In the HSE06 version of the functional [116], the exchange parameter α is set to 0.25. The only empirical parameter, the range-separation parameter ω , is set to 0.11 bohr^{-1} [116]. This value was chosen based on the performance of the functional for test sets of atoms, molecules and 29 solids covering insulators, semiconductors and metals, compared to experimental data. These tests showed that variation of the screening parameter strongly influences band gaps of solids, while properties of molecular thermochemistry or lattice constants of solids are not so sensitive to its variation. Apart from the enhancement in modeling solid-system properties, HSE06 also eases the computational effort as compared to hybrid functionals without range separation, especially for metallic systems where exchange interaction decays slowly with distance. In HSE06, the exact exchange needs to be evaluated only for the short-range part, and therefore computational costs are reduced, in particular for bulk and surface models of extended systems. Compared to GGA functionals, hybrid functionals, such as the B3LYP (Becke, three-parameter, Lee-Yang-Parr functional) and HSE06, are sometimes regarded as not truly *ab initio*, due to the fact that their parameters are obtained from fitting to experimental data [112] of molecular and bulk materials.

4.4. Beyond Hartree-Fock, local, semilocal , and hybrid DFT: MP2, RPA, rPT2

Although incorporating exact exchange into hybrid functionals, e.g. HSE06, can generally achieve higher accuracy than LDA and GGA, it is not guaranteed that a hybrid functional describes better a specific system. Thus, it is desirable to check the reliability of a to-be-used hybrid functional against more advanced methods. As classified in a hierarchical scheme termed "Jacob's ladder" a biblical passage, a more accurate treatment of the electron correlation in conjunction with the exact exchange is needed to go beyond the hybrid functionals. The exact correlation in principle can be achieved with quantum chemistry methods which go beyond Hartree-Fock by further considering correlation between ground and excited electron configurations. However, the scaling of computational efforts rises steeply with the excitation level. For example, the second-order Møller-Plesset perturbation theory (MP2) [117] has the $O(N^5)$ scaling, while the coupled-cluster theory including single and double excitation (CCSDT) scales as $O(N^8)$, where N is roughly the number of basis functions (or occupied plus empty one-electron states). The random phase approximation (RPA) using Kohn-Sham orbitals treats the long-range part of the correlation energy accurately [118], and the scaling can be reduced to lower than $O(N^5)$. A recently developed method based on RPA, the renormalized second-order perturbation theory (rPT2), is used in this thesis for benchmark purposes. The theoretical background of RPA and rPT2 is briefly reviewed in the following paragraphs.

Starting from the Slater determinant that solves the Hartree-Fock equations (Eq. 4.5), some methods aim to improve the model by introducing the missing correlation between electrons that is so far neglected. This can be done by considering excited electronic configurations, generated by replacing occupied states in the Slater determinant with the unoccupied states (virtual orbitals). Replacing one, two, three,... orbitals means to consider single, double, triple,... excitations. The resulting determinants are eigenfunctions of the sum of one-electron Hamiltonian operators acting on every electron in the system, and form a many-electron basis. The sum of the one-electron operators can be interpreted as a zeroth-order Hamiltonian of the many-electron system, and the difference between the exact Hamiltonian and this zero-order Hamiltonian can be treated as perturbation using the Rayleigh-Schrödinger perturbation theory. The resulting approach is called Møller-Plesset perturbation theory [117]. The deviation between the exact electronic Hamiltonian \hat{H} and the HF mean-field Hamiltonian \hat{H}^{HF} can be expressed as:

$$\hat{H}' = \hat{H} - \hat{H}^{\text{HF}} = \sum_{i < j}^{N_{\text{el}}} \frac{1}{|\mathbf{r}_i - \mathbf{r}_j|} - \sum_{i=1}^{N_{\text{el}}} v_i^{\text{HF}}. \quad (4.29)$$

The unperturbed energy E_0^{HF} (Eq. 4.9) is already exact to first order, so that, following Rayleigh-Schrödinger perturbation theory, the ground-state energy in second-order perturbation (MP2) is

$$E_0 \approx E_0^{\text{HF}} + \sum_{l \neq 0} \frac{|\langle \Psi_l^{\text{HF}} | \hat{H}' | \Psi_0^{\text{HF}} \rangle|^2}{E_0^{\text{HF}} - E_l}. \quad (4.30)$$

Excited Slater determinants are denoted Ψ_l^{HF} , and E_l are the respective energy eigenvalues. According to the Brillouin theorem, singly excited HF states do not contribute in Eq. 4.30 (see

for example Ref. [119] for derivation). Also, excitations of higher order than double excitations do not contribute, since \hat{H}' is a two-particle operator.

Drawbacks of the MP2 method are divergence of the energy for metals and often an overestimation of the absolute value of the correlation energy for systems with a small HOMO-LUMO gap due to the truncation of the expansion. The random-phase approximation (RPA) is a method that overcomes these problems. RPA was originally used as an approximation to describe the homogeneous electron gas by Bohm and Pines in the 1950s [120, 121, 122]. The general idea is the following. Two kinds of the response of electrons to an oscillating component of the Fermi vacuum perturbation are distinguished. One is in phase with the perturbation, so the phase difference between the particle response and the wave producing it is independent of the position of the particle. This response contributes to the organized behaviour of the system. The other response has a phase difference with the wave producing it which depends on the position of the particle. Due to the generally random location of the particles, the second response can be considered to average out to zero when a large number of electrons are present. The procedure of neglecting the contribution of the second part of the response is termed random-phase approximation. In the form it is applied today, RPA can be formulated in different ways, for example via adiabatic connection (AC) approach, Green's-function-based many-body perturbation theory, or through a link with the coupled-cluster theory, as reviewed by X. Ren *et al.* [123]. The derivation of correlation energy via AC approach is sketched here (details can be found in Ref. [123]).

A mean-field reference system (e.g., the Kohn-Sham ground state) and many-body interacting system can be adiabatically connected [124, 125, 126] via a continuous set of coupling-strength-dependent states. Within this framework, an exact expression for exchange-correlation energy depends on the exchange-correlation hole which describes the fact that an electron located at \mathbf{r} reduces the probability of another electron being present in its vicinity at \mathbf{r}' . The exchange-correlation hole can be expressed in terms of density-density correlations which are formally fluctuations of the density operator around its expectation value. According to the fluctuation-dissipation theorem [127], the response of a system in thermal equilibrium to a small external perturbation is equal to its response to a spontaneous internal fluctuation in the absence of a perturbation. This provides a link between the fluctuations and response properties of the system, converting the challenge of finding a suitable approximation to the exchange-correlation energy in the context of DFT to the question of how to approximate the response functions of a series of fictitious systems along the adiabatic connection path. This is where RPA is applied – as an approximation to the response function $\chi^\lambda(\mathbf{r}, \mathbf{r}', i\omega)$, where λ is the coupling strength. The exchange-correlation energy can be written as the sum of exact-exchange energy E_{xx} and RPA correlation energy E_c^{RPA} ,

$$E_c^{\text{RPA}} = -\frac{1}{2\pi} \int \int d\mathbf{r} d\mathbf{r}' v(\mathbf{r}, \mathbf{r}') \times \int_0^\infty d\omega \left[\int_0^1 d\lambda \chi_{\text{RPA}}^\lambda(\mathbf{r}, \mathbf{r}', i\omega) - \chi^0(\mathbf{r}, \mathbf{r}', i\omega) \right] \quad (4.31)$$

where $v(\mathbf{r}, \mathbf{r}') = \frac{1}{|\mathbf{r} - \mathbf{r}'|}$ is the unscreened Coulomb interaction kernel. The independent-particle response function of the Kohn-Sham reference system $\chi^0(\mathbf{r}, \mathbf{r}', i\omega)$ is

$$\chi^0(\mathbf{r}, \mathbf{r}', i\omega) = 2 \sum_i^{\text{occ}} \sum_j^{\text{unocc}} \frac{\varphi_i^*(\mathbf{r}) \varphi_j(\mathbf{r}) \varphi_j^*(\mathbf{r}') \varphi_i(\mathbf{r}')}{i\omega + \epsilon_i - \epsilon_j} + \text{c.c.}, \quad (4.32)$$

with the single-particle orbitals $\varphi_i(\mathbf{r})$ and corresponding energies ϵ_i calculated using a mean-field approach of choice, while c.c. denote the complex conjugate. The same wave functions are also used to calculate E_{xx} , like in the hybrid DFT approach. RPA is typically calculated non-self-consistently due to its computationally heavy load.

The main improvement of RPA compared to MP2 is that it takes into account the screened instead of the bare Coulomb interaction. The RPA correlation energy comprises the response of the non-perturbed system to a perturbation as well as the response of the response, etc., such that the contributions are summed up to infinite order in the perturbation. Furthermore, the exact-exchange energy cancels the spurious self-interaction error in the Hartree energy, although there is still an RPA self-correlation error. The fully non-local RPA correlation energy also includes long-range van der Waals effects. Quantitatively, however, evaluating both exact exchange and RPA correlation does not always provide desired accuracy, and it has been found in practice that it leads to a systematic underestimation of binding energies in both molecules and solids [128, 129, 130] and an inaccurate description of the short-range correlation [131].

To alleviate the problems of RPA, beyond-RPA schemes have been developed, including the second-order screened exchange (SOSEX) and the single-excitation correction (SE). SOSEX, originating from the coupled-cluster theory, accounts for the antisymmetric nature of the many-electron wavefunction. A self-correlation-corrected approach is obtained by adding SOSEX to RPA. The SE correction is introduced to account for the orbital relaxation effects. Including single excitations at all orders of the perturbation theory leads to what is called renormalized single-excitation (rSE) contribution to the correlation energy. Combining RPA, SOSEX and rSE yields the renormalized second-order perturbation theory (rPT2)[46]. The benchmark results by the inventors show that rPT2 represents an overall improvement over RPA.

4.5. Dispersion correction to the approximate DFT functionals

Van der Waals (vdW) or dispersion interactions play a major role in a wide variety of molecules and materials, defining their structure, stability, and functions. These interactions originate from the quantum fluctuations of the electron density, which lead to instantaneous dipole moments and higher-order multipole moments. The interaction of the multipoles results in an attractive force, known as London dispersion. Although often used synonymously with dispersion interaction, van der Waals interaction includes also the permanent dipole-dipole interactions (Keesom force) and permanent dipole-induced dipole interactions (Debye force). In the classical picture, the electric field at position \mathbf{R} arises from an instantaneous dipole $\mathbf{E}_1 \propto \mathbf{p}_1/\mathbf{R}^3$, the dipole induced by this field at \mathbf{R} is $\mathbf{p}_2 = \alpha\mathbf{E}_1 \propto \mathbf{p}_1/\mathbf{R}^3$, so the interaction energy can be written as $E_{\text{disp}} = \mathbf{p}_2\mathbf{E}_1 \propto p_1^2/\mathbf{R}^6$, or $E_{\text{disp}} = C_6/\mathbf{R}^6$, where C_6 is known as dispersion coefficient. Casimir and Polder formulated the dispersion energy in terms of quantum electrodynamics, with atoms interacting with the zero-point oscillations of electric field permeating the system. This interaction, as a consequence, is frequency-dependent. The dispersion coefficient for interacting atoms or molecules A and B is given by Casimir-Polder integral:

$$C_6^{AB} = \frac{3}{\pi} \int_0^\infty \alpha(i\omega)^A \alpha(i\omega)^B d\omega, \quad (4.33)$$

where $\alpha_{A/B}(i\omega)$ are the frequency-dependent polarizabilities of A and B evaluated at imaginary frequencies.

The dispersion interaction is highly non-local, and it is one of the missing parts in local, semi-local, and hybrid DFT functionals. There are several approaches (a recent review can be found in [132]) to remedy this deficiency of the approximate DFT. One way, proposed by Langreth, Lundqvist and co-workers, is to construct a non-local correlation functional. These functionals, known as vdW-DF and the improved version vdW-DF2, are conceptually at higher rung in the formal hierarchy of computational methods. However, they suffer from low accuracy higher computational cost when compared to other methods in the market. An alternative treatment is to add a pairwise dispersion interaction correction to the exchange-correlation energy using the general form:

$$E_{\text{disp}} = -\frac{1}{2}s \sum_{A,B} f_{\text{damp}}(R_{AB}, R_A^0, R_B^0) \frac{C_6^{\text{AB}}}{R_{AB}^6}. \quad (4.34)$$

The sum runs over all atom pairs, and the factor $\frac{1}{2}$ is to correct the double counting. R_A^0 and R_B^0 are the van der Waals radii of the respective atoms. The damping functional $f_{\text{damp}}(R_{AB}, R_A^0, R_B^0)$ is chosen to avoid the singularities of R^{-6} and to smoothly join the short-range part described by the DFT functional and the long-range dispersion contribution. The scaling factor s is used to adjust the correction to repulsive behaviour for a chosen density functional. If some or all the parameters are obtained using an experimental information, the method is empirical.

Grimme and coworkers developed an early version of such a method, termed DFT-D2 [133], based on fixed C_6 parameters which are independent of the chemical environment of the atoms. The C_6 parameters, along with other parameters used in Eq. 4.34, are obtained by fitting to experimental data. To account for the variations of the polarizability (which can change by as much as 50%) depending on the chemical environment, in a recent version DFT-D3 C_6 parameters were calculated from time-dependent DFT and the concept of fractional coordination numbers. DFT-D3 is more accurate than DFT-D2, but still relies on experimental data, although to a lesser extent.

4.5.1. Tkatchenko-Scheffler (TS) scheme

In 2009, Tkachenko and Scheffler [134] developed a scheme to calculate the C_6 parameters and vdW radii explicitly from the mean-field ground-state electron density. The basic idea is to evaluate the effective C_6 parameters and vdW radii of an atom in a molecule or a solid by referring to the respective values of free atoms whose electronic structure can be calculated with high accuracy. As derived by Tang [135], the heteronuclear C_6 coefficient can be expressed in terms of homonuclear C_6 coefficients as follows:

$$C_6^{\text{AB}} = \frac{2C_6^{\text{AA}}C_6^{\text{BB}}}{\left[\frac{\alpha_B^0}{\alpha_A^0}C_6^{\text{AA}} + \frac{\alpha_A^0}{\alpha_B^0}C_6^{\text{BB}}\right]}, \quad (4.35)$$

where α_A^0 and α_B^0 are the static polarizabilities of A and B. The effective coefficient $C_6^{\text{eff,AA}}$ of atom A in its chemical environment is calculated based on the value for the atom in vacuum

$C_6^{\text{free,AA}}$ through:

$$C_6^{\text{eff,AA}} = \left(\frac{V^{\text{eff,A}}}{V^{\text{free,A}}} \right)^2 C_6^{\text{free,AA}} = \left(\frac{\int r^3 n^{\text{eff,A}}(\mathbf{r}) d\mathbf{r}}{\int r^3 n^{\text{free,A}}(\mathbf{r}) d\mathbf{r}} \right)^2 C_6^{\text{free,AA}}. \quad (4.36)$$

The $C_6^{\text{free,AA}}$ coefficients and the static polarizabilities of free atoms can be found in the database of Chu and Dalgarno [136], who calculated these properties via linear-response time-dependent DFT. The effective density $n^{\text{eff,A}}(\mathbf{r})$ is obtained via Hirshfeld partitioning:

$$n^{\text{eff,A}}(\mathbf{r}) = n(\mathbf{r}) \frac{n^{\text{free,A}}}{\sum_B n^{\text{free,B}}(\mathbf{r})}. \quad (4.37)$$

Eq. 4.34 with $s = 1$ is used to calculate van der Waals energy. The damping function takes the form:

$$f_{\text{damp}}(R_{\text{AB}}, R_{\text{AB}}^0) = \frac{1}{1 + \exp \left[-d \left(\frac{R_{\text{AB}}}{s_R R_{\text{AB}}^0} \right) - 1 \right]}, \quad (4.38)$$

where R_{AB}^0 is the sum of van der Waals radii R_{B}^0 and R_{A}^0 . Analogously to $C_6^{\text{eff,AA}}$, the effective van der Waals radius of an atom in its environment is calculated via:

$$R^{0,\text{eff}} = \left(\frac{V^{\text{eff}}}{V^{\text{free}}} \right)^{1/3} R^{0,\text{free}}. \quad (4.39)$$

The parameter s_R controls the value of R_{AB} at which the damping function approaches zero and also the onset of dispersion correction. The value of s_R is in practice determined by fitting to S22 database [137], and depends on the functional used. The parameter d was found to have negligible influence once the value of s_R is optimized with $12 < d < 45$ [134].

4.5.2. Many-body effects of van der Waals interactions

As described in the preceding subsection, the original TS scheme is based on two approximations: (i) effective treatment of electrostatic screening, and (ii) neglecting the non-additive many-body contribution. In physical terms, TS takes into account the influence of local environment on polarizability, but the polarizability of an atom can be also influenced by the fluctuating dipoles of atoms located at larger distances. To go beyond the pairwise contributions, Taktchenko and co-workers proposed a method [45], referred to as MBD@rsSCS, to account for both the full screening effects and the many-body dispersion contributions for finite-gap molecules and solids.

The MBD@rsSCS adopts the coupled fluctuating-dipole model (CFDM) [138], and models the atoms in a molecule/solid as spherical quantum harmonic oscillators (QHOs), coupled to each other through dipole-dipole interactions. By representing all atoms in a given molecular system as a collection of N QHOs, the CFDM Hamiltonian can be written as:

$$H = -\frac{1}{2} \sum_{p=1}^N \nabla_{\chi_p}^2 + \frac{1}{2} \sum_{p=1}^N \omega_p^2 \chi_p^2 + \sum_{p>q}^N \omega_p \omega_q \sqrt{\alpha_p \alpha_q} \chi_p \mathcal{T}_{pq} \chi_q, \quad (4.40)$$

where $\chi_p = \sqrt{m_p \mu_p}$, with μ_p being the displacement of oscillator p from the equilibrium, $m_p = (\alpha \omega_p^2)^{-1}$, ω_p is the characteristic excitation frequency, α_p is the polarizability of the QHO at position p , and \mathcal{T}_{pq} is the dipole-dipole interaction tensor discussed in detail below.

Using the adiabatic-connection fluctuation-dissipation theorem (ACFDT), Taktchenko and co-workers showed that the van der Waals interaction energy between the QHOs can be computed as the difference between the zero-point energies of the coupled and uncoupled QHOs:

$$E_{\text{MBD}}^{\text{vdW}} = \frac{1}{2} \sum_{p=1}^{3N} \sqrt{\lambda_p} - \frac{3}{2} \sum_{p=1}^N \omega_p^{\text{SCS}}, \quad (4.41)$$

where λ_p are the Hamiltonian eigenvalues. Since semi-local and hybrid exchange-correlation functionals already efficiently account for short-range correlation, only the long-range correlation remains to be corrected. In order to avoid double counting of the short-range correlation, a range-separating (for which "rs" stands) scheme is adopted in the MBD@rsSCS method. $\mathcal{T}_{pq} = \nabla_{r_q} \bullet \nabla_{r_p} W(r_{pq})$, $W(r_{pq}) = \text{erf}[r_{pq}/(\sqrt{2}R)]/r_{pq}$ is the Coulomb potential for the interaction between two spherical Gaussian distributions, with r_p and r_q being the QHO positions, $r_{pq} = |r_p - r_q|$. The short-range part of the dipole-dipole interaction tensor is given by:

$$\mathcal{T}_{\text{SR},pq} = (1 - f(r_{pq}))\mathcal{T}_{pq}, \quad (4.42)$$

where $f(r_{pq})$ is the Fermi-type damping function as in TS approach (Eq. 4.38). The frequency-dependent self-consistently screened (SCS) polarizability for the spherical QHOs can be written as follows:

$$\alpha_p^{\text{rsSCS}}(i\omega) = \alpha_p^{\text{TS}}(i\omega) + \alpha_p^{\text{TS}}(i\omega) \sum_{q \neq p}^N \mathcal{T}_{\text{SR},pq} \alpha_q^{\text{rsSCS}}(i\omega) \quad (4.43)$$

where $\alpha_p^{\text{TS}}(i\omega)$ denotes the frequency-dependent polarizability obtained from the TS scheme, $\mathcal{T}_{\text{SR},pq}$ is the short-range dipole-dipole interaction tensor. Solving iteratively the Eq. 4.43 gives the self-consistent polarizability which includes all screening effects.

The steps to obtain the MBD@rsSCS long-range correlation energy correction can be summarized as follows:

1. The unscreened polarizabilities are obtained with the TS scheme.
2. The short-range self-consistently screened polarizabilities α^{rsSCS} are obtained via the iterative procedure defined in Eq. 4.43.
3. The Hamiltonian in Eq. 4.40 is calculated using the obtained α^{rsSCS} and the long-range dipole-dipole tensor, and diagonalized.
4. The many-body long-range correlation energy is calculated via Eq. 4.41.

4.5.3. The vdW^{surf} method

As noted in Sec. 4.5.2, the described method for the many-body effects on the van der Waals interaction is applicable only for molecules and solids with a finite electronic gap. For metal

surfaces, as well as interfaces with a metal, Ruiz and co-workers developed an approach [139] beyond pairwise description by combining the original TS scheme [134] with the Lifshitz-Zaremba-Kohn (LZK) theory [140, 141]. Hereafter we refer to this method as vdW^{surf} .

As derived by Zaremba and Kohn [141], the van der Waals interaction between an atom and a solid surface is given by:

$$E_{\text{vdW}} \simeq -C_3^{aB}/(Z - Z_{\text{vdW}})^3, \quad (4.44)$$

where Z is the distance from the top atomic plane to the adsorbate atom, and $Z_{\text{vdW}} = d/2$ for jellium solid, with d being the distance between equally spaced atomic layers parallel to the surface. The vdW coefficient C_3^{aB} for atom a interacting with the surface B , according to Zaremba and Kohn, can be calculated from:

$$C_3^{aB} = \frac{\hbar}{4\pi} \int_0^\infty d\omega \alpha(i\omega) \frac{\varepsilon_B(i\omega) - 1}{\varepsilon_B(i\omega) + 1}, \quad (4.45)$$

where $\alpha(i\omega)$ is the polarizability of the atom a and $\varepsilon_B(i\omega)$ is the dielectric function of the solid B . A convenient approach [142] to recover the LZK formula is summing up all the pairwise vdW interactions between atom a and atoms b in the infinite half-space of the solid B . Thus, the C_3^{aB} coefficient can be obtained as:

$$C_3^{aB} = n_s \left(\frac{\pi}{6} \right) C_{6,\text{LZK}}^{ab}, \quad (4.46)$$

where n_s is the number of atoms per unit volume in the bulk. Although the form is pairwise, the vdW interaction calculated based on the screened $C_{6,\text{LZK}}^{ab}$ coefficient “inherits” the many-body screening effects from Eq. 4.45. The Padé-approximation model is adopted to disentangle $C_{6,\text{LZK}}^{ab}$ into homonuclear C_6^{aa} and $C_{6,\text{LZK}}^{bb}$ coefficients, similarly to the original TS scheme:

$$C_{6,\text{LZK}}^{ab} = \frac{2C_6^{aa}C_{6,\text{LZK}}^{bb}}{\frac{\alpha_{\text{LZK}}^b}{\alpha_0^a}C_6^{aa} + \frac{\alpha_0^a}{\alpha_{\text{LZK}}^b}C_{6,\text{LZK}}^{bb}} \quad (4.47)$$

Here, α_0^a and α_{LZK}^b correspond to static polarizabilities of the adsorbate atom and the effective “atom-in-solid”, respectively. In the LZK theory, the frequency-dependent polarizability of an adsorbed atom is equal to the one of the isolated free atom. Since accurate α_0^a and C_6^{aa} values are known, the remaining unknown parameters in Eq. 4.47 are α_{LZK}^b and $C_{6,\text{LZK}}^{bb}$. In practice, they are obtained using the following procedure:

1. For a given metal substrate, choose any two different atoms (H, C, Ne, Ar, Kr,...) whose α_0^a and C_6^{aa} accurate values are available.
2. Calculate $C_{6,\text{LZK}}^{ab}$ value for the two chosen adsorbate atoms by using Eq. 4.45 and Eq. 4.46.
3. Substitute the values obtained in the previous step into Eq. 4.47 to get a set of linear equations from which the α_{LZK}^b and $C_{6,\text{LZK}}^{bb}$ can be obtained.

Once the parameters α_{LZK}^b and $C_{6,\text{LZK}}^{bb}$ are obtained, they are used as references for the DFT+vdW^{surf} polarizability and C_6 of the substrate atoms, respectively. The radius reference is obtained through the reference of free atom b :

$$R_{b,\text{LZK}}^0 = (\alpha_0^b / \alpha_{\text{free}}^b)^{1/3} R_{b,\text{free}}^0 \quad (4.48)$$

Like in the original TS scheme, polarizability, C_6 , and vdW radius values of atom-in-solid change according to a dimensionless volume which is determined by Hirshfeld partitioning:

$$v_{\text{eff}}^i = \frac{\int \mathbf{r}^3 w_i(\mathbf{r}) n(\mathbf{r}) d^3 \mathbf{r}}{\int \mathbf{r}^3 n_i^{\text{eff}}(\mathbf{r}) d^3 \mathbf{r}}, \quad (4.49)$$

where $w_i(\mathbf{r})$ is the Hirshfeld partitioning weight of species i , $n(\mathbf{r})$ is the total electron density and $n_i^{\text{eff}}(\mathbf{r})$ is the reference electron density. The effective vdW parameters are then determined through:

$$C_{6,\text{eff}}^{ii} = (v_{\text{eff}}^i)^2 C_{6,\text{ref}}^{ii} \quad (4.50)$$

$$\alpha_{\text{eff}}^i = (v_{\text{eff}}^i) \alpha_{\text{ref}}^i \quad (4.51)$$

$$R_{i,\text{eff}}^0 = \left(\frac{\alpha_{\text{eff}}^i}{\alpha_{\text{ref}}^i} \right)^{1/3} R_{i,\text{ref}}^0, \quad (4.52)$$

After all the C_6 , α , and R values for the substrate and adsorbate atoms are obtained, Eq. 4.47, Eq. 4.46, and Eq. 4.44 yield the vdW interaction energy.

4.6. Electronic-structure code of choice: FHI-aims

The electronic-structure code used in this thesis is the Fritz Haber Institute *ab initio* molecular simulations (FHI-aims) program package. For details of the implementation and usage, the reader is referred to the original references [143, 144]. Here we briefly outline the implementation features.

In order to solve the Kohn-Sham equations Eq. 4.16, the single-particle orbitals $\varphi_i(\mathbf{r})$ have to be cast in a known mathematical form. Commonly in electronic structure codes, $\varphi_i(\mathbf{r})$ are expanded as a linear combination of basis functions:

$$\varphi_i(\mathbf{r}) = \sum_j c_{ij} \phi_j(\mathbf{r}), \quad (4.53)$$

where c_{ij} are the expansion coefficients. As a result, the eigenvalue problem of solving the Kohn-Sham equations or the HF equations becomes a generalized eigenvalue problem of finding the expansion coefficients:

$$\sum_j h_{ij} c_{jl} = \epsilon_l \sum_j s_{ij} c_{jl}, \quad (4.54)$$

where $h_{ij} = \langle \phi_i | \hat{h} | \phi_j \rangle$ and $s_{ij} = \langle \phi_i | \phi_j \rangle$. The basis functions should have a known mathematical form which is calculable in computers. In general, one can distinguish two main types of basis functions: delocalized (e.g., plane waves), which extend over the whole space, and localized. The former are used in several popular codes such as VASP and CASTEP, while the

latter are used e.g., in the Gaussian code and NWchem. The FHI-aims code used in this thesis employs a type of localized basis functions: the numeric atom-centered orbitals (NAOs). The NAOs takes the following form:

$$\phi_i(\mathbf{r}) = \frac{u_i(\mathbf{r})}{r} Y_{lm}(\Theta, \Phi) \quad (4.55)$$

where $Y_{lm}(\Theta, \Phi)$ are the spherical harmonics and $u_i(\mathbf{r})$ are radial functions determined by the Schrödinger-like equations:

$$\left[-\frac{1}{2} \frac{d^2}{dr^2} + \frac{l(l+1)}{r^2} + v_i(\mathbf{r}) + v_{\text{cut}}(\mathbf{r}) \right] u_i(\mathbf{r}) = \epsilon_i u_i(\mathbf{r}). \quad (4.56)$$

Here, $v_i(\mathbf{r})$ is the potential defining the shape of $u_i(\mathbf{r})$, and v_{cut} is a cut-off potential which ensures that $u_i(\mathbf{r})$ becomes exactly zero when r is larger than r_{cut} . The cut-off potential in the FHI-aims code takes the form:

$$v_{\text{cut}}(\mathbf{r}) = \begin{cases} 0 & r \leq r_{\text{onset}}, \\ s \cdot \exp\left(-\frac{\omega}{r-r_{\text{onset}}}\right) \cdot \frac{1}{(r-r_{\text{cut}})^2} & r_{\text{onset}} < r < r_{\text{cut}}, \\ \infty & r \geq r_{\text{cut}}, \end{cases}$$

where the parameter s is a global scaling factor, and r_{onset} is the radius where the potential starts from zero, approaching smoothly to infinity at r_{cut} . Such a confining potential enables linear scaling of computational effort in the limit of large system size due to the fact that all integration beyond r_{cut} vanishes. The radial functions are evaluated on a logarithmic grid, which is denser close to the nucleus and coarser far from the nucleus. The radial functions are chosen from a pool of candidate radial functions including hydrogen-like, cation-like, or atom-like functions with a variable confinement potential. An iterative scheme is adopted to obtain hierarchical sets of basis functions for a given chemical element. All basis functions in the candidate pool are organized in tiers according to different levels of priority, with each tier containing several basis functions with different angular momenta (e. g., spd/spdfg/spdf... for oxygen) [143]. In each iteration, a tier of basis functions which recovers most of the dimer binding energy within a certain error margin among all candidates in the pool is added to the basis set. Three default tiers of basis functions for elements from hydrogen to nobelium are distributed in the official release, classified as *light*, *tight*, and *really tight (safe)*. Lists of standard basis in FHI-aims code are given in appendix (App. B) for all elements involved in this thesis.

In FHI-aims, several methods that involve exact exchange and non-local correlation terms, such as hybrid functionals, MP2, RPA, and rPT2 methods, are implemented by using the *resolution of identity* (RI) technique. The RI technique, also known as density fitting, approximates pair products of atomic basis functions $\phi_i(\mathbf{r})\phi_j(\mathbf{r})$ as a linear combination of auxiliary basis functions:

$$\phi_i(\mathbf{r})\phi_j(\mathbf{r}) \approx \sum_{\mu} C_{ij}^{\mu} P_{\mu}(\mathbf{r}), \quad (4.57)$$

where $P_{\mu}(\mathbf{r})$ are the auxiliary basis functions, and C_{ij} are the expansion coefficients. Using this expansion, the four-center electron repulsion integrals are reduced to:

$$(ij|kl) \approx \sum_{\mu\nu} C_{ij}^{\mu}(\mu|\nu) C_{kl}^{\nu} = \sum_{\mu\nu} C_{ij}^{\mu} \int \frac{P_{\mu}(\mathbf{r})P_{\nu}(\mathbf{r}')}{|\mathbf{r}-\mathbf{r}'|} C_{kl}^{\nu}, \quad (4.58)$$

where only three-center integrals and two-center integrals are required, which enormously decreases the cost of both the computational time and required memory. The approach makes use of the fact that many of the pair products of atomic functions are linearly-dependent, so that the number of the required auxiliary basis functions scales linearly rather than quadratically with the size of the atomic basis.

Part II.

Water on alkline-earth metal-oxide surfaces

5. Interaction of water with alkaline-earth metal-oxide surfaces

The interaction of water with solid surfaces is of fundamental importance in a broad range of fields, including geochemistry, environmental science, materials science, and heterogeneous catalysis. Therefore, intensive investigations have been carried out for adsorbed water structures on metal and metal-oxide surfaces [145]. Compared to many long-range-ordered structures observed on metal surfaces [145, 22], observations of ordered structures on oxides are rare. Adsorption of water on the MgO(001) surface is one example where ordered structures have been observed in one-monolayer regime, and have been intensively studied during last two decades [146, 147, 148, 24, 149, 150, 26, 25, 151]. Thanks to the intensive collaboration between theory and experiment, the atomic structure of two partially dissociated ordered monolayer phases were identified recently [146].

The water adsorption on oxides in the sub-monolayer regime is much less studied, although it is essential for understanding, for instance, first steps of surface wetting and ice formation. J.-H. Cho *et al.* [26] calculated the adsorption of water clusters from monomer to tetramer on MgO(001), and emphasized the importance of hydrogen bonding for water dissociation on the surface. Based on the calculated Gibbs free energy variation of the adsorption and dissociation of one, two, or three water molecules on MgO(001), Alvim and co-workers [152] concluded that the hydrolysis on the perfect MgO (001) surface starts from two water molecules. However, contrary to the full monolayer case, a global search for submonolayer adsorbed water structures, to the best of our knowledge, has not been reported.

Calcium oxide (CaO) is a material with various applications such as CO₂ capture and heterogeneous catalysis. As a CO₂ capturing material, CaO is widely used in industry to enhance hydrogen production from biomass [153], and to separate CO₂ from flue gas [154]. As a catalytic material, it is used to catalyze the conversion of different types of biomass to biodiesel [155, 156, 157], and also the de-NO_x reactions [158]. Although in all the applications mentioned above the co-existence of water with reactants is typical, there is a relatively small number of studies devoted to water interacting with CaO surface. In particular, first-principles theoretical studies [159, 160, 161, 162] on water interacting with CaO surface have only been carried out for water monomer, while other studies of this system, e.g. studies of hydration of CaO surface, were investigated using force fields [163]. First-principles studies of water-water interactions in this system, however, have not been reported, although adsorbate-adsorbate interactions have been found to be important for understanding water interaction with other oxide surfaces. In particular, the interaction between adsorbed molecules auto-catalyses the dissociation of water on MgO(001) surface, as has been shown both theoretically [152] and experimentally [164].

In spite of the same rock-salt crystal structure, similar melting temperature, and the size of the band gap (7.8 eV for MgO and 7.1 eV for CaO), CaO shows a largely different from MgO chem-

ical behaviour [165]. X-ray photoemission studies [166] revealed that water reacts with CaO (001) at water pressures lower than 5×10^{-10} Torr at 300 K, while MgO(001) was shown to be inert at water vapour pressures lower than 10^{-4} Torr. Moreover, temperature-programmed desorption studies [150] indicated that water adsorption on CaO(001) is 25-50 kJ/mol more stable than that on MgO(001). *Ab initio* molecular dynamics simulations [161] with PW91 functional showed that dissociative adsorption of water monomer on CaO (001) is favoured (different from what has been suggested previously [160]), while molecular adsorption of single water molecule is found on MgO(001). Hu *et al.* [162] reported a systematic density-functional theory (DFT) study (using PBE functional) of the trends in water monomer adsorption on insulating rocksalt crystal (001) surfaces, and found that MgO(001) is the only one among MgO(001), CaO(001), and SrO(001) that prefers molecular adsorption of isolated water molecule. So far, no theoretical work on the adsorption of water clusters or layers on CaO or SrO surfaces has been reported. In fact, water interacting with SrO surface is even less studied compared to CaO. Two theoretical studies [167, 162] show that water dissociative adsorption is preferred on SrO(001), and the adsorption is stronger than that on CaO(001). Water dissociative adsorption was also found on the SrO termination [168, 169] of SrTiO₃, which has same cubic arrangement of Sr and O atoms as SrO(001). Moreover, Zhang *et al.* [170] studied aldol addition of acetone catalysed by MgO, CaO, and SrO, and found that SrO shows highest activity among them. Pre-adsorption of water on MgO and CaO were found to increase the reactivity, while pre-adsorption effects on SrO were not studied.

An interesting aspect of the sub-monolayer adsorption of any species is the possibility of formation of ordered low-dimensional structures. Particularly intriguing are the cases of low-dimensional adsorption on flat terraces, where there is no explicit translational-symmetry breaking due to steps or other extended defects. One-dimensional (1D) structures serve as model systems with particularly simple boundary conditions [171] and peculiar transport phenomena of electrons and light [172, 173, 174]. In chemistry, they often form the target line for tailoring molecular interactions [175]. Various mechanisms have been identified to trigger the formation of 1D structures. The fundamental requirement is a loss in symmetry, which leads to the preference for one growth direction against the others. Such guided growth might be promoted by templates with linear topology, introduced for example by troughs or step edges on the surface, [176, 177, 178] or by using uniaxial building blocks with two reaction centers at opposite sides [175, 179]. In other cases, 1D growth was found to arise from a favorable alignment of intrinsic dipoles or charges along the growth direction [180]. In general, the exploration of 1D systems aims at a better understanding of interaction schemes between atomic and molecular entities. The propensity to develop 1D structures depends on the degree of asymmetry in a given system. Water appears to be a good candidate in this respect, as it has a strong dipole moment. So far, 1D water structures were mainly found on template surfaces, where the growth direction is governed by oriented troughs in the surface [22]. Prominent examples for such 1D assemblies are the water-induced superstructures on Cu(110) [21] and TiO₂(110) [181]. On most metallic and dielectric surfaces, on the other hand, water forms 2D networks as the interaction is not exclusively governed by dipole coupling but also by the development of hydrogen bonds between O and H species. The subtle interplay between both coupling regimes leads to the occurrence of 'magic' water clusters, e.g. pentagons and hexagons, as explored with scanning tunneling microscopy (STM) and density-functional theory [182, 183]. The situation becomes even more

complex, if a fraction of the H_2O dissociates upon adsorption, and 2D networks arise from the interplay of water and hydroxyl species, as well as from proton exchange between them [184]. The development of partly dissociated water ad-layers has been found on MgO both in experiment [25, 146] and theory [24, 146, 162]. Formation of 1D structures, on the other hand, has not been observed on any of those systems so far.

Recently, formation of 1D structures was observed by STM on CaO(001) exposed to water atmosphere under UHV conditions [1]. These 1D structures are typically 4-5 nm long and narrower than 1 nm. The atomic arrangement of the structures, however, could not be resolved from the STM images due to the resolution limitation of STM for such an insulator substrate with a large band gap. Nevertheless, the orientation of the 1D structures can be clearly identified to be (110). Starting from these observations, we have identified a distinct 1D configuration of partly dissociated H_2O molecules on a CaO(001) surface by means of GA. In addition to the translations, the symmetry group of the clean surface contains a four-fold axis, which implies four equivalent directions for an adsorbed structure growth. We explain the stabilization of linear structures on this four-fold symmetric support. We show that the initial symmetry breaking occurs at the level of H_2O tetramers featuring an excess proton, and can guide the growth of the water chains.

Ab initio atomic thermodynamic analysis of the PBE results indicates that the found 1D structure forms a thermodynamically stable phase in a narrow range of temperature and pressure of water which agrees well with the conditions at which the 1D structures were observed in STM. Furthermore, we calculated the IR spectra through both the harmonic approximation and MD simulations. Interestingly, a peak-splitting is found for vibrational spectra of the 1D structure at finite temperature by comparing the spectra obtained via the above mentioned two ways. Good agreement is found between the MD-based spectra and the measured IR spectra, which further reinforces our suggestion for the atomic arrangement of the 1D structure. The features of the MD-based IR spectra, including the peak splitting, were analysed in details by auto-correlation of the atomic velocities.

Water interacting with MgO(001) and SrO(001) surfaces is also investigated using the same methodology. 1D structures are also found on MgO(001) surface, although not thermodynamically stable according to *ab initio* atomistic thermodynamic analysis. On SrO(001), however, no 1D structures are found due to the strongest basicity of the surface and largest lattice parameters. General trends in water interaction with these three cubic oxide surfaces are discussed, and the thermodynamic stability of 1D structures on CaO(001) is attributed to a balance between adsorbate-adsorbate and adsorbate-substrate interactions.

6. Formation of water chains on CaO(001) surface

6.1. Computational Details

All DFT calculations are performed with the electronic structure code FHI-aims [143]. For the structural search, a two-layer periodic slab model and the PBE exchange-correlation functional [42] is used. The low-energy structures obtained from a global search algorithm (as described below) are further optimized using the HSE06 hybrid functional [43, 44], as implemented in FHI-aims [185], and four-layer substrate model. As demonstrated by Carrasco and coworkers [186], dispersion forces play an important role in water adsorption on metals. Therefore, an *ab initio* many-body dispersion interaction correction [134, 45] (abbreviated “+vdW” below) is added to final energetics. More details about can be found in C. Dispersion effects on energy hierarchy in GA can be found in Fig. 6.2) and is discussed later. Three different surface unit cell sizes are used: 3×2 (24 atoms per layer), 4×2 (32 atoms per layer), and 3×4 (48 atoms per layer) - to model a variety of adsorbate coverages. For these unit cells, $4 \times 6 \times 1$, $3 \times 6 \times 1$, and $4 \times 3 \times 1$ k -grids are used, respectively. Our tests show that doubling the k -grid density changes the calculated total energy by less than 0.001 eV. The convergence with respect to the numerical settings, basis set size, and the number of layers in the slab models for the three oxides (MgO, CaO and SrO) can be found in Appendix A.

The global structural search is performed using our implementation of *ab initio* GA (Chp. 3). For GA runs, periodic models are used consisting of two-layer 3×4 oxide slabs with different numbers of water molecules per unit cell. The slabs are separated by more than 40 Å of vacuum. Dipole correction is not employed in this study as our tests show it changes adsorption energies by less than 2 meV/molecule. Structures with 1-15 adsorbed water molecules per unit cell were calculated. Non-stoichiometric H_xO_y adsorbed structures ($x = 3, y = 3$; $x = 12, y = 0$; $x = 0, y = 12$; $x = 13, y = 15$; $x = 14, y = 27$) were also calculated (the last two compositions were chosen based on the results of a trial free-energy global optimization). The structures were relaxed with PBE and the default *light* numerical settings. During the atomic relaxation, the adsorbates and the topmost surface layer are relaxed, while the bottom layer is fixed at the bulk geometry. The lattice constant used for the slab models is the PBE lattice constant calculated with *tight* numerical settings: 4.258 Å, 4.834 Å, and 5.197 Å for MgO, CaO, and SrO, respectively. After the GA search, 50 most stable structures are selected (in the case of $6H_2O/CaO(001)$, the 50th is 0.46 eV less stable than the global minimum we found). Two more oxide layers are then added to the bottom of the two-layer slab models of the selected structures, and atomic relaxation is performed again with PBE/*tight* settings, this time with only the geometry of the two bottom layers fixed. Finally, the structures are relaxed at the HSE06/*tight* level of theory, with a many-body dispersion correction. To achieve self-consistency, the geometries are rescaled according to HSE06 lattice parameters (4.210 Å, 4.800 Å and 5.157 Å for MgO, CaO and SrO respectively) before doing the HSE optimization. A proof that the PBE-based GA does not lead to missing

low-energy structures at the HSE06 level is presented in the next section.

The adsorption energies are calculated as follows:

$$E_{\text{ads}} = \frac{1}{n} \left(E_{n\text{H}_2\text{O}/\text{slab}} - E_{\text{slab}} - nE_{\text{H}_2\text{O}} \right) + \Delta E^{\text{ZPE}}, \quad (6.1)$$

where n is the number of water molecules per unit cell, $E_{n\text{H}_2\text{O}/\text{slab}}$, E_{slab} , and $E_{\text{H}_2\text{O}}$ are the DFT total energies of the metal-oxide slab with adsorbed water, the slab without water, and the water molecule in the gas phase, respectively. The geometry of the gas-phase water molecule was relaxed at the same level of theory as the surface structures. The ZPE correction ΔE^{ZPE} is calculated according to:

$$\Delta E^{\text{ZPE}} = \frac{1}{n} \left(E_{n\text{H}_2\text{O}/\text{slab}}^{\text{ZPE}} - E_{\text{slab}}^{\text{ZPE}} - nE_{\text{H}_2\text{O}}^{\text{ZPE}} \right), \quad (6.2)$$

where $E_{n\text{H}_2\text{O}/\text{slab}}^{\text{ZPE}}$, $E_{\text{slab}}^{\text{ZPE}}$, and $E_{\text{H}_2\text{O}}^{\text{ZPE}}$ are the corresponding ZPEs.

Unless otherwise specified, vibrational spectra are calculated in the harmonic approximation using finite displacements of 0.025 Å from the optimized atomic positions. All atoms in adsorbates and also hydrated surface oxygen atoms are allowed to vibrate during the calculations of vibrational properties. Releasing all atoms in the top layer changes ZPE correction (Eq. 6.2) by less than 0.01 eV, and vibrational frequencies by less than 5 cm⁻¹. PBE functional and *tight* settings are mostly used in harmonic vibrational calculations. HSE06+vdW vibrational frequencies were also calculated for selected structures, and were found to differ from the PBE frequencies by no more than 15 cm⁻¹ in the region of interest (see Fig. 6.8). Due to the large size of the surface unit cells, vibrational frequencies are calculated only at the phonon Γ -point. Intensities are calculated from the dipole moment component parallel to the surface normal [187, 21]. To compare with the experimental results, D₂O spectra are calculated instead of H₂O. For the most stable 1D structure on CaO(001), anharmonic spectra at 300 K are calculated from the dipole-dipole autocorrelation function obtained from *ab initio* MD simulations [71]. A two-layer slab model is used, and all atoms except the bottom layer of CaO is fixed. For the sanity check of our MD approach, we have also calculated the spectrum at a low temperature (30 K), and we have found that it reproduces well the harmonic spectrum.

To compare the relative stability of different adsorption structures at realistic conditions, we use the *ab initio* atomistic thermodynamics approach [51, 188]. Gibbs free energies of H₂O adsorption per surface area unit are calculated as follows:

$$\Delta G^{\text{ad}}(T, p_{\text{H}_2\text{O}}) = \frac{1}{A} \left(E_{n\text{H}_2\text{O}/\text{slab}} - E_{\text{slab}} - n\mu_{\text{H}_2\text{O}}(T, p_{\text{H}_2\text{O}}) + \Delta F^{\text{vib}}(T) \right), \quad (6.3)$$

where A is the surface area of the unit cell, $p_{\text{H}_2\text{O}}$ is the partial pressure of water vapor, $E_{n\text{H}_2\text{O}/\text{slab}}$ and E_{slab} are total energies per unit cell of the slab with and without adsorbed species, respectively, and $\Delta F^{\text{vib}}(T)$ is the change of the surface vibrational free energy upon adsorption. The chemical potential of water $\mu_{\text{H}_2\text{O}}(T, p_{\text{H}_2\text{O}})$ is calculated using the ideal gas model:

$$\mu_{\text{H}_2\text{O}}(T, p_{\text{H}_2\text{O}}) = E_{\text{H}_2\text{O}}^{\text{total}} + E_{\text{H}_2\text{O}}^{\text{ZPE}} + \Delta\mu_{\text{H}_2\text{O}}(T, p_{\text{H}_2\text{O}}^0) + \frac{1}{2}k_{\text{B}}T \ln \left(\frac{p_{\text{H}_2\text{O}}}{p_{\text{H}_2\text{O}}^0} \right) \quad (6.4)$$

where $\Delta\mu_{\text{H}_2\text{O}}(T, p_{\text{H}_2\text{O}}^0)$ is obtained from the partition function based on DFT calculations (HSE06 functional) and the harmonic approximation (see Eq. 2.71), with $p_{\text{H}_2\text{O}}^0=1$ atm. We have also calculated the free energies for a set of non-stoichiometric adsorbed H_xO_y structures ($x : y \neq 2$). However, the non-stoichiometric structures are found to be thermodynamically unstable at any conditions.

If not stated otherwise, all the final DFT energies in the water/oxide project are obtained using 4-layer periodic slab models and HSE06 functional along with the first-principles many-body van der Waals interaction correction [45]. All the genetic algorithm runs and molecular dynamics simulations are performed with 2-layer periodic slab models and PBE functional. In all slab models, the vacuum distance between neighboring slabs is more than 30 Å.

6.2. Validation of DFT functionals and the atomic models

The accuracy of PBE+vdW and HSE06+vdW is analyzed by comparing the DFT adsorption energies for a water dimer on embedded cluster models (Fig. 6.1) of MgO and CaO (001) surfaces to the adsorption energies calculated with the renormalized second-order perturbation theory (rPT2) [46]. The reference electronic structure for the rPT2 calculations is always obtained with

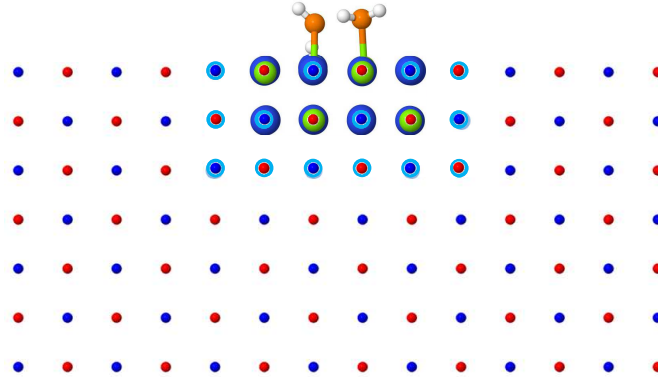


Figure 6.1.: Embedded cluster model (side view along [100] direction) for water dimer adsorbed on MgO (001). Mg and O atoms in the slab are represented by green and blue spheres, respectively. O and H atoms coming from water are shown as orange and grey spheres, respectively. Red dots represent the -2 point charges, blue dots the +2 point charges, and the pseudopotentials are signified with transparent light-blue spheres. Only a part of the point-charge embedding is shown.

PBE, denoted as rPT2@PBE. The cluster models consist of a two-layer metal oxide cluster with 8 MgO units per each square-shaped layer, plus a water dimer adsorbed on one side of the cluster. The cluster is embedded in a point charge array of +2 and -2 charges (replacing Mg and O, respectively), containing four layers of the charges on each side of the atomic cluster except the side with the adsorbed water dimer. The +2 point charges adjacent to the cluster are replaced with norm-conserving non-local Mg^{2+} pseudopotentials [189, 190, 191]. The geometry of the cluster is obtained by cutting a $(2 \times 2 \times 1)$ part from the relaxed unit cell containing the water dimer adsorbed on a four-layer slab. The PBE lattice constant (4.258 Å and 4.834 Å for MgO

Method	PBE+vdw	HSE06+vdw	rPT2@PBE
2H ₂ O/MgO(001)	-2.625	-2.874	-2.821
2H ₂ O/CaO(001)	-3.024	-3.304	-3.239

Table 6.1.: The energies (in eV) of a water dimer adsorption on MgO and CaO (001) surfaces calculated with PBE+vdW, HSE06+vdW, and rPT2@PBE. The adsorption energy is defined by Eq. 6.5.

and CaO respectively) is used in all embedded cluster calculations. The adsorption energies are converged to 1 meV with respect to the size of the point charge array and the number of the Mg²⁺ pseudopotential centers.

rPT2@PBE was shown to achieve accuracy close to the coupled-cluster method with single and double substitutions (CCSD) for a wide variety of systems [46]. Since basis set superstition error is known serve for RPA method [192], we calculate the counterpoise corrected adsorption energy [193] $E_{\text{ads}}^{\text{cc}}$ according to:

$$E_{\text{ads}}^{\text{cc}} = E_{2\text{H}_2\text{O}/\text{cluster}} - E_{\text{cluster}} - E_{2\text{H}_2\text{O}}^{\text{fixed}} \quad (6.5)$$

where $E_{2\text{H}_2\text{O}/\text{cluster}}$, E_{cluster} , and $E_{2\text{H}_2\text{O}}^{\text{fixed}}$ are total energies of the oxide cluster with the adsorbed water, pure oxide cluster, and “water dimer” in the gas phase at the exactly same geometry as on the cluster.

Tab. 6.1 summarizes the DFT energies of a water dimer adsorption on MgO and CaO (001) surfaces calculated with PBE+vdW, HSE06+vdW, and rPT2. Clearly, PBE+vdW underestimates the adsorption energy for these systems by about 0.2 eV, while HSE06+vdW overestimate the rPT2 results by about 0.06 eV, providing a considerably better (than PBE+vdW) description of the adsorption of water on the alkaline-earth metal oxide (001) surfaces. The accuracy of the HSE06+vdW approach is also confirmed by a comparison of theoretical and experimental results (see Sec. 7.2 for details).

As described in Sec. 6.1, the GA search is performed using computationally “light” settings: two-layer slab models, PBE functional, the standard FHI-aims *light* numerical settings (loose numerical grids and an atomic basis set of double-zeta quality with polarization functions), and the atomic relaxation of only the top layer of the slab in addition to the adsorbates. Fig. 6.2 shows the changes in the energy hierarchy of the global and local minima on the PES once the tighter computational settings are used, i.e., four-layer slabs with two top layers relaxed, *tight* numerical settings, and the HSE06+vdW functional for both the DFT total energies and the relaxation. As can be seen from the figure, the lowest-energy structure obtained with GA is relaxed into the global minimum (GM) for the tighter calculations, and the four lowest-energy structures in GA are still the four most favourable in PBE with tight settings and HSE06+vdW with tight numerical settings. This results support our scheme of running GA with light settings, followed by a further optimization for the lowest-energy structures.

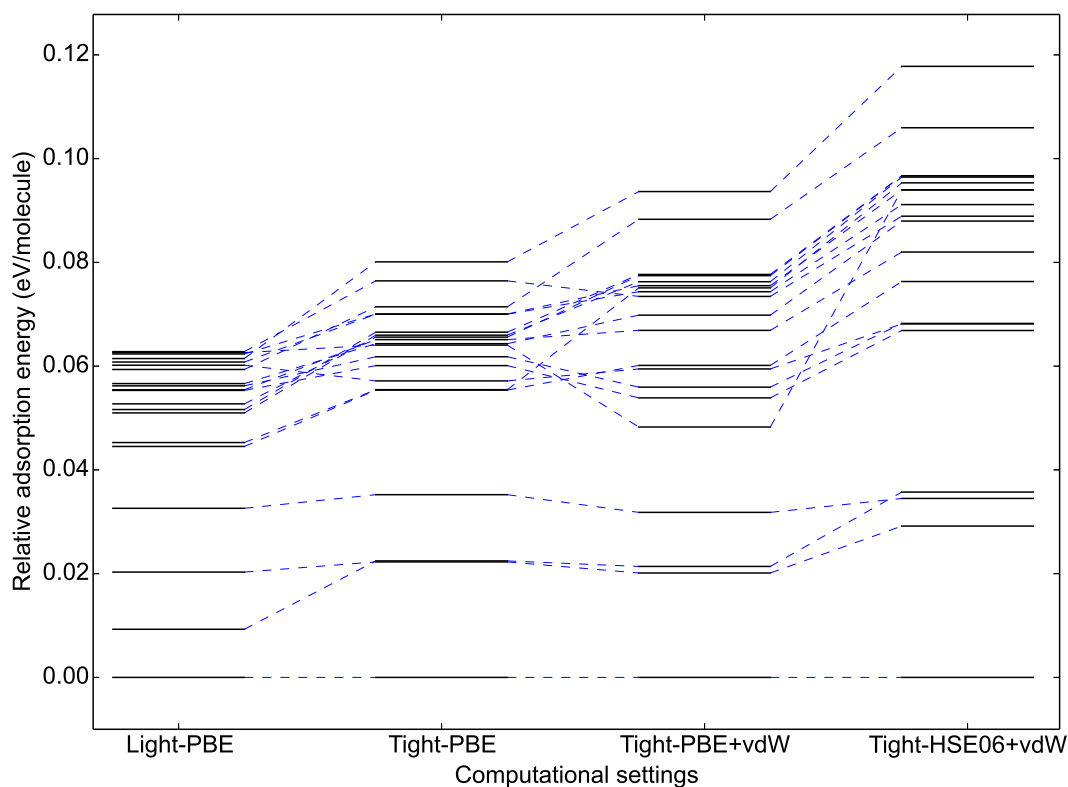


Figure 6.2.: Hierarchy of adsorption energies for the low-energy water structures of $6\text{H}_2\text{O}/\text{CaO}(001)$ found with computationally “light” settings and further optimized with “tight” settings (see text for details). Energy of the most stable structure is used as the reference for each type of settings. The dashed blue lines connect corresponding “light” and “tight” local minima.

6.3. Structures of water adsorbed on CaO(001)

Our investigation of water adsorption on CaO(001) starts from water monomer to small water clusters ($n\text{H}_2\text{O}$, $n \leq 4$) on the surface, and then we gradually increase the coverage until it reaches 1.25 monolayer (ML) (here and everywhere referred to the ratio between the number of water molecules and the surface oxygen atoms). Due to the limited number of configurations, $n\text{H}_2\text{O}$ ($n \leq 4$) adsorption structures are obtained through optimizing initial states where water molecules randomly distributed on the surface, without performing a GA search. 20 initial random structures of H_2O and $2\text{H}_2\text{O}$ are optimized, and 60 are optimized for each of $3\text{H}_2\text{O}$ and $4\text{H}_2\text{O}$. The sufficiency of these random structures is confirmed by the fact that only a small number of isomers can be obtained after optimization.

The most stable water clusters (from monomer to tetramer) are shown in Fig. 6.3. In line with previous PBE DFT study [162], the dissociative adsorption of the water monomer on CaO(001) is favoured over the molecular adsorption by 0.2 eV. Upon dissociation, two types of OH groups are formed: one is due to the proton transfer to the surface oxygen (denoted as O_sH), and the

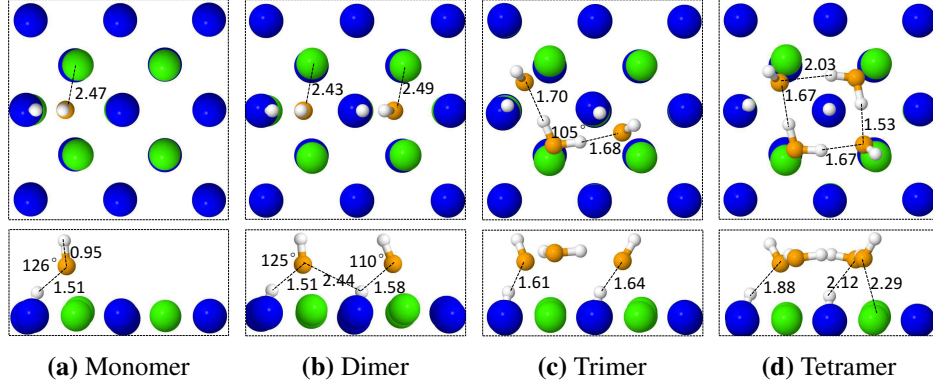


Figure 6.3.: Most stable (according to DFT with the HSE06+vdW functional and *tight* numerical settings) adsorbed water structures containing 1-4 water molecules on the CaO(001) surface. Only a part of the (3×4) surface unit cell is shown. The surface oxygen, calcium, oxygen from waters molecules, and hydrogen atoms are represented by blue, green, orange, and grey spheres, respectively. Selected geometric parameters are also shown. The unit for the distances is Å.

other is the remaining OH group from the water molecule (denoted as O_fH). The O-H bond length and H-O-H angle for the adsorbed monomer are shown in Fig. 6.3 (a). We find that the bond length in O_fH is very close to an isolated gas-phase water molecule (0.96 Å), while O_sH is elongated by about 0.05 Å. The distance between O_fH and O_sH is 1.51 Å, indicating a strong interaction between these two OH groups. The $H-O_s \cdots H$ angle is 126° , 21° larger than that of an isolated water molecule. In the case of the adsorption of water dimer, the most stable structure corresponds to both molecules being dissociated, different from the case of MgO(001) where one water molecule is dissociated and the other remains intact [152] (see also Sec. 7.1). As can be seen in Fig. 6.3 (b), the $O_sH \cdots O_fH$ hydrogen bond length is 1.58 Å in the water molecule with O_fH tilted to the center of the dimer, while the counter part in the other water molecule is 1.51 Å. The fact that the geometric parameters of similar adsorbed fragments are different clearly indicates that there is an interaction between the two adsorbed water molecules. The interaction is also reflected in the adsorption energetics which will be discussed later.

Different from the monomer and the dimer, full dissociation into adsorbed H and OH is less stable than a partial dissociation for the trimer (Fig. 6.3 (c)). One of the three water molecules stays intact, while connecting with the two dissociated water molecules via hydrogen bonds of length 1.71 Å and 1.68 Å. The inert water molecule has two O-H bonds 0.02 Å longer than in an isolated gas-phase water molecule.

The GM structure of the adsorbed water tetramer consists of two intact and two dissociated molecules. The molecules and OH groups form a square structure, which maximizes the hydrogen bonding within the structure. The square shape is governed by the surface Ca atoms that are 3.4 Å apart ($1/\sqrt{2}$ times the CaO lattice constant). Whereas one O_sH species sits inside of the square, the other one occupies an adjacent O position outside of the tetramer square.

As the diversity of structures increases exponentially with the number of building blocks, GA is used to search for most stable structures of adsorbed nH_2O ($n = 5, 6, 9, 12, 13, 15$). The GM

structures for 5 and 6 water molecules adsorbed on a CaO(001) slab within the 3×4 surface supercell (24 atoms per layer) are shown in Fig. 6.4, while for 9, 12, 13, and 15 water molecules the GM structures are shown in Fig. 6.5).

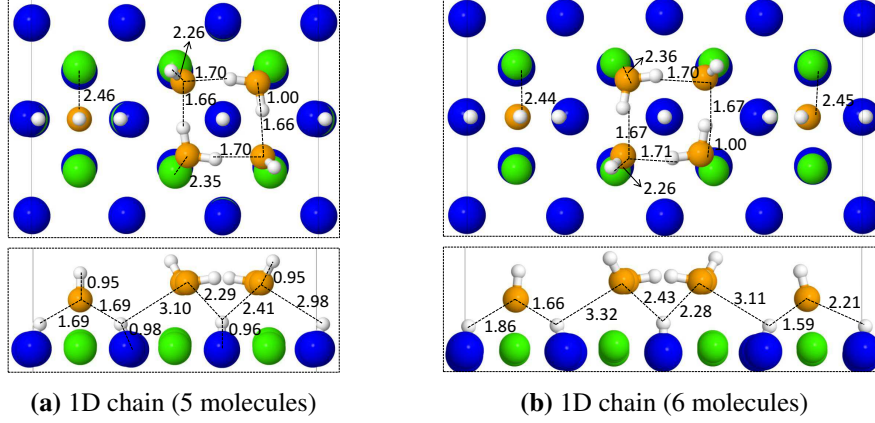


Figure 6.4.: Most stable (according to DFT with the HSE06+vdW functional and *tight* numerical settings) adsorbed water structures containing 5 (a) or 6 (b) water molecules on the CaO (001) surface. Only a part of the (3×4) surface unit cell is shown. The unit cell borders are shown as grey lines. The surface oxygen, calcium, oxygen from waters molecules, and hydrogen atoms are represented by blue, green, orange, and grey spheres, respectively. Selected geometric parameters are also shown. The unit for the distances is Å.

Two different types of 1D structures are found by GA: one has a periodicity of 10.2 Å and consists of five water molecules (Fig. 6.4 (a) and Fig. 6.5 (a)) while the other one has six water molecules in a period of 13.6 Å (Fig. 6.4 (b)). Despite the differences, these two 1D structures have similar building blocks. The five-water chain can be considered as a combination of a C_{4v} -symmetric “square” unit and a “linker” unit. The “square” unit contains two inert water molecules, two O_fH groups and one O_sH in the center of the “square”, while the “linker” unit consist of two symmetric O_sH groups, both of which interact with the O_fH group in the middle through two hydrogen bonds with the length of 1.69 Å. One can see that the “square” unit has the structure similar to the structure of the adsorbed water tetramer. The six-water chain differs from the five-water chain only by one additional water molecule in the “linker” unit, which lowers the symmetry of the “linker” unit. This symmetry lowering has a profound effect on the vibrational spectrum of the structure (see Sec. 6.5).

Comparison of the 1D structures with the most stable tetramer water cluster reveals that it is the extra hydroxyl added to a side of the tetramer that breaks the symmetry and paves the road for the chain formation found in experiment. In fact, the fifth molecule attaches to this extra O_sH , in a dissociated configuration again, and creates a linker to the next stable tetramer cluster. By this means, a 1D water structure develops on the CaO surface, being composed of water tetramers connected via dissociated molecular linkers (Fig. 6.4 (a) and (b)). As the symmetry-breaking O_sH always occupies a surface oxygen adjacent to the cluster, the growth proceeds along a closed-packed O row, hence along a [110] direction, in agreement with experiment.

cluster/Surface	PBE	PBE+vdw	HSE06	HSE06+vdw	ZPE correction
monomer/CaO(001)	-0.823	-1.027	-0.900	-1.092	0.059
dimer/CaO(001)	-0.837	-1.053	-0.921	-1.122	0.077
trimer/CaO(001)	-0.842	-1.033	-0.909	-1.089	0.085
tetramer/CaO(001)	-0.848	-1.031	-0.904	-1.080	0.085
1D-a/CaO(001)	-0.893	-1.092	-0.962	-1.152	0.090
1D-b/CaO(001)	-0.877	-1.084	-0.954	-1.149	0.088
2D-a/CaO(001)	-0.786	-1.002	-0.813	-1.018	0.103
2D-b/CaO(001)	-0.773	-0.977	-0.818	-1.012	0.090
2D-c/CaO(001)	-0.736	-0.939	-0.780	-0.972	0.100

Table 6.2.: DFT adsorption energies (in eV) per H₂O molecule (see Eq. 6.1) for water adsorption structures on CaO(001). The unit-cell size is (4×3). 1D-a/CaO(001) and 1D-b/CaO(001) represent two 1D structures found on CaO(001), with the a, b labels correspond to the panels in Fig. 6.4. 2D-a,b,c/CaO(001) represent the 2D structures shown in Fig. 6.4 with 12, 13, and 15 H₂O molecules, respectively. The ZPE correction (see Eq. 6.2) is also given.

The structure containing 9 water molecules per (3×4) surface unit cell corresponds to 2/3 ML coverage. Interestingly, even at this coverage we still found 1D structures as most stable configuration of the adsorbed water layer. The structure consists of two 1D structures: one similar to the five molecule structure, and the other one also similar but with one water molecule missing from a complete 1D chain. As the coverage is further increased to 1 ML, however, qualitative changes appear: 12 water molecules on the periodic slab form a 2D hydrogen-bonded network. Also here, intact and dissociated entities form square-shaped building blocks; however, they homogeneously cover the entire surface as each Ca ion carries either a H₂O or O_sH unit. It is therefore the high surface coverage that triggers a breakdown of the 1D regime. For even higher loads (13 and 15 molecules per 3×4 cell), both anionic and cationic surface sites get occupied with either intact molecules or O_fH groups, producing a dense hydrogen-bonded network (Fig. 6.4 (c) and (d)).

DFT adsorption energies for the water structures described above are summarized in Tab. 7.1. ZPE corrections are calculated using Eq. 6.2, with the hydrated surface oxygen atoms allowed to move in the calculations of $E_{n\text{H}_2\text{O}/\text{slab}}^{\text{ZPE}}$ and $E_{\text{slab}}^{\text{ZPE}}$. We find that the difference in ZPE correction can be up to 0.02 eV per adsorbate if only atoms in the adsorbates are allowed to vibrate. The following observations can be made from the analysis of Tab. 7.1. First of all, the interaction of water with the CaO(001) surface is strongest for 1D structures and weakest for 2D structures. Moreover, the dispersion forces contribute about 0.2 eV/molecule. The ZPE correction is in the range of about 0.06 eV to 0.1 eV. The ZPE corrections are always positive due to the fact that each water molecule has three vibrational degrees of freedom, while as an adsorbate each water molecules contributes nine vibrational degrees of freedom.

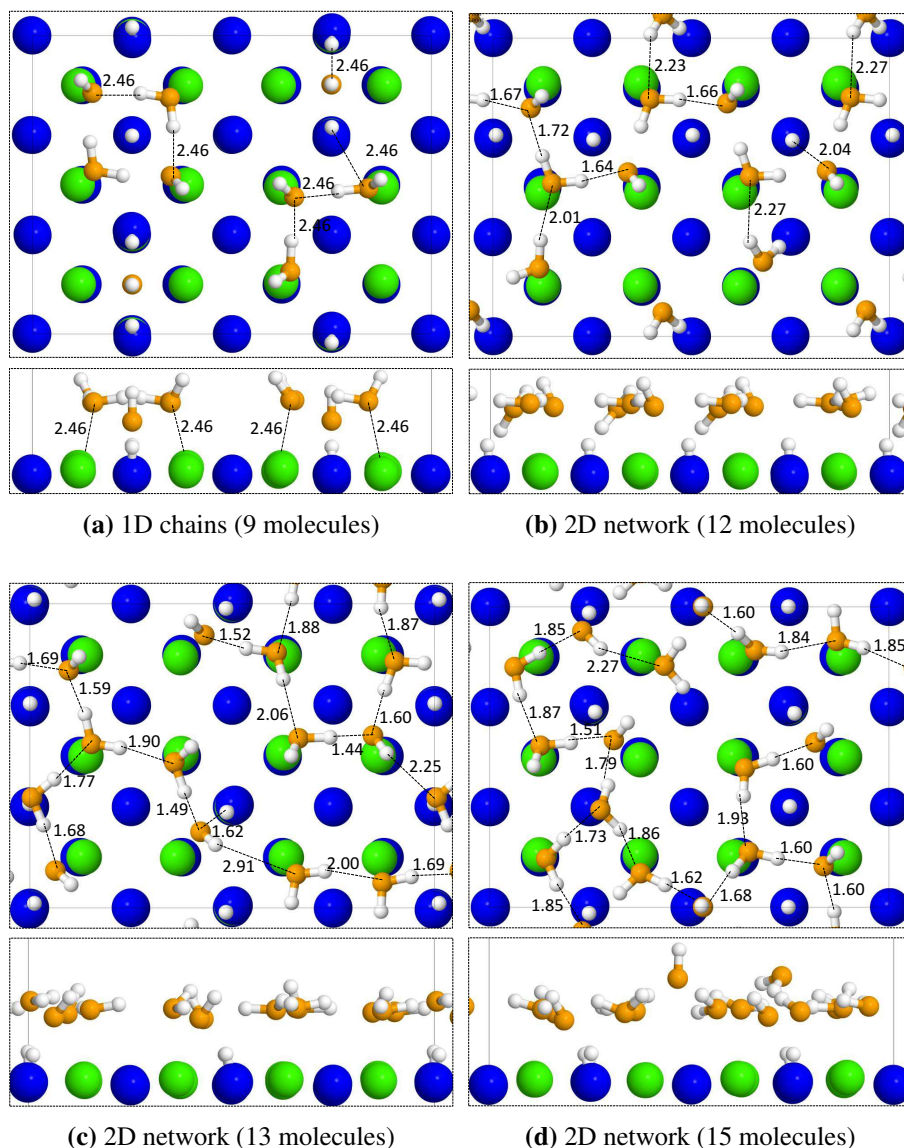


Figure 6.5.: Most stable (according to DFT with the HSE06+vdW functional and *tight* numerical settings) adsorbed water structures containing 9 (a), 12 (b), 13 (c), or 15 (d) water molecules on the CaO(001) surface. Only a part of the (3×4) surface unit cell is shown. The unit cell borders are shown as grey lines. The surface oxygen, calcium, oxygen from waters molecules, and hydrogen atoms are represented by blue, green, orange, and grey spheres, respectively. Selected geometric parameters are also shown. The unit for the distances is Å.

6.4. Temperature-pressure phase diagram

Fig. 6.6 shows phase diagrams for water adsorbed on CaO(001), calculated using the *ab initio* atomistic thermodynamics, as described in Sec. 6.1. The Gibbs free energy of formation that

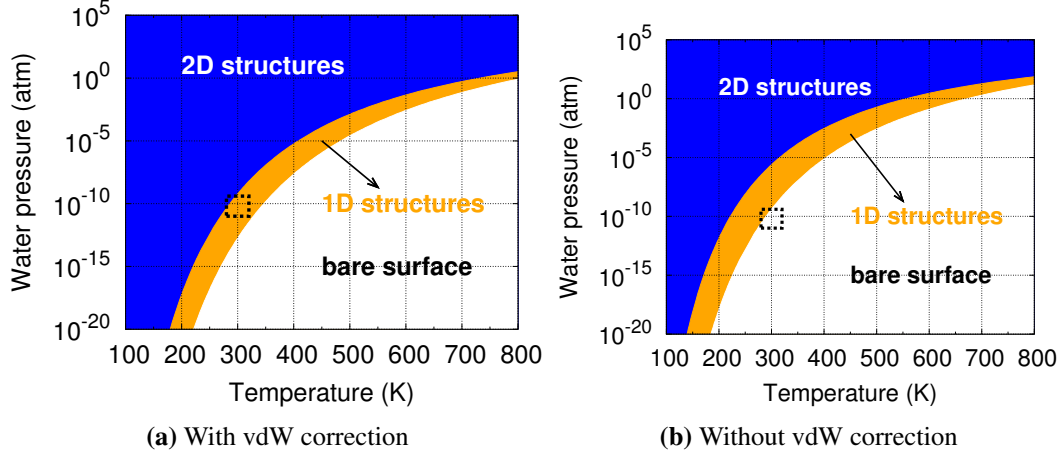


Figure 6.6.: $(T, p_{\text{H}_2\text{O}})$ phase diagrams for CaO(001) with water adsorbed on the surface with (a) or without (b) vdW interaction correction included. The diagrams are based on the HSE06+vdW adsorption energies and include vibrational free energies calculated using the PBE+vdW vibrational frequencies. The square-shaped area with the dashed borders denotes experimental conditions. The detailed meaning of the labels and their limitations are described in the text.

determines which phase dominates a $(T, p_{\text{H}_2\text{O}})$ point is defined by Eq. 6.1. The phase diagrams are constructed based on the structures that we have calculated, *i.e.*, small water clusters as well as 1D and 2D structures with coverages up to 1.25 ML. Thus, the area of the calculated stability of the 2D structures also includes conditions where three-dimensional structures (multilayers) may be thermodynamically stable. Also, due to the limited size of the surface supercell, the conditions labelled as “bare surface” in reality correspond to some (small) coverage of adsorbed water.

Fig. 6.6 shows that 1D adsorbed water structures are thermodynamically stable on CaO (001) at a range of temperature and pressure conditions. In particular, this range agrees well with the STM measurements. These results suggest that the formation of 1D structures on CaO(001) is dominated by thermodynamic factors. In contrast, we note that 1D structures found on MgO (001) are only metastable – they are thermodynamically less favoured than 2D structures (see Fig. 7.7). Fig. 6.6 also shows that, if vdW interactions are not included, the predicted range of stability of the 1D adsorbed water structures does not agree with the experimental observations.

6.5. Vibrational spectra of water on CaO(001)

In order to identify which structure corresponds to the 1D structures observed with STM, we further characterize the structures by calculating the IR vibrational spectra in two ways: one is

from dynamic matrix under harmonic approximation, and the other one is from autocorrelation of dipole moments derived from MD. Details of the methods can be found in Sec. 2.4.

Since two 1D structures are found and are close in adsorption energy per molecule, we calculate vibrational spectra for both of the 1D structures. Moreover, since deuterized water (D_2O) is used in the IR experiments, $5D_2O$ and $6D_2O$ are used to calculate the vibrational spectra. The harmonic spectra of $5D_2O$ and $6D_2O$ calculated with PBE are presented in Fig. 6.7. Har-

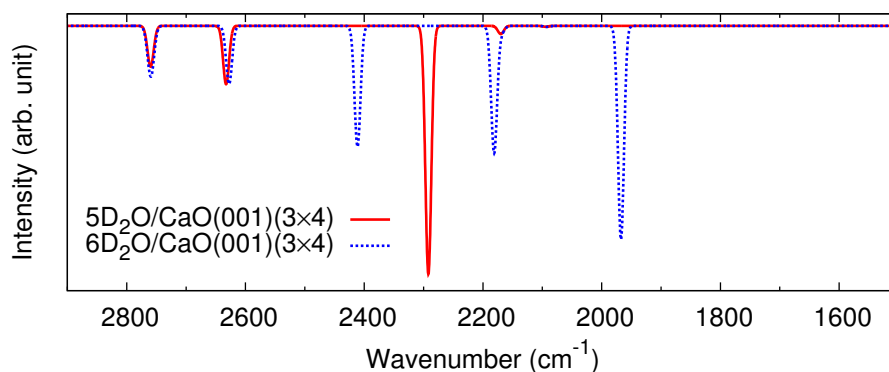


Figure 6.7.: IR vibrational spectra of $5D_2O$ (red solid line) and $6D_2O$ (blue dashed line) 1D structures on CaO(001) surface, calculated using the harmonic approximation and PBE DFT functional.

monic vibrational spectrum for $5D_2O/CaO(001)$ is also calculated with HSE06 for comparison (see Fig. 6.8). We find that for the systems of interest the differences between HSE06 and PBE spectra, as well as between the spectra obtained with *light* and *tight* numerical settings are insignificant in the sense that they do not affect any of our analysis and conclusions. For the $5D_2O/CaO(001)$ structure, the harmonic spectrum consists of four noticeable vibrational peaks (see also Fig. 6.10) within the range of 1200 cm^{-1} to 2900 cm^{-1} . The highest-frequency peak around 2760 cm^{-1} is due to two quasidegenerate vibrations: one at 2758 cm^{-1} is due to the O_fD group in the “square” element of the structure, and the other one at 2761 cm^{-1} is due to the O_fD group in the “linker”. The peak at 2634 cm^{-1} originates from stretching of the O_sD group in the middle of the “square”. Below 2300 cm^{-1} lies the most distinguishable feature in this spectrum: the peak at 2274 cm^{-1} , originating from the symmetric stretch of the two tilted O_sD groups in the “linker”. The small peak at 2182 cm^{-1} is from the symmetric stretch of the two intact D_2O molecules. The intensity of this peak is small due to the fact that the OD groups in the intact molecules are nearly parallel to the surface.

For the $6D_2O/CaO(001)$ structure, the vibrations around 2760 cm^{-1} and 2630 cm^{-1} have frequencies and intensities very similar to the $5D_2O/CaO(001)$ structure. At lower frequencies, however, there are now three high-intensity peaks at 1967 cm^{-1} , 2181 cm^{-1} and 2411 cm^{-1} . The lowest-frequency peak in the considered frequency range is due to the O_sD group immediately to the right of the “square” in Fig. 6.4 (b). The other two peaks originate from stretching of the two O_sD groups to the left of the “square” element of the structure. These two vibrations are counterparts of the symmetric and anti-symmetric stretching vibrations of the O_sD groups in

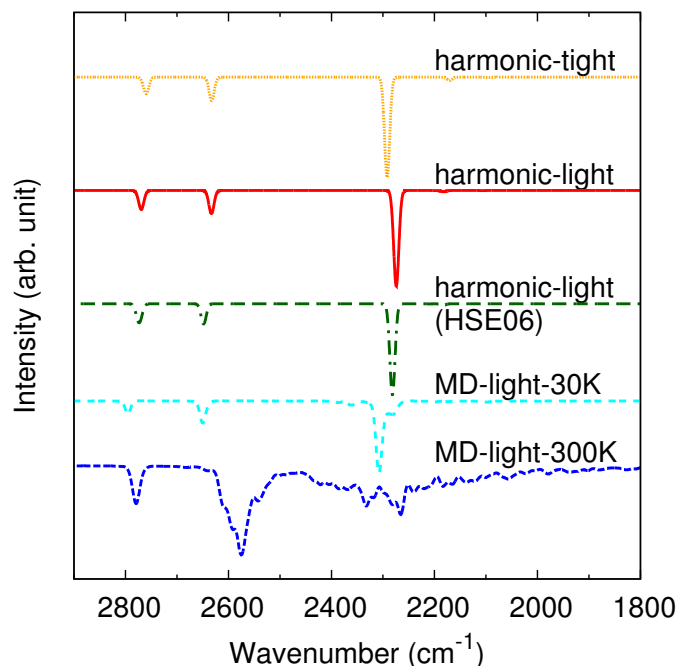


Figure 6.8.: Comparison of vibrational spectra of $5\text{D}_2\text{O}/\text{CaO}(001)$ calculated with different methods. PBE functional is used for all cases except the case where the functional HSE06 is noted in the plot. The “light” label signifies both the default *light* basis sets and grid settings, as well as the two-layer slab model, while the “tight” label indicates the default *tight* basis sets and grid settings, as well as the four-layer model.

the “linker” in the $5\text{D}_2\text{O}/\text{CaO}(001)$ structure. The crucial difference is that due to the symmetry of the “linker” in $5\text{D}_2\text{O}/\text{CaO}(001)$ the optical selection rules render the asymmetric stretch undetectable in this structure, which is not the case in $6\text{D}_2\text{O}/\text{CaO}(001)$.

In order to check whether anharmonic effects play a role in the vibrational spectra, we calculate finite-temperature vibrational spectra derived from MD for the most stable 1D adsorbed water structure on $\text{CaO}(001)$ (shown in Fig. 6.4 (a)). The MD spectra are obtained via time-autocorrelation of the dipole moment component along the z direction 2.57. Detailed description of the method can be found in Sec. 2.4.2. The time-step used in our MD simulations is 1 fs. Even though the convergence of the time-step in our MD runs was not tested due to the high computational cost of the calculations for our relatively large system, we note that 0.75 fs was enough to converge all features of a peptide vibrational spectrum in the work of Schubert *et al.* [194], and 1 fs was shown to be small enough in the work of Carvalho *et al.* on peptides [195]. Thus, we believe that 1 fs is sufficiently small for our *deuterated* system. The time of our MD runs is 40 ps. The convergence of the results with the MD run time is shown in Fig. 6.9. It can be seen in the figure that all main features of the spectrum are converged for MD runs within 40 ps.

For a direct comparison with experiment, the MD simulations and the harmonic spectra are calculated for D_2O instead of H_2O . Fig. 6.10 (a) shows the calculated IR spectra at two differ-

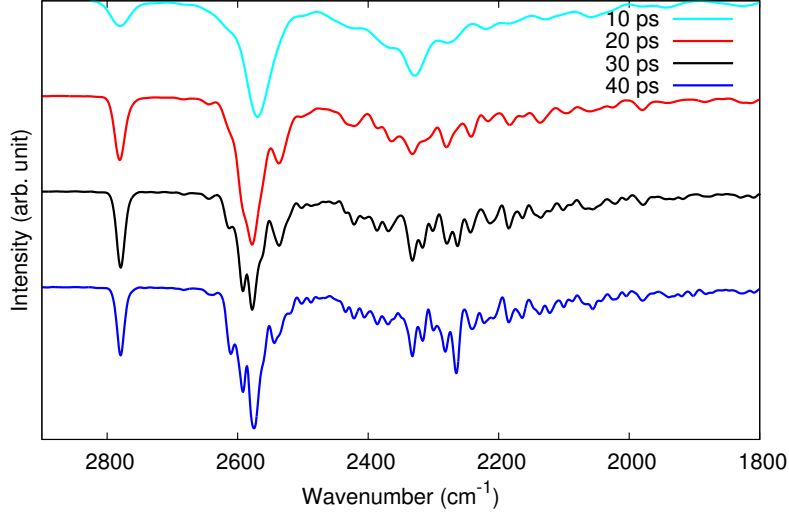


Figure 6.9.: Convergence of MD time, illustrated by the convergence of spectrum features of 1D structure on CaO(001).

ent temperatures: (i) experimental (300 K) and (ii) a low temperature (30 K) for checking the consistency of our MD simulations. The MD-derived spectra at 30 K essentially reproduce the spectra calculated in the harmonic approximation. Moreover, the finite-temperature spectrum of the 5D₂O/CaO(001) structure (Fig. 6.10 (a)) shows a transformation of the single harmonic peak at 2274 cm⁻¹ into a double-peak feature as the temperature is increased from 30 K to 300 K. This splitting reveals the anharmonic coupling between the symmetric and antisymmetric stretching vibrations of the O_sD groups in the “linker”, and is a distinct feature of this 1D ordered adsorbed water structure.

To obtain a deeper understanding about the peak splitting, we further analyze the spectra in the following two ways. The first way is to identify motion of which D atoms contribute most to the intensity of the peaks at 300 K. This can be done by calculating the velocity autocorrelation for given atoms, since:

$$I_D(\omega) \propto \int_0^{\tilde{t}} \langle v_z(0)v_z(t) \rangle e^{i\omega t} dt, \quad (6.6)$$

where $I_D(\omega)$ is the part of the vibrational intensity due to the motion of the D atoms. As one can see in Fig. 6.11, considering just the atoms D1 and D2 in the “linker” (see the inset) allows to reproduce the peak splitting.

The second way is to project velocities onto specific harmonic normal modes. In other words, we decompose the velocities into a linear combination of the normal modes. Since the set of all harmonic modes can be considered as a complete basis for any atomic movement, the calculated anharmonic spectra can also be decomposed as a linear combination of harmonic modes.

$$\mathbf{v}(t)\mathbf{Q}_q = v_q(t), \quad (6.7)$$

$$\mathbf{v}(t) = \sum_q v_q(t)\mathbf{Q}_q, \quad (6.8)$$

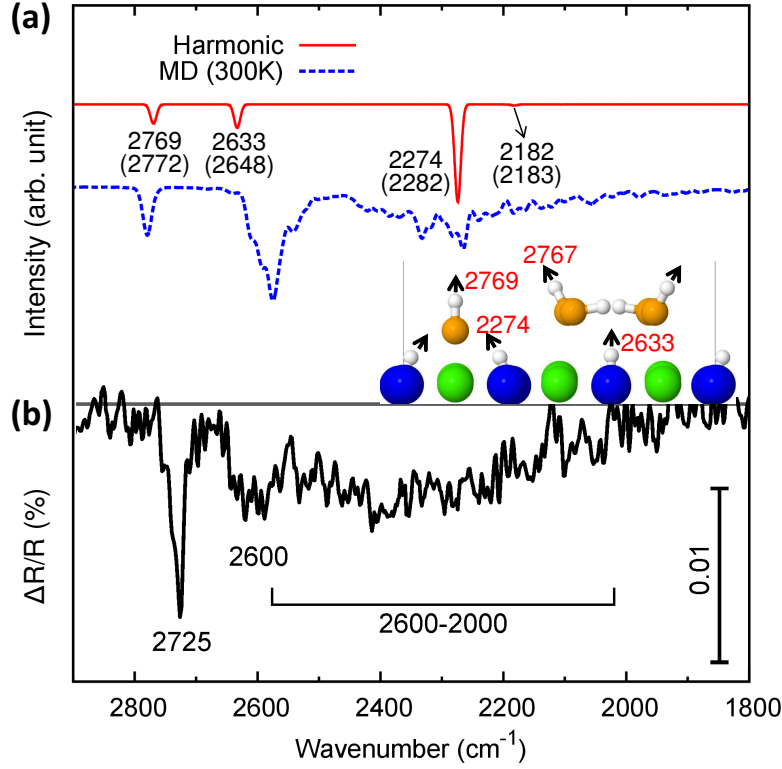


Figure 6.10.: (a) Harmonic (red) and MD-derived anharmonic (blue) vibrational spectra (300 K) of 5D₂O chains on CaO(001), calculated with PBE. HSE06 harmonic frequencies are shown in parentheses. The inset shows an assignment of the individual vibrational modes in the water ad-chains. (b) Experimental IR spectrum of ~0.15 ML D₂O dosed onto a 20-layer CaO(001) film at 300 K.

$$I_q(\omega) \propto \int_0^{\tilde{t}} \langle v_q(0)v_q(t) \rangle e^{i\omega t} dt \quad (6.9)$$

where $v_q(t)$ represents the velocity component in the direction of the normal mode \mathbf{Q}_q . The autocorrelation in Eq. 6.9 gives contribution of each mode to the power spectrum. The contributions of selected modes are shown in Fig. 6.12. Although the surface selection rules are not taken into account in this approach, one can see from Fig. 6.12 that (i) the IR peak at about 2200 cm⁻¹ is due to the antisymmetric vibration of the “linker”, and (ii) in-plane modes associated with the symmetric and antisymmetric vibrations of the non-dissociated water molecules in the “square” (see Fig. 6.13) are significantly broadened into wide bands spread from 1800 cm⁻¹ to 2600 cm⁻¹.

The IR spectrum measured with infrared reflection absorption spectroscopy (IRAS) is presented in Fig. 6.10 (b). The spectrum reveals two characteristic OD stretch vibrations at 2725 and 2600 cm⁻¹. By comparison with previous IR data acquired on MgO-supported water structures [146], they are assigned to free O_fD (2725 cm⁻¹) and surface O_sD groups (2600 cm⁻¹).

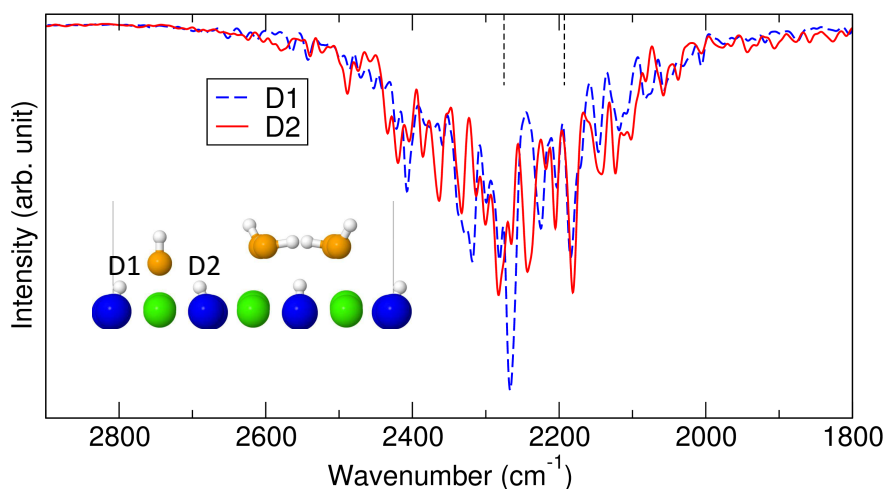


Figure 6.11.: Velocity (z-component only) autocorrelation (see Eq. 6.6) for the two symmetric D atoms (labelled D1 and D2 in the insert panel) in the most stable 1D structure ($5\text{D}_2\text{O}/\text{CaO}(001)$). The dashed lines show harmonic frequencies of the symmetric (2274 cm^{-1}) and antisymmetric (2197 cm^{-1}) stretch.

While the former constitutes the residual OD of a dissociated molecule, the latter contains an O ion of the oxide film. Besides these narrow maxima, a broad band is found between 2600 and 2000 cm^{-1} that, following the assignment on $\text{MgO}(001)$, is attributed to molecular D_2O . Both spectral fingerprints indicate a coexistence of molecular and dissociated water in the 1D structures on $\text{CaO}(001)$. Although the double-peak feature is not resolved (possibly due to limit of the resolution) in the IR experiment, the rest characteristics including the peaks around 2725 and 2600 cm^{-1} and the broad band from 2000 to 2600 cm^{-1} are qualitatively in line with our calculated finite-temperature IR spectra. This agreement further supports our claim that the 1D structure found with GA is the 1D structure observed in experiments.

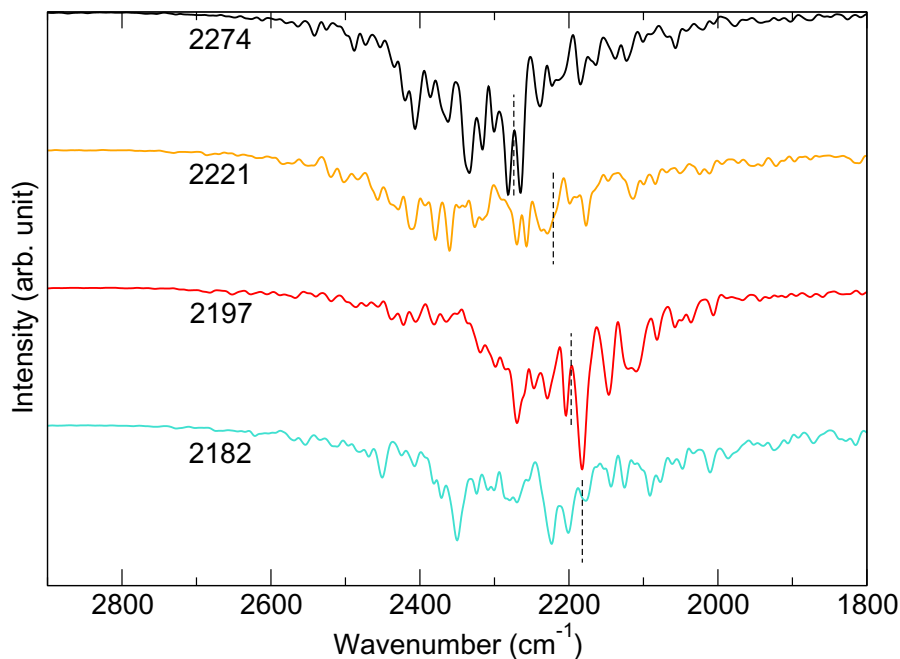


Figure 6.12.: Autocorrelation of velocities projected onto selected harmonic modes. Harmonic frequency of each mode is shown and noted by dashed line on the spectrum. See the text and Eq. 6.9 for the details of the projection method.

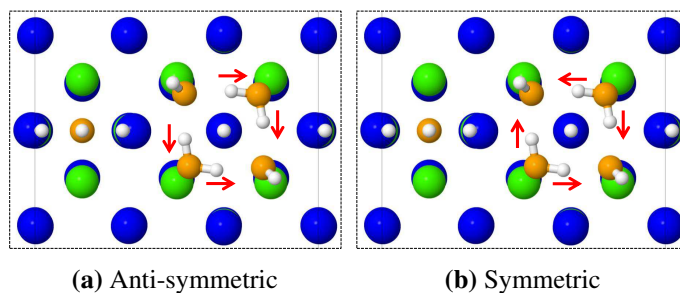


Figure 6.13.: Planer vibrational modes associated with the intact water molecules in the “square” element of the linear $5\text{D}_2\text{O}/\text{CaO}(001)$ structure: 2221 cm^{-1} (a), 2182 cm^{-1} (b). The surface O and calcium atoms, oxygen from waters molecules, and hydrogen atoms are represented by blue, green, orange, and grey spheres, respectively.

7. Interaction of water with MgO(001) and SrO(001) surfaces

Although water interacting with MgO(001) surface has been extensively studied both experimentally and theoretically, the possibility of forming 1D structures has not been investigated in theory. As described in Chp. 6, such a study requires to advance three computational aspects: (i) the surface models should be large enough to allow enough flexibility for including adsorbate superstructures, (ii) adsorbate coverages in the whole range from 0 to full coverage must be considered, and (iii) advanced techniques for the global exploration of PES are required to find low-energy adsorbate superstructures. To the best of our knowledge, water interacting with MgO(001) and SrO(001) have not been studied with such an advanced approach.

As described below, we find that there is a qualitative difference between MgO(001) and CaO(001) in terms of their interaction with water: contrary to CaO(001), the 1D structures on MgO(001) are only metastable at any temperature and pressure conditions. On SrO(001), water monomers or dimers are thermodynamically preferred to any adsorbed superstructure. Based on the comparison of results for MgO, CaO, and SrO, we explain the stability of 1D structures on CaO(001) by a balance between adsorbate-adsorbate and adsorbate-substrate interactions, which is mostly defined by the lattice parameters of CaO crystal. This is confirmed by the fact that 1D structures on MgO(001) can be stabilized by increasing the crystal lattice parameter of the MgO surface.

7.1. Structures of water adsorbed on MgO(001)

Similar to the case of CaO(001), we first obtain atomic structure of most stable configurations for $n\text{H}_2\text{O}$ ($n \leq 4$) molecules adsorbed on MgO(001) through optimizing initial states where water molecules randomly distributed on the surface, without performing a GA search, which is unnecessary due to the relatively small number of possible configurations. 20 initial random structures of adsorbed H_2O and $2\text{H}_2\text{O}$, and 60 initial structures of adsorbed $3\text{H}_2\text{O}$ and $4\text{H}_2\text{O}$ are relaxed, and the lowest-energy configurations are obtained. These lowest-energy structures are shown in Fig. 7.1. The geometries of two previously studied clusters – monomer and dimer – are in line with that reported in literature [162, 152]. Different from CaO(001), a single adsorbed water molecule prefers to stay intact on MgO(001), while adsorbed dimer and trimer contain only one dissociated water molecule. The structure of the tetramer, however, is similar to the structure of the tetramer on CaO(001). We note that the stability of another tetramer “square” structure on MgO(001) has been reported previously by Cho *et al.* [26]. However, the structure of the adsorbed tetramer that we found is more stable (by 0.34 eV at the PBE+vdW level of theory, and 0.38 eV at the HSE06+vdW level of theory). The major difference between the previously published and our tetramer structure is that in our structure the O_sH is inside the “square”, while in the previous structure it was outside.

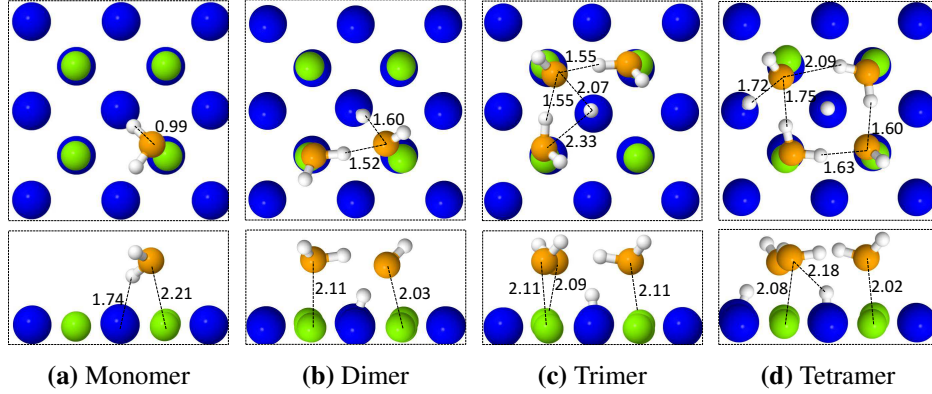


Figure 7.1.: Most stable (according to DFT with the HSE06+vdW functional and *tight* numerical settings) adsorbed water clusters containing 1-4 water molecules on the MgO(001) surface. Only a part of the (3×4) surface unit cell is shown. The surface oxygen, magnesium, oxygen from water molecules, and hydrogen atoms are represented by blue, green, orange, and grey spheres, respectively. Selected geometric parameters are also shown. The unit for the distances is Å.

For $n\text{H}_2\text{O}$ ($n \geq 5$) adsorption, GA is employed to search for the GM structure. The GM structure of 5 water molecules adsorbed within a (3×4) surface unit cell of MgO is presented in Fig. 7.2 (a). Although it has a 1D arrangement, no continuous hydrogen bonding is formed along the 1D orientation. Moreover, by total energy, it is only 0.04 eV more stable than the meta-stable structure which is a five-water cluster (shown in Fig. 7.2 (b)). By adsorption energy per molecule, it is close to tetramer cluster. Thus, we still consider it as a pentamer cluster, as presented in Tab. 7.1. We also find a $5\text{H}_2\text{O}/(3 \times 4)\text{MgO}(001)$ structure similar to the 1D structure on CaO(001) (Fig. 7.2 (c)), but it is 0.175 eV less stable than the lowest-energy structure.

For 6 molecules per (3×4) surface unit cell of MgO(001), the lowest-energy configuration are 1D structures (Fig. 7.3). In fact, four slightly different 1D structures are found within 0.1 eV of the most stable structure. These structures are different from the “square-linker” type of structure found on CaO(001) at the same coverage (see Fig. 6.4 (b)). The most stable 1D structure (Fig. 7.3 (a)) can be viewed as an array of water dimers, with each dimer having the configuration similar to the most stable structure of a single dimer on MgO(001). The other three 1D structures have two out of six water molecules dissociated, and they are only slightly less stable in energy. We note that the structure shown in Fig. 7.3 (c) was previously found by Delle Site and coworkers [196] via *ab initio* MD simulations.

For $9\text{H}_2\text{O}$ molecules on a (3×4) surface supercell (2/3 ML coverage), the GM structure can be viewed as a lattice formed by the 1D structures described above crossing each other at an angle of 90 degrees (Fig. 7.4).

The coverages from 1 ML and higher on MgO(001) were extensively studied previously [146]. As a benchmark of our GA approach, we have performed PBE GA runs for these higher coverages, and indeed we have found the same most stable structures as reported in the literature. The most stable (according to HSE06+vdW) high-coverage structures are shown in Fig. 7.5. These

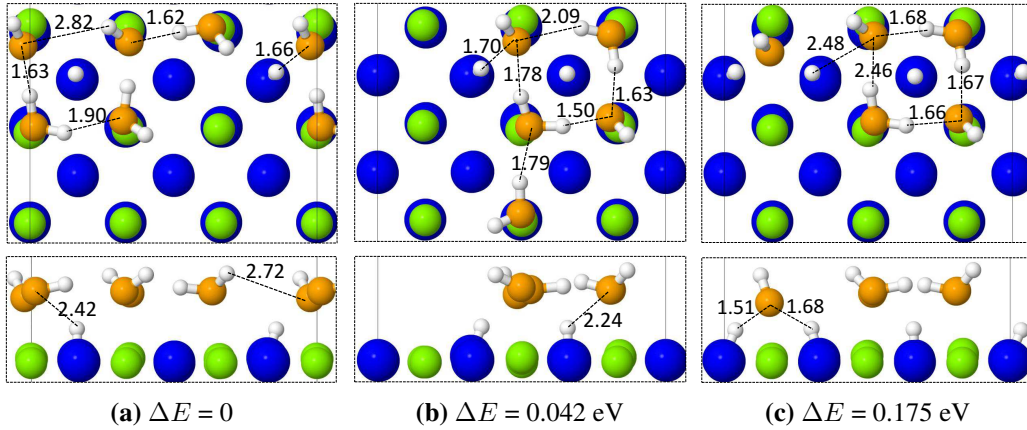


Figure 7.2.: Most stable and meta-stable (according to DFT with the HSE06+vdW functional and *tight* numerical settings) water structures containing 5 water molecules adsorbed within the (3×4) surface unit cell of MgO(001). Only a part of the (3×4) surface unit cell is shown. The surface oxygen, magnesium, oxygen from water molecules, and hydrogen atoms are represented by blue, green, orange, and grey spheres, respectively. Selected geometric parameters and the relative energy are also shown. The unit for the distances is Å.

high-coverage structures are discussed in more detail in Sec. 7.2.

The adsorption energies per water molecule, calculated according to Eq. 6.1, for the above described structures are presented in Tab. 7.1. One can see a general trend that the adsorption energy of water on MgO(001) decreases (absolute value increases) as the water coverage increases. Moreover, the ZPE correction for different structures can differ by as much as 0.03 eV per water molecule between different structures. As can be seen from the comparison of the four 1D structures in Tab. 7.1, this correction could be large enough to determine the qualitative predictions. More about adsorption energies will be discussed in Sec. 7.4

cluster/surface	PBE	PBE+vdW	HSE06	HSE06+vdW	ZPE contribution
monomer/MgO(001)	-0.403	-0.564	-0.421	-0.575	0.092
dimer/MgO(001)	-0.517	-0.671	-0.543	-0.691	0.096
trimer/MgO(001)	-0.573	-0.728	-0.609	-0.759	0.084
tetramer/MgO(001)	-0.604	-0.777	-0.647	-0.813	0.104
pentamer/MgO(001)	-0.620	-0.797	-0.658	-0.829	0.093
1D-a/MgO(001)	-0.637	-0.834	-0.672	-0.862	0.103
1D-b/MgO(001)	-0.639	-0.825	-0.680	-0.859	0.107
1D-c/MgO(001)	-0.637	-0.824	-0.679	-0.858	0.107
1D-d/MgO(001)	-0.625	-0.811	-0.669	-0.848	0.110
2D-a/MgO(001)	-0.662	-0.851	-0.691	-0.874	0.115
2D-b/MgO(001)	-0.666	-0.868	-0.708	-0.905	0.099

Table 7.1.: DFT adsorption energies (in eV; ZPE correction included) per H₂O molecule (see Eq. 6.1) for water adsorption structures on MgO(001). The unit cell size is (4×3) for water clusters and 1D structures while 2D-a structure is (2×4) periodic and 2D-b structure is (2×3) periodic. 1D-(a,b,c,d)/MgO(001) represent four 1D structures found on MgO(001), with the a, b, c, d labels corresponding to the panels in Fig. 7.3. 2D-a/MgO(001) and 2D-b/MgO(001) represent the two 2D structures shown Fig. 7.5 with the corresponding panel labels. The zero-point energy correction (see Eq. 6.2) is also given.

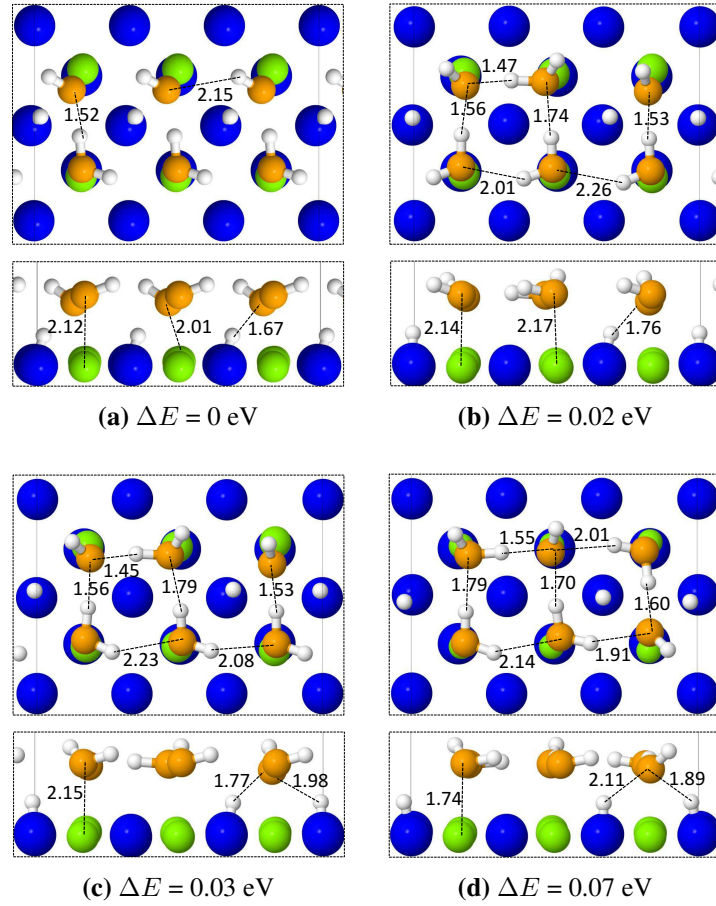


Figure 7.3.: Most stable (according to DFT with the HSE06+vdW functional and *tight* numerical settings) adsorbed water structures containing 6 water molecules within the (3×4) surface unit cell of the MgO(001). Only a part of the (3×4) surface unit cell is shown. The surface oxygen, magnesium, oxygen from water molecules, and hydrogen atoms are represented by blue, green, orange, and grey spheres, respectively. The unit cell borders are shown as thin grey lines. Selected geometric parameters and the relative energies are also shown. The unit for the distances is Å.

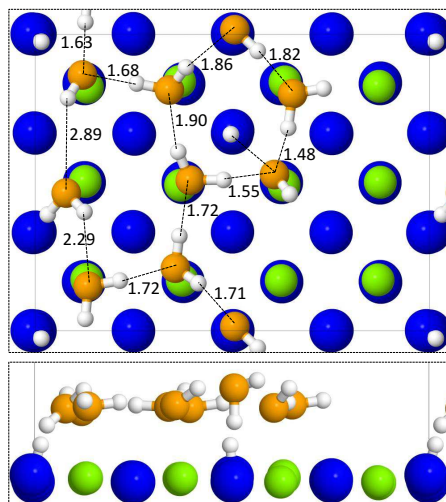


Figure 7.4.: The lowest-energy structure (according to DFT with the HSE06+vdW functional and *tight* numerical settings) of 9H₂O adsorbed within the (3×4) surface unit cell of MgO(001). The surface oxygen, magnesium, oxygen from water molecules, and hydrogen atoms are represented by blue, green, orange, and grey spheres, respectively. The unit cell borders are shown as thin grey lines. Selected geometric parameters are also shown. The unit for the distances is Å.

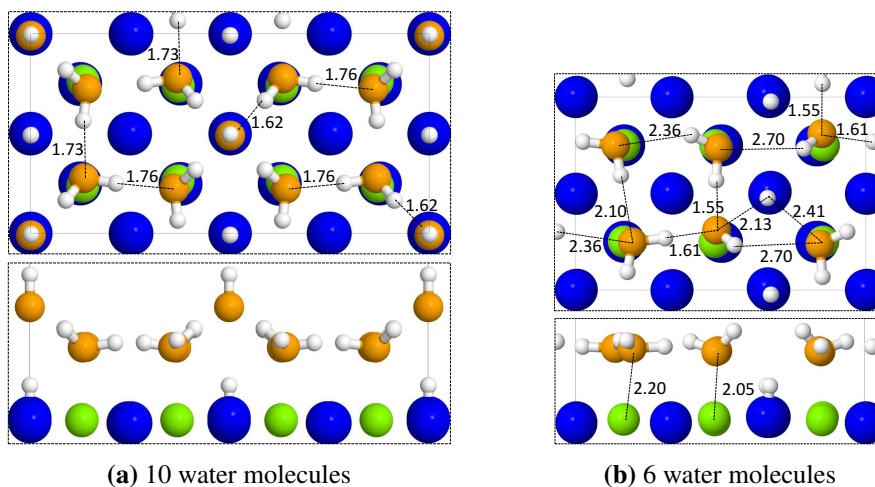


Figure 7.5.: (2×3) (a) and (2×4) (b) periodic 2D water layers adsorbed on the MgO(001) surface. The surface oxygen, magnesium, oxygen from water molecules, and hydrogen atoms are represented by blue, green, orange, and grey spheres, respectively. The unit cell borders are shown as thin grey lines. Selected geometric parameters calculated with HSE06+vdW and *tight* numerical settings are also shown. The unit for the distances is Å.

7.2. Temperature-pressure phase diagram

Although 1D structures are found for both CaO(001) and MgO(001) in our calculations, only 2D ordered structures have been reported for water interacting with MgO(001). In this section, the realistic temperature and partial pressure of water are taken into account to check the thermodynamics of the 1D and 2D structures found on MgO(001). Fig. 7.6 shows phase diagrams for water adsorbed on MgO(001) surface, calculated using the *ab initio* atomistic thermodynamics, as described in Sec. 6.1. The phase diagrams are constructed based on the structures that we

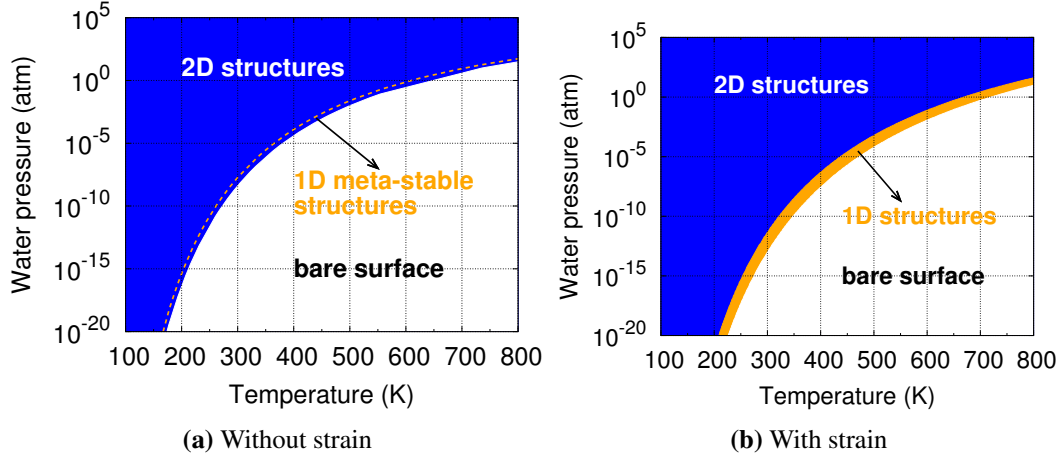


Figure 7.6.: $(T, p_{\text{H}_2\text{O}})$ phase diagrams for adsorbed water structures on MgO(001) surface without (a) or with (b) strain. The diagram is based on the HSE06+vdW total energies and include vibrational free energies calculated using the PBE+vdW vibrational frequencies. The constrained lattice parameter is 4.40Å, increased from optimized 4.21Å. More details about the strained MgO(001) model can be found in Sec. 7.4.

have calculated, *i.e.*, small water clusters as well as 1D and 2D structures with coverages up to 1.25 ML. Thus, the area of the calculated stability of the 2D structures also includes conditions where three-dimensional structures (multilayers) may be thermodynamically stable. Also, due to the limited size of the surface supercell, the conditions labelled as “bare surface” in reality correspond to some (small) coverage of adsorbed water.

The results show that 1D adsorbed water structures are not thermodynamically stable on MgO(001) at any conditions, in contrast with that on CaO(001) surface. However, the borders of stability of the 1D and 2D structures are close to each other, indicating the possibility that the 1D adsorbed water structures may be observed on MgO(001) at some stages of surface wetting even when the system is close to the thermodynamic equilibrium.

Experimental studies of the water adsorption on MgO(001) revealed the existence of two ordered surface phases [148, 197]. Based on DFT+D calculations [146] where the letter “D” denotes a semiempirical dispersion interaction correction [133], these phases were identified as the structures shown in Fig. 7.5. According to the experimental study, the more dense phase (identified as 2D-b) is stable at lower temperatures (up to $T \leq 185$ K) at the pressure $p_{\text{H}_2\text{O}} =$

10^{-10} mbar. The less dense phase (identified as 2D-a) becomes stable at $T > 185$ K at the same pressure. Upon increasing the temperature to about 220 K, most of the water leaves the surface. These observations are in good agreement with our free-energy calculations (Fig. 7.7) based on HSE06+vdW total energies: the calculated stability window of the less dense surface phase is from 191 K to 233 K at $p_{\text{H}_2\text{O}} = 10^{-10}$ mbar. The previously calculated value for this

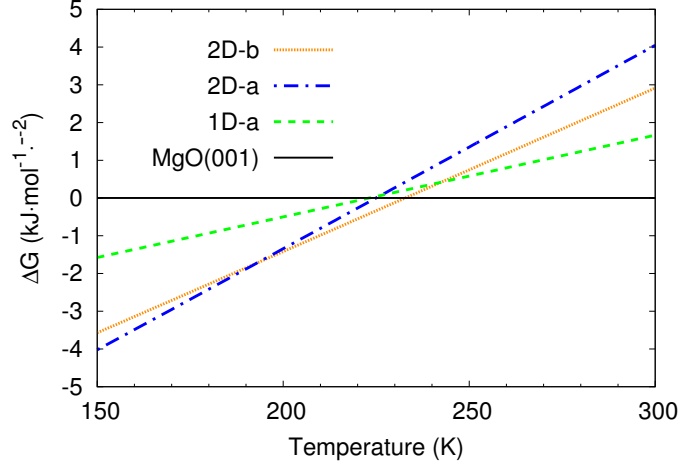


Figure 7.7.: Surface Gibbs free energy (see Eq. 6.1) of formation of the first 2D phase, the second 2D phase, and 1D structure phase, as a function of temperature at constant pressure of 10^{-10} mbar. The diagram is based on the HSE06+vdW total energies and include vibrational free energies calculated using the PBE+vdW vibrational frequencies. Figures of 2D-a, 2D-b, and 1D-a can be found in Fig. 7.5 (a) and (b), and Fig. 7.3 (a).

temperature window, however, was only 2 K [146]. We explain the better performance of the hybrid-functional-based approach by the more accurate description of the electron distribution between the cations and anions of the oxide surface, due to the reduced self-interaction error.

Ferry and coworkers [148] also reported isosteric heat of adsorption at half coverage determined from equilibrium adsorption isotherms. The measured adsorption energy is 0.884 ± 0.022 eV, in line with the calculated value based on HSE06+vdW (see Tab. 7.1).

7.3. Structures of water adsorbed on SrO(001)

In contrast to the partial dissociation of water on MgO and CaO(001) surface, the full dissociation into adsorbed H and OH species on SrO(001) is energetically preferred up to 10/12 ML coverage which we have calculated. Partially dissociated water clusters on SrO(001) are still local minima on the potential energy surface, and show structural features that are similar to the same type of clusters on MgO(001) and CaO(001), but they are significantly less stable than the fully dissociated structures (Fig. 7.8).

More precisely, the DFT adsorption energies of the partially dissociated water clusters on the surface calculated per water molecule, are found to be higher (lower in absolute value) than the

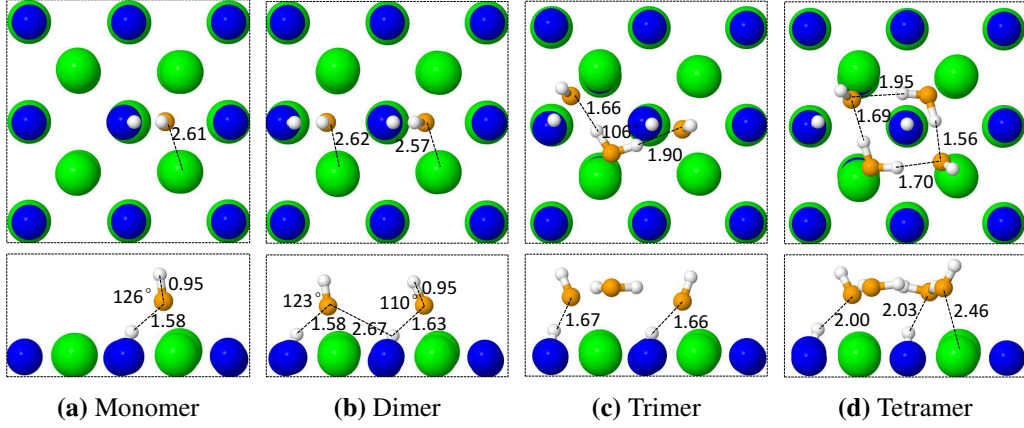


Figure 7.8.: Adsorbed water clusters (calculated with the HSE06 functional and *tight* numerical settings) containing 1-4 water molecules on the SrO(001) surface. Only a part of the (3×4) surface unit cell is shown. The structures are not the lowest-energy structures at each coverage, and are shown for the comparison only (see text). The surface oxygen, strontium, oxygen from water molecules, and hydrogen atoms are represented by blue, green, orange, and grey spheres, respectively. Selected geometric parameters are also shown. The unit for the distances is Å."

cluster/Surface	PBE	HSE06	ZPE correction
monomer/SrO(001)	-1.235	-1.495	0.062
dimer/SrO(001)	-1.256	-1.508	0.068
trimer/SrO(001)	-1.136	-1.379	0.084
tetramer/SrO(001)	-1.066	-1.288	0.086

Table 7.2.: DFT adsorption energies (in eV) per H_2O molecule (see Eq. 6.1) for water clusters on SrO(001). The unit cell size is in all cases (3×4) . The zero-point energy correction (see Eq. 6.2) is also given.

adsorption energy of the single water molecule on SrO(001), for the considered coverages. The most stable $n\text{H}_2\text{O}$ ($n \leq 4$) water clusters adsorbed on SrO(001) are shown in Fig. 7.8 and the corresponding energetics is shown in Tab. 7.2.

Although the main features look the same as water clusters on CaO(001), one can see that the hydrogen bonds between O_fH and O_sH are in general longer than the counterparts on CaO(001). This indicates that the larger lattice parameter of SrO destabilizes hydrogen bonds which is the key to form 1D or 2D superstructures. We have also performed a GA search for two different coverages: 6 water molecules and 10 water molecules both on (3×4) slab. The most stable structures found with GA are presented in Fig. 7.9 (a) and Fig. 7.9 (b). In both cases, the most stable structure contains only fully dissociated water molecules.

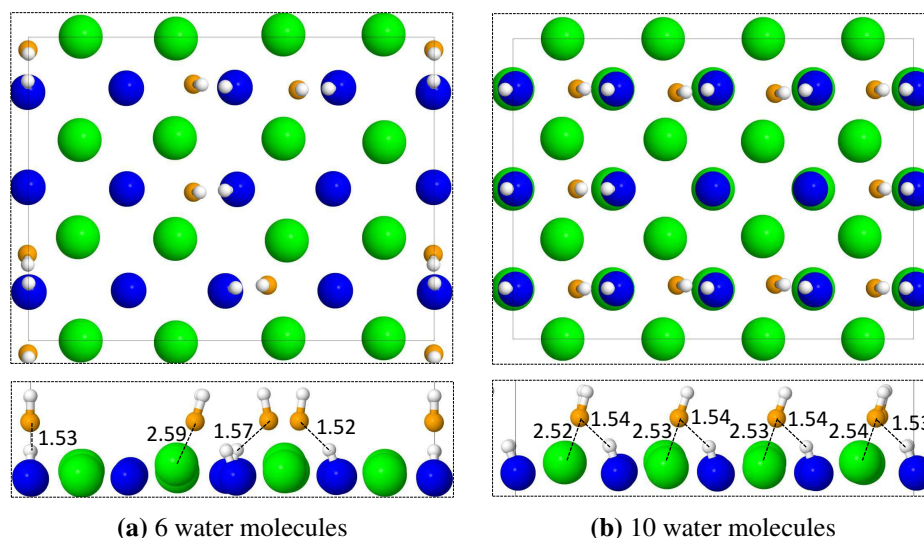


Figure 7.9.: Most stable (according to DFT with the HSE06 functional and *tight* numerical settings) water structures containing 6 water molecules (a) and 10 water molecules (b) adsorbed within the (3×4) surface unit cell of SrO(001). Unit cell boundary shown with grey lines. The surface oxygen, strontium, oxygen from water molecules, and hydrogen atoms are represented by blue, green, orange, and grey spheres, respectively. Selected geometric parameters and the relative energy are also shown. The unit for the distances is Å.

7.4. Discussion: What distinguishes CaO(001) from MgO(001) and SrO(001)?

As has been described in this chapter and the previous chapter, we have shown that 1D structures are found to be thermodynamic stable only on CaO(001) surface. On MgO(001), 2D structures are thermodynamically more stable, while on SrO(001) small clusters, *i.e.*, water monomer or dimer is more favoured. One might wonder what properties distinguish CaO(001) from MgO(001) and SrO(001) to support thermodynamically stable 1D structures. General trends among these three oxides and the uniqueness of CaO(001) are discussed in this section.

A graphical summary of the adsorption energies (including the ZPE contribution) for the most stable $n\text{H}_2\text{O}$ clusters and 1D, 2D structures (according to DFT) is presented in Fig. 7.10. The results clearly show the trends in adsorbate-adsorbate and adsorbate-surface components of the water-oxide interaction. For MgO(001), the water-water interaction leads to a strong stabilization of the adsorbed water for coverages up to 1 ML. According to HSE06+vdW with the ZPE correction, the most stable 1D adsorbed water structure on MgO is found to be 0.049 eV per molecule more stable than the tetramer, but it is still 0.092 eV less stable than the 2D structure. The water-surface interaction is significantly increased for CaO(001), which can be seen from the lower (*i.e.*, higher in absolute value) adsorption energies per water molecule compared to MgO(001) for all coverages up to 1 ML. However, the water-water interaction is much weaker

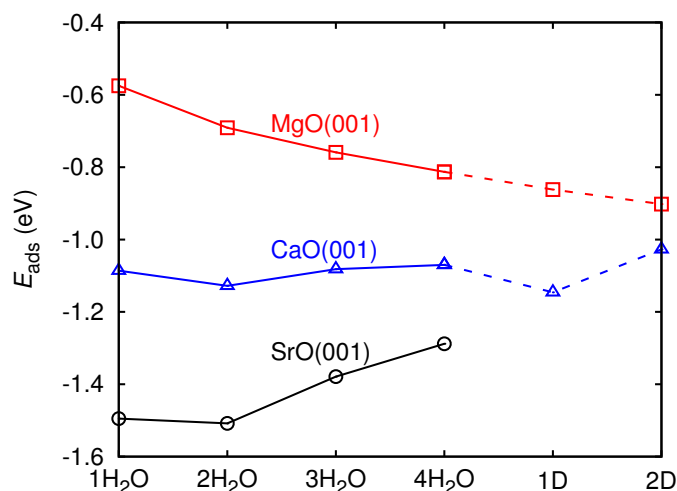


Figure 7.10.: HSE06+vdW adsorption energies (in eV) per H₂O molecule (see Eq. 6.1), including the ZPE contribution (Eq. 6.2), for the most stable adsorbed water clusters, 1D, and 2D structures listed in Tab. 7.1, Tab. 6.2, and Tab. 7.2. Note that two dimers are not considered as a tetramer.

for CaO(001) compared to MgO(001). In fact, among the considered cluster sizes (up to four molecules) the dimer has the lowest adsorption energy per molecule. However, the adsorption energy for the 1D structure is even lower (by 0.030 eV per molecule according to HSE06+vdW with the ZPE correction). For SrO(001), the adsorbed water is further stabilized, in agreement with the expected high basicity of this surface. In this case, dispersed water dimers are predicted to be the most stable form of adsorbed water based on DFT in a wide range of coverages, with water monomers being only slightly less stable.

In order to understand the differences in the stability of the 1D ordered water structures adsorbed on CaO(001) and MgO(001), we need to identify the surface properties that affect the interaction between the adsorbed water molecules. Using theoretical calculations, we find that the lattice constant of the substrate is the major factor influencing the relative stability of adsorbed water structures. Fig. 7.11 shows the DFT water adsorption energy per molecule for 1D and 2D structures on MgO(001) as a function of the lattice constant. The corresponding structures are shown in Fig. 7.12.

Upon increasing the strain in the substrate, first the 1D structure that was the metastable on the unstrained surface (Fig. 7.3 (a)) becomes thermodynamically stable. Increasing the strain further results in the thermodynamic stability of the 1D structure that is the most stable one on CaO(001) (Fig. 6.4 (a)). The effect of the strain is two-fold. First, it increases the distance between the adsorption sites and, consequently, affects the short-range interactions, in particular the hydrogen bonding. Second, it affects the electronic structure of the surface. In the case of the alkaline-earth oxides, the strain increases the surface basicity due to weakening of the anion-cation interaction, resulting in a stronger interaction of the water with the surface. This stronger interaction leads to dissociation of a larger portion of the adsorbed water molecules, which

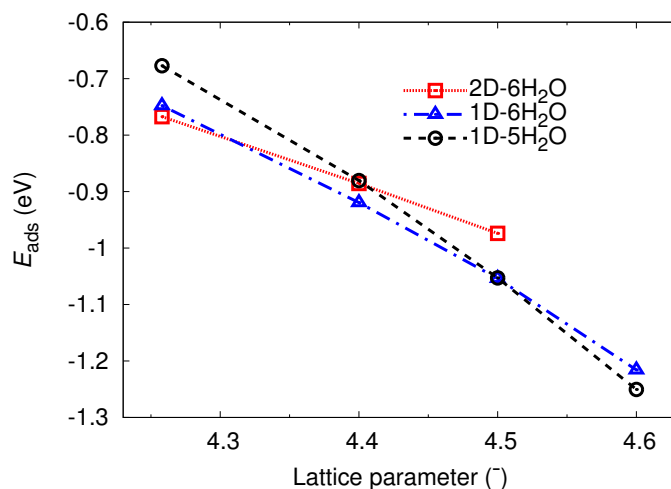


Figure 7.11.: The dependence of the HSE06+vdW water adsorption energies per molecule (Eq. 6.1) on the MgO lattice parameter for two 1D structures (Fig. 7.12 (a) and (b)) and one 2D structure on MgO(001) (Fig. 7.12 (c)) surface.

reduces the electrostatic dipole-dipole interaction that contributes to the water-water interaction when the water molecules are intact and oriented parallel to the surface.

In contrast to CaO(001), 1D structures found on MgO(001) are thermodynamically metastable, while water dimers are favoured over 1D structures on SrO(001). By comparing the adsorption energy dependence on the compaction of water structures and calculating water adsorption on strained MgO(001), the existence of the range of conditions for the thermodynamic stability of the 1D structures on CaO(001) is attributed to a balance between water-water and water-surface interactions. In the case of MgO(001), the smaller lattice constant results in a stronger hydrogen bonding between adsorbed water molecules. Moreover, stronger localization of the electrons on the oxygen anions at the surface of MgO leads to a weaker bonding of water molecules to the surface, and, as a consequence, to a larger portion of non-dissociately adsorbed molecules that lie flat on the surface and can have their dipole moments aligned, leading to a further stabilization of 2D adsorbed water structures. In the case of SrO(001), further increase in the adsorption site separation and a strong preference for the dissociative adsorption due to the higher basicity of the surface lead to the preference for the formation of isolated adsorbed water dimers.

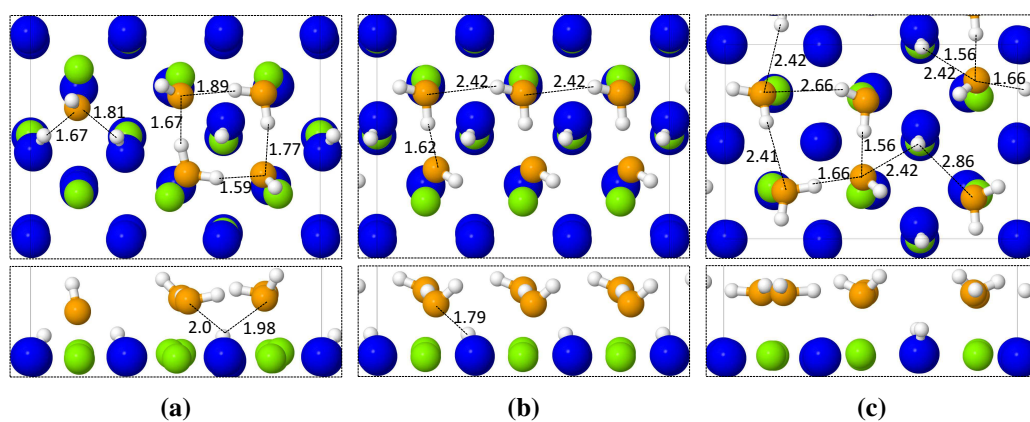


Figure 7.12.: Water adsorption structures on the strained MgO(001) surface. The structures from left to right are obtained via rescaling the structures in Fig. 6.4 (a), Fig. 7.3 (a) and Fig. 7.5 (a), respectively, to a cubic crystal parameter of 4.60 Å followed by atomic relaxation with the HSE06+vdW functional. The HSE06 lattice parameter is 4.21 Å for MgO and 4.80 Å for CaO.

Part III.

Hydrocarbon species on Ru(0001) surface

8. CH_x chemistry at the Ru(0001) surface: An introduction

The one-carbon (C_1) species play an important role in heterogeneous catalysis of hydrocarbon synthesis, activation, and conversion, including steam reforming of methane (overall reaction: $\text{CH}_4 + \text{H}_2\text{O} \leftrightarrow \text{CO} + 2\text{H}_2$), and the Fischer-Tropsch synthesis which converts syngas ($\text{CO} + \text{H}_2$) into long-chain hydrocarbons. Large number of prior studies [198, 199, 31, 32, 200, 36] have illustrated that in these catalytic processes the relative stability of the surface-bound CH_x ($x=0, 1, 2, 3, 4$) species is of paramount importance.

While several decades of work have clarified that long-chain hydrocarbon growth during the Fischer-Tropsch synthesis occurs via the addition of reduced C_1 compounds, the identification of the C_1 building block for this process has proven challenging. Although both product distributions and isotope studies of reactions at various transition-metal catalysts (in particular cobalt, ruthenium, and iron) suggest that adsorbed CH_2 species are the basic building blocks [39, 40], other experiments as well as theory find this species unstable and suggest other chain growth mechanisms in which the growth propagates via adding adsorbed CH or CO species [36]. From the steam reforming perspective, it is clear that methane dehydrogenation and adsorption of CH_3 radicals is the necessary first step of methane activation. However, the details of the subsequent reaction paths [201] are strongly dependent on the relative stabilities and reactivities of CH_3 , CH_2 , CH and C on a particular transition metal for a particular surface structure. Thus, the thermodynamics and kinetics of the $\text{CH}_2 \rightarrow \text{CH}$ reaction are of general importance.

In engineering applications the hydrocarbon chemistry is typically performed in reactors at high temperatures and pressures with high-surface-area transition-metal catalysts. Intrinsic reactions underlying the catalytic processes are affected by structural complexity, mass transport, and other phenomena. To gain detailed mechanistic understanding at the molecular level, much attention has been focussed on model systems, in particular on the adsorption of methane, its dehydrogenation, and the (possible) coupling of the resulting C_1 radicals on a variety of single crystal transition-metal surfaces (e.g. Ru, Ni, Rh, Co) under ultra-high vacuum (UHV) conditions [202, 203, 199, 31, 32, 200]. This approach allows to disentangle the effects of the structural heterogeneity and enables the straightforward preparation of clean samples. Because of its high thermal stability and reactivity, ruthenium single crystals, and particularly the Ru(0001) surface, have become a favorite for investigation of the C_1 surface chemistry.

Due to a low initial sticking probability of CH_4 on Ru(0001), prior workers typically used a high-pressure cell to enhance dissociative adsorption, and then transferred the sample to UHV for characterization. Characterization of samples prepared in this manner at 370 K suggests significant concentration of C , CH or two-carbon compounds, but essentially no adsorbed CH_3 or CH_2 [33, 204]. It was concluded that CH_3 or CH_2 are thermodynamically unstable on Ru(0001) compared to the other C_1 species at the preparation conditions. Indeed, experiments that directly produce CH_3 species on Ru(0001) are consistent with this picture. Zhou and coworkers [55]

have shown for Ru(0001) in UHV that by dosing CH₃I at the partial pressure of 10⁻¹⁰ mbar at sample temperatures below 200 K one can generate adsorbed CH₃ species, but that they rapidly disappear with increasing sample temperature: between 250 K and 300 K virtually all CH₃ is converted to CH, indicating that neither CH₃ nor CH₂ dissociation has a high reaction barrier.

Prior theoretical work is consistent with the experimental indications of the relative instability of CH₂/Ru(0001) and its fast conversion to CH. Van Santen and coworkers [41] have calculated the barrier for the CH₂ + x H → CH + ($x + 1$)H reaction about 16 kJ/mol by using a 2×2 slab model. Moreover in the same study they predicted that the barrier for the CH→C reaction is 108 kJ/mol, substantially higher than the barrier for the dissociation of CH₂. Xing and co-workers [205] reproduced these results, and in addition found that the trend of CH₂ having lower dissociation barrier than CH is a general one for all the transition metals they studied (i.e., Ni, Pd, Pt, Ru, Rh, Os, Ir, and Mo).

Thus, the model experimental and theoretical studies agreed on the relative stabilities of CH₂ and CH on Ru(0001). However, the relevance of these results for understanding the hydrocarbon chemistry at realistic catalytic conditions remained unclear. The crucial issue is that the experimental studies in which CH₄ was dosed on Ru(0001) have largely focussed on the samples created at high temperatures and pressures, and then analyzed in UHV. It was unclear how the transfer to UHV may affect surface speciation. On the other hand, theoretical work has not exhaustively addressed the effects of temperature, pressure, and surface coverages of carbon and hydrogen on the stability of different C1 species. Recently, our collaborators employed a supersonic molecular beam source to dose the Ru(0001) surface with methane at temperatures below 250 K [2]. Employing such a source at these sample temperatures allows the preparation of surface-bound CH₂ radicals from CH₄ without leaving UHV. Having prepared such a sample, they characterized the surface population of CH₂ after annealing it to successively higher temperatures using the surface-specific laser-based technique, vibrational sum-frequency generation spectroscopy. By conducting a series of such experiments as a function of sample annealing temperature, they derived the activation energy (E_a) for conversion of CH₂ → CH to be about 65 kJ/mol, approximately four times higher than previous theoretical predictions. This observation indicates that there is a mechanism by which CH₂ can be stabilized at the Ru(0001) surface at realistic conditions.

To obtain a microscopic understanding of these experimental observations, we calculate adsorption of all relevant (see Chp. 9) CH _{x} + y H ($x = 0-3$, $y = 1-3$) species combinations at a (2×2) surface unit cell of Ru(0001), and compare their relative thermodynamic stability as a function of hydrogen chemical potential using the *ab initio* atomistic thermodynamics approach [52]. We also calculate the reaction pathways and transition states for CH₂ to CH conversion. We obtain the reaction barriers and heats for the dissociation of CH _{x} species in terms of free energy by taking into account the vibrational free-energy contributions at a given temperature. The results of these calculations demonstrate two important points: (i) none of the configurations containing CH₂ is thermodynamically stable at realistic conditions, and (ii) the H surface coverage at realistic conditions (i.e. 450 K, 1 MPa) can be higher than what was previously assumed in theoretical calculations. Moreover, the barrier for the CH₂+ y H → CH+($y + 1$)H reaction increases dramatically when $y = 3$. Thus, although CH₂ is found to be thermodynamically unstable at realistic temperatures and H₂ partial pressures, there are kinetic limitations that can stabilize CH₂ at the surface. Evidently, non-equilibrium distributions of coadsorbed species dramatically

change CH_2 reactivity on $\text{Ru}(0001)$. The dependence of CH_2 stability on coadsorbed hydrogen coverage provides a possible means of reconciling experiment and computation describing the C1 building block in the Fischer-Tropsch process and, more generally, suggests the importance of understanding surface concentrations of hydrogen in the heterogeneous chemistry of hydrocarbon conversion. We also study the stability and reaction paths for the formation of C_2 species, to elucidate the initial steps in chain growth at realistic pressures. One profound effect of hydrogen coadsorption is that it significantly decreases the reaction barriers in C-C coupling reactions, among which some reaction paths are specially preferred.

9. $\text{CH}_x + \text{H}_y$ adsorption on Ru(0001)

9.1. Surface model and computational settings

Several studies on the adsorption and chemistry of hydrocarbon species at the Ru(0001) surface have been reported prior to our work. In a plane-wave DFT study with PW91 functional [98], Ciobîcă and coworkers [37] adopted a periodic slab model using the (2×2) super cell. The unit cell contained four layers of Ru atoms and five-layer-equivalent space as vacuum. To avoid the artificial dipole-dipole interaction with the slab images, molecules were placed on both sides of the slab with an inversion center. Different adsorption sites, including atop sites, bridge sites, and three-fold hollow (fcc and hcp, see Fig. 9.1) sites were studied. For all studied CH_x species and H atoms, the site preference was found to increase in the order top \rightarrow bridge \rightarrow hollow. The same adsorption configurations have also been studied by Xing and coworkers [205] using plane-wave DFT with PW91 functional, however, with a different slab model. They used also a four-layer (2×2) periodic model to represent the metal surface, while adsorbates were placed on one side where two layers were allowed to relax, and the other two layers were fixed at the bulk geometry. The convergence of the model with respect to the number of layers and the vacuum distance was demonstrated by calculating the adsorption energy of CH_3 on Ni(100) surface for different models, but no convergence tests for Ru(0001) were reported in their work.

It is known from literature [206, 207] that different GGA functionals, namely PW91, PBE, and RPBE, predict rather different adsorption energies for atoms and molecules. For example, CH_2 adsorption energies calculated in this work are -5.47 eV for PBE and -4.95 eV for RPBE (the LDA adsorption energy is -6.71 eV). However, due to the lack of experimental values for CH_x adsorption on Ru(0001), none of these functionals is known to give better description than another for this system. Nevertheless, a single-crystal adsorption calorimetry study [208] has shown that the binding energy of CH_3 predicted by PBE agrees well with the measured value.

In our calculations, we employ periodic DFT with the PBE functional [42]. Moreover, van der Waals interaction is included by adopting the TS-vdW^{surf} scheme (introduced in Sec. 4.5.3). Localized numeric atom-centred basis is used, which enables large vacuum distances between the slab images with a minor increase in computational cost. Illustration of the Ru(0001) slab models used in this thesis is shown in Fig. 9.1. At most (2×2) supercell is used for all calculations in this chapter (larger model used in Chp. 11). Five fixed layers are used to represent the substrate bulk, and two topmost layers are relaxed along with adsorbates on the relaxed side of the slab. The numbers of the fixed and relaxed Ru layers, the k -mesh density, and the basis set are tested by converging the CH_2 and CH adsorption energy and geometry on Ru(0001). We find that at least seven layers of substrate are needed to converge the adsorption energies of *both* CH and CH_2 at *both* hcp and fcc sites to less than 0.02 eV, with the adsorption energy at fcc site converging slower.

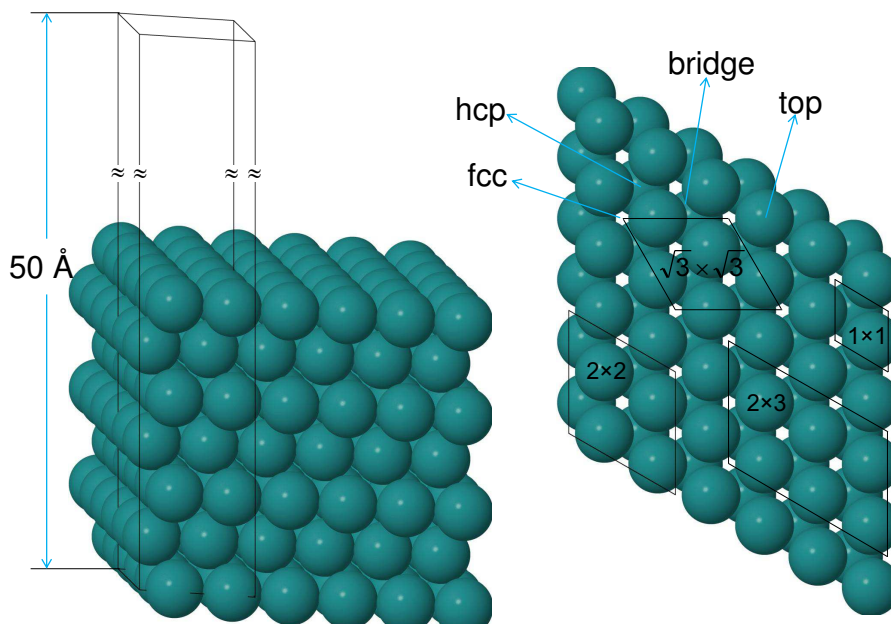


Figure 9.1.: Periodic slab model of Ru(0001) surface. Side view (left side) and top view (right side) with indicated surface unit cells used in this thesis are shown. hcp site, fcc site, bridge site, and top site are also indicated.

9.2. Convergence tests

Fig. 9.2 shows the convergence of CH_2 adsorption energy with the number of k -points. We find that a $9 \times 9 \times 1$ k -grid (Γ -centered) is sufficient to get results converged within 0.005 eV for the PBE functional. As noted in the previous section, we find that seven layers of Ru are necessary to produce converged adsorption energies for CH_2 and CH. In particular, since the relative stability of CH_2 and CH is our focus, we converged *both* CH *and* CH_2 adsorption energies at hcp and fcc sites with the number of layers in the slab. The convergence test results are summarized in Fig. 9.3 and Fig. 9.4. We find that seven layers or more are necessary to get convergence to 0.02 eV (2 kJ/mol) for different adsorbates at different sites. We note that one might be misled if the number of layers is tested with only one species in one specific site. For instance, six layers is enough for the adsorption energy of CH_2 at an hcp site to converge within 0.01 eV (1 kJ/mol). However, the deviation from converged values is still 0.06 eV for CH_2 or CH at an fcc site on such a slab. Interestingly, we find that the error in the adsorption energy at the thin slabs compared to the converged thickness is comparable in value, but different in sign for the fcc and hcp sites, for both CH and CH_2 (see Fig. 9.3 and Fig. 9.4). This indicates that the bottom layers of the slab model have more distinct effects on different sites rather than different adsorbates. This implies that convergence of adsorption energies at different sites with the slab thickness is a more stringent test for a model of a metallic surface than convergence of the adsorption energies for different adsorbates at the same type of sites. Moreover, as shown in the figures, the van der

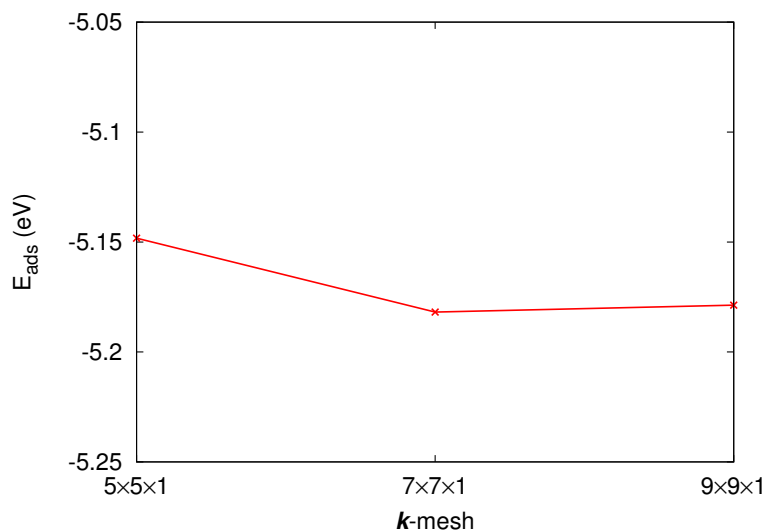


Figure 9.2.: Convergence of the CH_2 adsorption energy at hcp site with the k -mesh in the Ru (0001) (2×2) slab model. 7-layers model is used in the test. Only top two layers are relaxed since relaxing more layers leads to differences in adsorption energies smaller than 0.01 eV.

Waals interaction correction (see Sec. 4.5.3) is not sensitive to the number of layers in the tested cases. If not specified otherwise, the seven-layer model and the PBE functional with vdW^{surf} correction are used for all calculations of adsorption on the Ru(0001) surface.

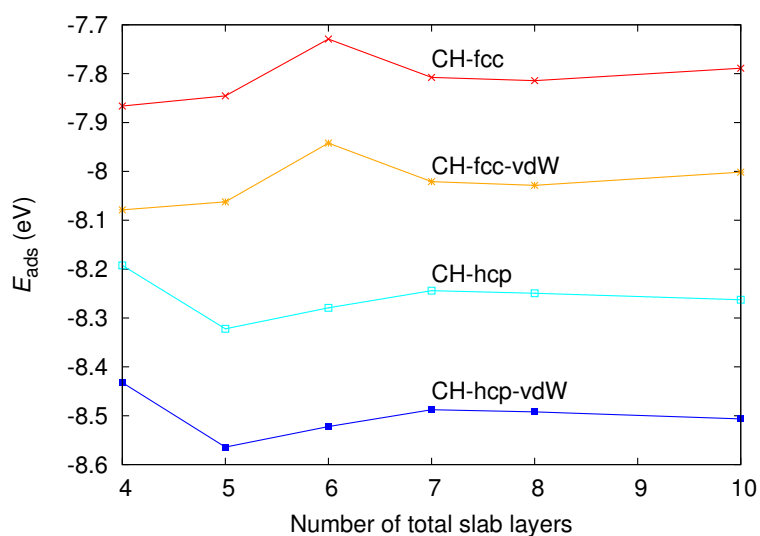


Figure 9.3.: Convergence of the CH adsorption energy ($E_{\text{ads}} = E_{\text{CH/slab}} - E_{\text{CH/slab}} - E_{\text{CH}}$) at hcp and fcc sites with the number of layers in the Ru (0001) (2×2) slab model. k -mesh $9 \times 9 \times 1$ is used in the tests. Only the top two layers are relaxed since relaxing more layers leads to differences in adsorption energies smaller than 0.01 eV. In all tests, PBE functional is used. The effects of including van der Waals interaction (denoted as "-vdW"; see Sec. 4.5.3) are also shown.

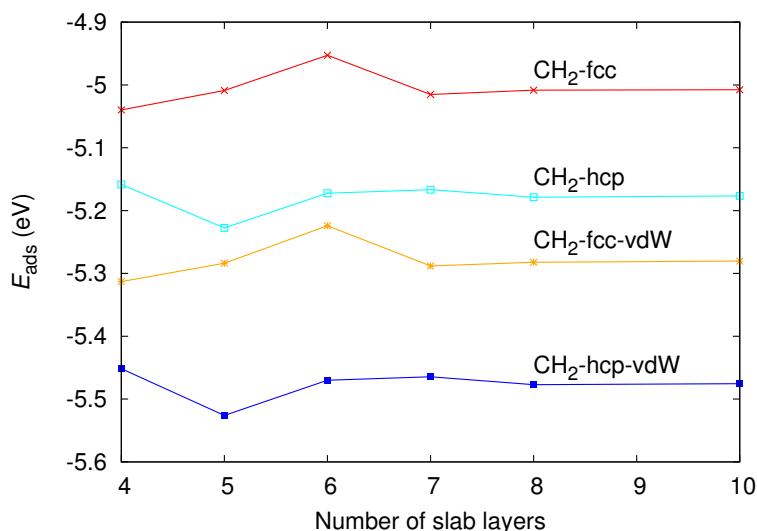


Figure 9.4.: Convergence of the CH₂ adsorption energy ($E_{\text{ads}} = E_{\text{CH}_2/\text{slab}} - E_{\text{CH}_2/\text{slab}} - E_{\text{CH}_2}$) at hcp and fcc sites with the number of layers in the Ru (0001) (2×2) slab model. k -mesh $9 \times 9 \times 1$ is used in the tests. Only top two layers are relaxed since relaxing more layers leads to differences in adsorption energies smaller than 0.01 eV. In all tests, PBE functional is used. The effects of including van der Waals interaction (denoted as "-vdW"; see Sec. 4.5.3) are also shown.

9.3. Adsorption geometries and energies

Finding all stable and metastable adsorption configurations for CH_{*x*}H_{*y*}/Ru(0001) ($x = 0-3$, $y=0-3$) is a challenging task, due to the large number of possible configurations, including the different types of the adsorption sites. Ciobîcă and coworkers reported that the hollow sites are energetically preferred by all CH_{*x*} species, when the single molecule is adsorbed within the (2×2) surface unit cell of Ru(0001) [37]. However, the possible effect of the coadsorbed species on the adsorption site preference has not been studied. In the next section, we address this question.

9.3.1. Adsorption at the top and bridge sites

Ciobîcă and coworkers [37] reported energies of CH_{*x*} ($x = 0-3$) adsorption at the top and bridge sites of Ru(0001). However, we find that neither of these two types of sites is a local minimum on the PES for the considered adsorption model. Moreover, the top or bridge adsorption sites are not preferred by any of the adsorbates for the CH_{*x*}+*y*H ($x = 1-3$, $y=0-3$) adsorption. This is concluded based on the results of the atomic relaxation of more than 200 randomly-generated structures.

9.3.2. Adsorption at the hollow sites

Based on the above results, we calculate all possible configurations for the CH_x ($x=1-3$) and $y\text{H}$ ($y=0-3$) coadsorption, with the adsorbates occupying only hcp and/or fcc hollow sites. The adsorption energy is defined as follows:

$$E_{\text{CH}_x+y\text{H}}^{\text{ads}} = E_{\text{CH}_x+y\text{H}/\text{slab}} - E_{\text{slab}} - E_{\text{CH}_4} - \frac{(x+y-4)}{2}E_{\text{H}_2} + \Delta E^{\text{ZPE}} \quad (9.1)$$

The first three terms on the right-hand side are the total energies of the slab model with adsorbates, slab model without adsorbates, and methane molecule, respectively, E_{H_2} is the total energy of the hydrogen molecule, and the last term is the zero-point energy correction derived from harmonic vibrational frequencies. The adsorption energies are summarized in Tab. 9.1, while the corresponding adsorption configurations can be found in Fig. 9.5-9.10. As presented in Tab. 9.1, the site preference for single CH_x adsorbed within the (2×2) supercell agrees with that in reference [37]. However, the adsorption energy difference between the hcp and fcc sites is gradually changed and in some cases even reversed by the coadsorption of hydrogen. For instance, CH adsorption at an hcp site is 0.664 kJ/mol stronger than at an fcc site, while this value is 0.307 kJ/mol for CH+H, and is further decreased to 0.177 kJ/mol for CH+2H and 0.066 kJ/mol for CH+3H. The qualitative change is found for CH_2 adsorption: a single CH_2 species prefers to adsorb at hcp sites, and so does CH_2 with one coadsorbed H atom, but the coadsorption of two or three H atoms changes the preferred adsorption site from hcp to fcc.

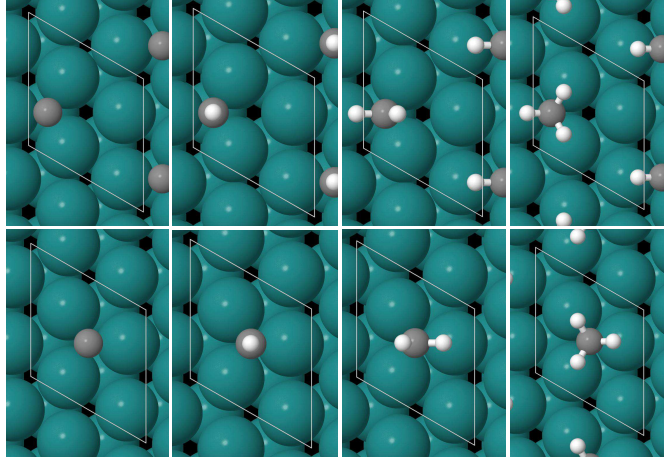


Figure 9.5.: Most stable structures of CH_x adsorbed on Ru (0001) (2×2) surface supercell. $x = 0-3$ (see Tab. 9.1 for corresponding adsorption energies) are shown from left to right. The upper panels show structures with CH_x at hcp sites, while the lower panels show structures with CH_x at fcc sites.

Based on the results presented in Tab. 9.1 and Fig. 9.5-9.10, several conclusions can be drawn. CH_x species, as well as H atoms, generally repel each other at Ru(0001). This can be understood in terms of a competition for the Ru electrons that are available for bonding [209]. The site

CH_x	hcp	fcc	CH_x preferred site	$E_{\text{CH}_x+y\text{H}}^{\text{repulsion}}$
$x=0$	0.164	0.828	hcp	
$x=1$	-0.547	-0.081	hcp	
$x=2$	-0.550	-0.374	hcp	
$x=3$	-0.712	-0.814	fcc	
CH_x+1H				
$x=1(\text{a})$	-1.118	-0.811	hcp	0.275
$x=1(\text{b})$	-1.018	-0.720		
$x=2(\text{a})$	-1.053	-1.009	hcp	0.343
$x=2(\text{b})$	-1.035	-0.952		
$x=2(\text{c})$	-0.933	-0.863		
$x=3(\text{a})$	-1.154	-1.257	fcc	0.301
$x=3(\text{b})$	-1.129	-1.212		
CH_x+2H				
$x=1$	-1.481	-1.303	hcp	0.759
$x=2(\text{a})$	-1.418	-1.450	fcc	0.792
$x=2(\text{b})$	-1.263	-1.277		
$x=3$	-1.531	-1.683	fcc	0.823
CH_x+3H				
$x=1$	-1.925	-1.859	hcp	1.161
$x=2$	-1.767	-1.881	fcc	1.208
$x=3$	-1.872	-2.075	fcc	1.277

Table 9.1.: Adsorption energy (in eV) for CH_x+yH ($x=0-3$; $y=0-3$) on a Ru (0001) (2×2) surface supercell, calculated using Eq. 9.1. All possible configurations of CH_x and H species at the hollow sites are considered. (a), (b) and (c) indicate different adsorption structures for the same stoichiometry. The bold numbers indicate the most stable configuration for a certain stoichiometry.

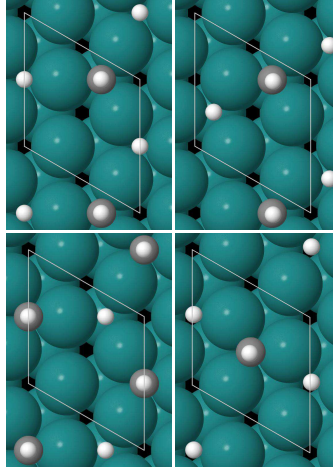


Figure 9.6.: Structures of CH+H adsorbed on Ru (0001) (2×2) surface supercell. (a) and (b) isomers (see Tab. 9.1 for corresponding adsorption energies) are shown on the left to right, respectively. The upper panels show structures with CH at hcp sites, while the lower panels show structures with CH at fcc sites.

preference for CH_x is affected by the repulsive interaction with coadsorbed H. For example, for CH_2+H , the CH_2 molecule does not have neighboring H at hcp sites, while for CH_2+2H every hcp site has neighboring H atoms at other hcp sites (see Fig. 9.9), which destabilizes the adsorption of CH_2 at hcp sites.

To quantify the repulsion between the adsorbates at the surface, we calculate how much the surface energy of the adsorbed CH_x+yH increases at a certain coverage of hydrogen y compared to a separate adsorption of CH_x ($x = 1-3$) and hydrogen atoms each adsorbed at its favoured site at 0.25 ML coverage:

$$E_{\text{CH}_x+y\text{H}}^{\text{repulsion}} = (E_{\text{CH}_x+y\text{H}/\text{slab}} - E_{\text{slab}}) - (E_{\text{CH}_x/\text{slab}} - E_{\text{slab}}) - y(E_{\text{H}/\text{slab}} - E_{\text{slab}}) \quad (9.2)$$

As shown in Tab. 9.1, the repulsion among H atoms and CH_x species can be rather significant. As the number of hydrogen atoms increases, the repulsion energy increase from about 0.3 eV for one coadsorbed hydrogen atom to about 1.2 eV for three coadsorbed hydrogen atoms. In general, the repulsion increases with x , while the difference between different CH_x ($x = 1-3$) is not larger than 0.1 eV for a given coadsorbed hydrogen coverage.

Our results also indirectly indicate that care must be taken when comparing DFT results with calorimetry measurements. For instance, it is possible that coadsorption of iodine with CH affects the results of calorimetry studies. In this case, the seemingly poor correspondence between the PBE and calorimetry results, and the better agreement of the latter with RPBE results, for the CH adsorption on Pt(111) [210] may be actually due to the influence of the coadsorbed iodine at saturation coverage. Indeed, the low-coverage (~ 0.04 ML) measurements of CH_3 adsorption [208] are in agreement with our PBE results. We also note that PBE functional underestimates bonding energy in H_2 molecule by 0.208 eV. However, no significant improvements are found

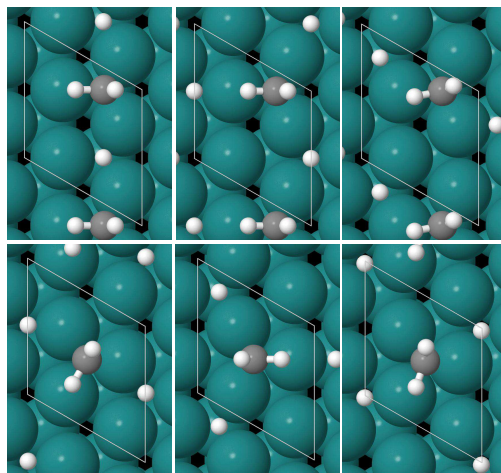


Figure 9.7.: Structures of CH_2+H adsorbed on Ru (0001) (2×2) surface supercell. (a), (b), and (c) isomers (see Tab. 9.1) are shown on the left, middle, and right, respectively. The upper panels show structures with CH_2 at hcp sites, while the lower panels show structures with CH_2 at fcc sites.

for functionals we tested: RPBE underestimates the bonding energy by 0.169 eV, and HSE06 by 0.222 eV.

We have also performed calculations of “isolated” CH using larger unit cells (so that the corresponding coverage is below 0.25 ML). The results show that the adsorption energy pre CH at the 0.25 ML coverage is within 0.02 eV of the low-coverage limit (see also Fig. 11.4).

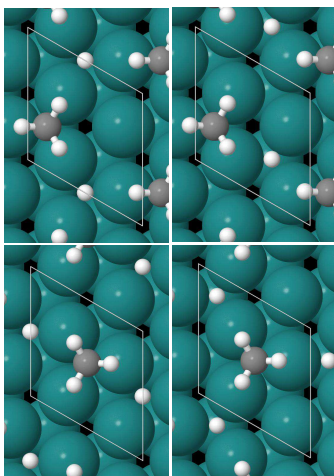


Figure 9.8.: Structures of CH_3+H adsorbed on Ru (0001) (2×2) surface supercell. (a) and (b) isomers (see Tab. 9.1 for corresponding adsorption energies) are shown on the left and right, respectively. The upper panels show structures with CH_3 at hcp sites, while the lower panels show CH_3 at fcc sites.

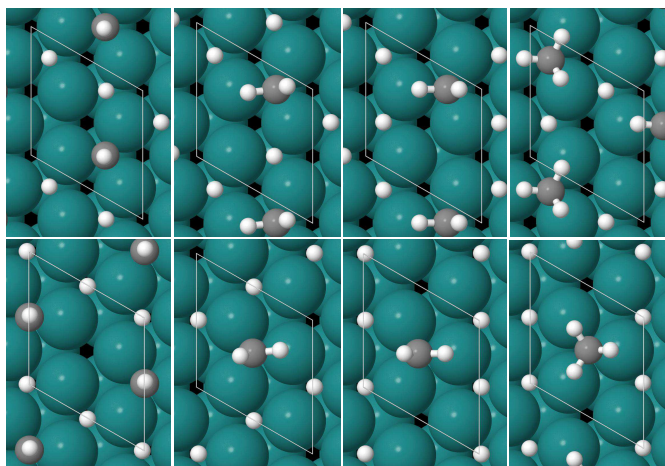


Figure 9.9.: Structures of CH_x+2H adsorbed on Ru (0001) (2×2) surface supercell. $x = 1$, $x = 2$ (a), $x = 2$ (b), and $x = 3$ (see Tab. 9.1 for corresponding adsorption energies; (a) and (b) denote different isomers) are shown from left to right. The upper panels show structures with CH_x at the hcp sites, while the lower panels show structures with CH_x at the fcc sites.

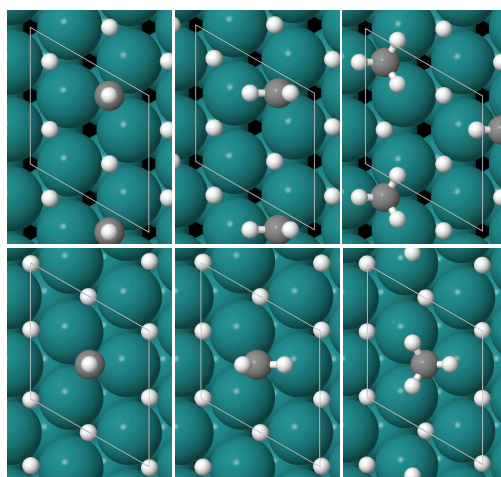


Figure 9.10.: Structures of $\text{CH}_x + 3\text{H}$ adsorbed on Ru (0001) (2×2) surface supercell. $x = 1$, $x = 2$, and $x = 3$ (see Tab. 9.1 for corresponding adsorption energies) are shown on the left, middle, and right, respectively. The upper panels show structures with CH_x at the hcp sites, while the lower panels show structures with CH_x at the fcc sites.

9.4. Thermodynamic stability analysis

We use *ab initio* atomistic thermodynamics [78, 51, 52, 53] to estimate the relative thermodynamic stability of different CH_x+yH phases at Ru(0001) as a function of temperature T and H_2 partial pressure p_{H_2} . The thermodynamic equilibrium is calculated under the constraints of the (2×2) surface unit cell, $x + y < 6$, and single C per unit cell. The Gibbs free energies of adsorption (ΔG) for different adsorbate configurations are calculated according to:

$$\Delta G(T, p_{\text{H}_2}) = E_{(\text{CH}_x+y\text{H})/\text{slab}} - E_{\text{C}/\text{slab}} + \Delta F^{\text{vib}}(T) - (x + y)\mu_{\text{H}}(T, p_{\text{H}_2}), \quad (9.3)$$

where the first and second terms are the total energy of the Ru slab with adsorbed CH_x+yH and of the slab with only C atom adsorbed at hcp site, respectively, the third term is the Helmholtz vibrational free energy of the $(\text{CH}_x+y\text{H})/\text{Ru}(0001)$ system in the harmonic approximation,

$$\Delta F^{\text{vib}}(T) = \sum_{i=1}^{N_{\text{vib}}} \left[k_{\text{B}} T \ln(1 - e^{-\frac{\hbar \omega_i}{k_{\text{B}} T}}) \right] + E_{\text{CH}_x+y\text{H}/\text{slab}}^{\text{ZPE}} - E_{\text{C}/\text{slab}}^{\text{ZPE}}, \quad (9.4)$$

and the last term is the chemical potential of hydrogen:

$$\mu_{\text{H}}(T, p_{\text{H}_2}) = \frac{1}{2}(E_{\text{H}_2}^{\text{total}} + E_{\text{H}_2}^{\text{ZPE}}) + \Delta\mu_{\text{H}}(T, p_{\text{H}_2}^0) + \frac{1}{2}k_{\text{B}}T \ln \left(\frac{p_{\text{H}_2}}{p_{\text{H}_2}^0} \right) \quad (9.5)$$

where $\Delta\mu_{\text{H}}(T, p_{\text{H}_2}^0)$ is obtained from partition function based on DFT calculations by using Eq. 2.71, $p_{\text{H}_2}^0 = 1$ atm. The vibrations are calculated using the harmonic approximation approach (see Sec. 2.4).

The calculated free energies of adsorption are plotted in Fig. 9.11. As expected, increasing chemical potential of hydrogen leads to the increase of the amount of hydrogen at the surface. Interestingly, structures with a high hydrogen coverage (three coadsorbed H atoms per unit cell) are stable in a wide range of conditions. CH_2 species are found to be thermodynamically unstable at any conditions. This suggests that CH_2 observed in the SFG experiments [211] is kinetically stabilized. The most thermodynamically stable species at realistic conditions are found to be CH, but CH_3 can be stabilized by coadsorbed hydrogen at high hydrogen chemical potentials. At 300 K, CH_3+3H becomes the most stable phase among all others studied phases once the pressure is higher than ~ 16 atm.

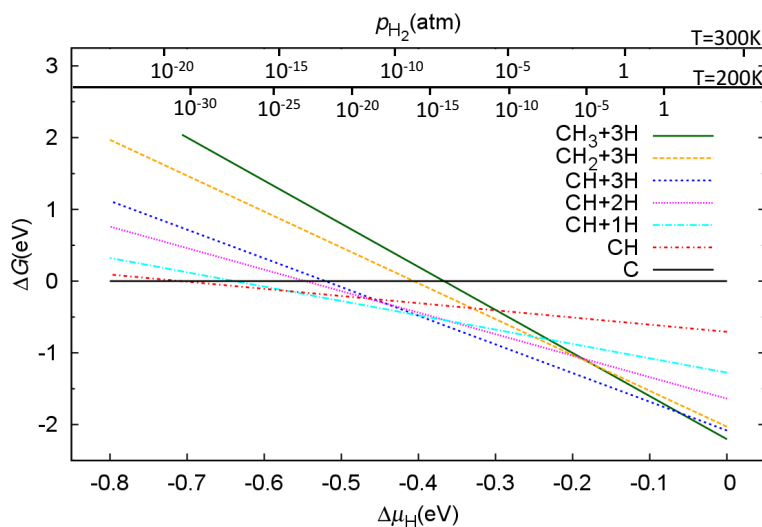


Figure 9.11.: Gibbs free energy of adsorption for CH_x+yH ($x + y = 0-6$) configurations on a (2×2) Ru (0001) surface model, calculated using Eq. 9.3 ($\Delta F^{\text{vib}}(300 \text{ K})$ is used; the maximum difference between $\Delta F^{\text{vib}}(300 \text{ K})$ and $\Delta F^{\text{vib}}(200 \text{ K})$ is less than 0.02 eV) as a function of the hydrogen chemical potential defined by Eq. 9.5. For clarity, only the most stable adsorption configuration for each value of $x + y$ is shown. PBE functional and default-tight basis are used in all the calculations. All calculated structures can be found in Fig. 9.5-9.10.

10. CH₂ dissociation: The effects of coadsorbed hydrogen

10.1. Reaction paths

According to previous studies [41, 205], the barrier for the dissociation of CH₂ into CH and H at the Ru(0001) surface is about 16 kJ/mol. This value is much smaller than the dissociation barrier of 65±6 kJ/mol derived by correlating the decrease of CH₂ SFG signal intensity with the increase of temperature [2]. In the earlier calculations, a single CH₂ molecule per (2×2) unit cell was considered. However, our results reported in the previous chapter indicate that a significant amount of hydrogen can be coadsorbed at the surface at realistic conditions. This prompts us to investigate the effect of coadsorbed hydrogen on the dissociation of CH₂. Starting with reproducing the results on the dissociation of single CH₂ reported in the literature, we further consider two additional dissociation scenarios, both of which start from CH₂ with coadsorbed H atoms at the surface. The main difference between these two paths is in the final state: the hydrogen atom coming from CH₂ either stays at the surface or leaves in the form of an H₂ molecule after combining with another H atom adsorbed at the surface. Both paths are endothermic. However, due to the entropy increase upon the desorption of the H₂ molecule, the second path is exergonic, i.e., more favoured in terms of the free energy. By examining details of the reaction and comparing with experimental observations, we argue that the existence of the second dissociation path explains all the observations.

Free energy and total energy (in parenthesis) of initial states, transition states and final states along different CH₂ dissociation paths are presented in Fig. 10.1, and the corresponding atomic configurations can be found in Fig. 10.2. The reaction energy barrier (the activation energy) is defined as:

$$E_a = E_{TS} - E_{IS}, \quad (10.1)$$

where E_{TS} and E_{IS} are the total energies of the transition and initial states, respectively. The reaction energy is defined as

$$E_r = E_{FS} - E_{IS}, \quad (10.2)$$

where E_{FS} is the total energy of the final state. The total-energy-based reaction barrier and reaction energy describe the reaction at 0 K which might be misleading in explaining experimental observations, while the corresponding free-energy-based quantities include the effects of temperature and pressure. The free-energy counterparts of the activation energy E_a and reaction energy E_r are defined as:

$$F_a = F_{TS} - F_{IS} \quad (10.3)$$

and

$$F_r = F_{FS} - F_{IS}, \quad (10.4)$$

Reaction	E_a (kJ/mol)	E_r (kJ/mol)
$\text{CH}_2 \rightarrow \text{CH} + \text{H}$	11.2	-49.0
$\text{CH}_2 + \text{H} \rightarrow \text{CH} + 2\text{H}$	10.8	-35.0
$\text{CH}_2 + 2\text{H} \rightarrow \text{CH} + 3\text{H}$	12.4	-39.5
$\text{CH}_2 + 3\text{H} \rightarrow \text{CH} + 4\text{H}$	61.8	53.1
$\text{CH}_2 + 3\text{H} \rightarrow \text{CH} + 2\text{H} + \text{H}_{2,\text{gas}}$	95.6	51.8

Table 10.1.: Calculated reaction barrier (middle column) and reaction energy (right column) for CH_2 dissociation with different numbers of H atoms on a (2×2) supercell of Ru (0001). E_{IS} , E_{TS} , E_{FS} are total energies of initial state, transition state, and final state, respectively. The final state of reaction $\text{CH}_2 + 3\text{H} \rightarrow (\text{CH} + 4\text{H})$ is shown in Fig. 10.2, panel e). For each stoichiometry, the most stable configuration of the initial state is considered.

where F_{IS} , F_{TS} and F_{FS} are free energies of the initial state, transition state, and final state, respectively. In this thesis, they are obtained by assuming that the initial state, transition state, and final state keep their geometries unchanged with respect to the 0 K structures, and that the vibrational contributions from the surface species dominate all other contributions (namely, the contributions from the phonons in the substrate). The free energies are calculated using Eq. 9.3, Eq. 9.4, and Eq. 9.5. For transition states, the imaginary frequencies are omitted, since they correspond to the motion along the reaction path.

For the dissociation of single CH_2 ($i \rightarrow j \rightarrow k$ in Fig. 10.1), the reaction energy barrier and reaction energy is 11.6 kJ/mol and 49.0 kJ/mol, respectively. These values are close to 16 kJ/mol and 45 kJ/mol reported by Ciobîcă [41] and Bin [205]. The deviation of our results from the previous reports is possibly due to the thinner substrate models used in the earlier work (see Fig. 9.3). The free-energy barrier at 300 K is about one third of the barrier at 0 K, at the finite-temperature effects further stabilize the final state, which indicates that the ease of single CH_2 dissociation has even been underestimated by previous studies based on total energy differences. By analysing the vibrational free-energy contribution, the differences between E_a and F_a are attributed to weakening of the bond being broken, while the differences between E_r and F_r can be understood in terms of the vibrational contributions from the newly formed bonds between the hydrogen atom and the surface. The vibrations also contribute at 0 K via changes in ΔE^{ZPE} in Eq. 9.1. Quantitatively, ΔE^{ZPE} decreases the dissociation barrier for single CH_2 by 7 kJ/mol.

The free-energy dissociation barrier calculated for single CH_2 is too low to stabilize CH_2 at temperatures higher than 250 K in experiments. Dissociation of CH_2 with one or two H atom coadsorbed on (2×2) Ru(0001) makes no significant changes, as can be seen from Tab. 10.1. Dissociation of CH_2 coadsorbed with 3 H atoms on (2×2) Ru(0001), however, is significantly different. There are two possible scenarios. In the first scenario, the system follows the path shown in Fig. 10.2: $a \rightarrow b \rightarrow c \rightarrow d \rightarrow e$. Along this path, the number of hydrogen atoms at the surface is preserved. As the C-H bond breaks, the dissociated hydrogen goes to an hcp site which is surrounded by the three coadsorbed hydrogen atoms. The energetics of the key steps

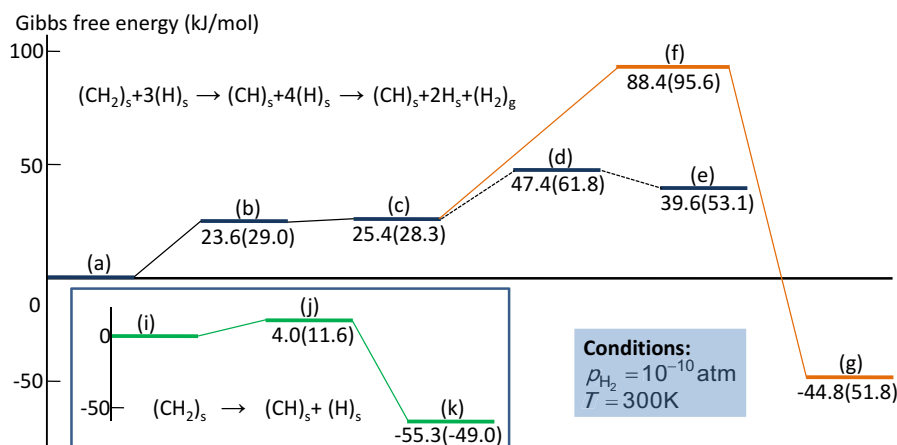


Figure 10.1.: Calculated free-energy profile for dissociation of $\text{CH}_2 + 3\text{H}$ on a Ru (0001) (2×2) surface supercell at $T = 300 \text{ K}$, $p_{\text{H}_2} = 10^{-10} \text{ atm}$. Total energy differences are shown in parenthesis. The structures are labeled according to Fig. 10.2. The inset shows the dissociation pathway for a CH_2 molecule in the absence of coadsorbed hydrogen for the same (2×2) unit cell.

of this process is shown in Fig. 10.1. It is interesting to note that state c is a local minimum in terms of total energy while state b is a transition state between state a and c. This is in contrast with the free-energy picture: state b is higher than state c for realistic temperatures, indicating that b is unlikely a transition state. The true transition state is the state d (see Fig. 10.1). The total-energy (including ΔE^{ZPE} correction) reaction barrier and reaction energy are 61.8 kJ/mol and 53.1 kJ/mol, respectively, while the free-energy barrier is 47.4 kJ/mol and the reaction free energy is 39.6 kJ/mol at 300 K. This free-energy barrier is not far from the measured barrier ($65 \pm 6 \text{ kJ/mol}$). However, the reverse barrier (7.8 kJ/mol) is much smaller than the direct one, implying that CH_2 dissociation is reversible. Assuming Boltzmann distribution of the reactants and products, the amount of the dissociated CH_2 is estimated to be $\sim 19 \text{ ppm}$ at 300 K. This is in contradiction with the experimentally observed decrease in the CH_2 signal with increasing annealing temperature [211].

The second path is CH_2 dissociation followed by the formation and desorption of an H_2 ($a \rightarrow b \rightarrow c \rightarrow f \rightarrow g$ in Fig. 10.1). The energetics of the key steps of this process is shown in Fig. 10.1, and the corresponding structures are presented in Fig. 10.2. The first part (from a to c) is the same as in the first scenario. However, the hydrogen atom from CH_2 goes to the nearest coadsorbed hydrogen atom and forms a hydrogen molecule, which then desorbs. For this path, E_a and E_r are 96.5 kJ/mol and 51.8 kJ/mol, respectively. At 0 K, this process is not qualitatively different from the first scenario: the forward reaction is endothermic and less favoured than the reverse reaction which has an energy barrier of 43.8 kJ/mol. However, at the experimental conditions ($T = 300 \text{ K}$, $p_{\text{H}_2} = 10^{-10} \text{ atm}$) the free-energy contributions to the final state g make the reaction strongly exergonic: the reaction free energy is -44.8 kJ/mol. This is due to the entropy increase of the hydrogen molecule in the gas phase, which results in the irreversible dissociation of CH_2 , in agreement with the experimental observations. The free-energy

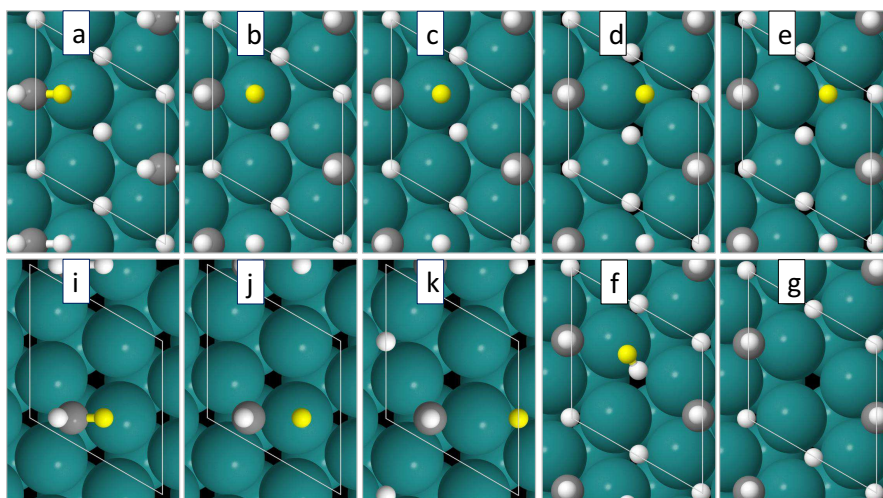


Figure 10.2.: Calculated local-minimum and transition-state structures for CH_2 dissociation. Blue, grey, white and black spheres are ruthenium, carbon, hydrogen, and unfilled sites respectively. The hydrogen atom coming from CH_2 is highlighted in yellow.

barrier is slightly reduced and becomes 88.4 kJ/mol.

10.2. Discussion

Of the two scenarios described above the second one agrees well with the new experimental observations [211]. It also sheds light on previous experimental results. Shimizu and coworkers [54] conducted a combined scanning tunneling microscopy (STM) and GGA-DFT study on hydrogenating C species on Ru(0001). Only one type of species, CH, was observed by the STM, but not CH₂. This was explained by a high calculated energy barrier (~ 60 kJ/mol) for the CH+H \rightarrow CH₂ reaction on Ru(0001), which would prevent the reaction at temperatures up to 300 K. Our results suggest, however, that CH is stabilized not only kinetically, but also thermodynamically, and that CH₂ cannot be formed by hydrogenating C or CH even at higher temperatures.

In summary, based on both the thermodynamics analysis presented in the preceeding chapter and the reaction profile comparison in the present chapter, we conclude that the dissociation of CH₂ at Ru(0001) is kinetically controlled by coadsorbed surface species (in particular hydrogen, but also other species can contribute). On the other hand, hydrogenating CH into CH₂ is thermodynamically prohibited at realistic conditions (see Fig. 10.2). Instead, CH₃ becomes thermodynamically stable at very high pressures of H₂, skipping phases with CH₂ (although a small amount of adsorbed CH₂ can form according to the Boltzmann statistics).

We note that the calculated free-energy barrier for the CH₂ dissociation is slightly higher (by ~ 20 kJ/mol) than the experimentally-derived barrier. This could be due to either uncertainties in experiments or inaccuracy caused by the DFT functional used in the calculations. On the experimental side, the derived barrier relies on the assumption that the signal intensity is a perfectly linear function of the surface coverage. Also, in the experiment the surface is first annealed and then cooled for further SFG measurements. Even though the annealing-cooling procedure is relatively fast, a small number of reactions can take place during the process, effectively lowering the derived barrier value. On the theory side, the approximations in the DFT functional used (PBE+vdw^{surf}) can result in the overestimation of the reaction barrier. We also note that the energy of atomization of a hydrogen molecule is underestimated by most of the conventional functionals and hybrid functionals [212], including the PBE and the HSE06 functionals. The underestimation amount for the PBE functional is calculated to be 0.208 eV (compared to the experimental value of 4.48 eV [212]), in line with the results in the literature [212]. Since in the transition state of the hydrogen formation reaction (Fig. 10.2, panel f) the H-H bond is only 0.03 Å longer than in a hydrogen molecule (0.75 Å) in the gas phase, it is reasonable to guess that the energy of the transition state is slightly overestimated. The exact amount of the overestimation, however, is unknown, and this is the reason why such an effect has not been incorporated in Fig. 10.1 as a correction.

Although in the experiment the disappearance of the CH₂ signal could be detected also at temperatures below 300 K, a clear spectral response of CH was detected only at temperatures above 300 K. This can be understood by considering the calculated signal intensities. The IR intensities of gas-phase CH and CH₂, single adsorbed CH and CH₂, as well as adsorbed CH+3H and CH₂+3H, calculated with the same (2 \times 2) Ru(0001) surface model, are presented in Tab. 10.2. It turns out that the relative intensity of surface species is strongly affected by the coadsorption of hydrogen. The intensity of isolated CH is about 20 times larger than that of CH₂. However, CH+3H has a much weaker (0.3%) IR response compared to CH₂+3H. This explains why CH

Configuration	Sites	Intensity (arb. unit)	Frequencies (cm^{-1})
CH	gas phase	0.98	3031
CH ₂	gas phase	0.01;0.005	3307;3066
CH	hcp	1.02	2994
CH ₂	hcp	0.05;0.00	2975;2073
CH+3H	fcc	0.002	3056
CH ₂ +3H	fcc	0.64;0.47	3017;2598

Table 10.2.: Calculated vibrational frequencies of the stretching modes of CH and CH₂ in the gas phase or adsorbed on Ru(0001), with or without hydrogen coadsorption. For CH₂, the number for the anti-symmetric mode is followed by the symmetric mode frequency.

signal is not observed while CH₂ is stabilized by surrounded hydrogen.

11. C-C coupling and C-chain propagation at high (T, p_{H_2})

The natural gas resources are comparable in quantity with crude oil. Methane typically constitutes more than ninety percent of natural gas [213]. However, due to its stability with respect to hydrogen abstraction, the major usage of methane is currently as fuel [214]. Longer-chain hydrocarbons, either as liquid fuel or basic chemicals, depend heavily on the availability of petroleum instead. For example, the major approach to obtain ethylene in industry is steam cracking of complex hydrocarbons [215]. Ethylene is the most produced organic compound [216] due to its versatile usages in polymer industry and other important chemical processes such as production of ethylene oxide [217] which is a key material in the production of surfactants and detergents. Therefore, it is of high interests to convert methane into ethylene and longer-chain hydrocarbons through carbon coupling reactions. Conventional ways to produce gasoline from methane in industry include converting methane into syngas ($\text{CO} + \text{H}_2$) followed by Fischer-Tropsch synthesis (FTS) [39, 40]. Although FTS has been industrialized since 1920s, its mechanism is still in huge debate [36, 218], where the main controversial aspects include how carbon-oxygen bond is broken, how the carbon chain grows, and which carbon unit is the building block. This lack of understanding prohibits both the rational design of optimal catalysts and process design from the engineering perspective.

The formation of long-chain hydrocarbons in FTS has been intensively studied. However, studies of such a complex reaction network in real catalysis present many challenges. The first big challenge is the structure and active part of the catalysts [219]. Stepped or roughed surfaces have been argued to be the active ones for catalysis due to their unsaturated geometry and electronic structure [209, 220, 219]. However, a recent combined experimental/theoretical study [218] suggests the opposite: such unsaturated sites are actually strongly blocked by reactants and do not play an important role in the catalytic process. This new evidence indicates that modelling stepped or rough surfaces, which is usually more difficult than modelling flat surfaces, is not necessary to understand the FTS mechanism. The second challenging for understanding part of FTS mechanism is how the carbon-oxygen bond is broken. In some proposed mechanisms, carbon-oxygen bond breaks after the carbon-carbon bond formation, while the carbide mechanism suggests that CH_x ($x = 1, 2$) are formed from CO at first, followed by adding CH_x up and hydrogenation in chain propagation. The carbide mechanism was initially proposed by the inventors of the reaction in 1920s [30], and obtained convincing experimental support in 1980s [39, 40]. By replacing the syngas with CH_2N_2 and hydrogen, Brady and Pettit reproduced the carbon chain length distribution in FTS products, suggesting that CH_2 is the basic building block. Furthermore, in experiments with isotope-labelled $\text{C}^{13}\text{O} + \text{C}^{12}\text{H}_2\text{N}_2$, H_2 as input, randomly distributed C^{13} and C^{12} were found in the products. This observation indicates that the origins where CH_x is from is essentially not distinguishable in the chain growth, and further supports the conjecture that the process of formation of CH_x and the carbon-chain propagation

can be considered as decoupled. Assuming such a decoupling allows researches to focus on different parts of the FTS process, either on CO activation and CH_x formation [221, 218] or chain-growth mechanisms [222]. This strategy is indeed adopted by some of prior studies. For instance, Brett and co-workers compared the direct and H-assisted CO activation paths on ruthenium clusters through a combination of DFT calculations and infrared spectroscopy [218]. The chain growth from CH_x taking place on flat Ru(0001), independent of the origin of CH_x , was studied by Ciobîcă and co-workers, while the chain propagation on a series of other transition metal surfaces are studied by Chen and co-workers [220, 223, 224].

Besides FTS, there are other attempts to directly convert methane into longer chain hydrocarbons. Goodmann and his group reported a two-step way [33, 31, 32] to achieve this. In the first step, methane dissociatively adsorbed on ruthenium surface, either flat Ru(0001) or the rough Ru(11 $\bar{2}$ 0) surface. A subsequent increase in the pressure of hydrogen up to 10 Torr leads to formation of ethane and propane in the gas phase. In the first step, CH species were detected, while in the second step CH totally converted to two-carbon (C2) and three-carbon (C3) species. In particular, during the hydrogenation step two distinguishable C2 species were identified in high-resolution electron-energy loss studies: CCH_3 and CCH_2 . Even though chains longer than C3 were not observed possibly due to the dramatic decrease of the population of carbon species at the surface, carbon-carbon coupling reactions in such a hydrogenation process might share similarities with FTS.

Recently, Kirsch and co-workers have studied the formation of C1 and C2 species at the Ru(0001) surface from methane and ethylene dissociation, respectively, using the vibrational SFG [211]. Thanks to the high resolution and surface sensitivity of the technique, four different peaks have been observed. Two of the peaks have been unambiguously assigned to the C-H stretch in CH and CCH_3 , and the third peak have been assigned to the C-H stretch in CCH_2 based on a comparison with previous high-resolution electron energy-loss spectroscopy (HREELS) results [31, 32]. The fourth peak was not previously observed, and have been assigned to the C-H stretch in CCH based on speculative arguments. Although in principle the adsorbed carbon species obtained from different sources, either methane dissociation or ethylene dissociation, should have the same physical and chemical properties, C2 species formed from methane dissociation have been detectable up to higher temperatures than the products of ethylene dissociation. These new observations emphasize the need for understanding the hydrocarbon dissociation/formation process at the atomic level.

In all previous theoretical studies of the C-C coupling reactions on Ru(0001) [222, 220, 223, 224] it was assumed that coadsorption effects on reaction barriers are negligible. However, as described in Chp. 10, we find that the coadsorption of hydrogen increases the barrier for CH_2 dissociation at the Ru(0001) surface at realistic conditions. In this chapter, we report the results of our study of the stability of C1 and C2 species at realistic temperatures and pressures. Also, we calculate reaction paths for the formation and dissociation of C2 species. Our aim in the first part of this chapter is to obtain a unified description and understanding of methane and ethylene dissociation. In the second part, we study the formation of C2 from C1 species and further chain-growth steps at pressures as high as in the industrial FTS catalysis. It is found that at typical FTS temperatures and pressures, the surface is saturated by hydrogen, and the hydrogen coadsorption has a profound influence on the C-C coupling reactions: while it generally reduces all the coupling reaction barriers, some reaction paths become more favoured in the presence of

the coadsorbed hydrogen.

11.1. Formation of C2 under UHV conditions

In this section, the formation of C2 species under UHV conditions is studied. We start from this since our experimental collaborators recently studied the formation of C2 from both methane and ethylene dissociation products [211]. Although there exist some theoretical studies [225, 222] about such carbon-carbon coupling reactions on Ru(0001) surface, several questions arise from previous and recent experiments [32, 211] that cannot be understood based on the reported theoretical studies. The controversies appear in the identification of the intermediate species and the reasons of different thermal stability of C2 products obtained from methane dissociation and ethylene dissociation. Furthermore, strong signal from the ethynylidyne group (CCH₃) has been observed in both methane and ethylene dissociation experiments, but the role of this C2 species has not been analyzed by theory.

Our theoretical study aims to obtain a detailed microscopic understanding of the formation of C2 species from both thermodynamic and kinetic perspectives. By conducting PBE+vdW^{surf} [42, 139] calculations, we studied the adsorption of both C1 species (C, CH, CH₂) and C2 species (CCH, CCH₂, HCCH, CCH₃) with or without coadsorbed hydrogen with the carbon coverage at 1/3 mono-layer (with respect to surface Ru atoms) – a coverage close to that in the experiments [211]. For C2 species, (2×3) slab model is used, while for C1 species, both ($\sqrt{3} \times \sqrt{3}$) and (2×3) slab models are used. The number of Ru layers in the slab is seven, with the topmost two layers fixed during atomic relaxation, in all calculations described here.

11.1.1. Adsorption and thermodynamics

The calculated structures of C1 and C2 adsorbed within the ($\sqrt{3} \times \sqrt{3}$) surface unit cell and (2×3) unit cell are presented in Fig. 11.1 and Fig. 11.2, respectively. We find that single CH, CCH, CCH₂, and CCH₃ species prefer hcp sites over fcc sites by more than 0.2 eV, while isolated hydrogen atoms prefer fcc sites. For higher coverages (around 1 ML), adsorbate species are calculated either all at hcp sites or all at fcc sites (to avoid strong repulsion between species at a pair of nearest hcp-fcc sites), the hcp sites are found being preferred (see Fig. 11.2). To verify that the obtained structures are indeed most stable, about 50 initial geometries for each composition are generated by randomly placing C, CH, and xH ($x = 3-8$), or CCH and xH ($x = 3-8$), per (2×3) unit cell in the vicinity of the Ru surface, and the initial geometries are then relaxed. The results confirm that the most stable CH and CCH_{*x*} structures with coadsorbed hydrogen within the (2×3) surface unit cell can be exhaustively explored using the above rules, so that further global optimization is unnecessary.

Ab initio atomistic thermodynamics is employed to study the thermodynamic stability of possible intermediates in surface reactions involving C1 and C2. The Gibbs free energies of formation for each adsorbed phase as a function of temperature and H₂ partial pressure are calculated according to:

$$\Delta G(T, p_{H_2}) = \frac{2}{x} E_{C_x H_y / \text{slab}} - 2 E_{C / \text{slab}} + \Delta F^{\text{vib}}(T) - \frac{2y}{x} \mu_H(T, p_{H_2}), \quad (11.1)$$

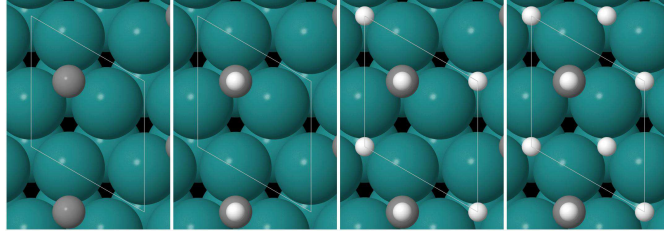


Figure 11.1.: Most stable adsorption configurations for (left to right) C, CH, CH+H, and CH+2H on a $(\sqrt{3} \times \sqrt{3})$ Ru(0001) slab model.

where $x = 1$ for the $(\sqrt{3} \times \sqrt{3})$ model, $x = 2$ for the (2×3) model, $E_{C_xH_y/\text{slab}}$ is the total energy per unit cell for C1 or C2 species with coadsorbed hydrogen, $E_{C/\text{slab}}$ is the total energy per $(\sqrt{3} \times \sqrt{3})$ unit cell for the C atom adsorbed at the hcp site, $\Delta F^{\text{vib}}(T)$ is the vibrational free energy of C_xH_y/slab (see Sec. 2.4.1 and Eq. 9.4), and $\mu_H(T, p_{H_2})$ is the chemical potential of hydrogen calculated via Eq. 9.5. We remind that PBE-DFT underestimates the energy of bonding in H_2 molecule by ~ 0.2 eV. Thus, there is an error of up to ~ 0.1 eV per additional/missing H atom in the relative energies calculated using Eq. 11.1.

The dependence of the free energy on temperature at $p_{H_2} = 10^{-12}$ atm is shown in Fig. 11.3. According to our results, the error due to neglecting the vibrational contribution to the free energy from the surface species can be as large as 0.2 eV per carbon atom at 600 K.

The predicted thermodynamic stability of the C1 and C2 species agrees well with the experimental observations where SFG signals of CH and CCH_3 are apparently stronger than others: CH is thermodynamically stable at higher temperatures, followed directly by CCH_3 at lower temperatures. The stability of CCH_3 at lower temperatures explains the emergence of a CCH_3 signal in both methane (250 K) and ethylene (200 K) dissociation experiments [211, 226]. Although CCH_2 and CCH are only metastable at any temperature, they are within 0.2 eV from the most stable species in a wide range of temperatures. Our *ab initio* thermodynamics results agree with the observation of weak experimental signals assigned to the CCH and CCH_2 species. The possible formation paths of these species are studied in the next subsection.

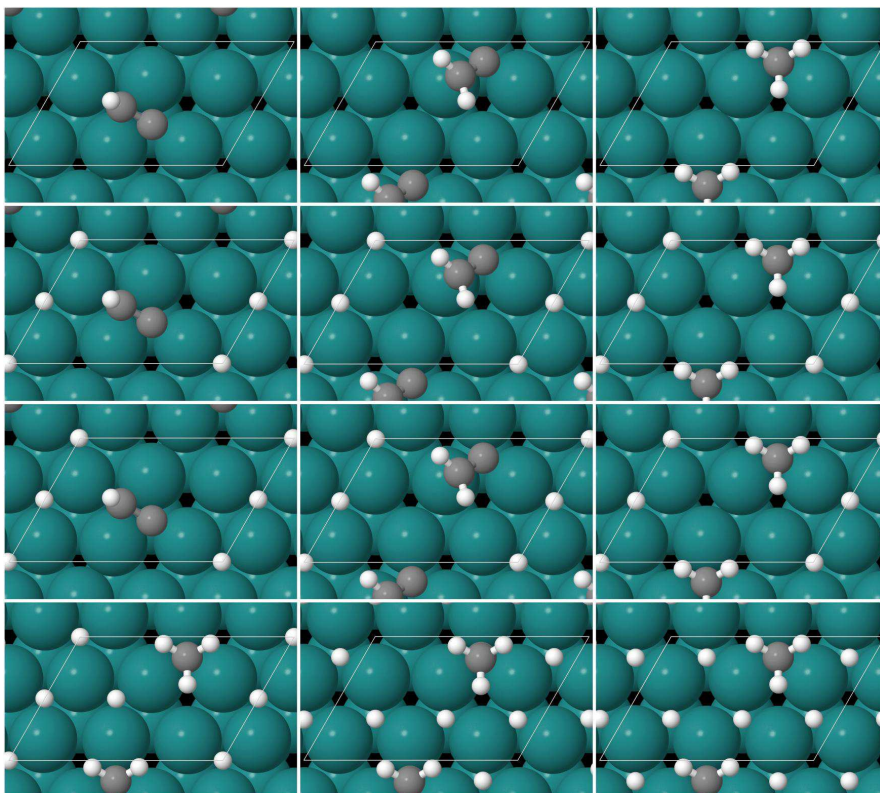


Figure 11.2.: Most stable adsorption configurations of CCH_x ($x = 1, 2, 3$ from left to right, first row), CCH_x+H ($x = 1, 2, 3$ from left to right, second row), CCH_x+2H ($x = 1, 2, 3$ from left to right, third row), CCH_3+yH ($y = 3, 4, 5$ from left to right, fourth row) on a (2×3) Ru(0001) slab model.

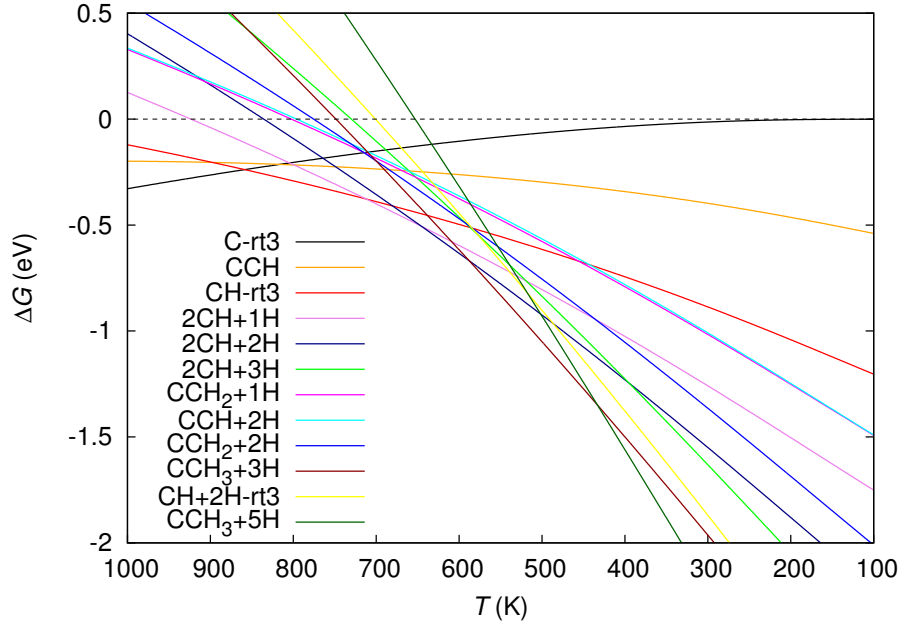


Figure 11.3.: Gibbs free energies of formation of the C1 and C2 adsorbed phases on Ru(0001) surface, calculated using Eq. 11.1, as a function of temperature at H_2 pressure 10^{-12} atm. “rt3” denotes that the $(\sqrt{3} \times \sqrt{3})$ surface unit cell was used to calculate the corresponding formation energy, while the other formation energies were calculated using the (2×3) unit cell. For clarity, only the configurations that have formation energies close to the most stable configurations for each value of $x + y$ are shown. The corresponding atomic structures and PBE-DFT formation energies are presented in Fig. 11.1 and Fig. 11.2.

11.1.2. Formation paths

In the experiments on methane dissociation at Ru(0001) [211], single SFG resonance of CH is observed as temperature is increased to 350 K, while a further increase in temperature leads to the appearance of C2 signals. This observation suggests that C2 species are formed from the C1 species, namely CH. We use the string method [50] to calculate the minimum energy paths (MEPs) and transition states for the coupling of CH species. The barriers and reaction energies for the formation of HCCH, CCH, CCH₂, CCH₃ are summarized in Tab. 11.2. Based on the calculated energy barriers, we conclude that the favoured path for CCH formation is CH+CH→HCCH→CCH+H, and the rate-determining step in this path is the CH coupling step. CCH₂'s favoured formation path includes one more step after the formation of CCH: CCH+H→CCH₂. Likewise, CCH₃ is formed by adding one more hydrogen to CCH₂, with a barrier of 0.48 eV, about half of the CH-CH coupling barrier. Other reaction paths are also calculated. The direct formation of CCH₂ from HCCH is found to have a barrier as high as 2.22 eV, while the direct transformation from CHCH₂ to CCH₃ has a barrier of 1.29 eV, which is 0.7 eV higher than the highest barrier in the indirect path CHCH₂→CCH₂+H→CCH₃.

Reaction	E_a	E_r
CH+CH → HCCH	0.940	0.056
HCCH → CCH+H	0.734	0.201
HCCH → CCH ₂	2.219	0.009
CCH ₂ → CCH+H	0.886	0.193
CCH ₂ +H → CCH ₃	0.574	0.04
CHCH ₂ → CCH ₃	1.287	-0.388
CHCH ₂ → CCH ₂ +H	0.580	0.435

Table 11.1.: Reaction barriers and reaction energies (in eV) for the CCH, CCH₂ and CCH₃ formation reactions, obtained by using a (2×2) model. The ZPE is not included.

11.1.3. Discussions

Above we have analyzed the thermodynamic stability of C2 species, and also the possible reaction paths starting from both methane and ethylene. Our results agree well with the assignments of the observed spectral signals to CH, CCH₃, and CCH₂. However, in addition to the C2 species that have been identified previously based on the experimental observations [32, 211], our results suggest that the HCCH is also likely to be an important intermediate. HCCH could be actually partly responsible for the peak assigned as CCH in the experiment [211]. The intensities of the peaks assigned to CCH and CCH₂ show synchronous changes with increasing annealing temperature [211]. This trend seems to be in contradiction with the fact that, according to our calculations, CCH is preferred over CCH₂ at low chemical potentials of hydrogen. In order to address this issue, we have performed a kinetic Monte Carlo (kMC) simulation for 0.5 ML C2 coverage. The results clearly indicate that CH, CCH₂, and HCCH show the same trend in coverage temperature dependence. However, CCH shows a very different temperature

dependence. In fact, HCCH, which is 0.1 eV less stable than CCH₂, is more likely to be the signal accompanying CCH₂, rather than CCH.

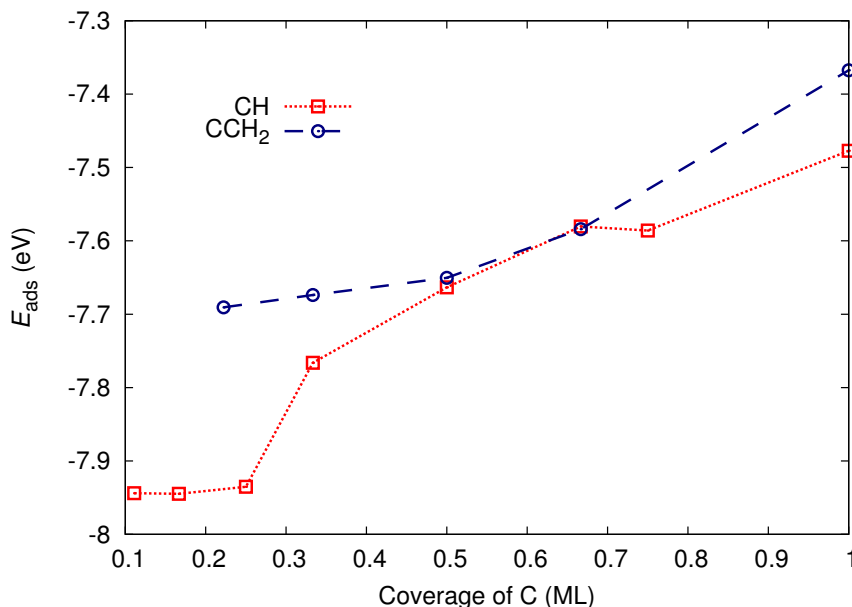


Figure 11.4.: Dependence of adsorption energies ($E_{ads} = E_{C_nH_{2n}/slab} - E_{slab} - nE_{CH} + \Delta^{ZPE}, n = 1,2$) on carbon coverage on Ru(0001). Two species with identical hydrogen-carbon ratio, CH and CCH₂ are compared.

The last unaddressed issue is that the two unresolved peaks lying between CH and CCH₃ signals show significantly higher thermo-stability in methane dissociation than that in ethylene dissociation, in contrast to CH and CCH₃ which have similar thermo-stability in both cases [211]. Since the assignment of CCH₂ is less controversial, CH and CCH₂ are chosen to theoretically study the coverage effects. As can be seen in Fig. 11.4, for C coverage lower than 1/3 ML or close to 1 ML, CH is preferred over CCH₂ by more than 0.1 eV (per molecule), while for an intermediate C coverage (0.5-0.66 ML), CH is only slightly more stable than CCH₂. These results offer an explanation for the above experimental observation: if the methane dissociation leads to an intermediate C coverage, while the C coverage in ethylene dissociation is either in the high or low range, the coverage effects could affect differently the thermal stability of the different species in the two cases.

11.2. C-C coupling at high (T, p_{H_2}) and new insights into chain propagation mechanism of Fischer-Tropsch synthesis

In this section, we adopt a model system to study the formation paths of the C2 and C3 products at FTS temperature and partial pressure of hydrogen. Our model involves merely two elements,

hydrogen and carbon, as in the experiments done in Goodman's group [31, 32, 33], and close to the experiments done by Brady and coworkers [39, 40]. In our calculations, the temperature is set to 500 K, and the pressure of hydrogen is varied in a wide range including 10 atm, which is close to typical FTS conditions. In the following, we first analyze the stability of C1 species, known as monomer in the carbide mechanism, then study the initiation of carbon-chain growth from two C1 species, and finally study the C3 formation as an example of further chain propagation in FTS. New insights into the FTS chain propagation mechanism and the limitations of the current model are discussed in the last part.

11.2.1. C1 species under at high (T, p_{H_2})

As shown in the last chapter, the relative thermodynamic stabilities of CH_x depend on temperature and partial pressure of hydrogen. The typical FTS temperature is about 500 K, and the partial pressure of hydrogen is about 10 atm, far from the conditions under which the species have been probed in UHV (added) studies. Although it has been intensively argued from both experimental and theoretical perspectives that CH is the most abundant C1 species on Ru(0001), based on which FTS mechanisms were proposed, it is still unclear whether CH is the most stable species under realistic FTS conditions.

To answer this question, we calculate Gibbs free energies of formation for CH_{x+y}H ($x + y = 1, \dots, 6$) adsorbed phases on Ru(0001) as a function of hydrogen pressure using Eq. 9.3. The results are presented in Fig. 11.5. Our results suggest that although CH is indeed the most thermodynamically stable species at the FTS pressure and temperature, CH_2 - and CH_3 -containing surface phases have close (within 0.25 eV at $p_{\text{H}_2} = 10$ atm) Gibbs free energies of formation.

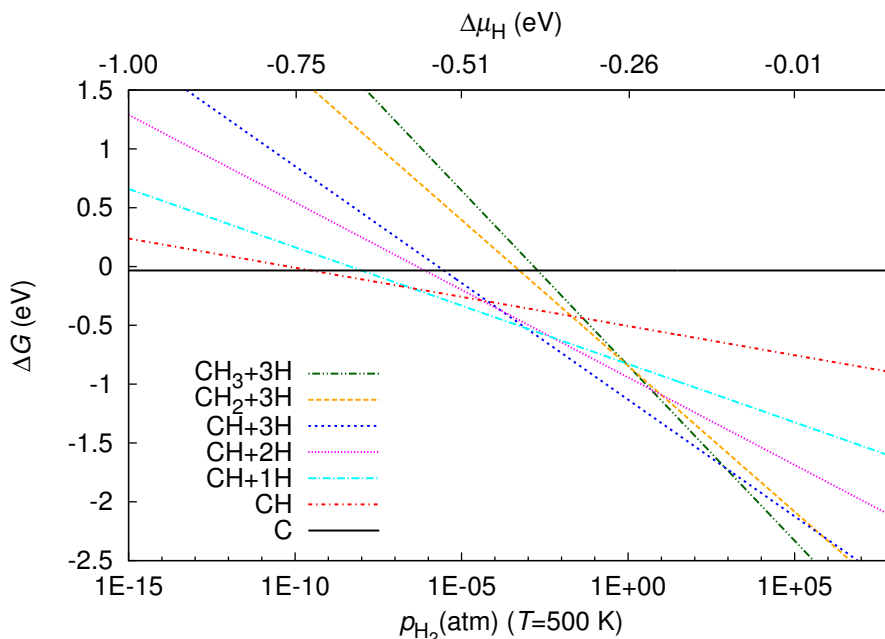


Figure 11.5.: Gibbs free energy of formation for CH_x+yH ($x + y = 0-6$) phases adsorbed on a (2×2) Ru(0001) surface model, calculated using Eq. 9.3 at $T = 500$ K as a function of the hydrogen pressure (and chemical potential defined by Eq. 9.5). For clarity, only the most stable adsorption configuration for each value of $x + y$ is shown. All calculated structures and corresponding energies can be found in Tab. 9.1 and Fig. 9.5-9.10.

11.2.2. C2 fromation from C1-C1 coupling precursors

As discussed in Chp. 9, C1 species on Ru(0001) show competing effects when sharing Ru atoms. Thus, it is reasonable to assume that at studied coverage of C1, most of C1 species do not have another adjacent C1. In principle, the C1 diffusion and hydrogenation/dehydrogenation processes need to be taken into account in a kinetic model. Despite of the extremely complex reaction network, kinetic Monte Carlo simulations with some simplifications have been performed for FTS [34, 35]. To make the model tractable, it was assumed that the reaction barriers and reaction energies of elementary reaction steps can be calculated neglecting coadsorption effects. However, we find that this assumption is in general incorrect. As shown later in this section, coadsorbed species, in particular hydrogen, are able to affect the carbon-carbon coupling reactions so significantly that the most favourable coupling paths are changed. Our reaction barriers and (meta)stable surface structures calculated without resolving to any empirical data can serve as input for future first-principles kinetic modelling.

In our model, hydrogen dissociative adsorption and associative desorption are assumed to have reached the equilibrium with the gas phase at $T = 500$ K. This is reasonable since the dissociative adsorption of hydrogen on Ru(0001) has no significant barrier, the barrier for the associative desorption is about 1 eV, and the diffusion barrier of H atom is less than 0.1 eV.

Furthermore, diffusion of C1 species is assumed to be fast enough so that the amount of *coupling precursors* (see text below) can be approximately determined by their thermodynamic stability at the FTS temperature and pressure. Indeed, the hydrogenation barrier and the diffusion barrier of CH_x ($x = 1-3$) are found to be less than 0.6 eV, lower than C-C coupling barriers reported for Ru(0001) surface previously. Thus, our focus in this section is the influence of coadsorbed hydrogen on C1-C1 coupling reactions.

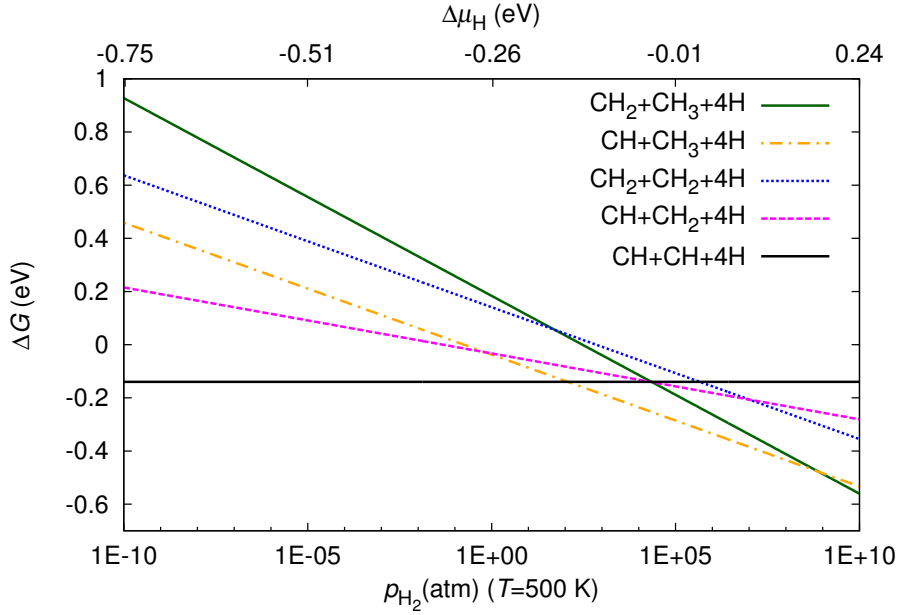


Figure 11.6.: Relative Gibbs free energies of formation for CH_x+CH_y ($x + y = 2-5$) *coupling precursors* coadsorbed with hydrogen atoms on a (2×3) Ru(0001) surface model, calculated using Eq. 11.2 at 500 K as a function of the hydrogen pressure (and chemical potential defined by Eq. 9.5). The corresponding structures can be found in left panels of Fig. 11.7 and Fig. 11.8.

The structures of two C1 species or one C1 species and one growing hydrocarbon chain adsorbed at two adjacent sites are referred to as *coupling precursors*. Geometries of C1-C1 *coupling precursors* can be found in left panels of Fig. 11.7 and Fig. 11.8, and the geometries of C1-chain precursors are presented in left panels of Fig. 11.10 and Fig. 11.11.

The relative free energies of the C1-C1 precursors are calculated using the following formula:

$$\Delta G(T, p_{\text{H}_2}) = E_{(\text{CH}_x+\text{CH}_y+4\text{H})/\text{slab}} + \Delta F^{\text{vib}}(T) - (x + y - 2)\mu_{\text{H}}(T, p_{\text{H}_2}) - E_{(\text{CH}+\text{CH}+4\text{H})/\text{slab}}, \quad (11.2)$$

where the first and last terms are the total energies of surface species adsorbed on the (2×3) Ru(0001) model, $\Delta F^{\text{vib}}(T)$ is the vibrational free energy contribution, and $\mu_{\text{H}}(T, p_{\text{H}_2})$ is the chemical potential of hydrogen calculated using Eq. 9.5. Since the adsorption of $\text{CH}+\text{CH}+4\text{H}$ at 0 K is taken as the reference state, the "CH+CH+4H" line shown in Fig. 11.6 deviates from the zero line. As expected, increasing the pressure of hydrogen leads to increasing the number of

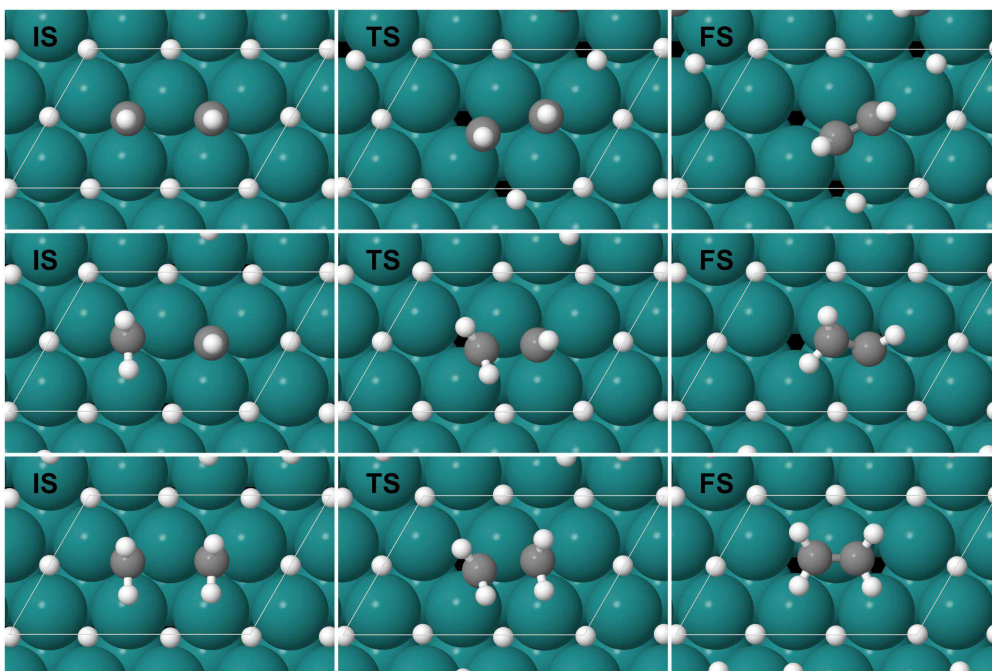


Figure 11.7.: Initial states (IS) (left panels), transition states (TS) (middle panels), and final states (FS) (right panels) of CH+CH (top), CH₂+CH (middle), and CH₂+CH₂ (bottom) coupling reactions in the presence of coadsorbed hydrogen.

hydrogen atoms in the *coupling precursors*. In particular, CH₃+CH is only 0.05 eV less stable than CH+CH at $p_{\text{H}_2} = 10$ atm, and in general the relative stability of all the considered *coupling precursors* have free energies within 0.4 eV under the FTS conditions. Such a close range of stability indicates that one cannot simply assume that CH is the dominating coupling carbon block based on its stability at low pressures.

As the next step, we calculate the barriers for the coupling of the precursors. The structures of the transition states and final states can be found in the middle and right panels, respectively, of Fig. 11.7 and 11.8. The corresponding PBE+vdW^{surf} reaction barriers and reaction energies (defined according to Eq. 10.1 and Eq. 10.2; ZPE correction is not included) are presented in Tab. 11.2. Different from previous theoretical barrier calculations [41, 227] that did not take into account the effects of hydrogen coadsorption, CH+CH is found to have the highest coupling barrier (1.03 eV) among C1-C1 precursors, 0.33 eV higher than CH₂+CH₃ and 0.35 eV higher than CH₂+CH₂ coupling barriers. For comparison, the CH_{*x*}+CH_{*y*} coupling reactions without coadsorbed hydrogen are also calculated. The DFT reaction barriers and reaction energies are presented in Tab. 11.3. A comparison of Tab. 11.2 and Tab. 11.3 reveals that the coadsorption of hydrogen in general decreases the coupling reaction barriers, thus accelerating all the calculated coupling reactions. Reaction energies are also decreased (towards more endothermic). Moreover, we find that the influence of the coadsorption increases with increasing $x + y$ in CH_{*x*}+CH_{*y*}. For instance, the coupling reaction barrier of CH+CH is decreased by 0.013 eV by coadsorption

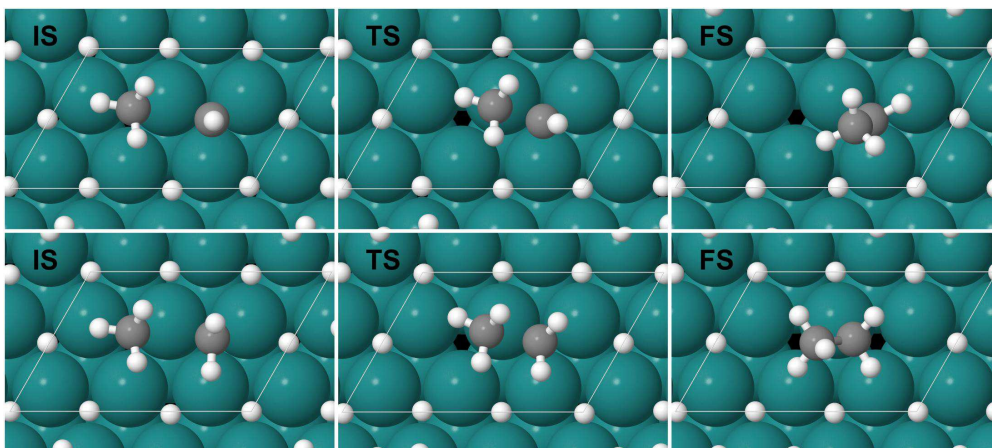


Figure 11.8.: Initial states (IS) (left panels), transition states (TS) (middle panels), and final states (FS) (right panels) of $\text{CH}+\text{CH}_3$ (top) and CH_2+CH_3 (bottom) coupling reactions in the presence of coadsorbed hydrogen.

Reaction	E_a	E_r
$\text{CH}+\text{CH} \longrightarrow \text{HCCH}$	1.029	0.281
$\text{CH}+\text{CH}_2 \longrightarrow \text{CHCH}_2$	0.722	-0.127
$\text{CH}_2+\text{CH}_2 \longrightarrow \text{CH}_2\text{CH}_2$	0.681	-0.523
$\text{CH}+\text{CH}_3 \longrightarrow \text{CHCH}_3$	0.741	-0.298
$\text{CH}_2+\text{CH}_3 \longrightarrow \text{CH}_2\text{CH}_3$	0.695	-0.530

Table 11.2.: Reaction barriers and energies (in eV) for the C1-C1 coupling reactions *in the presence* of coadsorbed hydrogen atoms. The geometries of initial states, transition states, and final states are presented in Fig. 11.7 and Fig. 11.8.

of hydrogen while the reaction barrier of CH_2+CH_3 is decreased by 0.277 eV. Corresponding to the barrier changes, it is also not surprising to find that reaction energy changes more to exothermic for reactions with larger $x + y$ values.

Reaction	E_a	E_r
$\text{CH}+\text{CH} \rightarrow \text{HCCH}$	1.006	-0.068
$\text{CH}_2+\text{CH}_2 \rightarrow \text{CH}_2\text{CH}_2$	0.824	-0.195
$\text{CH}+\text{CH}_3 \rightarrow \text{CHCH}_3$	1.152	0.170
$\text{CH}_2+\text{CH}_3 \rightarrow \text{CH}_2\text{CH}_3$	1.072	0.490

Table 11.3.: Reaction barriers and energies (in eV) for the C1-C1 coupling reactions *without* coadsorbed hydrogen atoms.

11.2.3. Carbon chain growth mechanisms on Ru(0001) at high (T, p_{H_2})

While coupling of two C1 species is the chain initiation step in carbide mechanism, the coupling between C1 and C2 species can be considered as a general representation of chain growth. Similar to the C1-C1 precursors, we study the thermodynamic stability of the C1-C2 *coupling precursors* and the coupling barriers. The geometries of the precursors are shown in Fig. 11.10 and Fig. 11.11, left panels.

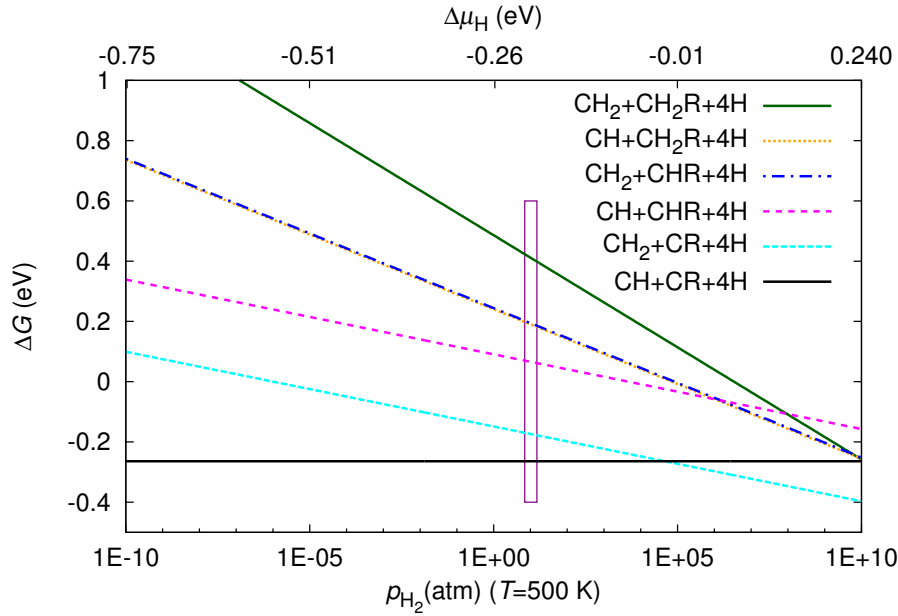


Figure 11.9.: Relative Gibbs free energies of formation for $\text{CH}_x+\text{CH}_y\text{R}$ ($x+y=2-5$; $\text{R}=\text{CH}_3$) *coupling precursors* coadsorbed with hydrogen atoms on a (2×3) Ru(0001) surface model, calculated using Eq. 11.3 at 500 K as a function of the hydrogen pressure (and chemical potential defined by Eq. 9.5). The corresponding structures can be found in left panels of Fig. 11.10 and Fig. 11.11. The purple rectangle denotes typical FTS pressure of hydrogen.

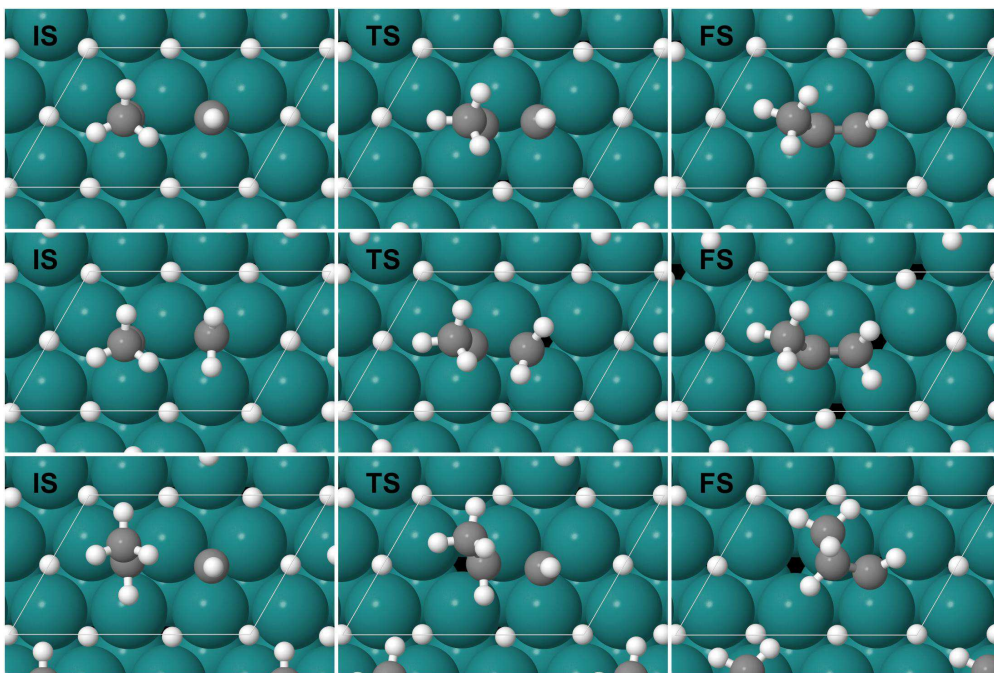


Figure 11.10.: Initial states (IS), transition states (TS) and final states (FS) of $\text{CH} + \text{CCH}_3$ (top), $\text{CH}_2 + \text{CCH}_3$ (middle), and $\text{CH} + \text{CHCH}_3$ (bottom) coupling precursors with coadsorbed hydrogen atoms.

The relative Gibbs free energies of formation C1-C2 precursors are calculated as follows:

$$\Delta G(T, p_{\text{H}_2}) = E_{(\text{CH}_x + \text{CH}_y\text{R} + 4\text{H})/\text{slab}} + \Delta F^{\text{vib}}(T) - (x + y - 2)\mu_{\text{H}}(T, p_{\text{H}_2}) - E_{(\text{CH} + \text{CR} + 4\text{H})/\text{slab}}, \quad (11.3)$$

where the first and last terms are the total energies of surface species adsorbed on the (2×3) Ru(0001) model, $\text{R} = \text{CH}_3$ to represent the saturated end of hydrocarbon intermediates in FTS process, $\Delta F^{\text{vib}}(T)$ is the vibrational free energy contribution, and $\mu_{\text{H}}(T, p_{\text{H}_2})$ is the chemical potential of hydrogen calculated via Eq. 9.5. The formation energies (referenced to $\text{CH} + \text{CR}$ at 0 K) as a function of hydrogen pressure at $T = 500$ K are shown in Fig. 11.9.

The results show that $\text{CH}_2 + \text{CR}$ intermediates are almost as easily accessible thermodynamically under FTS conditions as $\text{CH} + \text{CR}$, since the latter is only 0.07 eV more stable at these conditions. In general, all the studied *coupling precursors* are within a 0.6 eV range of $\text{CH} + \text{CR}$.

The PBE+vdW^{surf} barriers for the coupling of the C1-C2 precursors are summarized shown in Tab. 11.4. The geometries of the transition states and final states are shown in the middle and right panels, respectively, of Fig. 11.10 and Fig. 11.11. Since CH_3 and H groups have roughly similar chemical properties in hydrocarbon chemistry, it is not surprising to find that the coupling reaction $\text{CH} + \text{CR} \rightarrow \text{CHCR}$ has the highest barrier, while $\text{CH}_2 + \text{CH}_2\text{R} \rightarrow \text{CH}_2\text{CH}_2\text{R}$ has the lowest barrier, similar to $\text{CH} + \text{CH}$ and $\text{CH}_2 + \text{CH}_3$ couplings. The barrier for the $\text{CH}_2 + \text{CR}$ coupling reaction is 0.14 eV lower than for $\text{CH} + \text{CR}$, with the free-energy difference between the

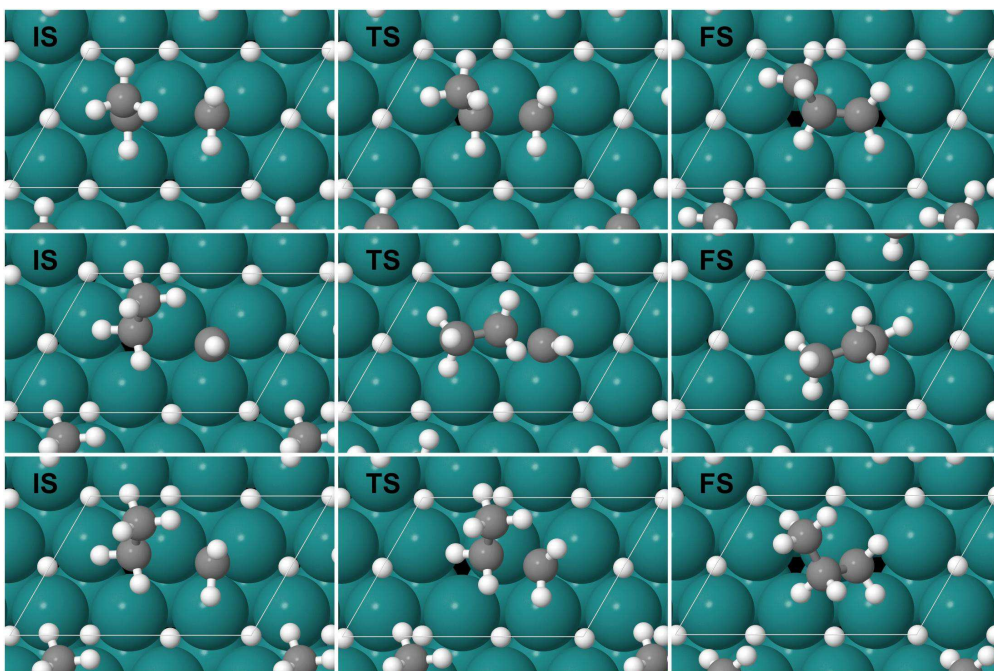


Figure 11.11.: Initial states (IS), transition states (TS) and final states (FS) of $\text{CH}_2+\text{CHCH}_3$ (top), $\text{CH}+\text{CH}_2\text{CH}_3$ (middle), and $\text{CH}_2+\text{CH}_2\text{CH}_3$ (bottom) coupling precursors with coadsorbed hydrogen atoms.

two precursors being less than 0.1 eV under the FTS conditions. In contrast to C1+C1 coupling reactions, the coupling of CH_2R , a counterpart of the CH_3 group, to CH_2 is significantly favored over the coupling to CH , which is indicated by the barrier difference of 0.46 eV. This can be understood from an analysis of the corresponding reaction paths (Fig. 11.11, middle and bottom panels). The path for the $\text{CH}_2+\text{CH}_2\text{R}$ coupling process looks similar to CH_2+CH_3 , but the coupling of CH and CH_2R involves a transformation as the first step, and only then the coupling with the CH group. We have checked carefully that for the other possible paths of the $\text{CH}+\text{CH}_2\text{R}$ coupling reaction the same transition state is always found.

We have shown that the coadsorption of hydrogen significantly changes the C-C coupling barriers. CH_2+CH_3 , as well as $\text{CH}_2+\text{CH}_2\text{R}$, have the lowest reaction barriers among C1+C1 and C1+C2 reactions, respectively. However, the information on the reaction barriers is not in general sufficient to identify the fastest reaction, since a reaction rate depends also on the concentrations of the reactants. The concentration effects can be roughly accounted for with a Boltzmann exponential factor containing the free energy of formation for the initial state [228]:

$$r_{\text{coupling}} \propto E \frac{-\left(\Delta G(T, p_{\text{H}_2}) + E_a\right)}{k_{\text{B}} T} \quad (11.4)$$

The $\Delta G(T, p_{\text{H}_2}) + E_a$ values at FTS conditions are listed in Tab. 11.4. According to this estimate, CH_2+CR coupling is the most favourable path. However, we note that there are additional

11.2. C-C coupling at high (T, p_{H_2}) and new insights into chain propagation mechanism of Fischer-Tropsch synthesis

Reaction	E_a	E_r	$\Delta G(500\text{K}, 10 \text{ atm}) + E_a$
$\text{CH}+\text{CR} \longrightarrow \text{CHCR}$	1.119	0.180	0.855
$\text{CH}_2+\text{CR} \longrightarrow \text{CH}_2\text{CR}$	0.982	0.160	0.832
$\text{CH}+\text{CHR} \longrightarrow \text{CHCHR}$	0.910	-0.160	1.000
$\text{CH}_2+\text{CHR} \longrightarrow \text{CH}_2\text{CHR}$	0.805	-0.420	1.047
$\text{CH}+\text{CH}_2\text{R} \longrightarrow \text{CHCH}_2\text{R}$	1.079	-0.382	1.317
$\text{CH}_2+\text{CH}_2\text{R} \longrightarrow \text{CH}_2\text{CH}_2\text{R}$	0.624	-0.598	1.108

Table 11.4.: Reaction barriers and energies (in eV) for $\text{CH}_x+\text{CH}_y\text{R}$ ($x + y = 2-5$; $\text{R}=\text{CH}_3$) coupling reactions in the presence of coadsorbed hydrogen. The sum of the reaction barrier and the initial-state free energy of formation ΔG at typical FTS conditions is also shown (see text). The geometries of initial states, transition states, and final states are presented in Fig. 11.10 and Fig. 11.11.

kinetic factors that can influence the reaction rate. For instance, the product of the $\text{CH}_2+\text{CH}_2\text{R}$ coupling reaction is at the same time an initial state ready for the next coupling with CH_2 , while the product of CH_2+CR needs dehydrogenation of the α -carbon and hydrogenation of the β -carbon, with the latter having generally a higher barrier. In summary, the entire chain-growth cycles need to be studied before a clear conclusion on the growth mechanism can be made.

Part IV.

Concluding remarks

12. Conclusions and outlook

12.1. Concluding remarks

In this thesis, the effects of adsorbate-adsorbate interactions have been studied using first-principles simulations for two distinct types of adsorbate/solid-surface systems: water adsorption on alkaline-earth metal oxides, and hydrocarbon adsorption and reactions on the Ru(0001) surface. In both cases we find that the equilibrium structure of the surface with adsorbates is affected by the adsorbate-adsorbate interactions. Moreover, the co-adsorption is found to have a strong effect on the surface chemistry of hydrocarbons at Ru(0001). Using these two examples, we have illustrated the challenges in modelling adsorbate-adsorbate interactions at gas-solid interfaces, explored the ways to meet the challenges, and obtained deeper understanding of the mechanisms of surface phenomena, which are currently not resolvable in state-of-the-art experiments.

The difficulties in accurately accounting for the adsorbate-adsorbate interactions are the following. First, adsorbate-adsorbate interactions increase the dimensionality of the configurational space, since there can be a large number (i.e., thousands or more) of local minima for a given composition, in contrast to the case of an isolated adsorbate, when only a couple of distinct configurations on a flat surface exist. Thus, an efficient way of exploring the configurational space is needed. Moreover, conventional DFT functionals (e.g., PBE or HSE06) do not describe the long-range part of the dispersion interaction correctly, which can lead to erroneous predictions of adsorbate structures. Furthermore, the self-interaction error in local and semilocal functionals leads to an incorrect description of the electron localization and transfer, in particular in oxides. Hybrid functionals, which include a part of the exact exchange, can be used to significantly reduce the self-interaction error. Last but not the least, the effects of finite temperature and pressure on the surface properties have to be taken into account to predict observables at realistic conditions, which can be compared with experimental measurements. In this thesis, a first-principles genetic algorithm is implemented to search for low-energy structures of a gas/solid interface. The hybrid functional HSE06 [43, 116] is used with many-body van der Waals interaction correction [134, 45] to calculate the ground state energy of the water/oxide structures. PBE+vdW^{surf} [139] is used for hydrocarbon adsorption and reaction on Ru(0001). *Ab initio* atomistic thermodynamics [78, 51, 52, 53] analysis is conducted to bridge the total energy results at 0 K with to finite temperatures and pressures.

To find the global minimum structure of adsorbates on a substrate, we have implemented an efficient genetic algorithm. Even though only first-principle calculations are used in the PhD work, force-field can be easily adopted to optimize targeted properties. By distributing the time-consuming local optimization to subdirectories, parallelization higher than 99% is achieved. The important factors that strongly influence the efficiency of the algorithm, such as purging similar structures to keep the diversity of the population, and proper mutations, are analysed and optimized.

Using our genetic algorithm [229], the structures of water adsorbed on alkaline-earth metal-oxide surfaces (MgO(001), CaO(001) and SrO(001)) have been studied. It is not surprising that water-water and water-oxide interactions enable a very high diversity of structures. In particular, 1D structures are found on MgO(001) and CaO(001), while the SrO's large lattice parameter destabilizes the hydrogen bonds on the surface and hinder the formation of 1D structures. Furthermore, our *ab initio* atomistic thermodynamics analysis suggests that 1D structures found on CaO(001) are thermodynamically stable at experimental conditions [1], while on MgO(001) 2D structures dominate. The vibrational spectra of 1D structures are calculated via both the harmonic approximation and the *ab initio* molecular dynamics. All our results about water at oxide surfaces are in line with recent and previous experimental observations [1]. The breaking of symmetry and the formation of 1D structures are carefully analysed, and the stability of the 1D water structures on CaO(001) at realistic temperatures and water vapor pressures is attributed to the moderate lattice constant of CaO.

We have also found that hydrogen coadsorption plays an important (critical in some cases) role in hydrocarbon chemistry on Ru(0001) surface, which is a typical model for realistic catalysts. In accordance with a recent observation that CH₂ is stabilized up to ~ 300 K in methane dissociation experiments [2], our calculations show that CH₂'s dissociation can be hindered by coadsorbed hydrogen atoms, although thermodynamically CH is still the most favourable C1 species at experimental conditions [2]. The combination of theory and experiment suggests for the first time a microscopic picture of how CH₂ dissociates at realistic temperatures and hydrogen pressures in the presence of coadsorbed hydrogen. As a further step, the formation of C2 hydrocarbon species is studied at low coverage of hydrogen which corresponds to high-temperature and low-pressure experiments, as well as at high coverage of hydrogen which mimics the Fisher-Tropsch synthesis conditions. For the former, reaction paths for possible C2 and C3 species are proposed while for the latter CH₂ is found to be a stable intermediate in the carbon-chain propagation steps, in contrast with previous theoretical work where coadsorption and other finite-pressure/temperature effects are neglected. Further studies are needed to identify the exact role of CH₂ in the chain growth mechanism of Fisher-Tropsch synthesis.

In summary, adsorbate-adsorbate interactions in two representative cases, water on oxide surfaces and hydrocarbon species on a metal surface, are found to play a critical role in determining the adsorbate structure and adsorption energetics, as well as chemical reactions of the adsorbates. A efficient genetic algorithm has been implemented to search for low-energy structures of a gas/solid interface.

12.2. Outlook

Based on the obtained results, and using the developed methodology, studies of CaO thin films on Mo(001) surface and the carbon-chain growth mechanism in Fischer-Tropsch synthesis can be performed. It is known that Mo atoms from the substrate can enter the CaO film, and, if the film is thin (< 10 layers), form a mixed Mo/CaO phase with a crystal structure different from pure CaO. Previous studies concentrated on a specific cubic structure of a MoCa₃O₄ thin film on Mo(001) [230]. However, preliminary calculations using the developed first-principles genetic algorithm revealed that the previously assumed structure may not be the most stable one.

According to our preliminary results, the model structure in the literature is >2.0 eV less stable (according to HSE06) than the most stable structure that we found with genetic algorithm. We also note that conventional genetic algorithm works for a fixed composition while in this case the composition of the thin film is not known. Thus, it is necessary to scan various compositions, for instance, by changing the number of oxygen atoms and molybdenum atoms. Regarding this problem, we are testing a new way of running genetic algorithm: allow the composition to change and optimize directly the Gibbs free energy at the experimental conditions. To obtain a deeper understanding of the role of CH_2 in FTS chain-growth mechanism, more work also needs to be done, for instance, the formation paths of C_3 alkane or olefin products must be studied.

Appendices

A. Convergence tests for basis sets and thickness of the oxide slab model

The default basis settings [231] are categorized as *light*, *tight*, and *really-tight*, with increasing number of basis functions per atom and tighter numerical settings (denser grids, longer confining potential cutoff, and larger maximum angular momentum for the multipole expansion of the electron density). In the default *tight* settings, the basis set level is set to tier 2 for the light elements 1-10, a modified tier 1 for the slightly heavier Al, Si, P, S, Cl, and tier 1 for all other elements.

The convergence tests for basis set size (Fig. A.1) and thickness of oxide slab models (Fig. A.2) are presented for MgO(001), CaO(001), and SrO(001). Both tests show that the default *tight* basis sets and the thickness of the slab model used in the thesis ensure that the adsorption energy is converged to within 0.005 eV for all DFT functionals.

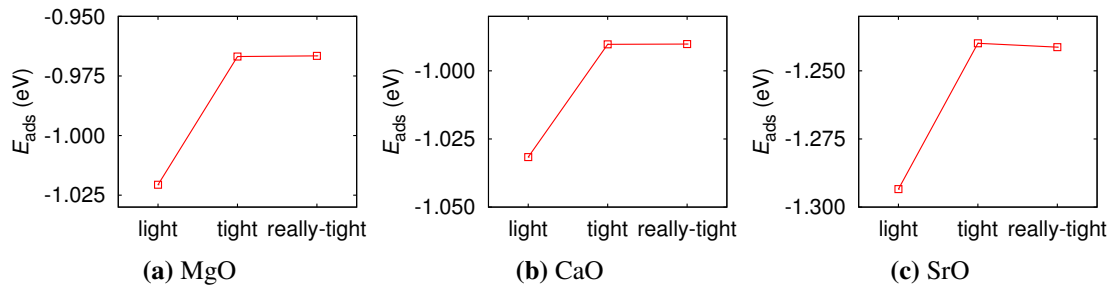


Figure A.1.: Convergence of water adsorption energies with the size of the basis sets for MgO(001), CaO(001), and SrO(001). The “light”, “tight”, and “really-tight” labels correspond to the three default levels for the basis set size and numerical settings in the FHI-aims program package. Four-layer models and PBE functional are used in the test. E_{ads} is defined as $E_{\text{ads}} = \frac{1}{n}(E_{n\text{H}_2\text{O}/\text{slab}} - E_{\text{slab}} - nE_{\text{H}_2\text{O}})$ where n is 6, 5, and 2 for MgO(001), CaO(001), and SrO(001), respectively, corresponding to a 2D structure on MgO, a 1D structure on CaO, and the water dimer on SrO.

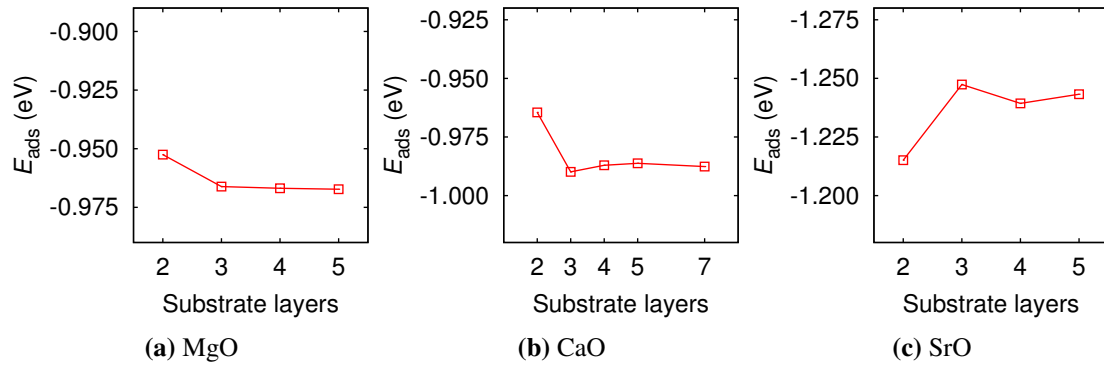


Figure A.2.: Convergence of adsorption energies with the number of layers in the slab models for MgO(001), CaO(001), and SrO(001). PBE functional and default *tight* basis sets and numerical settings are used in the test. E_{ads} is defined as $E_{\text{ads}} = \frac{1}{n}(E_{n\text{H}_2\text{O}/\text{slab}} - E_{\text{slab}} - nE_{\text{H}_2\text{O}})$, where n is 6, 5, and 2 for MgO(001), CaO(001), and SrO(001), respectively, corresponding to a 2D structure on MgO, a 1D structure on CaO, and the water dimer on SrO.

B. FHI-aims standard NAO basis sets for H, C, O, Mg, Ca, Sr, and Ru.

The standard NAO basis sets in FHI-aims are obtained by converging the binding energies of dimers for each element. The strategy starts with defining a large pool of possible radial function shapes with a variable confinement potential (Eq. 4.6) and choosing the minimal basis for the free atoms. The next step is to go over the functions in the pool and add the function that lowers the most the LDA total energy of the dimer to the initial basis set. Such process is repeated until there are no more significant improvements in the total energy.

The basis sets obtained in the above way are shown in Tab. B.1 for hydrogen, carbon, oxygen and magnesium, and Tab. B.2 for calcium, strontium and ruthenium. Two types of function are used: the hydrogen-like functions with effective ionic charge of Z , labeled as "hydro", and the ionic functions obtained by solving the radial Schrödinger equation for the doubly positively charged ion of the corresponding element. For instance, "hydro 2 p 1.8" denotes hydrogen-like function of the 2p type with an effective charge of 1.8, while "ionic 3 d auto" in the Mg basis set represents a 3d function of the Mg^{2+} ion.

	H	C	O	Mg
<i>minimal</i>	1s	[He]+2s2p	[He]+2s2p	[Ne]+3s2p
<i>tier 1</i>	hydro 2 s 2.1 hydro 2 p 3.5	hydro 2 p 1.7 hydro 3 d 6 hydro 2 s 4.9	hydro 2 p 1.8 hydro 3 d 7.6 hydro 3 s 6.4	hydro 2 p 1.5 ionic 3 d auto hydro 3 s 2.4
<i>tier 2</i>	hydro 1 s 0.85 hydro 2 p 3.7 hydro 2 s 1.2 hydro 3 d 7	hydro 4 f 9.8 hydro 3 p 5.2 hydro 3 s 4.3 hydro 5 g 14.4 hydro 3d 6.2	hydro 4 f 11.6 hydro 3 p 6.2 hydro 3 d 5.6 hydro 5 g 17.6 hydro 1 s 0.75	hydro 4 f 4.3 hydro 2 p 3.4 hydro 4 s 11.2 hydro 3 d 6.2
<i>tier 3</i>	hydro 4 f 11.2 hydro 3 p 4.8 hydro 4 d 9 hydro 3 s 3.2	hydro 2 p 5.6 hydro 2 s 1.4 hydro 3 d 4.9 hydro 4 f 11.2	ionic 2 p auto hydro 4 f 10.8 hydro 4 d 4.7 hydro 2 s 6.8	hydro 2 s 0.6 hydro 3 p 4.8 hydro 4 f 7.4 hydro 5 g 6.6 hydro 2 p 1.6 hydro 3 d 1.8
<i>tier 4</i>			hydro 2 p 2.1 hydro 5 g 16.4 hydro 4 d 13.2 hydro 3 s 13.6 hydro 4 f 16.7	hydro 4 p 0.45 hydro 5 g 10.4 hydro 2 s 12.4 hydro 4 d 1.7

Table B.1.: Standard numerical atom-centered orbital basis sets for hydrogen, carbon, oxygen, and magnesium, as distributed with the FHI-aims [143] package. The minimal basis consists of free-atom radial functions (notation: [noble gas configuration] + additional valence functions).

	Ca	Sr	Ru
<i>minimal</i>	[Ar]+4s3p	[Kr]+5s4p3d	[Kr]+5s4p4d
<i>tier 1</i>	ionic 3 d auto ionic 4 p auto hydro 3 d 2.3 hydro 4 f 4.8 ionic 4 s auto	ionic 4 d auto ionic 5 p auto hydro 4 f 5.6 ionic 5 s auto	hydro 4 f 8.8 ionic 4 d auto ionic 5 p auto hydro 5 g 12.4 hydro 3 s 2.4
<i>tier 2</i>	hydro 5 g 6.8 hydro 3 p 3.8 hydro 6 h 10.4 hydro 1 s 0.55 hydro 5 f 9.2 hydro 5 p 3.3 hydro 4 d 5	hydro 5 g 7.4 hydro 4 d 4.4 hydro 3 p 3.3 hydro 6 h 10.4 hydro 5 s 4.9 hydro 5 f 13.2	hydro 4 f 20 hydro 6 h 16.8 hydro 5 f 8.6 hydro 5 g 8 hydro 4 d 8 hydro 4 p 5.4 hydro 5 s 8.8
<i>tier 3</i>	hydro 5 p 5.4 hydro 5 f 5 hydro 5 s 4.6 hydro 2 p 4.2 hydro 5 g 9.8 hydro 4 d 5.2	hydro 6 p 4.8 hydro 5 f 6 hydro 2 p 1.2 hydro 1 s 0.55 hydro 5 d 3.6	hydro 6 h 12.4 hydro 5 f 38.4 hydro 3 d 2.6 hydro 5 p 10.4 hydro 4 s 3.7
<i>tier 4</i>		hydro 5 p 5.2 hydro 4 f 14.8 hydro 5 g 7.6 hydro 4 p 4.5 hydro 5 d 5.4 hydro 6 s 6.8	hydro 5 d 13.6 hydro 5 f 14 hydro 5 g 11.2 hydro 2 p 1.7 hydro 4 s 5.6

Table B.2.: Standard numerical atom-centered orbital basis sets for calcium, strontium, and ruthenium, as distributed with the FHI-aims [143] package. The minimal basis consists of free-atom radial functions (notation: [noble gas configuration] + additional valence functions).

C. vdW parameters

HSE06 functional with the many-body dispersion correction is used to calculate final DFT energies in the water/oxide project. The long-range correlation that are missing in HSE06 functional is taken into account by solving the self-consistent screening equation of classical electrodynamics as suggested by Tkatchenko and coworkers [45]. The TDDFT-based atom-in-solid reference polarizabilities, as discussed by Zhang *et al.* [232], are listed for MgO and CaO in the following table:

parameter	O-in-MgO	Mg-in-MgO	O-in-CaO	Ca-in-CaO
C_6^b (in hartree · bohr ⁶)	2.22	38.6	1.667	15.6
α^b (in bohr ³)	2.19	9.16	2.146	5.4
R^b (in bohr)	2.36	2.15	2.345	2.229
parameter	O atom	H atom		
C_6^{free} (in hartree · bohr ⁶)	15.6	6.5		
α^{free} (in bohr ³)	5.4	4.50		
R^{free} (in bohr)	3.19	3.10		

Table C.1.: Screened van der Waals parameters for atom-in-solid are presented in the first half (top) of the table, while van der Waals parameters for free atoms are shown in the second half (bottom) of the table.

For adsorption on Ru(0001) surface, the vdW^{surf} method is used and the screened van der Waals parameters are obtained in the way described in Ref. [139]. The values for ruthenium surface are $C_6^b = 54.63$ hartree · bohr⁶, $\alpha^b = 13.77$ bohr³ and $R^b = 2.37$ bohr.

Bibliography

- [1] X. Zhao, X. Shao, Y. Fujimori, S. Bhattacharya, L. M. Ghiringhelli, H.-J. Freund, M. Sterrer, N. Nilius, and S. V. Levchenko, "Formation of water chains on CaO (001): What drives the 1D growth?," *The Journal of Physical Chemistry Letters*, vol. 6, no. 7, pp. 1204–1208, 2015.
- [2] H. Kirsch, X. Zhao, Z. Ren, S. V. Levchenko, M. Wolf, and R. K. Campen, "Controlling CH₂ dissociation on Ru (0001) through surface site blocking by adsorbed hydrogen," *Journal of catalysis*, vol. 320, pp. 89–96, 2014.
- [3] W. S. Epling, L. E. Campbell, A. Yezerets, N. W. Currier, and J. E. Parks, "Overview of the fundamental reactions and degradation mechanisms of NO_x storage/reduction catalysts," *Catalysis Reviews*, vol. 46, no. 2, pp. 163–245, 2004.
- [4] M. Votsmeier, T. Kreuzer, and G. Lepperhoff, "Automobile exhaust control," *Ullmann's Encyclopedia of Industrial Chemistry*, 2009.
- [5] X. Zhou, J. Liu, C. Wang, P. Sun, X. Hu, X. Li, K. Shimanoe, N. Yamazoe, and G. Lu, "Highly sensitive acetone gas sensor based on porous ZnFe₂O₄ nanospheres," *Sensors and Actuators B: Chemical*, vol. 206, pp. 577–583, 2015.
- [6] L. Wang, Y. Kang, X. Liu, S. Zhang, W. Huang, and S. Wang, "ZnO nanorod gas sensor for ethanol detection," *Sensors and Actuators B: Chemical*, vol. 162, no. 1, pp. 237–243, 2012.
- [7] H. J. Yoon, J. H. Yang, Z. Zhou, S. S. Yang, M. M.-C. Cheng, *et al.*, "Carbon dioxide gas sensor using a graphene sheet," *Sensors and Actuators B: Chemical*, vol. 157, no. 1, pp. 310–313, 2011.
- [8] G. Ertl, H. Knözinger, and J. Weitkamp, "Handbook of heterogeneous catalysis," 1997.
- [9] H. Knözinger and K. Kochloefl, "Heterogeneous catalysis and solid catalysts," *Ullmann's Encyclopedia of Industrial Chemistry*, 2002.
- [10] Y. Yao, Q. Fu, Y. Zhang, X. Weng, H. Li, M. Chen, L. Jin, A. Dong, R. Mu, P. Jiang, *et al.*, "Graphene cover-promoted metal-catalyzed reactions," *Proceedings of the National Academy of Sciences*, vol. 111, no. 48, pp. 17023–17028, 2014.
- [11] V. Smil, *Enriching the earth: Fritz Haber, Carl Bosch, and the transformation of world food production*. 2004.
- [12] S. Matar and L. F. Hatch, *Chemistry of petrochemical processes*. Gulf Professional Publishing, 2001.

-
- [13] L. Silvester, A. Antzara, G. Boskovic, E. Heracleous, A. A. Lemonidou, and D. B. Bukur, "NiO supported on Al₂O₃ and ZrO₂ oxygen carriers for chemical looping steam methane reforming," *International Journal of Hydrogen Energy*, 2015.
- [14] S. Arndt, G. Laugel, S. Levchenko, R. Horn, M. Baerns, M. Scheffler, R. Schlögl, and R. Schomäcker, "A critical assessment of Li/MgO-based catalysts for the oxidative coupling of methane," *Catalysis Reviews*, vol. 53, no. 4, pp. 424–514, 2011.
- [15] P.-L. Boey, G. P. Maniam, and S. A. Hamid, "Performance of calcium oxide as a heterogeneous catalyst in biodiesel production: A review," *Chemical Engineering Journal*, vol. 168, no. 1, pp. 15–22, 2011.
- [16] M.-C. Hsiao, C.-C. Lin, and Y.-H. Chang, "Microwave irradiation-assisted transesterification of soybean oil to biodiesel catalyzed by nanopowder calcium oxide," *Fuel*, vol. 90, no. 5, pp. 1963–1967, 2011.
- [17] L. Yang, Y. Choi, W. Qin, H. Chen, K. Blinn, M. Liu, P. Liu, J. Bai, T. A. Tyson, and M. Liu, "Promotion of water-mediated carbon removal by nanostructured barium oxide/nickel interfaces in solid oxide fuel cells," *Nature communications*, vol. 2, p. 357, 2011.
- [18] T. Ito and J. H. Lunsford, "Synthesis of ethylene and ethane by partial oxidation of methane over lithium-doped magnesium oxide," 1985.
- [19] T. Ito, J. Wang, C. H. Lin, and J. H. Lunsford, "Oxidative dimerization of methane over a lithium-promoted magnesium oxide catalyst," *Journal of the American Chemical Society*, vol. 107, no. 18, pp. 5062–5068, 1985.
- [20] F. Trippe, M. Fröhling, F. Schultmann, R. Stahl, E. Henrich, and A. Dalai, "Comprehensive techno-economic assessment of dimethyl ether (DME) synthesis and Fischer-Tropsch synthesis as alternative process steps within biomass-to-liquid production," *Fuel Processing Technology*, vol. 106, pp. 577–586, 2013.
- [21] J. Carrasco, A. Michaelides, M. Forster, S. Haq, R. Raval, and A. Hodgson, "A one-dimensional ice structure built from pentagons," *Nature materials*, vol. 8, no. 5, pp. 427–431, 2009.
- [22] J. Carrasco, A. Hodgson, and A. Michaelides, "A molecular perspective of water at metal interfaces," *Nature materials*, vol. 11, no. 8, pp. 667–674, 2012.
- [23] M. Neurock, V. Pallassana, and R. A. van Santen, "The importance of transient states at higher coverages in catalytic reactions," *Journal of the American Chemical Society*, vol. 122, no. 6, pp. 1150–1153, 2000.
- [24] L. Giordano, J. Goniakowski, and J. Suzanne, "Partial dissociation of water molecules in the (3×2) water monolayer deposited on the MgO (100) surface," *Physical review letters*, vol. 81, no. 6, p. 1271, 1998.

- [25] Y. Kim, J. Stultz, and D. Goodman, "Dissociation of water on MgO (100)," *The Journal of Physical Chemistry B*, vol. 106, no. 7, pp. 1515–1517, 2002.
- [26] J.-H. Cho, J. M. Park, and K. S. Kim, "Influence of intermolecular hydrogen bonding on water dissociation at the MgO (001) surface," *Physical Review B*, vol. 62, no. 15, p. 9981, 2000.
- [27] J. R. Rostrup-Nielsen, J. Sehested, and J. K. Nørskov, "Hydrogen and synthesis gas by steam-and CO₂ reforming," *Advances in catalysis*, vol. 47, pp. 65–139, 2002.
- [28] Y. Xu, A. C. Lausche, S. Wang, T. S. Khan, F. Abild-Pedersen, F. Studt, J. K. Nørskov, and T. Bligaard, "In silico search for novel methane steam reforming catalysts," *New Journal of Physics*, vol. 15, no. 12, p. 125021, 2013.
- [29] A. Haghofer, K. Föttinger, F. Girgsdies, D. Teschner, A. Knop-Gericke, R. Schlögl, and G. Rupprechter, "In situ study of the formation and stability of supported Pd₂Ga methanol steam reforming catalysts," *Journal of Catalysis*, vol. 286, pp. 13–21, 2012.
- [30] F. Fischer and H. Tropsch, "Über die direkte Synthese von Erdöl-Kohlenwasserstoffen bei gewöhnlichem Druck.(Erste Mitteilung)," *Berichte der deutschen chemischen Gesellschaft (A and B Series)*, vol. 59, no. 4, pp. 830–831, 1926.
- [31] P. Lenz-Solomun, M.-C. Wu, and D. W. Goodman, "Methane coupling at low temperatures on Ru (0001) and Ru (11 $\bar{2}$ 0) catalysts," *Catalysis letters*, vol. 25, no. 1-2, pp. 75–86, 1994.
- [32] M. C. Wu and D. W. Goodman, "High-resolution electron energy-loss studies of hydrocarbon formation from methane decomposition on Ru (0001) and Ru (11 $\bar{2}$ 0) catalysts," *Journal of the American Chemical Society*, vol. 116, no. 4, pp. 1364–1371, 1994.
- [33] M.-C. Wu, P. Lenz-Solomun, and D. W. Goodman, "Two-step, oxygen-free route to higher hydrocarbons from methane over ruthenium catalysts," *Journal of Vacuum Science & Technology A*, vol. 12, no. 4, pp. 2205–2209, 1994.
- [34] R. A. van Santen, M. Ghouri, and E. M. Hensen, "Microkinetics of oxygenate formation in the Fischer–Tropsch reaction," *Physical Chemistry Chemical Physics*, vol. 16, no. 21, pp. 10041–10058, 2014.
- [35] I. A. Filot, R. A. van Santen, and E. J. Hensen, "The optimally performing Fischer–Tropsch catalyst," *Angewandte Chemie*, vol. 126, no. 47, pp. 12960–12964, 2014.
- [36] R. A. Van Santen, I. M. Ciobica, E. Van Steen, and M. M. Ghouri, "Mechanistic Issues in Fischer-Tropsch Catalysis," *Advances in catalysis*, vol. 54, p. 127, 2011.
- [37] I. M. Ciobîcă, F. Frechard, R. Van Santen, A. Kleyn, and J. Hafner, "A theoretical study of CH_x chemisorption on the Ru (0001) surface," *Chemical physics letters*, vol. 311, no. 3, pp. 185–192, 1999.

- [38] I. M. Ciobica, *The molecular basis of the fischer tropsch reaction*. PhD thesis, Technische Universiteit Eindhoven, 2002.
- [39] R. C. Brady III and R. Pettit, "Reactions of diazomethane on transition-metal surfaces and their relationship to the mechanism of the Fischer-Tropsch reaction," *Journal of the American Chemical Society*, vol. 102, no. 19, pp. 6181–6182, 1980.
- [40] R. C. Brady III and R. Pettit, "Mechanism of the Fischer-Tropsch reaction. The chain propagation step," *Journal of the American Chemical Society*, vol. 103, no. 5, pp. 1287–1289, 1981.
- [41] I. M. Ciobîcă, F. Frechard, R. A. Van Santen, A. W. Kleyn, and J. Hafner, "A DFT study of transition states for C-H activation on the Ru (0001) surface," *The Journal of Physical Chemistry B*, vol. 104, no. 14, pp. 3364–3369, 2000.
- [42] J. P. Perdew, K. Burke, and M. Ernzerhof, "Generalized gradient approximation made simple," *Physical review letters*, vol. 77, no. 18, p. 3865, 1996.
- [43] J. Heyd, G. E. Scuseria, and M. Ernzerhof, "Hybrid functionals based on a screened coulomb potential," *The Journal of Chemical Physics*, vol. 118, no. 18, pp. 8207–8215, 2003.
- [44] J. Heyd, G. E. Scuseria, and M. Ernzerhof, "Erratum: "Hybrid functionals based on a screened Coulomb potential" [J. Chem. Phys. 118, 8207 (2003)]," *The Journal of Chemical Physics*, vol. 124, no. 21, p. 219906, 2006.
- [45] A. Tkatchenko, R. A. DiStasio Jr, R. Car, and M. Scheffler, "Accurate and efficient method for many-body van der waals interactions," *Physical review letters*, vol. 108, no. 23, p. 236402, 2012.
- [46] X. Ren, P. Rinke, G. E. Scuseria, and M. Scheffler, "Renormalized second-order perturbation theory for the electron correlation energy: Concept, implementation, and benchmarks," *Physical Review B*, vol. 88, no. 3, p. 035120, 2013.
- [47] J. H. Holland, *Adaptation in natural and artificial systems: An introductory analysis with applications to biology, control, and artificial intelligence*. U Michigan Press, 1975.
- [48] F. Chuang, C. V. Ciobanu, V. Shenoy, C.-Z. Wang, and K.-M. Ho, "Finding the reconstructions of semiconductor surfaces via a genetic algorithm," *Surface science*, vol. 573, no. 2, pp. L375–L381, 2004.
- [49] M. Sierka, T. K. Todorova, J. Sauer, S. Kaya, D. Stacchiola, J. Weissenrieder, S. Shaikhutdinov, and H.-J. Freund, "Oxygen adsorption on Mo (112) surface studied by ab initio genetic algorithm and experiment," *The Journal of chemical physics*, vol. 126, no. 23, p. 234710, 2007.
- [50] E. Weinan, W. Ren, and E. Vanden-Eijnden, "String method for the study of rare events," *Phys Rev B*, vol. 66, p. 052301, 2002.

- [51] M. Scheffler and J. Dabrowski, "Parameter-free calculations of total energies, interatomic forces and vibrational entropies of defects in semiconductors," *Philosophical Magazine A*, vol. 58, no. 1, pp. 107–121, 1988.
- [52] K. Reuter, C. Stampf, and M. Scheffler, "Ab initio atomistic thermodynamics and statistical mechanics of surface properties and functions," in *Handbook of Materials Modeling* (S. Yip, ed.), pp. 149–194, Springer Netherlands, 2005.
- [53] J. Rogal and K. Reuter, "Ab initio atomistic thermodynamics for surfaces: A primer," in *VT-142 RTO AVT/VKI Lecture Series*, pp. 2–1, NATO Research and Technology Organisation, 2007.
- [54] T. K. Shimizu, A. Mugarza, J. I. Cerdá, and M. Salmeron, "Structure and reactions of carbon and hydrogen on Ru (0001): A scanning tunneling microscopy study," *The Journal of chemical physics*, vol. 129, no. 24, p. 244103, 2008.
- [55] Y. Zhou, M. Henderson, W. Feng, and J. White, "Decomposition of methyl iodide on Ru (001)," *Surface science*, vol. 224, no. 1, pp. 386–406, 1989.
- [56] J. Nocedal and S. Wright, *Numerical optimization*. Springer Science & Business Media, 2006.
- [57] H. Eyring, "The activated complex in chemical reactions," *The Journal of Chemical Physics*, vol. 3, no. 2, pp. 107–115, 1935.
- [58] G. Henkelman and H. Jónsson, "A dimer method for finding saddle points on high dimensional potential surfaces using only first derivatives," *The Journal of chemical physics*, vol. 111, no. 15, pp. 7010–7022, 1999.
- [59] H. Jónsson, G. Mills, and K. W. Jacobsen, "Nudged elastic band method for finding minimum energy paths of transitions," p. 385, 1998.
- [60] G. Henkelman and H. Jónsson, "Improved tangent estimate in the nudged elastic band method for finding minimum energy paths and saddle points," *The Journal of chemical physics*, vol. 113, no. 22, pp. 9978–9985, 2000.
- [61] G. Henkelman, B. P. Uberuaga, and H. Jónsson, "A climbing image nudged elastic band method for finding saddle points and minimum energy paths," *The Journal of chemical physics*, vol. 113, no. 22, pp. 9901–9904, 2000.
- [62] E. Weinan, W. Ren, and E. Vanden-Eijnden, "Simplified and improved string method for computing the minimum energy paths in barrier-crossing events," *The Journal of Chemical Physics*, vol. 126, no. 16, p. 164103, 2007.
- [63] F. Schubert, M. Rossi, C. Baldauf, K. Pagel, S. Warnke, G. von Helden, F. Filsinger, P. Kupser, G. Meijer, M. Salwiczek, B. Koksche, M. Scheffler, and V. Blum, "Exploring the conformational preferences of 20-residue peptides in isolation: Ac-Ala19-Lys + H⁺ vs. Ac-Lys-Ala19 + H⁺ and the current reach of DFT," *Phys. Chem. Chem. Phys.*, vol. 17, pp. 7373–7385, 2015.

-
- [64] E. B. Wilson, J. C. Decius, and P. C. Cross, *Molecular vibrations: The theory of infrared and Raman vibrational spectra*. Courier Corporation, 2012.
- [65] P. A. Dirac, “The quantum theory of the emission and absorption of radiation,” in *Proceedings of the Royal Society of London A: Mathematical, Physical and Engineering Sciences*, vol. 114, pp. 243–265, The Royal Society, 1927.
- [66] E. Le Ru, S. Meyer, C. Artur, P. Etchegoin, J. Grand, P. Lang, and F. Maurel, “Experimental demonstration of surface selection rules for sers on flat metallic surfaces,” *Chemical Communications*, vol. 47, no. 13, pp. 3903–3905, 2011.
- [67] I. Zawisza, M. Nullmeier, S. E. Pust, R. Boukherroub, S. Szunerits, and G. Wittstock, “Application of thin titanium/titanium oxide layers deposited on gold for infrared reflection absorption spectroscopy: structural studies of lipid bilayers,” *Langmuir*, vol. 24, no. 14, pp. 7378–7387, 2008.
- [68] H. Sanders, P. Gardner, D. King, and M. Morris, “A RAIRS investigation of desorption and dissociation of water on NiO thin films probed by NO and CO titration,” *Surface science*, vol. 304, no. 1, pp. 159–167, 1994.
- [69] M. Moskovits, “Surface selection rules,” *The Journal of Chemical Physics*, vol. 77, no. 9, pp. 4408–4416, 1982.
- [70] M.-P. Gaigeot, M. Martinez, and R. Vuilleumier, “Infrared spectroscopy in the gas and liquid phase from first principle molecular dynamics simulations: application to small peptides,” *Molecular Physics*, vol. 105, no. 19-22, pp. 2857–2878, 2007.
- [71] M. Thomas, M. Brehm, R. Fligg, P. Vöhringer, and B. Kirchner, “Computing vibrational spectra from ab initio molecular dynamics,” *Physical Chemistry Chemical Physics*, vol. 15, no. 18, pp. 6608–6622, 2013.
- [72] G. Bussi, D. Donadio, and M. Parrinello, “Canonical sampling through velocity rescaling,” *The Journal of chemical physics*, vol. 126, no. 1, p. 014101, 2007.
- [73] G. Bussi and M. Parrinello, “Stochastic thermostats: comparison of local and global schemes,” *Computer Physics Communications*, vol. 179, no. 1, pp. 26–29, 2008.
- [74] D. Frenkel and B. Smit, *Understanding molecular simulation: from algorithms to applications*, vol. 1. Academic press, 2001.
- [75] D. A. McQuarrie, *Statistical Mechanics*. Mill Valey, Calif.: University Science Books, 2000.
- [76] R. Ramírez, P. P. Kumar, D. Marx, *et al.*, “Quantum corrections to classical time-correlation functions: hydrogen bonding and anharmonic floppy modes,” *The Journal of chemical physics*, vol. 121, no. 9, pp. 3973–3983, 2004.

- [77] M. Schmitz and P. Tavan, "Vibrational spectra from atomic fluctuations in dynamics simulations. II. Solvent-induced frequency fluctuations at femtosecond time resolution," *The Journal of chemical physics*, vol. 121, no. 24, pp. 12247–12258, 2004.
- [78] E. Kaxiras, Y. Bar-Yam, J. Joannopoulos, and K. Pandey, "Ab initio theory of polar semiconductor surfaces. I. Methodology and the (22) reconstructions of GaAs (111)," *Physical Review B*, vol. 35, no. 18, p. 9625, 1987.
- [79] C. M. Weinert and M. Scheffler, "Mechanisms of defect pairing in semiconductors: A study for chalcogens in silicon," *Physical review letters*, vol. 58, no. 14, p. 1456, 1987.
- [80] L. B. Vilhelmsen and B. Hammer, "Systematic Study of Au₆ to Au₁₂ Gold Clusters on MgO (100) F Centers Using Density-Functional Theory," *Physical review letters*, vol. 108, no. 12, p. 126101, 2012.
- [81] R. L. Johnston, "Evolving better nanoparticles: Genetic algorithms for optimising cluster geometries," *Dalton Transactions*, no. 22, pp. 4193–4207, 2003.
- [82] S. Bhattacharya, S. V. Levchenko, L. M. Ghiringhelli, and M. Scheffler, "Stability and Metastability of Clusters in a Reactive Atmosphere: Theoretical Evidence for Unexpected Stoichiometries of MgMO_x," *Physical review letters*, vol. 111, no. 13, p. 135501, 2013.
- [83] A. R. Oganov and C. W. Glass, "Crystal structure prediction using ab initio evolutionary techniques: Principles and applications," *The Journal of chemical physics*, vol. 124, no. 24, p. 244704, 2006.
- [84] Y. Sugita and Y. Okamoto, "Replica-exchange molecular dynamics method for protein folding," *Chemical physics letters*, vol. 314, no. 1, pp. 141–151, 1999.
- [85] B. Hartke, "Global geometry optimization of clusters using genetic algorithms," *The Journal of Physical Chemistry*, vol. 97, no. 39, pp. 9973–9976, 1993.
- [86] T. N. Ellis, J. M. Hofer, G. M. Timmerman-Vaughan, C. J. Coyne, and R. P. Hellens, "Mendel, 150 years on," *Trends in plant science*, vol. 16, no. 11, pp. 590–596, 2011.
- [87] J. H. Nadeau and A. M. Dudley, "Genetics: Systems genetics," *Science (New York, NY)*, vol. 331, no. 6020, p. 1015, 2011.
- [88] G. L. Hart, V. Blum, M. J. Walorski, and A. Zunger, "Evolutionary approach for determining first-principles hamiltonians," *Nature materials*, vol. 4, no. 5, pp. 391–394, 2005.
- [89] V. Blum, G. L. Hart, M. J. Walorski, and A. Zunger, "Using genetic algorithms to map first-principles results to model hamiltonians: Application to the generalized ising model for alloys," *Physical Review B*, vol. 72, no. 16, p. 165113, 2005.
- [90] C. Wu, D. Schmidt, C. Wolverton, and W. Schneider, "Accurate coverage-dependence incorporated into first-principles kinetic models: Catalytic NO oxidation on Pt (111)," *Journal of Catalysis*, vol. 286, pp. 88–94, 2012.

-
- [91] W. Ritz, "Über eine neue Methode zur Lösung gewisser Variationsprobleme der mathematischen Physik.," *J. reine angew. Math.*, no. 135, pp. 1–61, 1909.
- [92] D. R. Hartree, "The wave mechanics of an atom with a non-Coulomb central field. Part I. Theory and methods," in *Mathematical Proceedings of the Cambridge Philosophical Society*, vol. 24, pp. 89–110, Cambridge Univ Press, 1928.
- [93] P. Hohenberg and W. Kohn, "Inhomogeneous electron gas," *Physical review*, vol. 136, no. 3B, p. B864, 1964.
- [94] W. Kohn and L. J. Sham, "Self-consistent equations including exchange and correlation effects," *Physical Review*, vol. 140, no. 4A, p. A1133, 1965.
- [95] A. Görling, "Density-functional theory for excited states," *Physical Review A*, vol. 54, no. 5, p. 3912, 1996.
- [96] P. A. Dirac, "Note on exchange phenomena in the Thomas atom," in *Mathematical Proceedings of the Cambridge Philosophical Society*, vol. 26, pp. 376–385, Cambridge Univ Press, 1930.
- [97] D. M. Ceperley and B. Alder, "Ground state of the electron gas by a stochastic method," *Physical Review Letters*, vol. 45, no. 7, p. 566, 1980.
- [98] J. P. Perdew and Y. Wang, "Accurate and simple analytic representation of the electron-gas correlation energy," *Physical Review B*, vol. 45, no. 23, p. 13244, 1992.
- [99] R. O. Jones and O. Gunnarsson, "The density functional formalism, its applications and prospects," *Reviews of Modern Physics*, vol. 61, no. 3, p. 689, 1989.
- [100] E. H. Lieb and S. Oxford, "Improved lower bound on the indirect coulomb energy," *International Journal of Quantum Chemistry*, vol. 19, no. 3, pp. 427–439, 1981.
- [101] V. N. Staroverov, G. E. Scuseria, J. Tao, and J. P. Perdew, "Tests of a ladder of density functionals for bulk solids and surfaces," *Physical Review B*, vol. 69, no. 7, p. 075102, 2004.
- [102] F. Tran, R. Laskowski, P. Blaha, and K. Schwarz, "Performance on molecules, surfaces, and solids of the Wu-Cohen GGA exchange-correlation energy functional," *Physical Review B*, vol. 75, no. 11, p. 115131, 2007.
- [103] V. N. Staroverov, G. E. Scuseria, J. Tao, and J. P. Perdew, "Erratum: Tests of a ladder of density functionals for bulk solids and surfaces [Phys. Rev. B 69, 075102 (2004)]," *Physical Review B*, vol. 78, no. 23, p. 239907, 2008.
- [104] M. C. Holthausen and W. Koch, "A chemist's guide to density functional theory," 2000.
- [105] E. Clementi and S. J. Chakravorty, "A comparative study of density functional models to estimate molecular atomization energies," *The Journal of Chemical Physics*, vol. 93, no. 4, pp. 2591–2602, 1990.

-
- [106] A. D. Becke, "A new mixing of hartree-fock and local density-functional theories," *The Journal of Chemical Physics*, vol. 98, no. 2, pp. 1372–1377, 1993.
- [107] J. Harris, "Adiabatic-connection approach to kohn-sham theory," *Physical Review A*, vol. 29, no. 4, p. 1648, 1984.
- [108] A. D. Becke, "Density-functional thermochemistry. IV. A new dynamical correlation functional and implications for exact-exchange mixing," *The Journal of chemical physics*, vol. 104, no. 3, pp. 1040–1046, 1996.
- [109] J. P. Perdew, M. Ernzerhof, and K. Burke, "Rationale for mixing exact exchange with density functional approximations," *The Journal of Chemical Physics*, vol. 105, no. 22, pp. 9982–9985, 1996.
- [110] A. Görling and M. Levy, "Correlation-energy functional and its high-density limit obtained from a coupling-constant perturbation expansion," *Physical Review B*, vol. 47, no. 20, p. 13105, 1993.
- [111] C. Adamo and V. Barone, "Toward reliable density functional methods without adjustable parameters: The PBE0 model," *The Journal of chemical physics*, vol. 110, no. 13, pp. 6158–6170, 1999.
- [112] A. D. Becke, "Density-functional thermochemistry. III. The role of exact exchange," *The Journal of Chemical Physics*, vol. 98, no. 7, pp. 5648–5652, 1993.
- [113] H. J. Monkhorst, "Hartree-fock density of states for extended systems," *Physical Review B*, vol. 20, no. 4, p. 1504, 1979.
- [114] J. Delhalle and J.-L. Calais, "Direct-space analysis of the hartree-fock energy bands and density of states for metallic extended systems," *Physical Review B*, vol. 35, no. 18, p. 9460, 1987.
- [115] J. Paier, M. Marsman, and G. Kresse, "Why does the B3LYP hybrid functional fail for metals?," *The Journal of chemical physics*, vol. 127, no. 2, p. 024103, 2007.
- [116] A. V. Krukau, O. A. Vydrov, A. F. Izmaylov, and G. E. Scuseria, "Influence of the exchange screening parameter on the performance of screened hybrid functionals.," *The Journal of chemical physics*, vol. 125, no. 22, pp. 224106–224106, 2006.
- [117] C. Møller and M. S. Plesset, "Note on an approximation treatment for many-electron systems," *Physical Review*, vol. 46, no. 7, p. 618, 1934.
- [118] J. P. Perdew and K. Schmidt, "Jacob's ladder of density functional approximations for the exchange-correlation energy," in *AIP Conference Proceedings*, pp. 1–20, IOP INSTITUTE OF PHYSICS PUBLISHING LTD, 2001.
- [119] A. Szabo, *Modern Quantum Chemistry: Introduction to Advanced Electronic Structure Theory*. Courier Corporation, 1996.

-
- [120] D. Bohm and D. Pines, "A collective description of electron interactions. I. Magnetic interactions," *Physical Review*, vol. 82, no. 5, p. 625, 1951.
- [121] D. Pines and D. Bohm, "A collective description of electron interactions: II. Collective vs individual particle aspects of the interactions," *Physical Review*, vol. 85, no. 2, p. 338, 1952.
- [122] D. Bohm and D. Pines, "A collective description of electron interactions: III. Coulomb interactions in a degenerate electron gas," *Physical Review*, vol. 92, no. 3, p. 609, 1953.
- [123] X. Ren, P. Rinke, C. Joas, and M. Scheffler, "Random-phase approximation and its applications in computational chemistry and materials science," *Journal of Materials Science*, vol. 47, no. 21, pp. 7447–7471, 2012.
- [124] D. C. Langreth and J. P. Perdew, "The exchange-correlation energy of a metallic surface," *Solid State Communications*, vol. 17, no. 11, pp. 1425–1429, 1975.
- [125] O. Gunnarsson and B. Lundqvist, "Exchange and correlation in atoms, molecules, and solids by the spin-density-functional formalism," *Physical Review B*, vol. 13, no. 10, p. 4274, 1976.
- [126] D. C. Langreth and J. P. Perdew, "Exchange-correlation energy of a metallic surface: Wave-vector analysis," *Physical Review B*, vol. 15, no. 6, p. 2884, 1977.
- [127] R. Kubo, "The fluctuation-dissipation theorem," *Reports on progress in physics*, vol. 29, no. 1, p. 255, 1966.
- [128] F. Furche, "Molecular tests of the random phase approximation to the exchange-correlation energy functional," *Physical Review B*, vol. 64, no. 19, p. 195120, 2001.
- [129] J. Harl and G. Kresse, "Accurate bulk properties from approximate many-body techniques," *Physical review letters*, vol. 103, no. 5, p. 056401, 2009.
- [130] X. Ren, A. Tkatchenko, P. Rinke, and M. Scheffler, "Beyond the random-phase approximation for the electron correlation energy: The importance of single excitations," *Physical review letters*, vol. 106, no. 15, p. 153003, 2011.
- [131] K. Singwi, M. Tosi, R. Land, and A. Sjölander, "Electron correlations at metallic densities," *Physical Review*, vol. 176, no. 2, p. 589, 1968.
- [132] J. Klimeš and A. Michaelides, "Perspective: Advances and challenges in treating van der Waals dispersion forces in density functional theory," *The Journal of chemical physics*, vol. 137, no. 12, p. 120901, 2012.
- [133] S. Grimme, "Semiempirical GGA-type density functional constructed with a long-range dispersion correction," *Journal of computational chemistry*, vol. 27, no. 15, pp. 1787–1799, 2006.

-
- [134] A. Tkatchenko and M. Scheffler, "Accurate molecular van der Waals interactions from ground-state electron density and free-atom reference data," *Physical review letters*, vol. 102, no. 7, p. 073005, 2009.
- [135] K. Tang, "Dynamic polarizabilities and van der waals coefficients," *Physical Review*, vol. 177, no. 1, p. 108, 1969.
- [136] X. Chu and A. Dalgarno, "Linear response time-dependent density functional theory for van der waals coefficients.," *The Journal of chemical physics*, vol. 121, no. 9, pp. 4083–4088, 2004.
- [137] P. Jurečka, J. Šponer, J. Černý, and P. Hobza, "Benchmark database of accurate (MP2 and CCSD (T) complete basis set limit) interaction energies of small model complexes, DNA base pairs, and amino acid pairs," *Physical Chemistry Chemical Physics*, vol. 8, no. 17, pp. 1985–1993, 2006.
- [138] A. Donchev, "Many-body effects of dispersion interaction," *The Journal of chemical physics*, vol. 125, no. 7, p. 074713, 2006.
- [139] V. G. Ruiz, W. Liu, E. Zojer, M. Scheffler, and A. Tkatchenko, "Density-functional theory with screened van der Waals interactions for the modeling of hybrid inorganic-organic systems," *Physical review letters*, vol. 108, no. 14, p. 146103, 2012.
- [140] E. M. Lifshitz, "The theory of molecular attractive forces between solids," 1956.
- [141] E. Zaremba and W. Kohn, "Van der Waals interaction between an atom and a solid surface," *Physical Review B*, vol. 13, no. 6, p. 2270, 1976.
- [142] S. Patil, K. Tang, and J. Toennies, "Damping functions for the pairwise sum model of the atom–surface potential," *The Journal of chemical physics*, vol. 116, no. 18, pp. 8118–8123, 2002.
- [143] V. Blum, R. Gehrke, F. Hanke, P. Havu, V. Havu, X. Ren, K. Reuter, and M. Scheffler, "Ab initio molecular simulations with numeric atom-centered orbitals," *Computer Physics Communications*, vol. 180, no. 11, pp. 2175–2196, 2009.
- [144] V. Blum M. Scheffler *et al.*, "The Fritz Haber Institute ab initio molecular simulations package (FHI-aims)." <https://aimsclub.fhi-berlin.mpg.de>, 2009.
- [145] M. A. Henderson, "The interaction of water with solid surfaces: fundamental aspects revisited," *Surface Science Reports*, vol. 46, no. 1, pp. 1–308, 2002.
- [146] R. Włodarczyk, M. Sierka, K. Kwapień, J. Sauer, E. Carrasco, A. Aumer, J. F. Gomes, M. Sterrer, and H.-J. Freund, "Structures of the ordered water monolayer on MgO (001)," *The Journal of Physical Chemistry C*, vol. 115, no. 14, pp. 6764–6774, 2011.
- [147] J. Heidberg, B. Redlich, and D. Wetter, "Adsorption of water vapor on the MgO (100) single crystal surface," *Berichte der Bunsengesellschaft für physikalische Chemie*, vol. 99, no. 11, pp. 1333–1337, 1995.

- [148] D. Ferry, A. Glebov, V. Senz, J. Suzanne, J. Toennies, and H. Weiss, "Observation of the second ordered phase of water on the MgO (100) surface: Low energy electron diffraction and helium atom scattering studies," *The Journal of chemical physics*, vol. 105, no. 4, pp. 1697–1701, 1996.
- [149] M. Odelius, "Mixed molecular and dissociative water adsorption on MgO (100)," *Physical review letters*, vol. 82, no. 19, p. 3919, 1999.
- [150] M. Iedema, N. Kizhakevariam, and J. Cowin, "Mixed oxide surfaces: Ultrathin films of $\text{Ca}_x\text{Mg}_{(1-x)}\text{O}$," *The Journal of Physical Chemistry B*, vol. 102, no. 4, pp. 693–700, 1998.
- [151] Y. Yu, Q. Guo, S. Liu, E. Wang, and P. J. Møller, "Partial dissociation of water on a MgO (100) film," *Physical Review B*, vol. 68, no. 11, p. 115414, 2003.
- [152] R. S. Alvim, I. Borges Jr, D. G. Costa, and A. A. Leitao, "Density-functional theory simulation of the dissociative chemisorption of water molecules on the MgO (001) surface," *The Journal of Physical Chemistry C*, vol. 116, no. 1, pp. 738–744, 2011.
- [153] N. H. Florin and A. T. Harris, "Enhanced hydrogen production from biomass with in situ carbon dioxide capture using calcium oxide sorbents," *Chemical Engineering Science*, vol. 63, no. 2, pp. 287–316, 2008.
- [154] H. Gupta and L.-S. Fan, "Carbonation-calcination cycle using high reactivity calcium oxide for carbon dioxide separation from flue gas," *Industrial & engineering chemistry research*, vol. 41, no. 16, pp. 4035–4042, 2002.
- [155] C. R. Venkat Reddy, R. Oshel, and J. G. Verkade, "Room-temperature conversion of soybean oil and poultry fat to biodiesel catalyzed by nanocrystalline calcium oxides," *Energy & Fuels*, vol. 20, no. 3, pp. 1310–1314, 2006.
- [156] X. Liu, H. He, Y. Wang, S. Zhu, and X. Piao, "Transesterification of soybean oil to biodiesel using CaO as a solid base catalyst," *Fuel*, vol. 87, no. 2, pp. 216–221, 2008.
- [157] D. M. Alonso, R. Mariscal, M. L. Granados, and P. Maireles-Torres, "Biodiesel preparation using Li/CaO catalysts: activation process and homogeneous contribution," *Catalysis Today*, vol. 143, no. 1, pp. 167–171, 2009.
- [158] T. Anastasiadou, L. Loukatzikou, C. Costa, and A. Efstathiou, "Understanding the synergistic catalytic effect between La_2O_3 and CaO for the CH_4 lean de- NO_x reaction: Kinetic and mechanistic studies," *The Journal of Physical Chemistry B*, vol. 109, no. 28, pp. 13693–13703, 2005.
- [159] N. De Leeuw, J. Purton, S. Parker, G. Watson, and G. Kresse, "Density functional theory calculations of adsorption of water at calcium oxide and calcium fluoride surfaces," *Surface science*, vol. 452, no. 1, pp. 9–19, 2000.
- [160] N. De Leeuw and J. Purton, "Density-functional theory calculations of the interaction of protons and water with low-coordinated surface sites of calcium oxide," *Physical Review B*, vol. 63, no. 19, p. 195417, 2001.

- [161] J. Carrasco, F. Illas, and N. Lopez, "Dynamic ion pairs in the adsorption of isolated water molecules on alkaline-earth oxide (001) surfaces," *Physical review letters*, vol. 100, no. 1, p. 016101, 2008.
- [162] X. L. Hu, J. Carrasco, J. Klimeš, and A. Michaelides, "Trends in water monomer adsorption and dissociation on flat insulating surfaces," *Physical Chemistry Chemical Physics*, vol. 13, no. 27, pp. 12447–12453, 2011.
- [163] H. Manzano, R. J. Pellenq, F.-J. Ulm, M. J. Buehler, and A. C. van Duin, "Hydration of calcium oxide surface predicted by reactive force field molecular dynamics," *Langmuir*, vol. 28, no. 9, pp. 4187–4197, 2012.
- [164] J. T. Newberg, D. E. Starr, S. Yamamoto, S. Kaya, T. Kendelewicz, E. R. Mysak, S. Porsgaard, M. B. Salmeron, G. E. Brown Jr, A. Nilsson, *et al.*, "Autocatalytic surface hydroxylation of MgO (100) terrace sites observed under ambient conditions," *The Journal of Physical Chemistry C*, vol. 115, no. 26, pp. 12864–12872, 2011.
- [165] X. Shao, P. Myrach, N. Nilius, and H.-J. Freund, "Growth and morphology of calcium-oxide films grown on Mo (001)," *The Journal of Physical Chemistry C*, vol. 115, no. 17, pp. 8784–8789, 2011.
- [166] P. Liu, T. Kendelewicz, G. E. Brown, G. A. Parks, and P. Pianetta, "Reaction of water with vacuum-cleaved CaO (100) surfaces: an x-ray photoemission spectroscopy study," *Surface science*, vol. 416, no. 1-2, pp. 326–340, 1998.
- [167] W. A. Halim and A. Shalabi, "Surface morphology and interaction between water and MgO, CaO and SrO surfaces: Periodic HF and DFT calculations," *Applied surface science*, vol. 221, no. 1, pp. 53–61, 2004.
- [168] H. Guhl, W. Miller, and K. Reuter, "Water adsorption and dissociation on SrTiO₃ (001) revisited: A density functional theory study," *Physical Review B*, vol. 81, no. 15, p. 155455, 2010.
- [169] A. Becerra-Toledo, M. Castell, and L. Marks, "Water adsorption on SrTiO₃ (001): I. Experimental and simulated STM," *Surface Science*, vol. 606, no. 7, pp. 762–765, 2012.
- [170] G. Zhang, H. Hattori, and K. Tanabe, "Aldol addition of acetone, catalyzed by solid base catalysts: magnesium oxide, calcium oxide, strontium oxide, barium oxide, lanthanum (III) oxide and zirconium oxide," *Applied catalysis*, vol. 36, pp. 189–197, 1988.
- [171] N. Nilius, T. Wallis, and W. Ho, "Development of one-dimensional band structure in artificial gold chains," *Science*, vol. 297, no. 5588, pp. 1853–1856, 2002.
- [172] C. Blumenstein, J. Schäfer, S. Mietke, S. Meyer, A. Dollinger, M. Lochner, X. Cui, L. Patthey, R. Matzdorf, and R. Claessen, "Atomically controlled quantum chains hosting a Tomonaga-Luttinger liquid," *Nature Physics*, vol. 7, no. 10, pp. 776–780, 2011.
- [173] T. Nagao, S. Yaginuma, T. Inaoka, and T. Sakurai, "One-dimensional plasmon in an atomic-scale metal wire," *Physical review letters*, vol. 97, no. 11, p. 116802, 2006.

- [174] L. J. Sherry, R. Jin, C. A. Mirkin, G. C. Schatz, and R. P. Van Duyne, "Localized surface plasmon resonance spectroscopy of single silver triangular nanoprisms," *Nano letters*, vol. 6, no. 9, pp. 2060–2065, 2006.
- [175] J. V. Barth, G. Costantini, and K. Kern, "Engineering atomic and molecular nanostructures at surfaces," *Nature*, vol. 437, no. 7059, pp. 671–679, 2005.
- [176] P. Gambardella, A. Dallmeyer, K. Maiti, M. Malagoli, S. Rusponi, P. Ohresser, W. Eberhardt, C. Carbone, and K. Kern, "Oscillatory magnetic anisotropy in one-dimensional atomic wires," *Physical review letters*, vol. 93, no. 7, p. 077203, 2004.
- [177] O. Gurlu, O. A. Adam, H. J. Zandvliet, and B. Poelsema, "Self-organized, one-dimensional Pt nanowires on Ge (001)," *Applied physics letters*, vol. 83, no. 22, pp. 4610–4612, 2003.
- [178] D. Donadio, L. M. Ghiringhelli, and L. Delle Site, "Autocatalytic and cooperatively stabilized dissociation of water on a stepped platinum surface," *Journal of the American Chemical Society*, vol. 134, no. 46, pp. 19217–19222, 2012.
- [179] Q. Li, J. R. Owens, C. Han, B. G. Sumpter, W. Lu, J. Bernholc, V. Meunier, P. Maksymovych, M. Fuentes-Cabrera, and M. Pan, "Self-organized and Cu-coordinated surface linear polymerization," *Scientific reports*, vol. 3, 2013.
- [180] V. Simic-Milosevic, M. Heyde, X. Lin, T. König, H.-P. Rust, M. Sterrer, T. Risse, N. Nilius, H.-J. Freund, L. Giordano, *et al.*, "Charge-induced formation of linear Au clusters on thin MgO films: Scanning tunneling microscopy and density-functional theory study," *Physical Review B*, vol. 78, no. 23, p. 235429, 2008.
- [181] J. Lee, D. C. Sorescu, X. Deng, and K. D. Jordan, "Water chain formation on TiO₂ (110)," *The Journal of Physical Chemistry Letters*, vol. 4, no. 1, pp. 53–57, 2012.
- [182] A. Michaelides and K. Morgenstern, "Ice nanoclusters at hydrophobic metal surfaces," *Nature materials*, vol. 6, no. 8, pp. 597–601, 2007.
- [183] J.-W. Shin, N. Hammer, E. Diken, M. Johnson, R. Walters, T. Jaeger, M. Duncan, R. Christie, and K. Jordan, "Infrared signature of structures associated with the H+(H₂O)_n (n= 6 to 27) clusters," *Science*, vol. 304, no. 5674, pp. 1137–1140, 2004.
- [184] V. V. Rybkin, A. O. Simakov, V. Bakken, S. Reine, T. Kjærgaard, T. Helgaker, and E. Uggerud, "Insights into the dynamics of evaporation and proton migration in protonated water clusters from large-scale born–oppenheimer direct dynamics," *Journal of computational chemistry*, vol. 34, no. 7, pp. 533–544, 2013.
- [185] S. V. Levchenko, X. Ren, J. Wieferink, P. Rinke, V. Blum, M. Scheffler, and R. Johanni, "Hybrid functionals for large periodic systems in an all-electron, numeric atom-centered basis framework," *Computer Physics Communications*, 2015.

-
- [186] J. Carrasco, B. Santra, J. Klimeš, and A. Michaelides, “To wet or not to wet? Dispersion forces tip the balance for water ice on metals,” *Physical review letters*, vol. 106, no. 2, p. 026101, 2011.
- [187] A. Valcárcel, J. Ricart, F. Illas, and A. Clotet, “Theoretical interpretation of the IR spectrum of propyne on Cu (111),” *The Journal of Physical Chemistry B*, vol. 108, no. 47, pp. 18297–18305, 2004.
- [188] K. Reuter and M. Scheffler, “Composition, structure, and stability of RuO₂ (110) as a function of oxygen pressure,” *Physical Review B*, vol. 65, no. 3, p. 035406, 2001.
- [189] L. Kleinman and D. Bylander, “Efficacious form for model pseudopotentials,” *Physical Review Letters*, vol. 48, no. 20, p. 1425, 1982.
- [190] M. Fuchs and M. Scheffler, “Ab initio pseudopotentials for electronic structure calculations of poly-atomic systems using density-functional theory,” *Computer Physics Communications*, vol. 119, no. 1, pp. 67–98, 1999.
- [191] D. Berger, A. J. Logsdail, H. Oberhofer, M. R. Farrow, C. R. A. Catlow, P. Sherwood, A. A. Sokol, V. Blum, and K. Reuter, “Embedded-cluster calculations in a numeric atomic orbital density-functional theory framework,” *The Journal of chemical physics*, vol. 141, no. 2, p. 024105, 2014.
- [192] N. Richter, *Charged point defects in oxides—a case study of MgO bulk and surface F centers*. PhD thesis, Technische Universität Berlin, 2013.
- [193] S. F. Boys and F. d. Bernardi, “The calculation of small molecular interactions by the differences of separate total energies. some procedures with reduced errors,” *Molecular Physics*, vol. 19, no. 4, pp. 553–566, 1970.
- [194] F. Schubert, *Conformational equilibria and spectroscopy of gas-phase homologous peptides from first principles*. PhD thesis, Freie Universität Berlin, 2014.
- [195] M. Rossi, *Ab initio study of alanine-based polypeptide secondary-structure motifs in the gas phase*. PhD thesis, Technische Universität Berlin, 2011.
- [196] L. Delle Site, A. Alavi, and R. Lynden-Bell, “The structure and spectroscopy of monolayers of water on MgO: an ab initio study,” *The Journal of Chemical Physics*, vol. 113, no. 8, pp. 3344–3350, 2000.
- [197] C. Xu and D. Goodman, “Structure and geometry of water adsorbed on the MgO (100) surface,” *Chemical physics letters*, vol. 265, no. 3, pp. 341–346, 1997.
- [198] S.-G. Wang, D.-B. Cao, Y.-W. Li, J. Wang, and H. Jiao, “CH₄ dissociation on Ni surfaces: density functional theory study,” *Surface science*, vol. 600, no. 16, pp. 3226–3234, 2006.
- [199] M.-C. Wu and D. W. Goodman, “High-resolution electron energy-loss measurements of sticking coefficients of methane decomposition on Ru (0001),” *Surface science*, vol. 306, no. 1, pp. L529–L533, 1994.

- [200] J. H. Larsen, P. M. Holmblad, and I. Chorkendorff, "Dissociative sticking of CH₄ on Ru (0001)," *Journal of Chemical Physics*, vol. 110, no. 5, pp. 2637–2642, 1999.
- [201] J. Xu and G. F. Froment, "Methane steam reforming, methanation and water-gas shift: I. Intrinsic kinetics," *AIChE Journal*, vol. 35, no. 1, pp. 88–96, 1989.
- [202] R. Egeberg, S. Ullmann, I. Alstrup, C. Mullins, and I. Chorkendorff, "Dissociation of CH₄ on Ni (111) and Ru (0001)," *Surface science*, vol. 497, no. 1, pp. 183–193, 2002.
- [203] G. Jones, J. G. Jakobsen, S. S. Shim, J. Kleis, M. P. Andersson, J. Rossmeisl, F. Abild-Pedersen, T. Bligaard, S. Helveg, B. Hinnemann, *et al.*, "First principles calculations and experimental insight into methane steam reforming over transition metal catalysts," *Journal of Catalysis*, vol. 259, no. 1, pp. 147–160, 2008.
- [204] T. Choudhary and D. Goodman, "Methane activation on ruthenium: the nature of the surface intermediates," *Topics in catalysis*, vol. 20, no. 1-4, pp. 35–42, 2002.
- [205] B. Xing, X.-Y. Pang, and G.-C. Wang, "C–H bond activation of methane on clean and oxygen pre-covered metals: A systematic theoretical study," *Journal of Catalysis*, vol. 282, no. 1, pp. 74–82, 2011.
- [206] J. A. Herron, S. Tonelli, and M. Mavrikakis, "Atomic and molecular adsorption on Ru (0001)," *Surface Science*, vol. 614, pp. 64–74, 2013.
- [207] B. Hammer, L. B. Hansen, and J. K. Nørskov, "Improved adsorption energetics within density-functional theory using revised perdue-burke-ernzerhof functionals," *Physical Review B*, vol. 59, no. 11, p. 7413, 1999.
- [208] E. M. Karp, T. L. Silbaugh, and C. T. Campbell, "Energetics of Adsorbed CH₃ on Pt (111) by Calorimetry," *Journal of the American Chemical Society*, vol. 135, no. 13, pp. 5208–5211, 2013.
- [209] Z.-P. Liu and P. Hu, "General rules for predicting where a catalytic reaction should occur on metal surfaces: A density functional theory study of CH and CO bond breaking/making on flat, stepped, and kinked metal surfaces," *Journal of the American Chemical Society*, vol. 125, no. 7, pp. 1958–1967, 2003.
- [210] E. M. Karp, T. L. Silbaugh, and C. T. Campbell, "Energetics of Adsorbed CH₃ and CH on Pt (111) by Calorimetry: Dissociative Adsorption of CH₃I," *The Journal of Physical Chemistry C*, vol. 117, no. 12, pp. 6325–6336, 2013.
- [211] H. Kirsch, *Chemical reactions on surfaces-a SFG study*. PhD thesis, Freie Universität Berlin, 2014.
- [212] P. J. Linstrom and W. G. Mallard, "NIST Chemistry webbook; NIST standard reference database No. 69." <http://cccbdb.nist.gov/atomize2.asp>, 2015. (Visited on Apr. 22, 2015).
- [213] A. Demirbas, *Methane gas hydrate*. Springer Science & Business Media, 2010.

-
- [214] E. J. Moniz, H. D. Jacoby, A. Meggs, R. Armtrong, D. Cohn, S. Connors, J. Deutch, Q. Ejaz, J. Hezir, and G. Kaufman, "The future of natural gas," *Massachusetts Institute of Technology report*, 2011.
- [215] M. Picciotti, "Novel ethylene technologies developing, but steam cracking remains king," *Oil and Gas Journal*, vol. 95, no. 25, 1997.
- [216] M. McCoy, M. Reisch, A. Tullo, P. Short, J. Tremblay, and W. Storck, "Production: growth is the norm," *Chem. Eng. News*, vol. 84, pp. 59–68, 2006.
- [217] H. H. Voge and C. R. Adams, "Catalytic oxidation of olefins," *Advances in Catalysis*, vol. 17, p. 151, 1967.
- [218] B. T. Loveless, C. Buda, M. Neurock, and E. Iglesia, "CO chemisorption and dissociation at high coverages during CO hydrogenation on Ru catalysts," *Journal of the American Chemical Society*, vol. 135, no. 16, pp. 6107–6121, 2013.
- [219] R. A. van Santen, M. M. Ghouri, S. Shetty, and E. M. Hensen, "Structure sensitivity of the Fischer–Tropsch reaction; molecular kinetics simulations," *Catalysis Science & Technology*, vol. 1, no. 6, pp. 891–911, 2011.
- [220] J. Cheng, P. Hu, P. Ellis, S. French, G. Kelly, and C. M. Lok, "Chain growth mechanism in Fischer–Tropsch synthesis: A DFT study of CC coupling over Ru, Fe, Rh, and Re surfaces," *The Journal of Physical Chemistry C*, vol. 112, no. 15, pp. 6082–6086, 2008.
- [221] H. Li, G. Fu, and X. Xu, "A new insight into the initial step in the Fischer–Tropsch synthesis: CO dissociation on Ru surfaces," *Physical Chemistry Chemical Physics*, vol. 14, no. 48, pp. 16686–16694, 2012.
- [222] I. Ciobică, G. J. Kramer, Q. Ge, M. Neurock, and R. Van Santen, "Mechanisms for chain growth in Fischer–Tropsch synthesis over Ru (0001)," *Journal of Catalysis*, vol. 212, no. 2, pp. 136–144, 2002.
- [223] J. Cheng, X.-Q. Gong, P. Hu, C. M. Lok, P. Ellis, and S. French, "A quantitative determination of reaction mechanisms from density functional theory calculations: Fischer–Tropsch synthesis on flat and stepped cobalt surfaces," *Journal of Catalysis*, vol. 254, no. 2, pp. 285–295, 2008.
- [224] J. Cheng, P. Hu, P. Ellis, S. French, G. Kelly, and C. M. Lok, "A DFT study of the chain growth probability in Fischer–Tropsch synthesis," *Journal of Catalysis*, vol. 257, no. 1, pp. 221–228, 2008.
- [225] Z.-P. Liu and P. Hu, "A new insight into Fischer–Tropsch synthesis," *Journal of the American Chemical Society*, vol. 124, no. 39, pp. 11568–11569, 2002.
- [226] I. Ransley, L. Ilharco, J. Bateman, B. Sakakini, J. Vickerman, and M. Chesters, "Adsorption and thermal decomposition of ethene and propene on Ru (0001), studied by RAIRS," *Surface science*, vol. 298, no. 1, pp. 187–194, 1993.

-
- [227] I. Filot, R. van Santen, and E. Hensen, “Quantum chemistry of the Fischer–Tropsch reaction catalysed by a stepped ruthenium surface,” *Catalysis Science & Technology*, vol. 4, no. 9, pp. 3129–3140, 2014.
- [228] J. Cheng and P. Hu, “Theory of the kinetics of chemical potentials in heterogeneous catalysis,” *Angewandte Chemie International Edition*, vol. 50, no. 33, pp. 7650–7654, 2011.
- [229] X. Zhao, S. V. Levchenko, *et al.*, “Water interaction with alkaline earth metal oxide (001) surface: A genetic algorithm study,” *in preparation*, 2015.
- [230] X. Shao, N. Nilius, P. Myrach, H.-J. Freund, U. Martinez, S. Prada, L. Giordano, and G. Pacchioni, “Strain-induced formation of ultrathin mixed-oxide films,” *Physical Review B*, vol. 83, no. 24, p. 245407, 2011.
- [231] F. aims team, “Fritz haber institute ab initio molecular simulations: Fhi-aims — a user’s guide,” 2013.
- [232] G.-X. Zhang, A. Tkatchenko, J. Paier, H. Appel, and M. Scheffler, “Van der waals interactions in ionic and semiconductor solids,” *Physical review letters*, vol. 107, no. 24, p. 245501, 2011.

Publications related to this thesis

1. **X. Zhao**, X. Shao, Y. Fujimori, S. Bhattacharya, L. M. Ghiringhelli, H.-J. Freund, M. Sterrer, N. Nilius, and S. V. Levchenko, "Formation of water chains on CaO (001): What drives the 1D growth?," The Journal of Physical Chemistry Letters, vol. 6, no. 7, pp. 1204-1208, 2015.
2. H. Kirsch, **X. Zhao**^{*}, Z. Ren, S. V. Levchenko, M. Wolf, and R. K. Campen, "Controlling CH₂ dissociation on Ru (0001) through surface site blocking by adsorbed hydrogen," Journal of catalysis, vol. 320, pp. 89-96, 2014. (***co-first author**)
3. Y. Fujimori, X. Shao, **X. Zhao**, S. V. Levchenko, N. Nilius, M. Sterrer and H.-J. Freund, "Interaction of water with the CaO (001) surface". In preparation.
4. **X. Zhao**, S. V. Levchenko, et al. "Water interaction with alkaline earth metal oxide (001) surface: A genetic algorithm study". In preparation.

Acknowledgments

Finally comes the acknowledgment part of my thesis after four-years study in theory department of FHI. It has been a remarkable four years for me, working in an excellent group with extraordinary people here. I learned so much from people around me and visitors from all around the world.

Firstly, I would like to thank Prof. Matthias Scheffler for giving me an opportunity to study in FHI – otherwise I could be at some place totally different from Berlin, like Thuwal in Saudi Arab. Moreover, Matthias, thank you very much for all your insightful comments on my papers, posters, presentations, thesis etc. I learned so much from rethinking based on your comments.

To Sergey, you are the person I would to thank the most. As my tutor, you helped me so much in all my work with your knowledge, talent, and patience in particular. You are so open-minded to listen how I think about a problem, even though sometimes I am totally incorrect. It has been a great time working with you, learning from you.

I would like express my great thanks to Saswata and Luca for your help with our genetic algorithm code and other things. To Luca in particular, without your help, I would have spent more time to figure out problems in molecular dynamics simulations.

There are more people helped me in particular cases. Norina, Guoxu, Vivek, Victor helped me a lot in different versions of TS scheme for van der Waals interactions. Norina helped me also in many other problems, like embedded cluster model and so on. Thank you very much. Actually, I always feel not very difficult to find an expert around for help whenever I encounter some particular problem.

To my experimental collaborators, namely Xiang, Niklas, Fujimori, Martin, Harald, and Kramer, thank you for sharing brainstorm times to unified our understandings from theory and experimental perspectives.

I would also deliver my thanks to Amrita, Franz, Aliaksei, Sebas, Basti, Susmita, Maria, Mausumi etc. for your friendship and academic/nonacademic discussions. Talking with you broadened my insight about different academic topics, as well as the diversity of culture around the world. It is so great to share my years with you in Berlin and many other places. For Basti, I owe you a debt for translating my thesis abstract from English to German. Of course, I would also thank Julia, Birgit, and Hanna for your help with so many paper works.

I would like to thank Prof. Schomäcker for being my professor in TU Berlin.

To my parents, actually no words can express how much I owe you. Without your spiritual and material supports, I could not have gone so far from a remote village.

To Mengting, thank you so much for the time you share with me.